UNIVERSITÀ DEGLI STUDI DI TRIESTE

Sede amministrativa del Dottorato di Ricerca
FACOLTÀ DI SCIENZE MATEMATICHE, FISICHE, NATURALI

XXII CICLO DELLA
SCUOLA DI DOTTORATO DI RICERCA IN FISICA

Charm production in proton-proton collisions at the LHC with the ALICE detector

Settore scientifico-disciplinare: FIS/04

DOTTORANDO:
Andrea Rossi

COORDINATORE DEL COLLEGIO DEI DOCENTI:
Chiar.mo Prof. Gaetano Senatore (Univ. Trieste)

FIRMA: ____________________

TUTORE:
Dott. Enrico Fragiacomo (INFN Trieste)

FIRMA: ____________________

RELATORE:
Prof. Rinaldo Rui (Univ. Trieste)

FIRMA: ____________________

ANNO ACCADEMICO 2008/2009

A mio padre

Riassunto

La presente tesi si basa sul lavoro da me effettuato nell'ambito della collaborazione ALICE. L'esperimento ALICE (*A Large Ion Collider Experiment*) studierà collisioni tra nuclei di piombo effettuate al *Large Hadron Collider* (LHC) ad un'energia nel centro di massa per coppia di nucleoni ($\sqrt{\mathrm{s_{NN}}}$) di 5.5 TeV, la più alta mai raggiunta. Lo scopo principale dell'esperimento è quello di investigare le proprietà della materia fortemente interagente alle elevatissime densità di energia (> 10 GeV/fm^3) e temperatura ($\gtrsim 0.2$ GeV) che si aspetta caratterizzino il mezzo formato nelle collisioni tra ioni pesanti a queste energie. Calcoli di QCD su reticolo prevedono che, in queste condizioni, il confinamento dei quark in adroni privi di carica di colore sia rimosso e si formi un plasma di quark e gluoni, denominato *Quark-Gluon Plasma* (QGP). Nelle ultime due decadi, numerose indicazioni della formazione di questo stato della materia sono state osservate negli esperimenti al CERN-SPS ($\sqrt{\mathrm{s_{NN}}} = 17.3$ GeV) e al BNL-RHIC ($\sqrt{\mathrm{s_{NN}}} = 200$ GeV). I risultati principali sono descritti nel primo capitolo.

L'obiettivo del lavoro esposto in questa tesi è la preparazione della misurazione della sezione d'urto per la produzione di mesoni D^0 ($c\bar{u}$) in collisioni protone–protone (p–p), tramite la ricostruzione esclusiva del canale di decadimento $D^0 \to K^-\pi^+$. La misurazione della produzione di adroni con beauty e con charm in collisioni Pb–Pb è fra i punti principali del programma di fisica di ALICE perché permetterà lo studio dei meccanismi di propagazione e adronizzazione dei quark pesanti nella calda e densa materia fortemente interagente prodotta in queste collisioni. I quark pesanti possono essere considerati come sonde ideali per investigare la fase partonica del mezzo formato. Per estrarre informazioni sulle sue proprietà è tuttavia essenziale il confronto tra le quantità osservate in collisioni Pb–Pb e in collisioni p–p, dove la formazione del QGP non è prevista. La produzione di charm in collisioni p–p non è mai stata misurata ad energie paragonabili a quelle accessibili a LHC: l'energia nominale nel centro di massa è $\sqrt{\mathrm{s_{NN}}} = 14$ TeV, superiore di un fattore 7 rispetto all'energia raggiunta al Tevatron. ALICE sarà in grado di verificare le varie predizioni teoriche, basate su diversi approcci perturbativi alla QCD, in un nuovo regime energetico. Questi argomenti sono trattati nel secondo capitolo della tesi.

La strategia per estrarre il tasso di produzione di mesoni D^0 è focalizzata sull'analisi in massa invariante di tutte le possibili coppie di tracce ricostruite con carica opposta. Senza alcuna selezione sulle coppie, il rapporto tra segnale e fondo combinatorio sarebbe troppo piccolo per ottenere delle informazioni significative dalla distribuzione in massa invariante. E' perciò indispensabile pre–selezionare le tracce sulla base di proprietà cinematiche e topologiche. Grazie all'elevata precisione di tracciamento fornita dall'*Inner Tracking System* (ITS) di ALICE, rivelatore descritto nel terzo capitolo della tesi, è possibile ricostruire il punto d'interazione dei fasci di protoni/ioni (vertice primario) e i punti di decadimento (vertici secondari) con precisione sufficiente per distinguerli. Grazie alla micrometrica precisione dell'ITS, risulta possibile sfruttare la vita media relativamente lunga dei mesoni D^0 ($c\tau = 123\ \mu m$) per distinguere le tracce provenienti dal decadimento di una D^0 da quelle provenienti direttamente dal vertice primario di interazione, scartando così gran parte delle coppie di fondo combinatorio.

Un elemento chiave per l'analisi risiede quindi nella piena comprensione della risposta e delle proprietà dell'ITS. Questa comprensione va raggiunta attraverso una scrupolosa fase di messa a punto dell'apparato di cui l'allineamento costituisce l'aspetto cruciale per tutte le analisi di fisica dei quark pesanti. L'ITS è formato da sei strati concentrici di rivelatori al silicio di forma cilindrica. Ogni strato è composto da molti moduli (piú di 2000 in tutto), la cui posizione e orientazione nello spazio possono differire da quelle di progetto, a causa della precisione finita dell'assemblaggio. Questo può degradare la risoluzione spaziale del rivelatore e, di conseguenza, la qualità del tracciamento, riducendo le potenzialità dell'apparato e, perciò, delle analisi fisiche. E' essenziale stimare le reali posizioni dei moduli tramite opportune procedure di "allineamento". Le fonti d'informazione per l'allineamento sono di due tipi, il rilevamento della posizione dei moduli effettuato all'atto dell'assemblaggio e le tracce rilasciate da raggi cosmici (principalmente muoni) o da particelle generate in collisioni p–p. Durante l'estate 2008, l'esperimento ALICE ha collezionato un campione di circa 10^5 tracce da raggi cosmici che è stato usato per validare le misure di rilevamento effettuate per il rivelatore SSD (*Silicon Strip Detector*, i due strati più esterni dell'ITS) e per allineare una parte significativa dell'ITS. I Capitoli 4 e 5 sono interamente dedicati all'allineamento dell'ITS. Nel primo il problema dell'allineamento è introdotto e viene descritta la strategia generale di allineamento. Si passa quindi alla descrizione dettagliata della validazione delle misure di rilevamento effettuate per il rivelatore SSD e vengono mostrati i test fatti per monitorare lo stato dell'allineamento. Il Capitolo 5 è dedicato alla descrizione dei due metodi utilizzati per allineare, basati sulla minimizzazione dei residui tra le tracce ricostruite e i punti misurati. Il metodo principale sfrutta l'algoritmo Millepede e, tramite un fit globale di tutti i residui, estrae tutti i parametri di allineamento simultaneamente. Il secondo metodo, studiato e migliorato in questo lavoro di tesi, esegue una minimizzazione per ogni modulo (minimizzazione "locale") e tiene conto delle correlazioni tra i moduli iterando la procedura fino a quando i risultati non convergono. Questo approccio iterativo "modulo-per-modulo" è descritto in dettaglio: test effettuati su dati simulati per verificarne la funzionalità precedono i risultati ottenuti con i dati da eventi di raggi cosmici collezionati nel 2008. Dalle stime sulla qualità dell'allineamento dell'ITS, effettuate per entrambi i metodi, e dal confronto tra i parametri di allineamento ricavati, si può concludere che i due metodi forniscono prestazioni simili. Dopo la presa-dati di cosmici del 2008, si può inoltre affermare che le procedure di allineamento funzionano e che, per i moduli illuminati dai raggi cosmici, il peggioramento della risoluzione spaziale dovuta al "dis–allineamento" residuo è contenuto entro il 20% della risoluzione ideale del rivelatore.

I risultati promettenti ottenuti con i dati da raggi cosmici permettono di ipotizzare che la stessa qualità di allineamento sarà ottenuta per tutti i moduli dell'ITS pochi mesi dopo la partenza di LHC. Perciò è stato possibile testare le procedure di analisi per la ricostruzione del canale di decadimento $D^0 \to K^-\pi^+$ in simulazioni di collisioni p–p che tenessero conto di uno scenario di allineamento del rivelatore al contempo realistico ma non lontano dallo stato ideale. Gli ultimi due capitoli della tesi sono dedicati a questo argomento. Nel primo viene discussa la strategia di analisi. Dopo la già menzionata selezione sulle coppie di tracce di carica opposta, necessaria per aumentare il rapporto tra segnale e fondo, è possibile, tramite un fit della distribuzione in massa invariante, stimare la quantità di segnale, ovvero il numero di mesoni D^0 decaduti nel canale di decadimento selezionato che hanno oltrepassato la selezione dei tagli e sono stati ricostruiti. Per ricavare il numero di D^0 prodotti, il segnale stimato deve essere diviso per un fattore di efficienza che tenga conto della frazione di mesoni D^0 che non sono ricostruiti a causa della limitata accettanza del rivelatore o che sono rigettati dai tagli. La correzione per l'efficienza è calcolata, usando eventi Monte Carlo, come il rapporto tra le D^0 selezionate e generate: è fondamentale che la simulazione riproduca fedelmente lo spettro in momento dei mesoni generati e le proprietà e la risposta dell'apparato. L'allineamento, in particolare, ha un ruolo centrale: se le risoluzioni spaziali dei vari rivelatori, comprensive dell'effetto dell'allineamento, non sono descritte correttamente nella simulazione, l'efficienza dei tagli calcolata sulla base delle simulazioni Monte Carlo sono in generale diverse da quelle reali, con la conseguente introduzione di un errore sistematico. Questa e le altre principali fonti di errori sistematici sono elencate e discusse all'interno del capitolo.

Una frazione rilevante di D^0 deriva dal decadimento di mesoni B (mesoni contenenti un quark b) e un'appropriata correzione deve essere applicata al segnale estratto dalla distribuzione in massa invariante. A causa delle incertezze teoriche sulla produzione di quark b alle energie di LHC, questa correzione introduce un errore sistematico che, in precedenti studi, è stata valutata essere dell'ordine dell'8%. In questa tesi è presentato un metodo per stimare la frazione di D^0 secondarie (provenienti dal decadimento di un mesone B) direttamente dai dati, sfruttando l'elevata precisione di tracciamento fornita dall'ITS. Il metodo, già usato dall'esperimento CDF, si basa sull'osservazione che la vita media relativamente lunga dei mesoni B ($c\tau \sim 460 - 490$ μm) influenza fortemente la forma della distribuzione del parametro d'impatto dei mesoni secondari, che risulta diversa da quella dei primari. I dettagli del metodo e i risultati ottenuti con eventi simulati sono descritti nell'ultimo capitolo della tesi. I test effettuati indicano che la frazione di D^0 primarie viene stimata correttamente entro il 5%: questo approccio è quindi competitivo con le correzioni basate sui modelli teorici della produzione di quark b.

Contents

Introduction

This work of thesis was carried out in the context of the ALICE collaboration. The ALICE (A Large Ion Collider Experiment) experiment [1, 2, 3] will study Pb–Pb collisions at the Large Hadron Collider (LHC) at a centre of mass energy per nucleon pair $\sqrt{s_{NN}} = 5.5$ TeV, the highest ever reached. The main physics goal of the experiment is the investigation of the properties of strongly-interacting matter in the conditions of high energy density (> 10 GeV/fm^3) and high temperature ($\gtrsim 0.2$ GeV), expected to characterize the medium formed in central heavy ion collisions at these energies. Under these conditions, according to lattice QCD calculations, quark confinement into colourless hadrons should be removed and a deconfined Quark–Gluon Plasma (QGP) should be formed [2]. In the past two decades, experiments at CERN-SPS ($\sqrt{\mathrm{s}_{\mathrm{NN}}} = 17.3$ GeV) and BNL-RHIC ($\sqrt{\mathrm{s}_{\mathrm{NN}}} = 200$ GeV) have gathered ample evidence for the formation of this state of matter. An overview of the main results is given in the first chapter.

The target of this thesis is the preparation of the measurement of the cross section for the production of D^0 ($c\bar{u}$) mesons in proton-proton (p–p) collisions via the exclusive reconstruction of the decay channel $D^0 \to K^-\pi^+$. The measurement of charm and beauty hadron production in Pb–Pb collisions is one of the main items of the ALICE physics program, because it will allow to investigate the mechanisms of heavy–quark propagation and hadronization in the hot and dense strongly-interacting medium formed in such collisions [3]. Heavy quarks can be considered as probes of the medium in its partonic phase. To extract information on the medium properties the measurement performed with Pb–Pb collisions must be related to the same measurement in p–p collisions, where the formation of the QGP is not expected. Furthermore, the production of charm quarks in p–p collisions has never been measured at energies comparable to those accessible at the LHC: the design centre of mass energy is $\sqrt{s} = 14$ TeV, a factor 7 above the Tevatron energy. ALICE will have the capability to test the theoretical predictions of QCD in a new energy domain and to disentangle between the different perturbative approaches to QCD implemented in the calculations available [4]. These topics are described in the second chapter of the thesis.

The strategy to extract the D^0 production yield is based on an invariant mass analysis of all the possible pairs of opposite charge reconstructed tracks. Without any selection on the pairs, the signal-to-combinatorial background ratio would be too small to extract any information from the invariant mass distribution. It is then mandatory to preselect the tracks on the basis of kinematical and geometrical considerations. The ALICE Inner Tracking System (ITS) detector (described in the third chapter) provides the high precision tracking needed to reconstruct the proton/ion beams collision point (primary vertex) and the decay points (secondary vertices) of the charmed mesons with sufficient precision to distinguish between them. Thanks to the ITS micrometric resolution it is possible to exploit the relatively long decay length of the D^0 meson ($c\tau = 123\ \mu m$) and discern between tracks coming from the decay of a D^0 and those coming directly from the primary vertex of interaction, rejecting a large fraction of background pairs.

A key element for the analysis is thus a good understanding of the response and the properties of the ITS. This understanding is reached with a thorough commissioning phase. Alignment is the main commissioning task in view of heavy-flavour measurements. The ITS consists of six cylindrical layers of silicon detectors. Each layer is composed of many modules (more than 2000 in total) whose positions and orientations in space can differ from those by design due to the finite precision of the assembly. This can spoil the detector resolution, hence the tracking and physics performance. It is essential to recover the real module positions by means of "alignment" procedures. The sources of alignment information are the survey measurements done during the assembly and reconstructed tracks from cosmic-ray muons and from pp collisions. During summer 2008, the ALICE experiment collected a sample of about 10^5 tracks from cosmic-rays which was used to validate the survey measurements performed for the SSD (Silicon Strip Detector, the two outermost layers of the ITS) and to align a significant fraction of the ITS. Chapter 4 and Chapter 5 are fully devoted to the ITS alignment. In the first, the alignment problem is introduced and the general alignment strategy is described. Then the validation of the SSD survey measurement with cosmic–ray tracks is discussed in full details, along with the tests done to monitor the status of the alignment. Chapter 5 is devoted to the description of the two methods, based on tracks-to-measured-points residuals minimization, considered for the alignment. The main method, using the Millepede algorithm [5] performs a global fit to all residuals, extracting all the alignment parameters simultaneously. The second method, studied and improved in this work of thesis, performs a (local) minimization for each single module and accounts for correlations between modules by iterating the procedure until convergence is reached. This "module–by–module" iterative approach is described in full details: tests on simulation data to prove its applicability precede the results obtained with 2008 cosmic data. The evaluation of the ITS alignment quality, performed for both methods, along with the comparison between the alignment parameters recovered allow to conclude that a similar performance is obtained with the two methods. After the 2008 cosmic run it is possible to state that the ITS alignment procedures work and that, for the modules illuminated by cosmic rays, the worsening in the spatial resolution due to the residual misalignment is contained within about 20% of the ideal detector resolution.

The promising results obtained with cosmic data [6, 7] allow to be confident that the same alignment quality will be achieved for all the ITS modules few months after the start up of the LHC operations. Therefore the analysis procedures for the reconstruction of the $D^0 \to K^-\pi^+$ decay channel could be tested in p–p collision simulations taking into account a realistic alignment scenario close to the ideal one. The two last chapters of the thesis are devoted to this topic. In the first one the analysis strategy is outlined. After the already mentioned selection on the pairs of opposite charge tracks, needed to increase the signal–to–background ratio, it is possible to fit the invariant mass distribution and to get an estimate of the amount of signal, that is, the number of D^0 mesons, decayed in the selected channel, which survive the selection and are reconstructed. To recover the number of produced D^0, the signal must be divided by an efficiency factor that accounts for the fraction of D^0 mesons which are not reconstructed due to the limited detector acceptance or are rejected by the cuts. The efficiency correction is calculated, using Monte Carlo generated events, as the ratio between the selected and the generated D^0. It thus relies on the good description in the simulation of both the momentum spectrum of the generated mesons and the detector properties and response. The detector alignment plays a central role here: if the detector spatial resolution, including alignment effects, is not properly described in the simulation, the cut efficiency recovered from Monte Carlo data differs from the real one and a systematic error is introduced. This and the other main sources of systematic errors are listed and discussed in the chapter.

A large fraction of D^0 mesons comes from the decay of B mesons (mesons containing a b quark) and a proper correction must be applied to the signal extracted via the invariant mass analysis. As estimated in previous studies [3], a 8% systematic error arises from this correction due to the theoretical uncertainty on b quark production at LHC energies. In this thesis a possible way has been studied to extract the fraction of secondary D^0 coming from the decay of a B meson using the data and exploiting the high precision tracking provided by the ITS. The method, originally developed by the CDF experiment [8], exploits the long decay length of B mesons, reflected in a different shape of the impact parameter distributions of secondary and primary D mesons. The details and the results are described in the last chapter of the thesis.

Chapter 1

High density QCD with heavy ions at LHC

Ultra-relativistic heavy-ion collisions aim at studying matter under extreme conditions of high temperature and energy density. According to the Quantum Chromo Dynamics (QCD) theory of strong interaction, strongly interacting matter can exist in different phases. Up to now, heavy ion collisions are seen as the only human possibility to observe a phase transition to a new state of matter, called Quark-Gluon Plasma, in which quarks and gluons are not confined into hadrons. Lattice QCD calculations [9, 10] predict that the critical temperature is $T_c \approx 170$ MeV[1], corresponding to a critical energy density $\epsilon_c \approx 0.7$ GeV/fm^3. Collisions of atomic nuclei have been studied for more than 20 years at sufficiently high energies to cross into the deconfined phase. The first attempts were done since 1986 with light nuclei at the Alternating Gradient Synchrotron (AGS) at the Brookhaven National Laboratory (BNL) and at the Super Proton Synchrotron (SPS) at CERN, with Si and S respectively. Then, in the early 1990s, the acceleration of heavy nuclei began at both facilities: Au, mass number 197 at AGS and Pb, mass number 208, at SPS. The centre of mass energy per colliding nucleon–nucleon pair, ($\sqrt{\mathrm{s}_{\mathrm{NN}}}$), was 4.6 GeV at the AGS and 17.2 GeV at the SPS. Already in the late 1990s, at the CERN Super Proton Synchrotron (SPS), enough evidence was gathered to conclude that a new state of matter had been created [11]. When the Relativistic Heavy-Ion Collider (RHIC) went into operation at BNL, heavy-ion nuclei such as gold collided at a centre of mass energy per nucleon–nucleon pair $\sqrt{\mathrm{s}_{\mathrm{NN}}} = 200$ GeV. The huge step in collision energy meant a much larger, hotter, longer living QGP "fireball" than at the SPS. Only with the ongoing start up of the LHC at CERN a similar (and even larger) step will be attained. Pb nuclei will collide at a centre of mass energy of $\sqrt{\mathrm{s}_{\mathrm{NN}}} = 5.5$ TeV, about 30 times more than RHIC.

In this chapter, after recalling some of the main features of the strong interaction, the QCD phase diagram is shown along with lattice QCD predictions for the critical temperature and energy density at which the phase transition to the QGP should occur. The current picture of an heavy-ion collision consists in the creation of a QGP fireball that rapidly expands and cools down: when the temperature goes down below the critical temperature, hadronization occurs. The experimental observables used to access the medium properties will be presented and the most important experimental signatures gathered at the SPS and RHIC facilities will be

[1] Energy units for the temperature: the Boltzmann constant is taken equal to 1, $k_{\mathrm{B}} = 1$, and $[E] = [k_{\mathrm{B}}][T]$

recalled. Energetic partons, produced at the first stage of the collision before thermalization, can be considered as an unbiased probe to access the partonic stage of the medium. These "hard probes" have gained great importance with the energy domain available at RHIC and will cover a central role at the LHC. The main results obtained at RHIC for high–p_{t} particles and jets suppression are shown, while heavy–quarks and related issues are extensively treated in the next chapter. An overview of the novel aspects of heavy-ion physics accessible at the LHC concludes the chapter.

1.1 Quark and gluon interaction in an asymptotically free world

The strong interaction has been studied since the beginning of the 20^{th} century soon after the discovery of the atomic nucleus. The existence of a binding force holding together the nucleons in the nuclei was postulated to assure nucleus stability. The discovery of the neutron and, later, of the pion provided a rather complete and satisfactory picture of the nucleus with the pion recognized as the long searched Yukawa particle of the strong interaction. Very early this turned out to be only a simplified picture of a small piece of what strong interaction concerns. Lots of new particles were produced in the experiments leading to a complete new scenario of both strong and weak interactions. The idea that the proton, as all strongly interacting

Quark, spin=1/2		
Flavour	Mass (approx.) [GeV]	electric charge
u (up)	0.003	2/3
d (down)	0.006	-1/3
c (charm)	1.3	2/3
s (strange)	0.1	-1/3
t (top)	175	2/3
b (bottom)	4.8	-1/3

Table 1.1: The six quarks flavour.

particles (*hadrons*), were composed of more fundamental particles called quarks emerged. *Deep inelastic scattering* experiments further clarified the quark structure of hadrons and the properties of strong interaction. Hadrons are formed by elementary particles called quarks, which exists in six different flavour (see Table 1.1). Quarks carry strong "colour" charge in three different type (indicated as red, green and blue). The "mediators" of the strong force, playing the same role of the photon for electromagnetism, are called *gluons*, which come in eight colour combinations. A main difference with electromagnetism is that gluons do interact with each other while photons do not.

The two main strong interaction features of interest for heavy-ion physics are:

- **Colour confinement**: "free" quarks have never been observed. Quarks are confined in particular "colourless" combinations inside hadrons.

- **Asymptotic freedom**: the value of the strong coupling constant, α_S, depends on the momentum transfer (Q^2) at which an observed process occurs (*running coupling* *constant*). α_S decreases with increasing energy and asymptotically, at infinite energy, tends to zero.

Another fundamental aspect concerns hadron masses: light mesons/baryons are mainly composed by two/three light quarks (u, d, s). However, summing the masses of the constituent quarks, only a small fraction of the hadron mass is obtained. For instance, the proton (uud) mass is ~ 1 GeV/c^2 while the sum of the bare masses of its constituent quarks is $\lesssim 25$ MeV/c^2.

All these features are accomplished within the Quantum Chromo Dynamics (QCD) theory of strong interaction described in the following section. This theory predicts that strong interaction properties in a complex system may differ from those observed in the vacuum. Quark confinement inside hadrons can disappear at energy densities higher than those typical of normal nuclear matter, as described in Section 1.1.2. The study of the modification of strongly interacting matter properties in a medium started relatively recently (in the 1970s). Very soon it was realized that only ultra–relativistic heavy-ion collisions could gain experimental access to part of the QCD phase diagram. Sect 1.2 and 1.3 aim at briefly describing why and how this is possible and which are the main results achieved up to now.

1.1.1 The Quantum Chromo Dynamics theory of strong interaction

Quantum Chromo Dynamics (QCD) is the quantum field theory developed to describe strong interactions. It thus involve quarks, gluons and all hadrons. It is a quantum field theory described by the following Lagrangian, based on the "colour" SU(3) gauge symmetry group (as described in standard textbooks like [12, 13]):

$$\mathcal{L}_{\rm QCD} = -\frac{1}{4}F^a_{\mu\nu}F^{\mu\nu}_a + \sum_{flav.} i\bar{\psi}\gamma^\mu\left(\partial_\mu - ig\frac{\lambda_a}{2}A^a_\mu\right)\psi - \sum_{flav.} m\bar{\psi}\psi, \tag{1.1}$$

with the non-Abelian gluon field strength tensor

$$F^a_{\mu\nu} = \partial_\mu A^a_\nu - \partial_\nu A^a_\mu + g f_{abc} A^b_\mu A^c_\nu, \tag{1.2}$$

The fundamental degrees of freedom of the theory are the 3×6 quarks fermionic fields ψ and the eight gluonic fields A_μ. λ_a and f_{abc} are the eight SU(3) group generators (3×3 matrices) and structure constants. In the definition above ψ represents, for each flavour, a vector $(\psi_{\rm red}, \psi_{green}, \psi_{\rm blue})$ of fermionic fields. Being based on a non abelian symmetry group, interaction terms between the vector bosons of the theory, the gluons, are present.

Chiral symmetry and constituent quark masses

As already mentioned, for light hadrons, only a small fraction of the hadron masses are recovered when the masses of the quarks they are composed of are summed. In the QCD theory this is motivated by the *spontaneous chiral symmetry breaking* mechanism. If the mass term is neglected, the QCD Lagrangian defined in Eq. 1.1 becomes chirally symmetric, i.e. invariant under separate flavour rotations of right- and left–handed quarks. Neglecting the mass term is a good approximation for the up and down quarks and quite good for the strange quark (see Table 1.1). The non-zero vacuum expectation value of the scalar quark density operator $\bar{\psi}\psi$ ("chiral condensate") breaks this symmetry and generates a dynamic mass of order 300 MeV for the up and down quarks and about 450 MeV for the strange quarks.

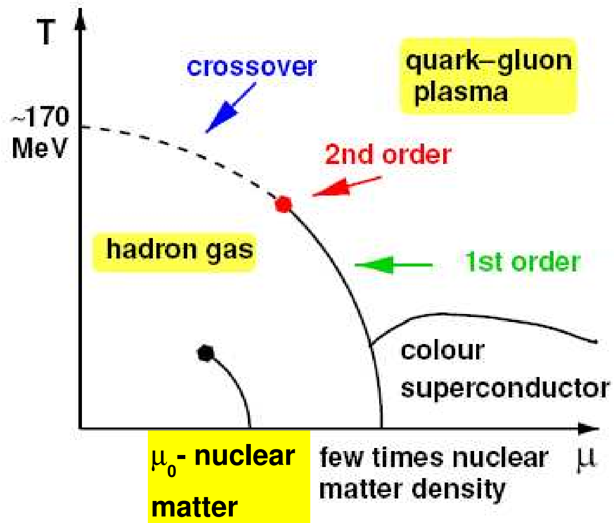

Figure 1.1: Generic phase diagram of QCD.

1.1.2 QCD phase diagram

On the basis of thermodynamical considerations and of QCD calculations, strongly interacting matter is expected to exist in different states. Its behaviour, as a function of the baryonic chemical potential[2] $\mu_{\rm B}$ (a measure of the baryonic density) and of the temperature T, is displayed in the phase diagram reported in Fig. 1.1. At low temperatures and for $\mu_{\rm B} \simeq m_{\rm p} \simeq 940$ MeV, we have ordinary matter. Increasing the energy density of the system, by "compression" (towards the right) or by "heating" (upward), a hadronic gas phase is reached in which nucleons interact and form pions, excited states of the proton and of the neutron (Δ resonances) and other hadrons. If the energy density is further increased, the transition to the deconfined QGP phase is predicted: the density of partons (quarks and gluons) becomes so high that the confinement of quarks in hadrons vanishes.

The phase transition can be reached along different "paths" on the ($\mu_{\rm B}$, T) plane. In the primordial Universe, the transition QGP-hadrons, from the deconfined to the confined phase, took place at $\mu_{\rm B} \approx 0$ (the global baryonic number was approximately zero) as a consequence of the expansion of the Universe and of the decrease of its temperature (path downward along the vertical axis) [14]. On the other hand, in the formation of neutron stars, the gravitational collapse causes an increase in the baryonic density at temperatures very close to zero (path towards the right along the horizontal axis) [14, 15].

In heavy ion collisions, both temperature and density increase, possibly bringing the system to the phase transition.

1.1.3 The phase transition in lattice QCD

Exploring from a theoretical point of view the qualitative features of the QGP and making quantitative predictions about its properties is the central goal of the numerical studies of

[2] The baryonic chemical potential $\mu_{\rm B}$ of a system is defined as the change in the energy E of the system when the total baryonic number $N_{\rm B}$ (baryons − anti-baryons) is increased by one unit: $\mu_{\rm B} = \partial E/\partial N_{\rm B}$.

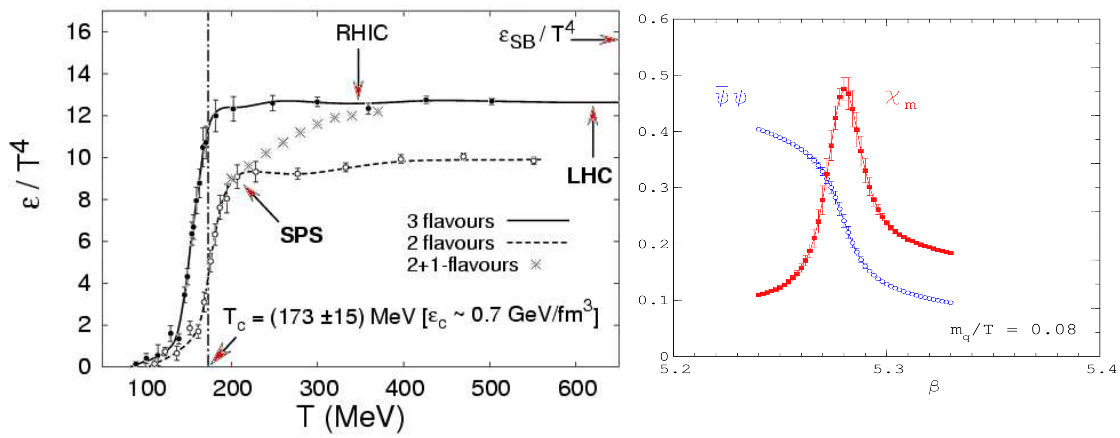

Figure 1.2: On the left: the energy density in lattice QCD with 2 and 3 light quarks and with 2 light plus 1 heavier (strange) quarks [9]. The calculation uses $\mu_{\rm B} = 0$. On the right: the chiral condensate $\langle\bar\psi\psi\rangle$ and the negative of its temperature derivative (chiral susceptibility χ_m) as a function of temperature [16].

strongly interacting matter thermodynamics within the framework of lattice QCD [9, 10].

Phase transitions are related to large-distance phenomena in a thermal medium. Because of the increasing strength of QCD interactions with the distance, such phenomena cannot be treated using perturbative methods. Lattice QCD provides a first-principle approach that allows to study large-distance aspects of QCD and to partially account for non-perturbative effects. However, at present, most calculations are limited by the fact that they do not include a finite baryo-chemical potential $\mu_{\rm B}$ (i.e. they assume a baryonic density equal to zero).

Results of a recent calculation of ε/T^4 are shown in Fig. 1.2 (left panel), for 2- and 3-flavours QCD with light quarks and for 2 light plus 1 heavier (strange) quarks (indicated by the stars) [9]. The latter case is likely to be the closest to the physically realized quark mass spectrum. The number of flavours and the masses of the quarks constitute the main uncertainties in the determination of the critical temperature and critical energy density. The critical temperature is estimated to be $T_c = (175 \pm 15)$ MeV and the critical energy density $\varepsilon_c \simeq (6 \pm 2)\, T_c^4 \simeq$ (0.3-1.3) GeV/fm^3. Most of the uncertainty on ε_c arises from the 10% uncertainty on T_c.

Although the transition is not a first order one (which would be characterized by a discontinuity of ε at $T = T_c$), a large 'jump' of $\Delta\varepsilon/T_c^4 \simeq 8$ in the energy density is observed in a temperature interval of only about 40 MeV (for the 2-flavours calculation). Considering that the energy density of an equilibrated ideal gas of particles with $n_{\rm dof}$ degrees of freedom is

$$\varepsilon = n_{\rm dof}\,\frac{\pi^2}{30}\,T^4, \tag{1.3}$$

the dramatic increase of ε/T^4 can be interpreted as due to the change of $n_{\rm dof}$ from 3 in the pion gas phase to 37 (with 2 flavours) in the deconfined phase, where the additional colour and quark flavour degrees of freedom are available[3].

[3]In a pion gas the degrees of freedom are only the 3 values of the isospin for π^+, π^0, π^-. In a QGP with 2 quark flavours the degrees of freedom are $n_g + 7/8\,(n_q + n_{\bar q}) = N_g(8)\,N_{\rm pol}(2) + 7/8 \times 2 \times N_{\rm flav}(2)\,N_{\rm col}(3)\,N_{\rm spin}(2) = 37$. The factor 7/8 accounts for the difference between Bose-Einstein (gluons) and Fermi-Dirac (quarks) statistics.

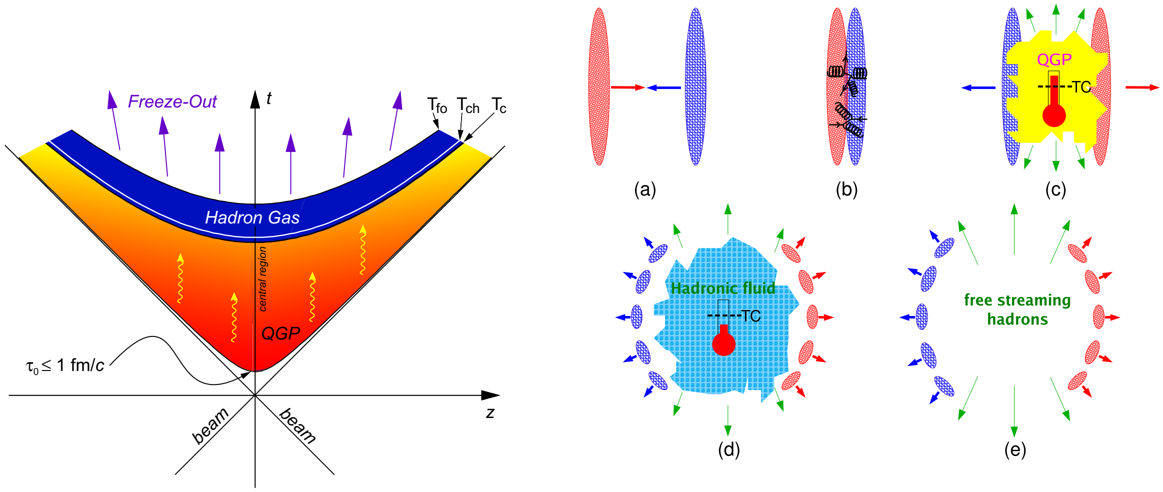

Figure 1.3: Schematic view of the different stages of a heavy-ion collision assuming that the QGP is formed (see text). In the light cone representation (left panel) beam particles move at almost the speed of light along the z–axis and collide in the origin.

On the right panel in Fig. 1.2, lattice QCD calculations for the chiral condensate $\langle\bar{\psi}\psi\rangle$ and the negative of its temperature derivative (chiral susceptibility χ_m) are shown as a function of temperature: the dynamically generated mass, arising from chiral symmetry breaking, melts away above T_C. Hence, in a quark-gluon plasma, quarks are characterised by their *bare* masses listed in Table 1.1.

1.2 Heavy-ion collisions: a QGP factory?

Concepts like thermodynamic phases, phase transition and temperature are properly defined only for complex systems, composed of many particles, behaving like 'matter' rather than like individual elementary particles or a group of elementary particles [11]. In particular, the system must match two main conditions:

1. it must consist of a *large number of particles* (thousands or better tens of thousands)

2. it must reach the *local equilibrium*.

Only in such a scenario variables like temperature, pressure, energy density and thermodynamics relations between those quantities (equation of state, speed of sounds) can be investigated. Collisions of protons (or electrons) produce too few particles to fulfil these conditions. Since the early 1980s, heavy nuclei collisions at as large energies as possible have been seen as the ideal way to probe matter in the extremely high temperature and density conditions required to test the phase diagram of QCD. At high energy, the thousands of particles produced in these collisions create a 'fireball' in local thermal equilibrium that rapidly expands and cools down. If the collision energy is large enough, the fireball is initially made of interacting quarks and gluons that hadronize only when the medium temperature falls down below the critical temperature for the phase transition to occur. In the next section experimental evidences to support this as the realistic picture of what is going on in very high energy heavy ions collisions are described.

As outlined in the introduction to this chapter, the first experiments with heavy nuclei collisions (Au and Pb) were made in the early 1990s at the AGS and at the SPS with a centre of mass energy per colliding nucleon pair $\sqrt{\mathrm{s}_{\mathrm{NN}}} = 4.6$ GeV and 17.2 GeV respectively.

The Relativistic Heavy-Ion Collider (RHIC) has been operated since 2000 at BNL. The centre of mass energy per nucleon pair can reach up to $\sqrt{\mathrm{s}_{\mathrm{NN}}} = 200$ GeV. At the LHC at CERN Pb nuclei will collide at a centre of mass energy per nucleon pair $\sqrt{\mathrm{s}_{\mathrm{NN}}} = 5.5$ TeV.

An expanding *fireball*: the dynamics of heavy-ion collisions

The most supported picture describing what happens in an heavy-ion collision consists of the creation of a rapidly expanding fireball made of quarks and gluons. The fireball undergoes thermalization, cooling by expansion, hadronization, chemical and thermal freeze–out, a pattern resembling the evolution of the Early Universe after the Big Bang [15]. The hot big bang model of cosmology assumes that soon after the electro-weak phase transition ($\approx 10^{-11}$ s after the Big Bang), the expanding Universe was a plasma of free quarks and gluons. When the temperature went down T_c at about $\approx 10^{-5}$ s because of the expansion, a phase transition to an Universe populated by hadrons occurred. Due to this, the creation of a fireball in relativistic heavy-ion collision is often referred to as *Little Bang*. The main stages of a collision, as depicted in Fig. 1.3, are the following:

1. Two disk–like nuclei approach each other, Lorentz contracted along the beam direction by a factor $\gamma = E_{\mathrm{beam}}/M$ (E_{beam} is the beam energy per nucleon and $M \approx 0.94$ GeV is the nucleon mass, $\gamma \approx 110$ at RHIC and ≈ 3000 at the LHC).

2. After impact, hard collisions with large momentum transfer $Q \gg 1$ GeV between partons inside the two nuclei (quarks, antiquarks and gluons) produce high energetic secondary partons. The hard scatterings happen at early times, $\approx 1/Q \ll 10^{-24}$ s.

3. The remnants of the original nuclei, called "spectator nucleons", fly along the beam line. The "participants" nucleons that do not survive the collision form the mentioned *fireball*, so called because of the high energy density of the system and its rapid expansion. If the energy density is high enough, the fireball can consists of a "droplet" of Quark Gluon Plasma. Soft collisions with small momentum exchange $Q \ll 1$ GeV produce many more particles and thermalize the QGP after about 1 fm$/c$ (at the SPS energy). The resulting thermalized QGP fluid expands hydrodynamically and cools down approximately adiabatically.

4. As the fireball cools down two relevant processes occur:

   - when the temperature goes down below the critical temperature for the phase transition to occur, the QGP converts to a gas of hadrons (mainly pions)
   - the available energy is insufficient to alter the specie of the particles, that is, for inelastic scattering among partons, among hadrons and between partons and hadrons to occur. Therefore, the "chemical composition" of the hadronic system is frozen (*"chemical freeze–out"*).

   It is very likely (see next section) that the hadronization and the chemical freeze–out happen very close in time.

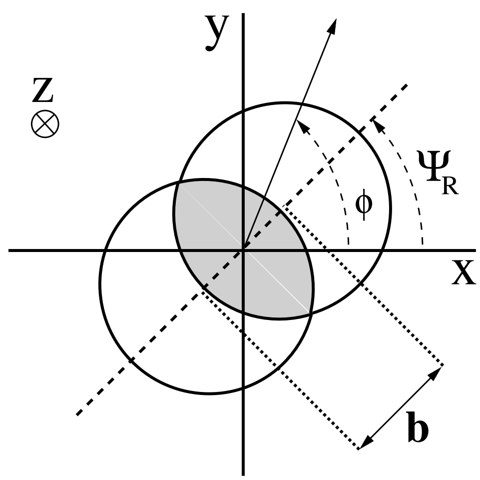

Figure 1.4: Geometry of a nucleus–nucleus collision. $\vec{b}$ is the impact parameter vector of the collision, Ψ_{R} defines the reaction plane.

5. The hadrons continue to interact quasi–elastically, cooling the fireball until the *kinetic (or thermal) freeze–out*, defined as the moment in which all interactions among particles cease. Unstable particles, like resonances, decay and the decay products stream freely towards the detector.

Collision geometry: impact parameter and centrality

Nuclei are extended objects for all the scales of interest in high-energy physics. The geometry of the collision plays a central role in the analysis and in the interpretation of the experimental results. In Fig. 1.4 the collision of two nuclei is schematically represented as seen in the plane transverse to the beam direction (z axis). Their transverse size is of the order $2R_A \approx 2A^{1/3}r_0$, with $r_0 \sim 1.25$ fm and A the mass number of the nuclei. The most relevant quantity is the impact parameter vector $\vec{b}$, that is, the vector joining the centers of the two colliding nuclei in the transverse plane. The impact parameter characterizes the *centrality* of the collision. A central collision is that with small impact parameter, in which the two nuclei collide almost head–on; a peripheral collision is that with large impact parameter. Usually, centrality classes (quoted by percentage) are defined on the basis of the collision impact parameter. The number of participant nucleons N_{part} is the total number of protons and neutrons taking part in the collision The number of spectator nucleons is usually inferred from the zero-degree energy deposited in forward detectors, as the ALICE Zero-Degree Calorimeter (ZDC, Section 3.1). The impact parameter and the collision centrality can be estimated in several methods, from ZDC energy as well as from charge hadron multiplicity (the methods ALICE planned to use are described in [3]). A relevant quantity related to the collision geometry is the number of collisions N_{coll} defined as the number of incoherent nucleon–nucleon collisions. The impact parameter vector characterizes also the collision symmetry: the reaction plane is defined by the beam direction (z axis) and the impact parameter vector and can be identified with the angle Ψ_{R} between the x axis and the impact parameter direction. The collision symmetry strongly influences the azimuthal distribution of the particles produced in the collision.

1.3 Global properties of the medium

The hypothesis that an expanding fireball in local thermal equilibrium is created in heavy-ion collisions is supported by many experimental evidences. Information on the energy density, on the chemical and thermal freeze–out temperatures, on the baryon chemical potential are extracted from particle abundances and transverse momentum spectra.

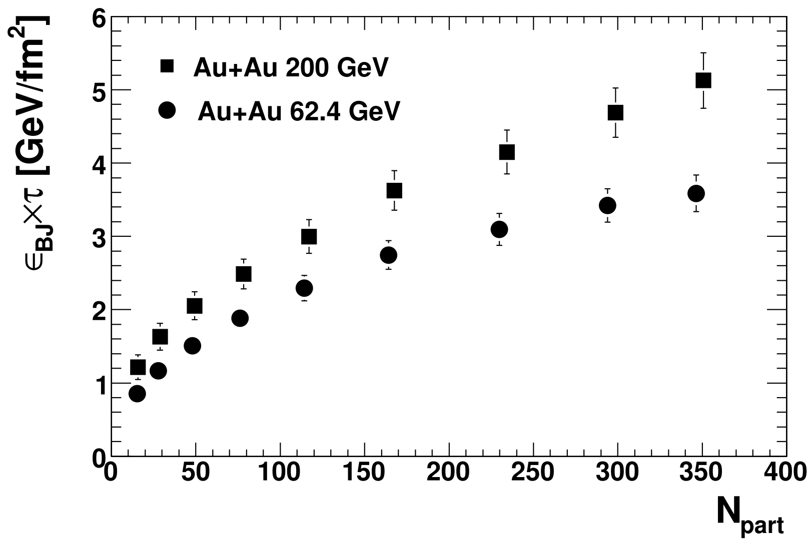

Figure 1.5: Estimate of the product of the Bjorken energy density and the formation time as a function of centrality N_{part} at RHIC (from STAR) [17].

1.3.1 Energy density estimation

The energy density of the central rapidity[4] region in the collision zone can be estimated via the Bjorken formula [18]:

$$\epsilon_{Bj}(\tau) = \frac{1}{S_\perp \tau} \frac{dE}{dy}\bigg|_{y=0}, \tag{1.4}$$

where τ is the evaluation time, $S_\perp$ is the transverse overlap area of the colliding nuclei and E is the total energy. Usually $\frac{dE}{dy}\big|_{y=0}$ is approximated to $\frac{dE_\mathrm{T}}{dy}\big|_{y=0} \approx \langle E_T \rangle \cdot \frac{dN}{dy}\big|_{y=0}$ with $\frac{dN}{dy}\big|_{y=0}$ the hadron multiplicity at $y = 0$ and $\langle E_\mathrm{T} \rangle$ the average hadron transverse energy in the same rapidity interval considered. The Bjorken formula is based on the assumptions of longitudinal boost invariance and formation of a thermalized central region at an initial time τ_0. Usually, a reference *QGP formation time* τ_0 is considered for τ even if its value is not exactly defined and different values, between 0.2 and 1 fm/c, are used. At the SPS with $\tau_0 = 1$ fm/c the estimated energy density was $\epsilon_{Bj} = 3.1 \pm 0.3$ GeV/fm^3 [19], a sufficient value for the phase transition to occur. In Fig. 1.5, the estimated values of $\epsilon_{Bj}\tau$ (from STAR at RHIC, [17]) are reported as a function of centrality N_part, for two different collision energies. The energy

[4] The rapidity for a particle with four–momentum $(E, \vec{p})$ is defined as $y = \frac{1}{2} \ln \frac{E+p_z}{E-p_z}$ where z is the beam direction. For particles in the relativistic limit ($E \approx p$) it is often approximated with the *pseudo–rapidity* $\eta = \frac{1}{2} \ln \frac{p+p_z}{p-p_z} = -\ln[\tan(\theta/2)]$ with θ being the polar angle with respect to beam direction.

density is estimated to lie between 5 and 25 GeV/fm^3, depending on the chosen formation time.

1.3.2 Collective flows

A collective flow describes a correlation between the average momentum of the particles and their space–time position. It is defined by the following procedure: at any space–time point x in the fireball an infinitesimal volume element centred at that point is considered and all the 4–momenta of the quanta in it are added up. The obtained total 3–momentum $\vec{P}$ is divided by the associated total energy P^0 to define the average *flow velocity* $\vec{v}(x)$ of the matter at point x. The flow velocity is usually separated into its components along the beam direction ("longitudinal flow" v_{L}) and in the transverse plane to the beam direction ("transverse flow" $\vec{v}_{\perp}$). The magnitude $v_{\perp}$ may depend on the azimuthal angle around the beam direction, especially for non central collisions with a non null impact parameter $\vec{b}$: in this case the transverse flow is called *anisotropic* or *elliptic*. Its azimuthal average is called *radial flow*.

A quark–gluon plasma is by definition an approximately-thermalized system of quarks and gluons and, thus, it has thermal pressure: the pressure gradients with respect to the surrounding vacuum cause the quark–gluon plasma to explode. An explosion can be seen as a collective expansion. Hence, absence of collective flow would indicate absence of pressure and imply absence of a hot thermalized system and, *a fortiori*, of a QGP [20]. It is thus very interesting to study the possible presence and consequences of collective flows in nucleus–nucleus collisions.

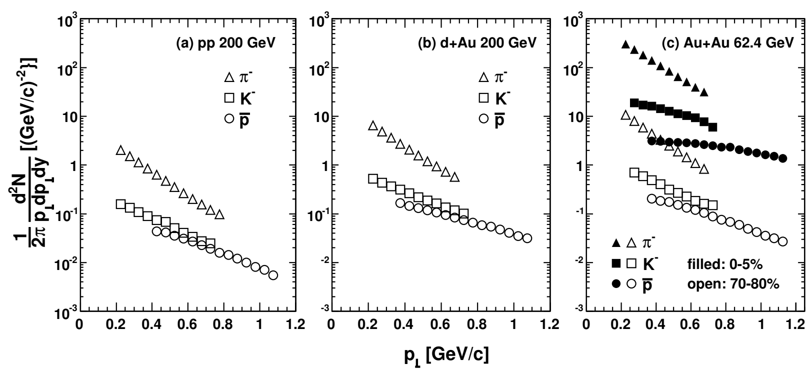

Figure 1.6: Comparison of π^-, K^- and $\bar{p}$ transverse momentum spectra observed by STAR in p–p and d–Au collisions ($\sqrt{s}_{\mathrm{NN}} = 200$ GeV) and Au–Au collisions at ($\sqrt{s}_{\mathrm{NN}} = 62.4$ GeV) for central (filled symbols) and peripheral (open symbols) collisions [17].

Kinetic freeze–out temperature and radial flow

A common flow velocity field results in a larger transverse momentum for heavier particles, leading to a dependence of the observed spectral shape on the particle mass. The kinetic freeze-out temperature T_{kin}, defined as the temperature at the surface of "last scattering", is estimated by the analysis of the measured transverse momentum spectral shapes of different particles. Fig. 1.6 shows a comparison of the measured transverse momentum spectra for π^-, K^- and $\bar{p}$ in p–p, d–Au (deuterium–gold) and Au–Au for central and peripheral collisions.

The spectra are described by the hydrodynamics–motivated blast–wave model [17]. The blast–wave model assumes that particles are locally thermalized at a kinetic freeze–out temperature and are moving with a common collective transverse radial flow velocity field. As reported in [17] (by STAR) the expected momentum spectral shape is used to fit six particle spectra ($\pi^{\pm}$,$K^{\pm}$,p,$\bar{p}$) simultaneously. Both $T_{\rm kin}$ and the average transverse flow velocity $\langle\beta\rangle$ are free parameters of the fit. In Fig. 1.8, lower panel on the left, the kinetic freeze–out temperature obtained in different experiments is reported along with the chemical freeze–out temperature as a function of the collision energy. In the lower panel on the right the values recovered for $\langle\beta\rangle$ are shown. The extracted average transverse flow velocity $\langle\beta\rangle$ increases with the centrality in Au–Au collisions as expected if a stronger pressure gradient develops in more central collisions. Quite large values of $\langle\beta\rangle$ are observed also in p–p and d–Au collisions mainly due to hard–scattering and jet production. If this latter contribution is subtracted, a value $\langle\beta\rangle_{\rm flow} = 0.54$ is found in Au–Au collisions. The magnitudes of both the kinetic freeze–out temperature and the radial flow velocity found by STAR are very similar for $\sqrt{\rm s_{NN}} = 62.4, 130, 200$ GeV, while they strongly depend on the charged particle multiplicity and, thus, on the initial energy density. This suggests that a higher initial energy density results in a larger expansion rate and longer expansion time, yielding a larger flow velocity and lower kinetic freeze–out temperature.

Elliptic flow: the perfect liquid QGP at RHIC

Flow anisotropies are generated mostly during the early stages of the collision. They are driven by spatial anisotropies of the pressure gradients due to the initial spatial deformation of the nuclear reaction zone in non–central collisions, as the one depicted in Fig. 1.4. This deformation decreases with time as a result of anisotropic flow: matter accelerates more rapidly in the direction where the fireball is initially shorter, due to larger pressure gradients. With the disappearance of pressure gradient anisotropies, the driving force for flow anisotropies vanishes, and, due to this "self–quenching" effect, the elliptic flow saturates early. If the fireball expansion starts at sufficiently high temperature, it is possible that all elliptic flow is generated before matter reaches $T_{\rm c}$ and hadronizes. In this case, elliptic flow is a clean probe of the equation of state of the QGP phase. Re-scattering processes among the produced particles transfer the spatial initial deformation onto momentum space, i.e. the initially locally isotropic transverse momentum distribution of the produced matter begins to become anisotropic. The momentum anisotropy manifests itself as an azimuthal anisotropy of the measured hadron spectra. The azimuthal particle distributions are studied by analysing the differential production cross–sections in terms of a Fourier expansion:

$$\frac{dN}{p_{\rm t}dp_{\rm t}dyd\phi} = \frac{1}{2\pi}\frac{dN}{p_{\rm t}dp_{\rm t}dy}\{1 + 2\sum_{i=1}^{\infty} v_i(y, p_{\rm t}, b)\cos[i(\phi - \Psi_{\rm RP})]\}\,, \quad (1.5)$$

where $\Psi_{\rm RP}$ is the *reaction plane* angle (see Fig. 1.4), y is the particle rapidity, b is the impact parameter of the collision and v_i are the Fourier coefficients. The sine terms in the expansion vanish due to reflection symmetry with respect to the reaction plane. The Fourier coefficients are given by:

$$v_i(y, p_{\rm t}, b) = \langle\cos[i(\phi - \Psi_{\rm RP})]\rangle\,, \quad (1.6)$$

the angular brackets denoting an average over the particles, summed over all events, in the $(p_{\rm t}, y)$ bin of interest. The lowest order Fourier terms are the so called direct flow (v_1)

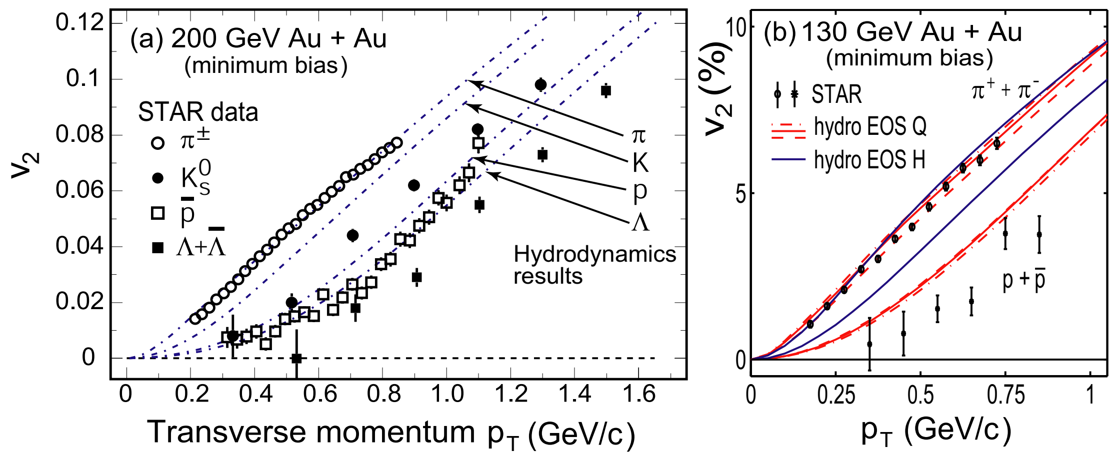

Figure 1.7: Left panel. STAR experimental results of the transverse momentum dependence of the elliptic flow parameter in 200 GeV Au–Au collisions for different particles [21]. Hydrodynamics calculations assuming early thermalization, ideal fluid expansion (no viscosity) and an equation of state (EOS) consistent with lattice QCD calculations including a phase transition at $T_c = 165$ MeV and a sharp kinetic freeze-out at $T = 130$ MeV are shown as dot–dashed lines. Right panel. Comparison between hydrodynamics prediction for the QGP (EOS Q) and hydrodynamics calculations for an hadron gas (EOS H) of the same sort as in the left panel, both compared to STAR v_2 measurements for pions and protons in minimum–bias Au–Au collisions at $\sqrt{s_{\mathrm{NN}}} = 130$ GeV [22].

and elliptic flow (v_2). For collisions between equal nuclei v_2 is, at mid–rapidity, the first non vanishing Fourier coefficient. The dependence on the centrality and on the spatial eccentricity reported in many papers (for instance [23, 24]) confirms that the v_2 is tied to the spatial asymmetry of non–central collisions. This indicates that a high level of collectivity is present at an early stage of the collision. Each particle species has its own v_2 coefficient: at low p_{t} the elliptic flow depends on the mass of the particle, being smaller for larger masses, as expected if a common radial flow velocity is present. Figure 1.7 from [23] shows the v_2 distributions at low–p_{t} as measured in 200 and 130 GeV Au–Au minimum bias (i.e. no centrality selection is applied) collisions. The clear, systematic mass–dependence of v_2 shown by the data is a strong indicator that a common transverse velocity field underlies the observations. The mass–dependence, as well as the absolute magnitude of v_2, is reproduced within $\pm 20\%$ by hydrodynamics calculations. Model parameters have been tuned to achieve good agreement with the measured spectra for different particles, implying that they account for the observed radial flow and elliptic flow simultaneously. In particular, since all the parameters are fixed from central collisions data (where $v_2 = 0$) the prediction of the v_2 at different centralities represents a significant test of hydrodynamics calculations. The experimental data are in quite good agreement with the theoretical predictions from a QGP like equation of state and from ideal fluid dynamics, leaving very little room for viscosity, which would reduce the theoretical value for elliptic flow. This is the cornerstone of the "perfect fluid" paradigm for the QGP that has emerged from the RHIC data.

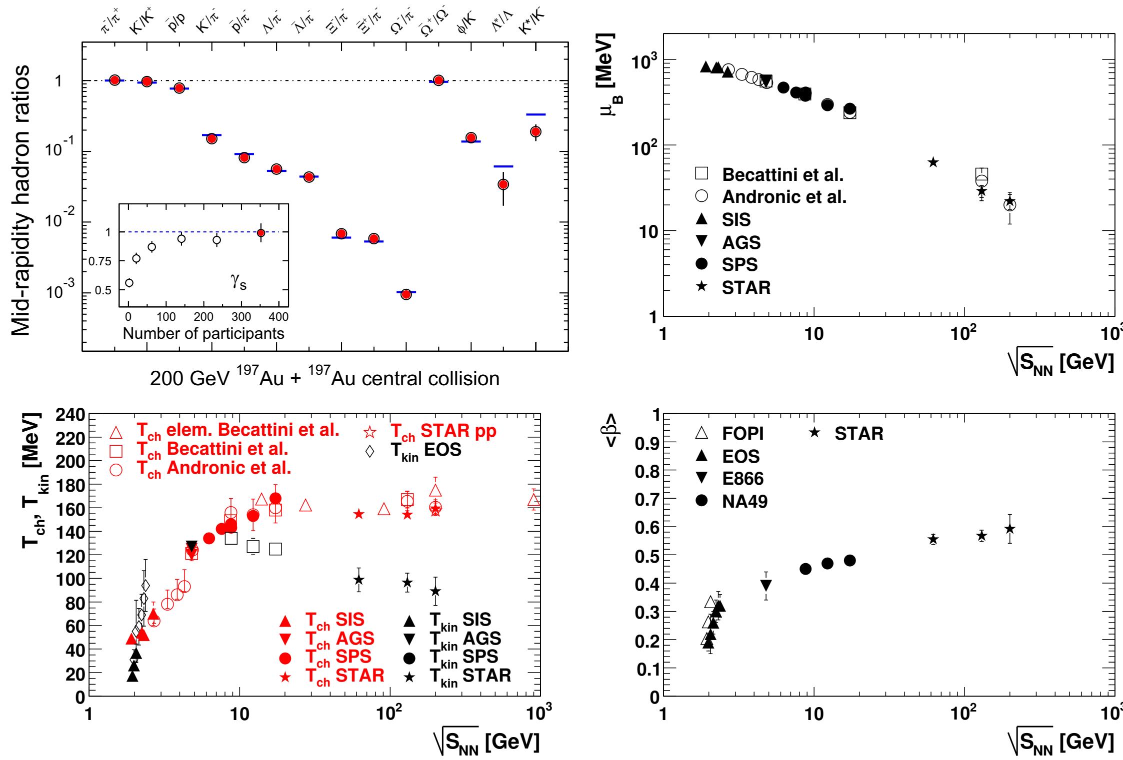

Figure 1.8: Upper left panel: ratios of p_T–integrated mid-rapidity yields for different hadron species measured in STAR for central Au–Au collisions at $\sqrt{s_{\rm NN}}$ = 200 GeV (from [23]). The horizontal bars represent statistical model fits to the measured yield ratios for stable and long-lived hadrons. The variation of γ_s with centrality is shown in the inset, including the value (leftmost point) from fits to yield ratios measured by STAR for 200 GeV p–p collisions. Then, from [17], in clockwise order: baryon chemical potential (μ_B), chemical ($\rm T_{ch}$) and kinetic ($\rm T_{kin}$) freeze out temperatures, average transverse-radial flow velocity ($\langle\beta\rangle$) extracted in different experiments for central heavy-ion collisions as a function of the collision energy.

1.3.3 Chemical freeze–out properties: temperature, baryon–chemical potential and strangeness suppression factor

The fireball yields hadrons that are in chemical equilibrium forming a statistical ensemble. In the chemical equilibrium model [17, 20], the system is described in a *grand–canonical ensemble* and distribution functions for each particle specie are derived via the Maximum Entropy Principle by imposing global energy, baryon and strangeness conservation. Particle abundances in a thermal system of volume V are then governed by only few parameters [17]:

$$N_i/V = \frac{g_i}{(2\pi)^3}\gamma_S^{S_i}\int\frac{1}{\exp\left(\frac{E_i-\mu_B B_i-\mu_S S_i}{T_{\rm chem}}\right)\pm 1}d^3p\,. \tag{1.7}$$

In the above expression, N_i is the abundance of particle species i, g_i the spin degeneracy, B_i and S_i are the baryon and strangeness number carried by the particle species i, E_i is the particle energy and the integral is over the whole momentum space. The parameters in the model are the temperature of the system, the baryon and strangeness chemical potentials, μ_B and μ_S and the ad–hoc strangeness suppression factor, γ_S. The measured particle abundance ratios are fit by the chemical equilibrium model to obtain the system parameters at the chemical freeze–out.

In Fig. 1.8 (upper left panel) the results obtained by the STAR collaboration for the ratio of different particle abundances are shown [23]. On the upper right panel the baryon chemical potential extracted from the fits in different experiments is reported as a function of the collision energy. It decreases smoothly with the collision energy, so that new baryons and anti–baryons can be created with increasing ease. As shown in [17], the baryon chemical potential increases with centrality. The strangeness chemical potential is small and close to zero: the ratio μ_S/μ_B is approximately constant and equal to $\mu_S/\mu_B = 0.110 \pm 0.019$ [17].

The chemical freeze out temperature T_{chem}, extracted from the data of many different experiments at many different collision energies (Fig. 1.8, lower left panel), after an initial steep rise, plateaus abruptly near $\sqrt{s_{\text{NN}}} \approx 10$ GeV at a value slightly higher than 160 MeV. It is remarkable that the same temperature is recovered for systems with different initial conditions, that is, different centralities, different colliding nuclei and different collision energies: central heavy-ion collisions at high energies can be characterized by a unique, energy independent chemical freeze–out temperature. This temperature is rather close to the critical temperature that should characterize the hadronization phase as estimated by lattice QCD calculations. Thus chemical freeze–out must occur very soon after or in the meanwhile of hadronization. The success of chemical equilibrium model in describing the data should not be readily taken as a proof of chemical equilibrium of each individual collision [25]. In p–p and other collisions between elementary particles, particles abundances are well described by the chemical equilibrium model (but with the ad–hoc strangeness suppression factor significantly smaller than unity) suggesting that particle production in these collisions is a statistical process and the chemical temperature is a parameter governing the statistical production process.

Some important points emerges from collective flow and chemical freeze–out properties. The medium created in heavy-ion collision collectively expands very fast ($\langle\beta\rangle = 0.54$) and undergoes rapid cooling. Both $\langle\beta\rangle$ and the kinetic freeze–out temperature depends on the collision centrality while the chemical freeze–out does not. The former are controlled by a competition between local thermalization and expansion rate: the larger fireballs formed in central collisions live longer, develop more radial flow and cool down to lower kinetic freeze–out temperatures than in peripheral collisions. Conversely, T_{chem} is not the result of kinetic processes. The difference between the two freeze–out temperatures indicates that, after being formed, the hadrons continue to re-scatter quasi–elastically without changing their abundances. The hydrodynamical models describing the elliptic flow, along with many other signatures (see the following sections for some examples), support a scenario with the creation of a QGP. The chemical freeze–out temperature is very close to the critical temperature T_c predicted by lattice QCD at which the phase transition should occur. The rapid expansion (and thus cooling) along with the observation that strangeness is not suppressed as in elementary collisions (see next section) suggests the existence of a *pre–equilibrium* before hadronization because it would require time to reach the equilibrium starting from a non-equilibrium condition, implying a larger difference between T_c and T_{chem}. This would enforce the idea that the chemical freeze–out is related more to a statistical formation of the hadrons rather than to a kinetic process involving inelastic scattering among them. If this is the case, the observed plateau in Fig. 1.8 would indicate that a phase boundary is reached at a critical collision energy. Beyond that energy, all additional energy goes into heating the quark–gluon plasma which, in turn, cools again and freezes out at the critical temperature delimiting the phase boundary. A QCD phase diagram can be drawn in a similar fashion than Fig. 1.1 by plotting T_{chem} against μ_B as recovered from the chemical equilibrium model. The resulting trend [17] agrees with lattice QCD predictions for small chemical potentials ($\lesssim$ 400 MeV) within 10 MeV [11, 26].

1.4 QGP signatures at the SPS and RHIC

In the previous section we have seen how global properties of the medium produced in heavy-ion collisions, like temperature, energy density, chemical potential and collective flows are accessible. The strong radial and elliptic flow values suggests the presence of a thermalized medium characterized by strong pressure gradients with respect to the outside vacuum and by consequent particle collective motions. Hydrodynamical predictions strongly prefer a scenario with the creation of a QGP medium that undergoes a phase transition to a hadron gas at a critical temperature T_c in agreement with lattice QCD calculation. In this section we point to two of the most important effects observed at both the SPS and RHIC experiments, namely strangeness "enhancement" and J/Ψ suppression, which are regarded as signatures of the phase transition to a QGP.

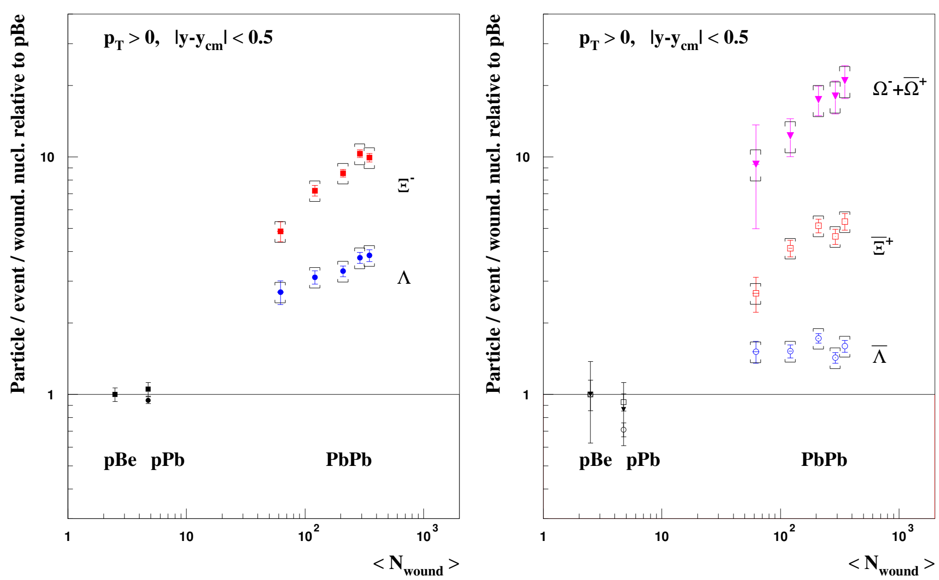

Figure 1.9: Strange baryon production enhancement in Pb–Pb collisions as measured by the NA57 experiment at the SPS. The observed baryon yields per participant nucleon, normalized to the ratio measured in p–Be collisions, are shown as a function of the number of participant nucleons [27].

Strangeness enhancement

If chiral symmetry is restored, as expected in a QGP medium, the threshold for the production of a $s\bar{s}$ pair reduces from twice the mass of the constituent strange quark ($\approx$ 1 GeV) to twice the mass of the bare strange quark ($\approx$ 300 MeV). This would point to a possible enhancement of strange hadron production in heavy-ion collisions. Moreover, the strangeness suppression factor γ_S, introduced in the previous section, is significantly smaller than unity in p–p, d–Au and peripheral Au–Au collisions, suggesting that strangeness production is strongly suppressed in these collisions. Conversely, as shown in Fig. 1.8 (small box in upper panel on the left), γ_S increases with centrality and is no longer strongly suppressed in central collisions: strangeness is nearly chemical equilibrated with the light flavours, suggesting a fundamental change from peripheral to central collisions. Strong interactions conserve net strangeness exactly: in principle [20] strangeness conservation should not be treated in a grand canonical ensemble where it is conserved only on average but in a canonical ensemble where it is fixed exactly. This implies that, in the small volume of the "fireball" created in elementary particle collisions, strange hadrons get suppressed since they must be created always in pair with an anti–strange hadron. The absence of canonical strangeness suppression in nuclear collisions implies that the creation of a strange hadron at a given position in the fireball does not require the production of a particle with balancing strangeness nearby, but strangeness can be balanced by production of an anti–strange hadron on the other side of the nuclear fireball. Since all microscopic QCD processes create $s\bar{s}$ pairs locally, i.e. the pairs are created at the same point, the "unsuppression" require that hadrons have lost their memory of the locality of the primary QCD process suggesting strangeness diffusion *before* hadronization.

Strangeness enhancement in heavy-ion collisions was one of the first and most important evidence for the restoration of chiral symmetry and the creation of a QGP. A small strangeness enhancement is expected in an hadron–gas via fast strong processes, like $\pi^+\pi^- \rightarrow K^+K^-$ or $\pi^-p \rightarrow \Lambda K^+$. However, this would imply a smaller enhancement for hadrons with an higher strangeness since their production requires a chain of interactions increasing the strangeness content of one unity per interaction. In Fig. 1.9 (from the NA57 experiment at the SPS) the number of produced strange hadrons per participating nucleon relative to p–Pb collisions is the more strongly enhanced the more strange (anti)quarks for its formation are required. For Ω and $\bar{\Omega}$ this enhancement factor is about 15.

J/Ψ suppression

In an electromagnetic plasma of charged particles, the binding potential between two opposite charged particles is reduced by the presence of the surrounding charges. In 1986 Matsui and Satz [28] predicted that the same effect, known as Debye screening, would cause the suppression of quarkonia production in ultra-relativistic heavy-ion collisions. This was expected to be an unambiguous signature for the formation of a QGP. At the SPS experiments NA38/50/60 both "normal" nuclear absorption and an "anomalous" suppression, maximal in central Pb–Pb collisions was indeed observed. Since, at RHIC, QGP has a longer lifetime and reaches a higher energy density, straightforward extrapolations of the naive J/Ψ melting scenarios predicted near-total suppression. The RHIC data apparently indicate a survival probability similar to that observed at the SPS. In Fig. 1.10 (left panel) the ratio between the measured J/Ψ suppression and the expected suppression from normal nuclear absorption (inferred from p–A collisions and Glauber model) is shown as a function of the energy density, as observed at the SPS and RHIC [29]. The ratio is called "survival probability". In the same figure (right panel) a recent result by PHENIX is reported for the *nuclear modification factor* ratio,

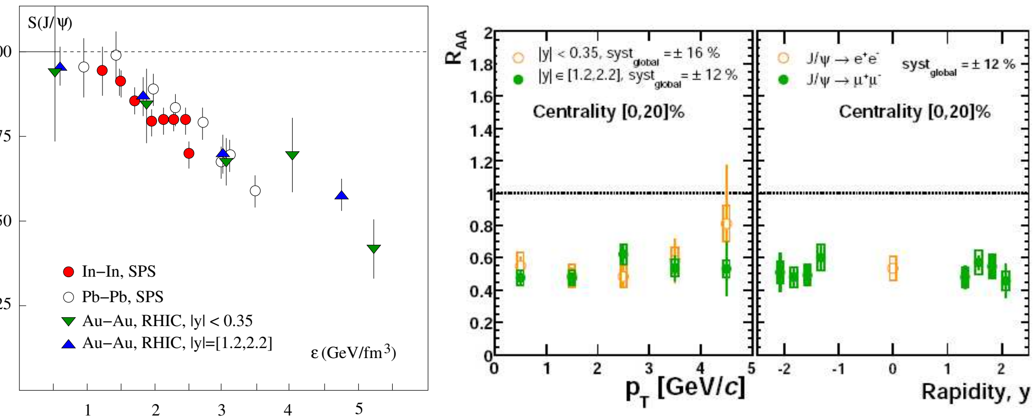

Figure 1.10: On the left: ratio of measured J/Ψ suppression over the expected suppression from nuclear absorption (inferred from p–A collisions data and Glauber model) as a function of the energy density, as observed at the SPS and RHIC [29]. On the right: a recent result for the same ratio (see $R_{\rm AA}$ definition in the text) as a function of $p_{\rm t}$ (left) and rapidity (right) for Cu–Cu at $\sqrt{s}_{\rm NN} = 200$ GeV observed by PHENIX [30].

$R_{\rm AA}$, defined as

$$R_{\rm AA}(p_{\rm t}) = \frac{dN_{\rm AA}/dp_{\rm t}}{N_{\rm coll} \times dN_{\rm pp}/dp_{\rm t}}\,, \tag{1.8}$$

where $dN_{\rm AA}/dp_{\rm t}$ and $dN_{\rm pp}/dp_{\rm t}$ are the observed differential yields in nucleus–nucleus and proton–proton collisions respectively and $N_{\rm coll}$ is the number of estimated binary collisions (see Appendix A). It is now recognized [31] that in order to interpret the J/Ψ production as a QGP probe one has to consider secondary production mechanisms, such as recombination of initially uncorrelated $c\bar{c}$ pairs [32], cold nuclear matter effects such as initial state energy loss [33] and shadowing [34], as well as charm quark energy loss [35], co-mover interactions [36] and corrections for feed-down from higher mass charmonium states.

1.4.1 Hard-probes as a medium tomography

At transverse momentum above ~ 2 GeV/c the observed elliptic flow at RHIC breaks away from the hydrodynamically predicted increase at larger $p_{\rm t}$. In the single particle spectra, the transition from collective hydrodynamic behaviour to hard scattering manifests itself by a change of shape [39]: for $p_{\rm t} \gtrsim 3-4$ GeV/c, the spectra change from a thermal exponential shape to the power low predicted by perturbative QCD. High $p_{\rm t}$ hadrons stem from the fragmentation of even–higher $p_{\rm t}$ partons, which are created in hard–scattering processes at the early stage of the collision ($\tau \sim 1/p_{\rm t}$). On their way out of the evolving collision fireball they lose energy by strongly interacting with the medium. Energy loss is not peculiar of a deconfined medium but, quantitatively, it is strongly dependent on the nature and on the properties of the medium, being predicted to be much larger in the case of deconfinement. The mechanism of in–medium partonic energy loss is one of the most interesting reasons for addressing charm quark production in heavy-ion collisions: it will be described in more details in the next chapter. In this section a short summary of the results obtained at RHIC is given. If high–$p_{\rm t}$ partons lose energy, the production rate of high–$p_{\rm t}$ hadrons should be reduced. Therefore, the main variable used to highlight this effect is the *nuclear modification factor*

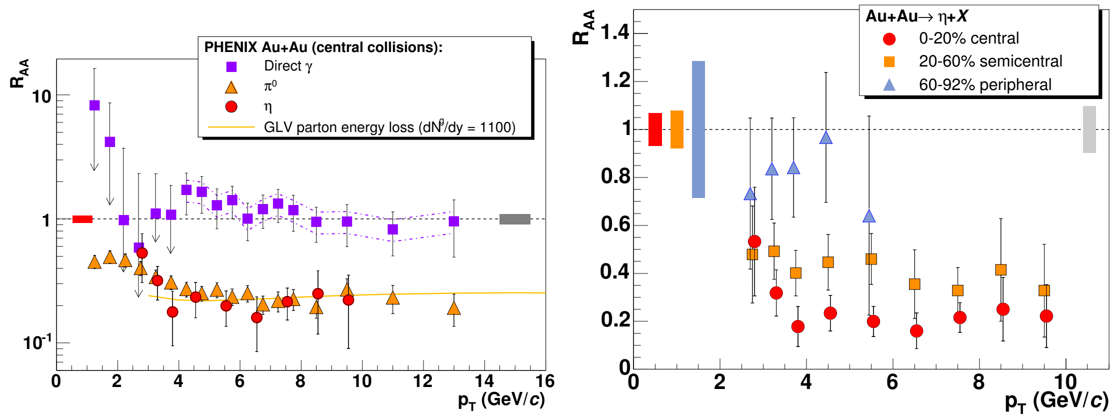

Figure 1.11: On the left: R_{AA} measured by the PHENIX experiment in central Au–Au collisions at $\sqrt{s}_{\mathrm{NN}} = 200$ GeV for η, π^0 and direct γ. On the right: R_{AA} for η mesons in different centrality intervals. In both figures, the error bars include all point–to–point errors. The absolute normalization error bands are shown at $R_{\mathrm{AA}} = 1$, on the left for the uncertainties in $\langle T_{AA}\rangle$ (see Appendix A), on the right the 9.7% uncertainty on the total p–p cross–section. Figures from [37] and references therein.

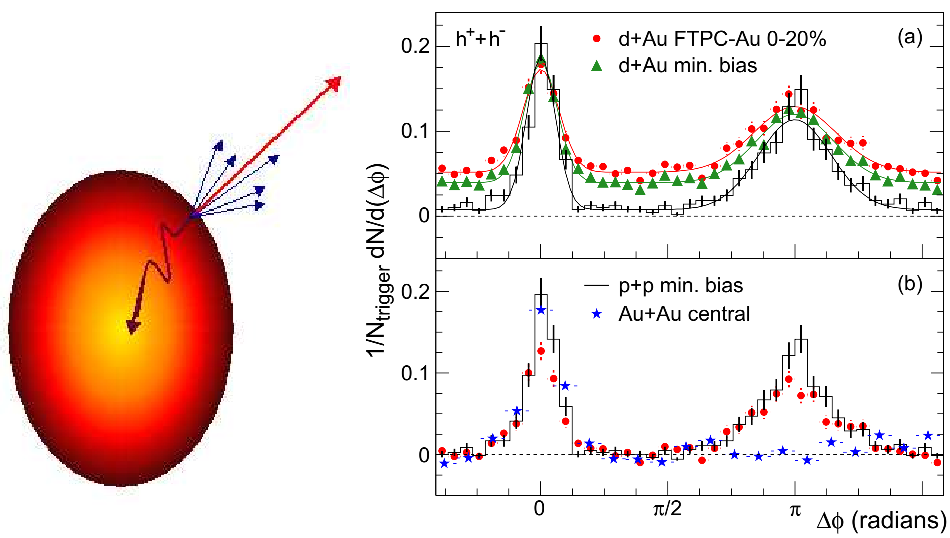

Figure 1.12: On the left: drawing illustrating jet emission from the fireball surface and quenching of its inward-moving partner. On the right: azimuthal angular correlations of charged particles with respect to a high-p_{t} trigger particle as observed by STAR [38] in p–p, minimum bias and central d–Au (upper panel) and p–p, central d–Au and central Au–Au collisions (lower panel).

defined in Eq. 1.8. In Fig. 1.11 (right panel) the R_{AA} for η mesons [37], π^0 [40] and direct γ [41] observed in Au–Au collisions at $\sqrt{s}_{\mathrm{NN}} = 200$ GeV are shown. Direct photons are not expected to undergo partonic energy loss, because they do not interact strongly and, thus, see the gluonic medium as "transparent". Conversely, π^0 and η mesons do interact strongly. As shown in the right panel for the η meson, the invariant yields per nucleon–nucleon collision are increasingly depleted with centrality in comparison to p–p results at the same centre of mass energy. The maximum suppression is ~ 5 in central collisions. The magnitude, p_t and centrality dependences of the suppression are the same for η and π^0, suggesting that the production of light neutral mesons at large p_t in nuclear collisions at RHIC is affected by the medium in the same way. This is expected if the suppression takes place at the parton level. In this case the high–p_t deficit depends only on the energy lost in the medium by the parent (u, d, s) light quark or gluon and not on the nature of the final leading hadron. Moreover, as reported in [37], the η/π^0 ratios are in agreement with the same ratios observed in more "elementary" collisions (p–p, e^+–e^-), suggesting that partons fragment outside the medium, according to the same fragmentation function governing hadron production in the "vacuum". The R_{AA} trend at low transverse momentum is understood to derive from the Cronin effect (see Appendix A or [42]). As described in Appendix A, the production of high–p_t particles is expected to scale with the number of binary collisions, while low–p_t particle production is expected to scale with the number of participant nucleons. In the absence of energy loss, $R_{AA} = 1$ is expected for particles whose production scales with N_{coll} and $R_{AA} \simeq 0.16$ is expected for particles whose production scales with N_{part}. However, due to the Cronin enhancement at intermediate p_t, the R_{AA} should approach the value 1 at high–p_t but not from *below* due to soft scaling at low p_t, but, rather, from *above*.

A very promising channel to investigate medium properties is jet analysis. Partons covering a significant distance through the dense fireball formed in the collision may lose so much energy to be almost absorbed by the medium, as schematically drawn in Fig. 1.12 (on the left). In the right panel of the same figure, the azimuthal correlations of charged particles with respect to a high-p_t trigger particle is shown as observed by STAR in p–p, d–Au (central and peripheral) and central Au–Au collisions. Energetic partons fragment into a jet of hadrons pointing within a relatively narrow angular cone: the peak at $\Delta\phi = 0$ can be interpreted as the consequence of jet formation. Hard partons are usually produced in pairs, with 180° opening angle in the transverse plane. This leads to the second peak at $\Delta\phi = \pi$ with respect to the trigger particle. In central collisions this opposite-side correlation is strongly suppressed with respect to the p–p and d–Au case. The effect, observed by both STAR [43, 44] and PHENIX ([45], recent results in [46]) suggests the absorption of one of the two back-to-back produced jets in the hot matter formed in central collisions. Azimuthal correlation is not a direct measurement of jets. Jets reconstruction is particularly challenging in heavy-ion collisions due to the large background induced by the high–multiplicity environment in these collisions. STAR has recently shown the first results for the full reconstruction of jets in Au–Au collisions at $\sqrt{s_{\mathrm{NN}}} = 200$ GeV [47, 48, 49]. At the LHC a much copious jet production is expected allowing a better separation from the background [50]. The comparison of full jet measurements at RHIC and the LHC will provide a crucial insight into the understanding of jet quenching and hot QCD matter.

1.5 QGP at the LHC: towards a real freedom for Quarks and Gluon?

Starting from the estimates of the charged multiplicity, many parameters of the medium produced in the collision can be inferred. Table 1.2 presents a comparison of the most relevant

Table 1.2: Comparison of the parameters characterizing central nucleus–nucleus collisions at different energy regimes [51].

Parameter		SPS	RHIC	LHC
$\sqrt{s_{\rm NN}}$	[GeV]	17	200	5500
$\mathrm{d}N_{\rm gluons}/\mathrm{d}y$		$\simeq 450$	$\simeq 1200$	$\simeq 5000$
$\mathrm{d}N_{ch}/\mathrm{d}y$		400	650	$\simeq 3000$
Initial temperature	[MeV]	200	350	> 600
Energy density	[GeV/fm^3]	3	25	120
Freeze-out volume	[fm^3]	few 10^3	few 10^4	few 10^5
Life-time	[fm/c]	< 2	2-4	> 10

parameters for SPS, RHIC and LHC energies [51]. At the LHC, the high energy in the collision centre of mass is expected to determine a large energy density and an initial temperature at least a factor 2 larger than at RHIC. This high initial temperature extends also the life-time and the volume of the deconfined medium. In addition, the expected large number of gluons favours energy and momentum exchange, considerably reducing the time needed for the thermal equilibration of the medium. To summarize, the LHC will produce *hotter, larger and longer-living* “drops” of QCD plasma than the present heavy ion facilities.

The key advantage in this new scenario is that the quark–gluon plasma studied by the LHC experiments will be much more similar to the quark–gluon plasma that can be investigated from a theoretical point of view by means of lattice QCD.

As mentioned, lattice calculations are mostly performed for a baryon-free system ($\mu_{\rm B} = 0$). In general, $\mu_{\rm B} = 0$ is not valid for heavy ion collisions, since the two colliding nuclei carry a total baryon number equal to twice their mass number. However, the baryon content of the system after the collision is expected to be concentrated rather near the rapidity of the two colliding nuclei. Therefore, the larger the rapidity of the beams, with respect to their centre of mass, the lower the baryo-chemical potential in the central rapidity region. The rapidities of the beams at SPS, RHIC and LHC are 2.9, 5.3 and 8.6, respectively. Clearly, the LHC is expected to be much more baryon-free than RHIC and SPS and, thus, closer to the conditions simulated in lattice QCD.

In addition to this effect, also the higher temperature predicted for the LHC favours the comparison with theory. This point can be better understood by going back to the lattice results for ε/T^4 (Fig. 1.2). If we now concentrate on the result obtained with 2+1 flavours, 2 light quarks plus a heavier one, we notice that ε/T^4 continues to rise for $T > T_c$, indicating that significant non-perturbative effects, not fully accounted for in the lattice formalism, are expected at least up to temperatures $T \simeq (2\text{-}3)\, T_c$. In Ref. [52] the strong coupling constant in this range is estimated as

$$\alpha_s(T) = \frac{4\pi}{18\,\ln(5\,T/\Lambda_{\rm QCD})} = \begin{cases} 0.43 & \text{for } T = T_c \\ 0.3 & \text{for } T = 2\,T_c \\ 0.23 & \text{for } T = 4\,T_c \end{cases} \tag{1.9}$$

using the fact that the QCD scaling constant $\Lambda_{\rm QCD}$ is of the same order of magnitude as T_c, ≈ 200 MeV. These values confirm that non-perturbative effects are larger in the range $T < 2\,T_c$.

The conditions produced in heavy ion collisions at SPS and RHIC are contained in this range ($T_{\mathrm{SPS}} \approx 1.2 \times T_c$ and $T_{\mathrm{RHIC}} \approx 2 \times T_c$), meaning that, in these cases, the comparison of experimentally determined quantities, such as temperature or energy density, to lattice QCD calculations is not fully reliable. With an initial temperature of $\sim$ (4-5) T_c predicted for central Pb–Pb collisions at $\sqrt{s_{\mathrm{NN}}} = 5.5$ TeV, the LHC will provide closer-to-ideal conditions (i.e. with smaller non-perturbative effects), allowing a direct comparison to the theoretical calculations. In this sense, the regime that will be realized at the LHC may be defined as "deep deconfinement".

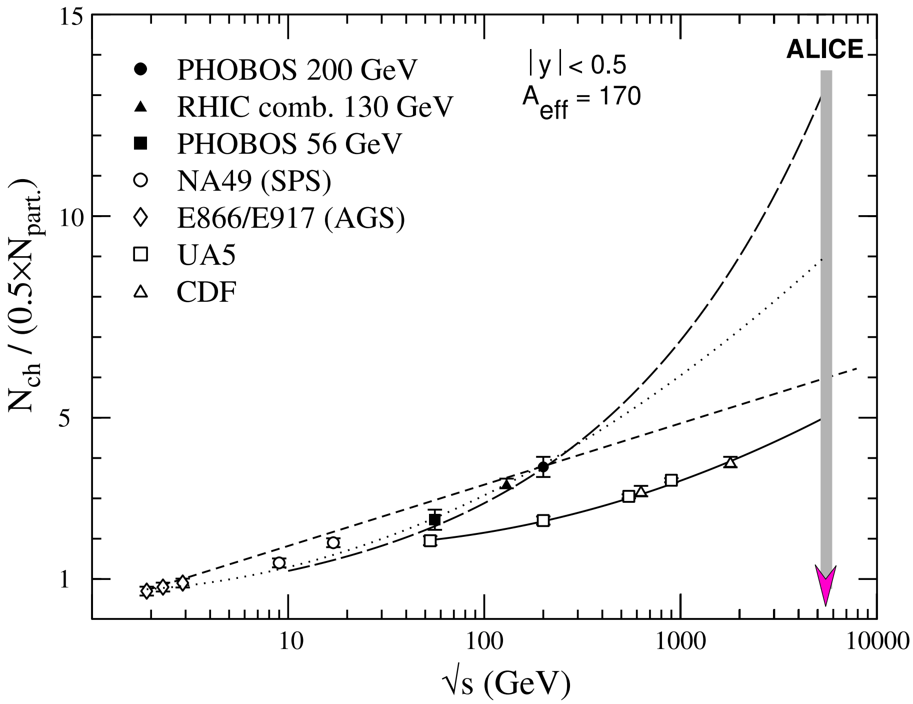

Figure 1.13: Charged-particle rapidity density per participant pair as a function of centre-of-mass energy for A–A and p–p collisions. Experimental data for p–p collisions are overlaid by the solid line. The dashed line is a fit $0.68 \ln(\sqrt{s}/0.68)$ to all the nuclear data. The dotted curve is $0.7 + 0.028 \ln^2 s$. It provides a good fit to data below and including RHIC, and predicts $N_{\mathrm{ch}} = 9 \times 170 = 1500$ at LHC. The long dashed line is an extrapolation to LHC energies using the saturation model [51]. Figure from [2].

1.5.1 Novel aspects of the heavy-ion physics at the LHC

One of the most important global observables is the average charged particle multiplicity per rapidity unit ($\mathrm{d}N_{ch}/\mathrm{d}y$) in central Pb–Pb collisions. On the theoretical side, since it is related to the attained energy density (see Bjorken's formula in equation 1.4), it enters the calculation of most other observables. On the experimental side, the particle multiplicity fixes the main unknown in the detector performance and the accuracy with which many observables can be measured.

There is no first principle calculation of $\mathrm{d}N_{ch}/\mathrm{d}y$ starting from the QCD Lagrangian, since particle production is dominated by soft non-perturbative QCD. Therefore, the large variety of available models of heavy ion collisions gives a wide range of predicted multiplicities. Before RHIC, the predictions for the LHC reached up to more than 8000 charged particles per unit of rapidity. The multiplicity measured at RHIC, $\mathrm{d}N_{ch}/\mathrm{d}y \simeq 650$ at $\sqrt{\mathrm{s}_{\mathrm{NN}}} = 200$ GeV, is about a factor 2 lower than what was predicted by most models. As it can be seen from Fig. 1.13, the multiplicity at the LHC is not expected to be larger than 3000-4000 charged particles per unit of rapidity. An approximate prediction for the LHC taken from the figure is $\mathrm{d}N_{\mathrm{ch}}/\mathrm{d}y \approx 2200$.

Hard partons at the LHC

The higher energy accessible at the LHC will imply not only a new regime concerning the properties of the produced QGP but will also allow to test them with new probes, in particular with hard-probes. At the LHC, hard processes contribute significantly to the total Pb–Pb cross–section. Hard partons are ideal probes of the medium because:

1. They are produced in the early stage of the collision in primary partonic scatterings, $gg \to gg$ or $gg \to q\bar{q}$, with large virtuality Q and, thus, on temporal and spatial scales, $\Delta\tau \sim 1/Q$ and $\Delta r \sim 1/Q$, which are sufficiently small for the production to be *unaffected* by the properties of the medium.

2. Given the large virtuality, the production cross–sections can be reliably calculated with the perturbative approach of pQCD. In fact, since

$$\alpha_s(Q^2) \propto \frac{1}{\ln(Q^2/\Lambda^2_{\mathrm{QCD}})},$$

   in an expansion of the cross–sections in powers of α_s, for large values of Q^2, the higher-order terms (in general higher than next-to-leading order, $\mathcal{O}(\alpha_s^3)$) are small and can be neglected. In this way, as already mentioned, one can safely use pQCD for the energy interpolations needed to compare p–p , p–A and A–A and disentangle initial and final state effects.

3. While propagating through the medium they lose energy via QCD energy loss mechanisms (see Section 2.4.1), which depend on the medium density, opacity and dimension. Thus, from their attenuation, it is possible to gain information on the early stage of the medium evolution, before hadronization.

The estimated yields for charm and beauty production are expected to be 10 and 100 times larger, respectively, at the LHC than at RHIC. At the LHC also weakly interacting hard probes become accessible [2]. Direct photons (but in principle also Z^0 and $\mathrm{W}^{\pm}$ bosons) produced in hard processes will provide information about nuclear parton distributions at very large virtuality (Q^2). Z^0 and $\mathrm{W}^{\pm}$ bosons that do not interact strongly could be an ideal unbiased reference to better clarify and understand the energy loss mechanism.

Parton Distribution Functions at low Bjorken–x: nuclear shadowing effect

Parton distribution functions (PDF) naively express the probability to find a parton with a given fraction (called Bjorken–x) of the proton (or nucleus) momentum. The PDF calculation is not possible from first principles starting from the QCD Lagrangian defined in Eq. 1.1. They

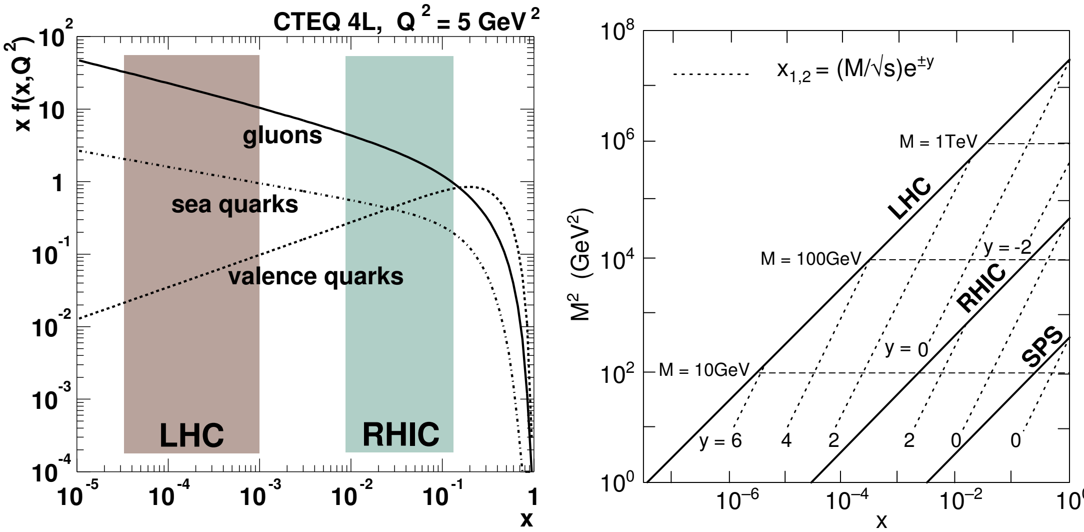

Figure 1.14: On the left: example of proton Parton Distributions Functions, obtained with CTEQ 4L parametrization at $Q^2 = 5$ GeV^2. On the right: the range of Bjorken–x and M^2 relevant for particle production in nucleus–nucleus collisions at the top SPS, RHIC, and LHC energies. Lines of constant rapidity are shown for LHC, RHIC and SPS.

are extracted from global fits to experimental data, mainly from *deep inelastic scattering* (DIS) experiments. By means of the DGLAP (Dokshitzer–Gribov–Lipatov,Altarelli–Parisi) evolution equations [53] describing the PDF Q^2 dependence, PDF values can be predicted at different Q^2. In Fig. 1.14 (left panel) an example of proton PDF at $Q^2 = 5$ GeV^2 obtained with CTEQ 4L parametrisation is reported, highlighting the different x regions accessible at RHIC and LHC. Reference PDFs for LHC, obtained from global fits from HERA data and using different schemes can be found in [54]. The large cross–sections for hard–scattering processes with large virtuality will allow to access the lowest Bjorken–x values ever access, as shown in Fig. 1.14 for nucleus–nucleus collisions. The extension of the x range down to $\lesssim 10^{-4}$ implies that, in a very simplified picture, a large-x parton in one of the two colliding nuclei "sees" the other incoming nucleus as a superposition of $\approx A \times 1/10^{-4} \approx 10^6$ gluons. These gluons are so many that the probability that the lower momentum ones merge together is not negligible: two gluons, with momentum fractions x_1 and x_2, merge in a gluon with momentum fraction $x_1 + x_2$ (i.e. $g_{x_1} g_{x_2} \rightarrow g_{x_1+x_2}$, where g stands for the gluon parton distribution function). As a consequence of this "migration" towards larger values of x the nuclear parton densities are depleted in the small-x region (and slightly enhanced in the large–x region) with respect to the proton parton densities. This phenomenon is known as *nuclear shadowing effect* and it has been experimentally studied in electron–nucleus DIS experiments in the range $5 \cdot 10^{-3} < x < 1$ [55]. Experimental data in the x range covered by the LHC are not available yet: the existing data provide only weak constraints for the gluon PDF. ALICE will probe a continuous range of x as low as about 10^{-5}, accessing a novel x regime where strong nuclear gluon shadowing is expected.

1.5.2 LHC heavy-ion programme

While this thesis was being written, the first events from p–p collisions were being collected at the LHC. The actual centre–of–mass (c.m.s.) energies were 0.9 TeV and 2.36 TeV: the data collected at these energies were used for detector calibration operations and, for first physics analysis [56].

The ion beams will be accelerated in the LHC up to a momentum of 7 TeV per unit of Z/A, where A and Z are the mass and atomic numbers of the ions, respectively. A generic ion (A,Z) will have momentum $p(\mathrm{A},\mathrm{Z}) = (\mathrm{Z}/\mathrm{A})\,p^{\mathrm{p}}$, where $p^{\mathrm{p}} = 7$ TeV is the momentum for a proton beam. The centre-of-mass energy per nucleon–nucleon pair in the collision of two generic nuclei $(\mathrm{A}_1,\mathrm{Z}_1)$ and $(\mathrm{A}_2,\mathrm{Z}_2)$ is:

$$\sqrt{\mathrm{s}_{\mathrm{NN}}} = \sqrt{(E_1+E_2)^2 - (\vec{p}_1+\vec{p}_2)^2} \simeq \sqrt{4\,p_1\,p_2} = \sqrt{\frac{\mathrm{Z}_1\mathrm{Z}_2}{\mathrm{A}_1\mathrm{A}_2}}\,14\ \mathrm{TeV}. \qquad (1.10)$$

The initial LHC running programme foresees:

- Regular p–p runs at $\sqrt{s} = 7$ TeV Then it will possible to reach the maximum c.m.s. energy $\sqrt{s} = 14$ TeV. At the ALICE interaction point the foreseen luminosity is $3 \cdot 10^{30}\mathrm{cm}^{-2}\mathrm{s}^{-1}$.
- 1-2 years with Pb–Pb runs (1 month per year) at $\sqrt{\mathrm{s}_{\mathrm{NN}}} = 5.5$ TeV (luminosity $10^{27}\ \mathrm{cm}^{-2}\mathrm{s}^{-1}$)
- 1 year with p–Pb runs (1 month per year) at $\sqrt{\mathrm{s}_{\mathrm{NN}}} = 8.8$ TeV (luminosity $8{\cdot}10^{28}\ \mathrm{cm}^{-2}\mathrm{s}^{-1}$)

At least for what concerns the hard observables, the fact of having different c.m.s. energies for the different systems is not expected to introduce large uncertainties in the comparisons, because perturbative QCD (pQCD) calculations can be used quite safely for the extrapolation to different energies (for example to scale the results measured in p–p at 14 TeV to the energy of Pb–Pb, 5.5 TeV) [2, 57].

Chapter 2

Probing QCD with Heavy Quarks

Heavy-quark production is one of the most promising observables to probe the properties of the medium produced in heavy-ion collisions. Heavy-quark (charm and beauty) production requires large momentum transfer ($Q^2 > 4\mathrm{M}^2_{c,b}$), larger than the possible thermal momentum transfer in the medium. Thus, it must occur in the early stage of the collision, in primary partonic scatterings and the production kinematics is not influenced by medium effects. While propagating through the medium they strongly interact with the hot and dense "coloured" matter and lose energy. Energy loss affects the momentum spectra of the hadrons produced in the later hadronization stage. Due to the large momentum transfer, heavy-flavour production can be calculated via perturbative QCD and, moreover, it is possible to safely use pQCD for the energy interpolations needed to compare observables in p–p and A–A collisions. Therefore, the comparison between the momentum spectra observed for heavy-flavoured hadrons in Pb–Pb and p–p collisions is a powerful tool to investigate the in–medium partonic energy loss mechanism as well as medium properties. To this purpose, the understanding of heavy-quark production in p–p collisions is essential. The theoretical description of the production of heavy-flavoured hadrons in p–p collisions relies on the factorization theorem. This organizes the calculation as a convolution of an hard–scattering term, that can be calculated with a perturbative approach, with non perturbative terms, namely the parton distribution functions, and the fragmentation functions. Theoretical predictions are affected by approximations on these three terms and on the scheme used to match them properly. Moreover, for heavy quarks, special care is required in the treatment of the large quark mass in the calculations. At LHC heavy quarks will be produced copiously and a new energy regime will be accessible to test parton distribution functions and disentangle among the different pQCD implementations. Due to the low magnetic field employed (0.5 T), the ALICE experiment will be able to measure charm production at low p_{t} and very low x.

In this chapter, heavy-quark production in p–p collisions is described along with the experimental results for the cross–section of charm production at RHIC and CDF. The extrapolations to the LHC energies are shown. Then, heavy-flavour production in heavy-ion collisions and the mechanism of in–medium partonic energy loss are discussed and the main experimental results from RHIC are shown. This work of thesis was carried out in the scope of the preparation for the measurement of charm production in p–p collisions. In the last section of this chapter, the strategy to perform this measurement via the exclusive reconstruction of hadronic decays of open charm mesons.

2.1 Heavy-flavour production in proton–proton collisions

Given their large mass ($M_{\rm b} \approx 4.8$ GeV $> M_{\rm c} \approx 1.2$ GeV [58]) heavy quarks (charm and beauty) are produced in hard–scattering processes with large momentum transfer ($Q^2 \gtrsim 4\mathrm{M}^2_{c,b}$). Due to asymptotic freedom, the QCD coupling constant decreases with increasing energy (Section 1.1). At the threshold for charm production it is small enough[1] to perform a perturbative calculation based on an expansion of the hard–scattering amplitude in terms of powers of α_S. According to the factorisation theorem, the single-inclusive differential cross–section for the production of a heavy flavour hadron H_Q can be written as:

$$\begin{aligned}\frac{\mathrm{d}\sigma^{\mathrm{NN}\to\mathrm{H}_Q X}}{\mathrm{d}p_{\rm t}}(\sqrt{\mathrm{s}}_{\rm NN}, M_Q, \mu_{\rm F}^2, \mu_{\rm R}^2) = \quad & \sum_{i,j=q,\overline{q},g} f_i(x_1,\mu_{\rm F}^2) \otimes f_j(x_2,\mu_{\rm F}^2) \otimes \\ & \mathrm{d}\hat{\sigma}^{ij\to Q(\overline{Q})\{k\}}(\alpha_{\rm s}(\mu_{\rm R}^2), \mu_{\rm F}^2, M_Q, x_1 x_2 s_{\rm NN}) \otimes \\ & D_Q^{\mathrm{H}_Q}(z,\mu_{\rm F}^2)\,, \end{aligned} \tag{2.1}$$

where Q is the heavy quark (either charm or beauty), M_Q is its mass, and $p_{\rm t}$ its transverse momentum. The sum runs over all possible sub-processes that lead to the heavy-flavour hadron. The formula is made up of three different terms:

- $f_i(x_i, \mu_F^2)$ is the parton distribution function, the probability of finding a quark or a gluon i with a momentum fraction x_i of the nucleon. The PDFs are evolved with the virtuality Q^2 up to the factorisation scale μ_F using the DGLAP equations [53].

- $\frac{\mathrm{d}\hat{\sigma}}{\mathrm{d}\hat{p}_{\rm t}}(ij \to Q(\overline{Q}))$ is the partonic cross–section. Given the high mass of the quarks involved ($M_{\rm b} > M_{\rm c} > \Lambda_{QCD}$) it is related to interactions of partons at high Q^2. This means that it can be computed by perturbative QCD. It is a function of the heavy-quark mass (M_Q), of the parton-parton centre of mass energy squared ($x_1 x_2 s$) and of the quark transverse momentum ($\hat{p}_{\rm t}$). In pQCD the cross–section is calculated in a power expansion in terms of of α_s. The total cross–section for heavy-flavour production has been calculated up to next-to-leading order (NLO, see Ref. [59]), that corresponds to $O(\alpha_s^3)$).

- $D_Q^{H_Q}(z, \mu_F^2)$ is the fragmentation function, that represents the probability for the heavy quark Q to hadronize as a specific hadron H_Q with a momentum fraction $z = p_{\mathrm{H}_Q}/p_Q$. This is usually extracted by fitting a phenomenological model to fragmentation data in e^+e^-.

2.1.1 Parton Distribution Functions at the LHC: x range accessible with heavy flavours

The Bjorken–x range accessible in the production of a $Q_H\bar{Q}_H$ pair ($Q_H \equiv c, b$ quarks) in p–p and Pb–Pb collisions at the LHC can be estimated from the invariant mass and the rapidity

[1] $0.25 \lesssim \alpha_S(Q^2, \mu_R)) \lesssim 0.6$ depending on the renormalization scale μ_R.

of the pair as follows:

$$M^2_{Q_H\bar{Q_H}} = \hat{s} = x_1\frac{Z_1}{A_1}x_2\frac{Z_2}{A_2}s_{\mathrm{p-p}} \tag{2.2}$$

$$y_{Q_H\bar{Q_H}} = \frac{1}{2}\ln\left[\frac{E+p_z}{E-p_z}\right] = \frac{1}{2}\ln\left[\frac{x_1}{x_2}\cdot\frac{Z_1A_2}{Z_2A_1}\right], \tag{2.3}$$

where Z_1,Z_2 and A_1,A_2 are the atomic and mass numbers of the two incident nuclei and the relation $\sqrt{s_{NN}} = \sqrt{(Z_1Z_2/A_1A_2)}\sqrt{s}_{\mathrm{p-p}}$ is used. Thus,

$$x_1 = \frac{A_1}{Z_1}\cdot\frac{M_{Q_H\bar{Q_H}}}{\sqrt{s}_{\mathrm{p-p}}}\exp(+y_{Q_H\bar{Q_H}}) \qquad x_2 = \frac{A_1}{Z_1}\cdot\frac{M_{Q_H\bar{Q_H}}}{\sqrt{s}_{\mathrm{p-p}}}\exp(-y_{Q_H\bar{Q_H}}) \tag{2.4}$$

In the central rapidity region ($y \simeq 0$), $x_1 \simeq x_2$ the value depending on the invariant mass and the collision energy. At the threshold for $Q_H\bar{Q}_H$ production ($M_{c\bar{c}} = 2m_c \simeq 2.4$ GeV, $M_{b\bar{b}} = 2m_b \simeq 9$ GeV), the x values accessible at the SPS, RHIC and LHC experiments are those reported in Table 2.1. Due to the lower mass, lower x values are accessible from the

Table 2.1: x Bjorken values accessible in the various experiment in the central rapidity region and at the threshold for $c\bar{c}$ ($b\bar{b}$) production.

Machine	SPS	RHIC	LHC	LHC
System	Pb–Pb	Au–Au	Pb–Pb	p–p
$\sqrt{s_{NN}}$	17 GeV	200 GeV	5.5 TeV	14 TeV
$c\bar{c}$	$x \simeq 10^{-1}$	$x \simeq 10^{-2}$	$x \simeq 4\cdot10^{-4}$	$x \simeq 2\cdot10^{-4}$
$b\bar{b}$	-	-	$x \simeq 2\cdot10^{-3}$	$x \simeq 6\cdot10^{-4}$

analysis of charm production. The pseudo–rapidity interval covered by the ALICE detector (Section 3.1) is $|\eta| < 0.9$ for the central barrel while the forward rapidity muon arm covers the region $2.5 < \eta < 4$, allowing to probe x values down to $x \sim 10^{-6}$.

2.1.2 Experimental results at CDF and RHIC

Charm and beauty production has been measured at the Tevatron at $\sqrt{\mathrm{s}_{\mathrm{NN}}} = 1.96$ TeV, the highest energy available, by the CDF and D0 experiments. The cross–section for charm production has been measured in CDF via the exclusive reconstruction of D mesons decays in hadronic channels (Fig. 2.1 from [8]). Among other possibilities, ALICE will perform a very similar study to measure the cross–section for charm production at the LHC, as it is outlined in Section 2.5. Theoretical predictions using the FONLL (fixed-order-plus-next-to-leading-log) scheme (described in [54]) seem to slightly underpredict CDF results, even if they are compatible with the data within uncertainties. Conversely, beauty production at Tevatron is fairly well described by FONLL calculations, as can be seen by comparing data and theoretical predictions for the p_{t} distribution of J/Ψ from B meson decays in Fig. 2.1 (right panel). The p_{t}–differential cross–section for charm production has been measured at RHIC in p–p, Au–Au and d–Au collisions mainly via the analysis of non–photonic identified electrons. More details on the experimental technique are given in Section 2.4.2 or can be found in the PHENIX ([60, 61]) and STAR ([62, 63]) papers. Figure 2.2 (a) shows the

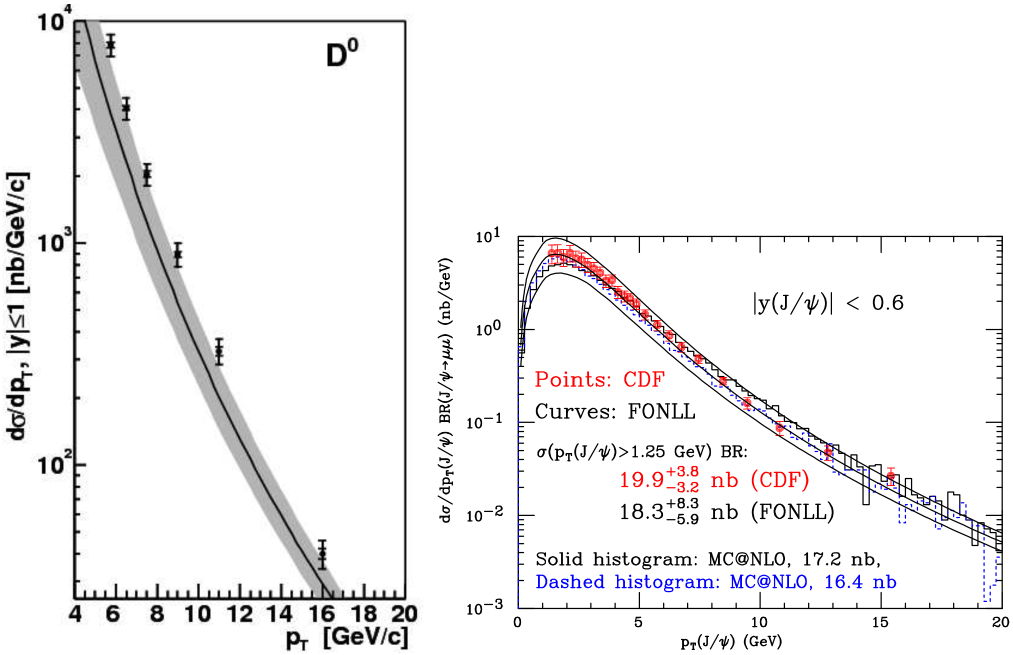

Figure 2.1: Left panel: p_t differential cross–section for D^0 mesons production observed by CDF and compared to FONLL predictions. Right panel: p_t distribution for J/Ψ from B decays as observed by CDF, compared to FONLL predictions.

invariant differential cross–section for the production of electrons from heavy-flavour decays in p–p collisions, as measured by PHENIX. The data are compared with FONLL pQCD calculations [64]. The top curve in Fig. 2.2 shows the central values of the FONLL calculation. The predicted contributions of charm and beauty are also shown separately. For $p_\mathrm{t} > 4$ GeV/c, the beauty contribution becomes dominant. In Fig. 2.2 (b), the ratio of the data to the FONLL calculations is shown. The ratio is nearly p_t independent over the entire p_T range. Fitting it to a constant for $0.3 < p_\mathrm{t} < 9.0$ GeV/c yields a ratio of $1.72 \pm\ 0.02^{\mathrm{stat}} \pm\ 0.19^{\mathrm{sys}}$. Similar ratios are observed for charm production at high p_t at the Tevatron [8]. The upper limit of the FONLL calculation is compatible with the data. The estimated total charm cross–section is $\sigma_{c\bar{c}} = 567 \pm\ 57^{\mathrm{stat}} \pm\ 224^{\mathrm{sys}}$ μb, compatible with the FONLL cross–section (256^{+400}_{-146} μb) within errors.

2.2 Predictions for heavy-quark production at the LHC

The cross–sections for heavy-flavour production at LHC energies ($\sqrt{s}$ = 5.5 and 14 TeV) have been estimated [65] from the NLO pQCD calculations implemented in the program HVQMNR [4] with the two sets of PDFs, MRST HO [66] and CTEQ 5M1 [67], which include the small-x HERA results. The fixed–order NLO order calculation in HVQMNR coincides with the FONLL (Fixed–Order Next–to–Leading–Log) calculation in the low and intermediate p_t region while the latter is more accurate at high p_t where large logarithmic terms beyond next–to–leading order are accounted for in next–to–leading–log resummation. The results are reported in Table 2.2. The difference due to the choice of the parton distribution functions

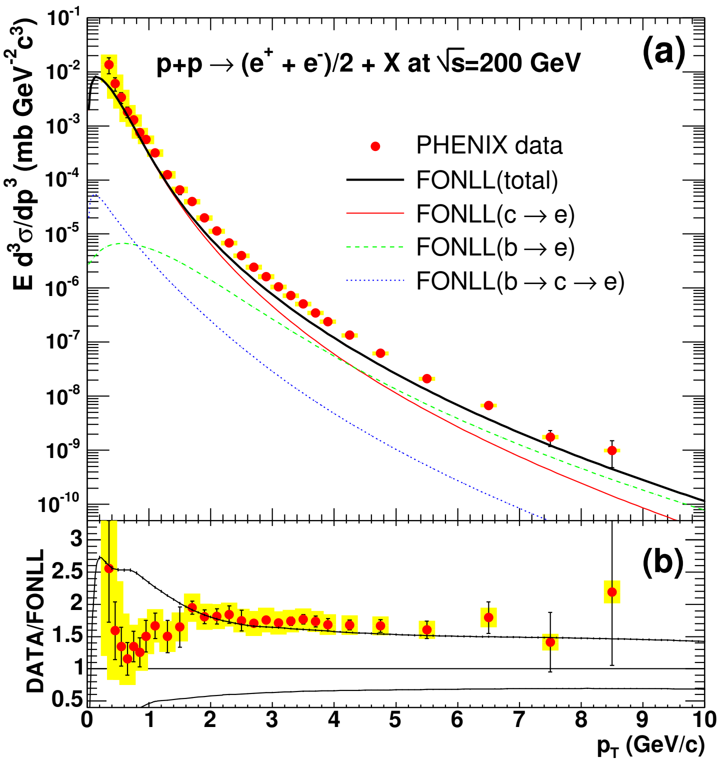

Figure 2.2: (a) Invariant differential cross–section for electrons from heavy-flavour decays. The error bars (bands) represent the statistical (systematic) errors. The curves represent the FONLL calculations (see text). (b) Ratio of the data and the FONLL calculation. The upper (lower) curve shows the theoretical upper (lower) limit of the FONLL calculation. In both panels a 10% normalization uncertainty is not shown.

is relatively small ($\sim$ 20-25% at 5.5 TeV, slightly lower at 14 TeV). The average of the values obtained with these two sets of PDF is used as a baseline. The dependence on the PDF set represents only a part of the uncertainty on the theoretical prediction. To estimate the theoretical uncertainties on the single–inclusive $p_{\rm t}$–differential cross–sections for c and b quarks, the quark masses (m_c, m_b) and the renormalization and factorization scales ($\mu_{\rm R}, \mu_{\rm F}$) were varied in the ranges $1.3 < m_c < 1.7$ GeV, $4.5 < m_b < 5.0$ GeV, $0.5 < \mu_{\rm F}/\mu_0 < 2$ and $0.5 < \mu_{\rm R}/\mu_0 < 2$, with μ_0 approximately equal to the transverse mass of the produced heavy quarks ($\mu_0 \equiv \sqrt{(p_{{\rm t},Q}^2 + p_{{\rm t},\overline{Q}}^2)/2 + m_Q^2} \approx m_{{\rm t},Q}$). The two scales $\mu_{\rm F}$ and μ_R were varied independently within the above constraint. The uncertainty bands shown in Fig. 2.3 are the envelope of the resulting cross–sections. The contribution due to the mass uncertainty, shown separately, is significantly smaller than that due to the variation of the scales. The total uncertainties span, approximately $p_{\rm t}$–independently, a factor about 2-3 for $p_{\rm t} \gtrsim 5$ GeV/c, while they become larger at lower transverse momenta where the scales, $\mu_{\rm F}$ and μ_R, and the momentum fractions, x_1 and x_2 are small and the scale–dependence of the PDFs is large. Fig. 2.4 shows the corresponding theoretical uncertainty band for the ratio of the single-inclusive heavy-quark cross–section at $\sqrt{s} = 14$ TeV and $\sqrt{s} = 5.5$ TeV. Despite the large spread in the absolute cross–section at a given energy, the ratio is much less dependent on the choice of the parameters. In particular, no dependence is observed on the value of the heavy-quark mass m_Q and on the value of the renormalisation scale $\mu_{\rm R}$. The uncertainty on the ratio is solely determined by the variation of the factorisation scale $\mu_{\rm F}$. This is due to the fact that, for the same heavy-quark $p_{\rm t}$, different Bjorken–x ranges are probed at 5.5 TeV and 14 TeV and changing the factorisation scale affects the x dependence of the PDFs. These results indicate that a pQCD–based extrapolation can be used to compare the cross–sections measured in Pb–Pb collisions at $\sqrt{s_{\rm NN}} = 5.5$ TeV with those measured in p–p collisions at $\sqrt{s_{\rm NN}} = 14$ TeV. The systematic error introduced by the extrapolation is about 12% for charm and 8% for beauty, as shown in the lower panels of Fig. 2.4.

Yields in p–p and Pb–Pb collisions at $\sqrt{s} = 14$ TeV and $\sqrt{s} = 5.5$ TeV

Using a p–p total inelastic cross–section $\sigma_{\rm pp}^{\rm inel} = 70$ mb at 14 TeV [2] and the heavy flavour cross–sections in Table 2.2, the yields for the production of $Q\overline{Q}$ pairs are:

$$N_{\rm pp}^{Q\overline{Q}} = \sigma_{\rm pp}^{Q\overline{Q}} \Big/ \sigma_{\rm pp}^{\rm inel}. \tag{2.5}$$

Thus, using the average of MRST HO and CTEQ 5M1, 0.16 $c\bar{c}$ pairs and 0.0072 $b\bar{b}$ pairs per event is obtained for $\sqrt{s} = 14$ TeV. Table 2.3 summarizes the predicted $c\bar{c}$ and $b\bar{b}$ pairs production yields at the LHC in p–p with CTEQ 6M PDF and in Pb–Pb collisions with the average of MRST HO and CTEQ 5M1. The binary scaling (see Appendix A) based on the Glauber model has been used to estimate the yields in Pb–Pb collisions.

2.3 Heavy flavours in heavy–ion collisions

As explained in the introduction to this chapter hard partons are ideal probes of the medium produced in heavy ion collisions because:

1. They are *produced in the early stage of the collision*, in primary partonic scatterings, $gg \to gg$ or $gg \to q\overline{q}$, with large virtuality Q and, thus, on temporal and spatial scales, $\Delta\tau \sim 1/Q$ and $\Delta r \sim 1/Q$, which are sufficiently small for the production to be *unaffected* by the properties of the medium.

Table 2.2: NLO predictions for the cross–sections for $c\bar{c}$ and $b\bar{b}$ production in p–p collisions at 5.5 and 14 TeV, obtained using the HVQMNR program [4] with MRST HO e CTEQ 5M1 PDF. The masses and factorization/renormalization scales used are $m_c = 1.5$ GeV and $\mu_{\rm F} = \mu_{\rm R} = 2\mu_0$ for charm, $m_b = 4.75$ GeV and $\mu_F = \mu_R = \mu_0$ for beauty.

σ	$\sigma_{\rm pp}^{\rm c\bar{c}}$[mb]				$\sigma_{\rm pp}^{\rm b\bar{b}}$[mb]			
$\sqrt{s}$	5.5 TeV	7 TeV	10 TeV	14 TeV	5.5 TeV	7 TeV	10 TeV	14 TeV
MRST HO	5.9	–	–	10.3	0.19	–	–	0.46
CTEQ 5M1	7.4	–	–	12.1	0.22	–	–	0.55
CTEQ 6M	5.81	6.91	8.87	11.2	0.183	0.232	0.326	0.447

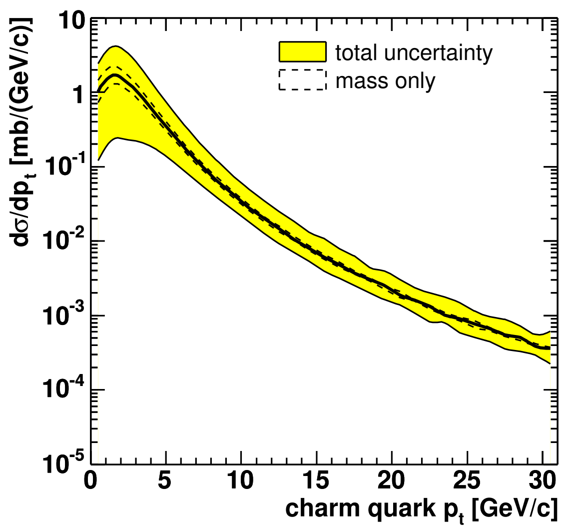

Figure 2.3: Evaluation of the theoretical uncertainty on the single–inclusive c and b quark p_t–differential cross–sections at $\sqrt{s}$ = 14 TeV performed using the HVQMNR program [4]. No rapidity selection is applied.

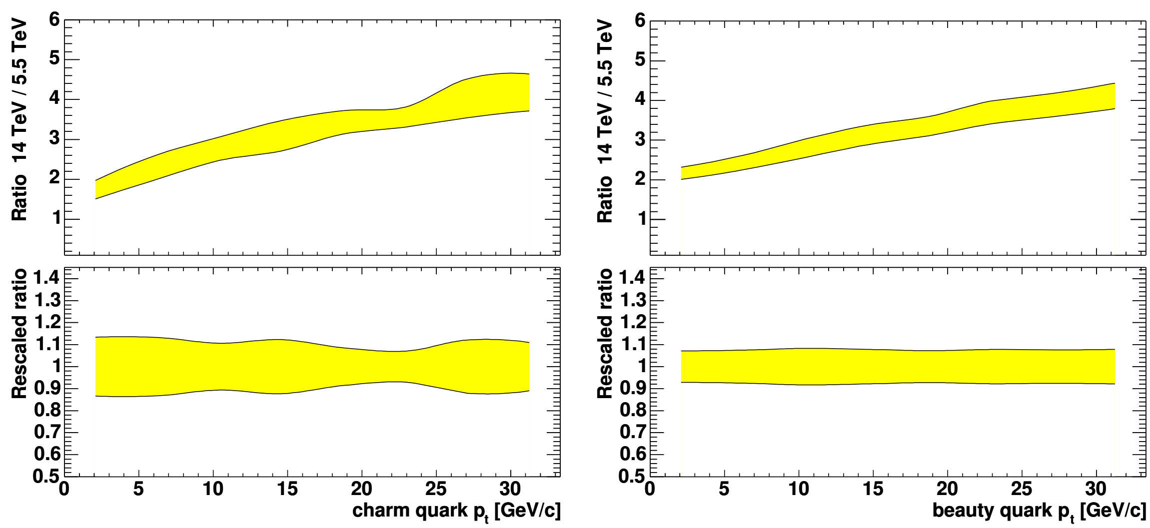

Figure 2.4: Upper panels: the theoretical uncertainty on the ratio of single–inclusive heavy-quark p_t–differential cross–sections at $\sqrt{s}$ = 14 TeV and at $\sqrt{s}$ = 5.5 TeV (left panel for charm, right panel for beauty). The method used for the estimation of the uncertainty bands is described in the text. Lower panels: the same bands are normalized to unity, i.e. divided by its central value, in order to quantify its relative width. No rapidity selection is applied.

2. Given the large virtuality, the production cross–sections can be reliably calculated with the perturbative approach of pQCD. Thus perturbative QCD calculations can be safely

Table 2.3: Summary table for the predicted production yields of $c\bar{c}$ and $b\bar{b}$ pairs in p–p and Pb–Pb collisions at the LHC. The values for p–p collisions are calculated using CTEQ 6M PDF while those for Pb–Pb collisions are calculated from the average of MRST HO and CTEQ 5M1 PDF and on the basis of binary scaling from the Glauber model.

	Charm					Beauty				
System	p–p				Pb–Pb	p–p				Pb–Pb
Centrality	min.-bias				centr.	min.-bias				centr.
$\sqrt{s_{NN}}$ [TeV]	5.5	7	10	14	5.5	5.5	7	10	14	5.5
$N^{Q\overline{Q}}$/ev	0.08	0.10	0.13	0.16	115	0.0026	0.0033	0.0047	0.0064	4.56

used for the energy interpolations needed to compare p–p, p–A and A–A collisions and disentangle between initial and final state effects.

3. While propagating through the medium they lose energy via QCD energy loss mechanisms (see Section 2.4.1), which depends on the medium density, opacity and dimension. Thus, from their attenuation is possible to gain information on the early stage of the medium evolution, before hadronization.

As explained in Section 2.4.1, in-medium partonic energy loss is predicted to depend on the parton nature (larger for gluons than quarks) and on the parton mass (larger for light quarks than for heavy quarks). Therefore, the study of heavy-quark production in heavy-ion collisions covers a special role, allowing to test the energy loss dependence on the quark mass.

2.4 Heavy-quark production in heavy-ion collisions: medium effects

2.4.1 In medium partonic energy loss

While traversing the dense matter produced in nucleus–nucleus collisions, the initially-produced hard partons lose energy, mainly on account of multiple scatterings and medium-induced gluon radiation, and become quenched. An intense theoretical activity has developed around the subject [68, 69, 70, 71, 72]. Here the general lines of the so-called "BDMPS" model [69, 70] are summarised. In a simplified picture, an energetic parton produced in a hard collision undergoes, along its path in the dense medium, multiple scatterings in a Brownian-like motion with mean free path λ, which decreases as the medium density increases. In this multiple scattering process, the gluons in the parton wave function pick up transverse momentum k_t with respect to its direction and they may eventually "decohere" and be radiated.

The scale of the energy loss is set by the characteristic energy of the radiated gluons, which depends on the path length, L, and on the properties of the medium:

$$\omega_c = \hat{q}\, L^2/2 \tag{2.6}$$

where $\hat{q}$ is the transport coefficient of the medium, defined as the average transverse momentum squared transferred to the projectile per unit path length, $\hat{q} = \langle k_\mathrm{t}^2 \rangle_\mathrm{medium}/\lambda$ [73].

In the case of a static medium, the distribution of the energy ω of the radiated gluons (for $\omega \ll \omega_c$) is of the form:

$$\omega \frac{\mathrm{d}I}{\mathrm{d}\omega} \simeq \frac{2\,\alpha_s\,C_R}{\pi}\sqrt{\frac{\omega_c}{2\omega}} \tag{2.7}$$

where C_R is the QCD coupling factor (Casimir factor), equal to 4/3 for quark–gluon coupling and to 3 for gluon–gluon coupling. The integral of the energy distribution up to ω_c estimates the average energy loss of the parton:

$$\langle \Delta E \rangle = \int_0^{\omega_c} \omega \frac{\mathrm{d}I}{\mathrm{d}\omega}\mathrm{d}\omega \propto \alpha_s\,C_R\,\omega_c \propto \alpha_s\,C_R\,\hat{q}\,L^2\,. \tag{2.8}$$

The average energy loss is: proportional to $\alpha_s\,C_R$ and, thus, larger by a factor $9/4 = 2.25$ for gluons than for quarks; proportional to the transport coefficient of the medium; proportional to L^2; independent of the initial parton energy E. It is a general feature of all parton energy loss calculations [68, 69, 70, 71, 72, 73, 74, 75, 76] that the gluon energy distribution (Eq. 2.7) does not depend on E. Depending on how the kinematic bounds are taken into account, the resulting ΔE is then independent [69, 70] or logarithmically dependent on E [74, 75, 76]. However, there is always an intrinsic dependence of the radiated energy on the initial energy, determined by the fact that the former cannot be larger than the latter, $\Delta E \leq E$. As discussed in [77], this effectively results in reducing the difference between quark and gluon average energy losses and in changing the L dependence from quadratic to approximately linear. Moreover, since a consistent theoretical treatment of the finite-energy constraint is at present lacking in the BDMPS framework, approximations have to be adopted, thus introducing uncertainties in the results [77, 78].

The transport coefficient is proportional to the density of the scattering centres and to the typical momentum transfer in gluon scattering off these centres. A review of the estimates for the value of the transport coefficient in media of different densities can be found in [79]: the estimate is $\hat{q}_{\rm cold} \simeq 0.05$ GeV^2/fm for cold nuclear matter and, for a QGP formed at the LHC with energy density $\epsilon \sim 50$–100 GeV/fm^3, $\hat{q}$ may be as large as 100 GeV^2/fm.

The medium-induced energy loss of heavy quarks was first studied in [80, 81]. Subsequently, in [82], it was argued that for heavy quarks, because of their large mass, the radiative energy loss should be lower than for light quarks. The predicted consequence of this effect was an enhancement of the ratio of D mesons to pions (or light-flavoured hadrons in general) at moderately-large (5–10 GeV/c) transverse momenta, with respect to that observed in the absence of energy loss.

Heavy quarks with moderate energy, i.e. $m/E > 0$, propagate with a velocity $\beta = \sqrt{1-(m/E)^2}$ significantly smaller than the velocity of light, $\beta = 1$. As a consequence, in the vacuum, gluon radiation at angles Θ smaller than the ratio of their mass to their energy $\Theta_0 = m/E$ is suppressed[2] [83]. The relatively depopulated cone around the heavy-quark direction with $\Theta < \Theta_0$ is called the "dead cone".

In [82], the dead-cone effect is assumed to characterise also in-medium gluon radiation, and the energy distribution of the radiated gluons (Eq. 2.7), for heavy quarks, is estimated to be suppressed by a factor:

$$\omega \frac{\mathrm{d}I}{\mathrm{d}\omega}\bigg|_{\rm Heavy} \bigg/ \omega \frac{\mathrm{d}I}{\mathrm{d}\omega}\bigg|_{\rm Light} = \left[1 + \frac{\Theta_0^2}{\Theta^2}\right]^{-2} = \left[1 + \left(\frac{m}{E}\right)^2 \sqrt{\frac{\omega^3}{\hat{q}}}\right]^{-2} \equiv F_{\rm H/L}(m/E, \hat{q}, \omega)\,, \tag{2.9}$$

[2]A term $(\Theta^2 + \Theta_0^2)^{-2}$ governs the angular dependence of the propagator of the gluon-radiation process $Q \to Qg$.

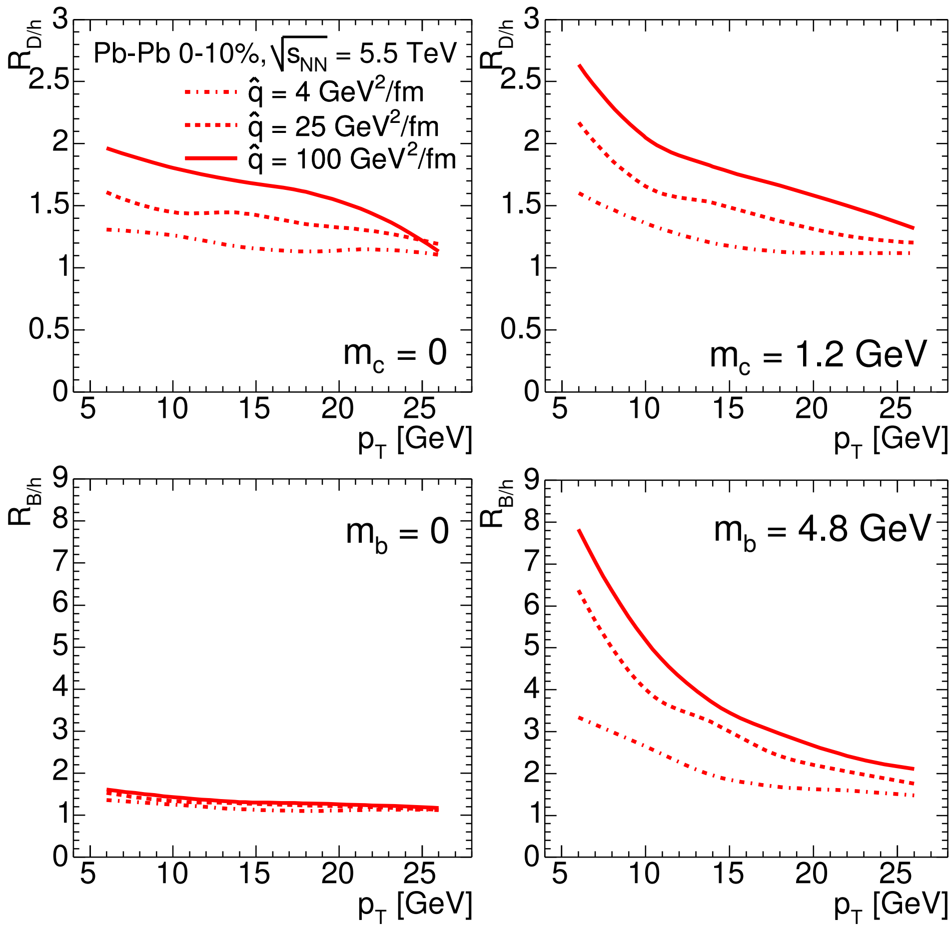

Figure 2.5: Heavy-to-light ratios, Eq. (2.10), for D mesons (upper plots) and B mesons (lower plots) for the case of a realistic heavy quark mass (plots on the right) and for a case study in which the quark-mass dependence of parton energy loss is neglected (plots on the left). From [85].

where the expression for the characteristic gluon emission angle [82] $\Theta \simeq (\hat{q}/\omega^3)^{1/4}$ has been used. The dead-cone suppression factor $F_{\mathrm{H/L}}$ in Eq. (2.9) increases (less suppression) as the heavy-quark energy E increases (the mass becomes negligible) and it decreases at large ω, indicating that the high-energy part of the gluon radiation spectrum is drastically suppressed by the dead-cone effect. A detailed calculation of the radiated-gluon energy distribution $\omega\,\mathrm{d}I/\mathrm{d}\omega$ in the case of massive partons [84] confirms the qualitative feature of lower energy loss for heavy quarks, although the effect is found to be quantitatively smaller than that derived with the dead-cone approximation of used in [82]. A comparison of the results obtained in the two cases for the D meson suppression in central Pb–Pb collisions at the LHC can be found in [86]. Calculation results published in [85] and based on the BDMPS formalism (modified for massive partons according to [84]) and on a Glauber-model description of the collision geometry, indicate the *heavy-to-light ratios* at the LHC as promising new observables to test the partonic mechanism expected to underlie jet quenching. The heavy-to-light ratios for D and B mesons, $R_{\mathrm{D}/h}$ and $R_{\mathrm{B}/h}$, are defined as the ratio of the nuclear modification factors of the heavy flavoured mesons to that of light flavoured hadrons (h):

$$R_{D(B)/h}(p_t) = R_{AA}^{D(B)}(p_t)/R_{AA}^{h}(p_t) = \frac{d^2N_{AA}^{D(B)}/dp_t dy}{d^2N_{pp}^{D(B)}/dp_t dy} \Bigg/ \frac{d^2N_{AA}^{h}/dp_t dy}{d^2N_{pp}^{h}/dp_t dy}\,. \tag{2.10}$$

Heavy-to-light ratios are suggested to be sensitive to the colour charge and to the mass dependence of medium-induced parton energy loss [85], as illustrated in Fig. 2.5 where $R_{D/h}(p_t)$ and $R_{B/h}(p_t)$ are shown, without and with the effect of the c and b masses, for the transport coefficient range $\hat{q} = 25$–100 GeV^2/fm, expected for central Pb–Pb collisions at the LHC on the basis of the R_{AA}^h values measured at RHIC [87, 39] (the curves for the much lower value $\hat{q} = 4$ GeV^2/fm are reported as well for comparison).

- For D mesons (see upper panels of Fig. 2.5 for $M_c = 0,\ 1.2$ GeV) the effect of the charm mass is expected to be small and limited to the range $p_t < 10$ GeV/c, where initial-state effects, like shadowing, or final-state effects other than parton energy loss, like in-medium hadronization, may prevent a clear analysis of heavy-to-light ratios. For higher transverse momentum ($10 \le p_t \le 20$ GeV/c), charm quarks would behave essentially like massless quarks. However, since at LHC energy light-flavoured hadron yields are dominated by gluon parents, $R_{D/h}$ would be enhanced with respect to unity as a consequence of the larger colour charge (reflected in the Casimir factor C_R) of gluons relative to quarks. Therefore, $R_{D/h}$ would be a sensitive probe of the colour charge dependence of parton energy loss.

- For B mesons (see lower panels of Fig. 2.5 for $M_b = 0,\ 4.8$ GeV), in contrast, the heavy-to-light ratio would be strongly enhanced due to the large b mass even in the range $10 \le p_t \le 20$ GeV/c, thus providing a sensitive test of the mass dependence of parton energy loss.

2.4.2 Charm production and energy loss in heavy-ion collisions at RHIC

Charm production at RHIC has been studied mainly via three different measurements [88, 23, 61, 89]: the first is based on the exclusive reconstruction of D mesons decays in hadronic–channels, the others consist of an inclusive measurement of D (and B) mesons production via the analysis of muons or non–photonic electrons.

The reconstruction of D mesons decays to charged hadrons gives the cleanest signal and the full momentum of the initial D meson is reconstructed. STAR reconstructed exclusively $D^0 \to K^-\pi^+$ decays in d–Au [63] and Au–Au [62] collisions by an invariant mass analysis of identified opposite charged kaon and pion pairs. However, it is rather difficult to perform this measurement without a vertex detector, especially in Au–Au collisions because of the large combinatorial background. Both the statistical and systematic uncertainties are very large. The presence of the Inner Tracking System detector will allow ALICE to perform this analysis with very good significance [3].

In the analysis of semi–leptonic decays, identified electron (muon) spectra (after background subtraction) are considered. The initial D meson momentum remains undetermined. The main sources of background are electrons coming from photon conversion in the detector material and π^0 and η Dalitz decays ($\pi^0(\eta) \to \gamma e^+e^-$). In the PHENIX experiment, background subtraction is performed by the converter and the cocktail methods [61, 90], which

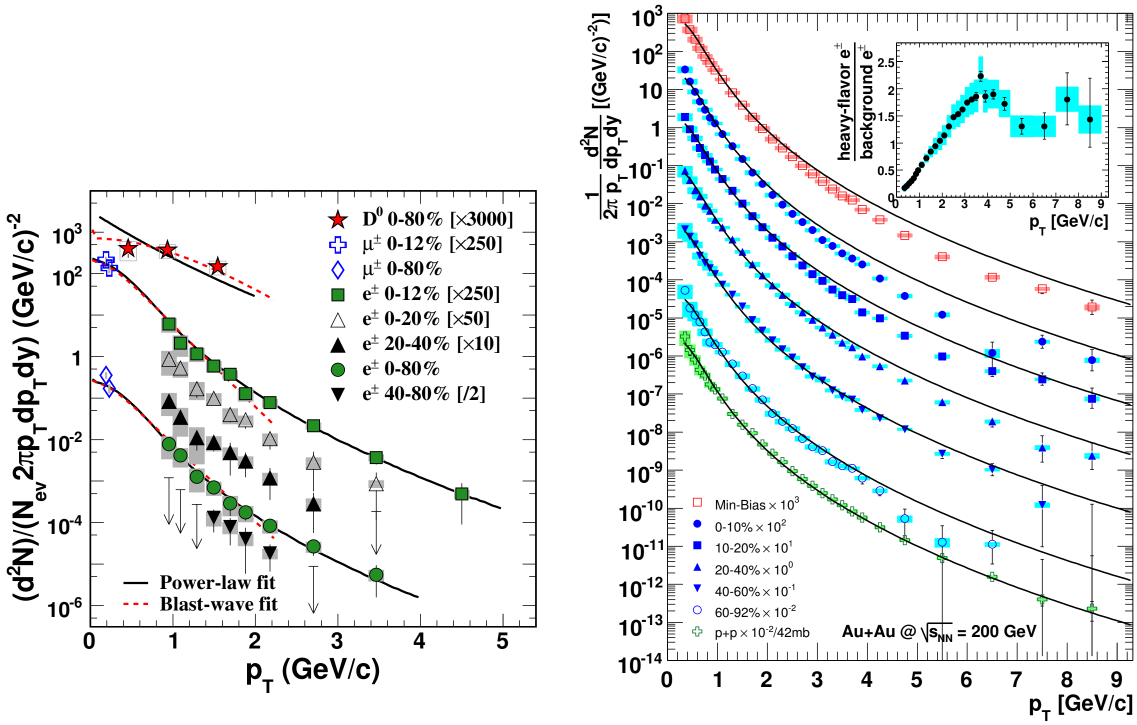

Figure 2.6: Left panel: p_{t} distributions of invariant yields for reconstructed D^0, charm–decayed prompt μ and non–photonic electrons in different centralities as observed by STAR [62]. The grey bands are bin–to–bin systematic uncertainties. Right panel: p_{t} distributions of invariant yields of electrons from heavy-flavour decays for different Au–Au centralities and p–p data compared with theoretical predictions based on FONLL calculations normalized to p–p data and scaled with $\langle T_{AA}\rangle$ (see Appendix A). Error bars (boxes) depict statistical (systematic) uncertainties. The inset shows the ratio of heavy-flavour to background electrons for minimum bias Au–Au collisions.

give similar results. In the converter method a thin brass sheet acting as a photon converter is placed around the beam pipe, enhancing the photonic background which can be properly analyzed and subtracted. In the cocktail methods, Monte Carlo simulations tuned to reproduce the measured π^0 and π^+ spectra, are used to estimate the background electrons yield. In the STAR experiment, the background contribution from photonic sources is subtracted statistically from an invariant mass analysis of (e^+e^-) pairs [62].

D meson decays in muonic channels have been studied by STAR through the analysis of identified muon spectra exploiting the different shape of the dca distribution (distance of closest approach of a track to the primary vertex) for μ coming from charm decays and μ coming from π/K decays. The latter particles have a much longer lifetime and, consequently, the daughter muon tracks are rather displaced from the primary vertex.

The p_{t} invariant yields recovered with the different techniques by the two experiments are shown in Fig. 2.6. On the right panel (PHENIX measurement) the continuous curves are the fit to the corresponding data from p–p collisions with the spectral shape taken from a FONLL calculation and scaled by the nuclear overlap integral $\langle T_{AA}\rangle$ (see Appendix A) for each centrality class. For all centralities, the Au–Au spectra well agree with the p–p reference at low p_{t} while a suppression develops towards high p_{t}. In Fig. 2.7 and 2.8, this

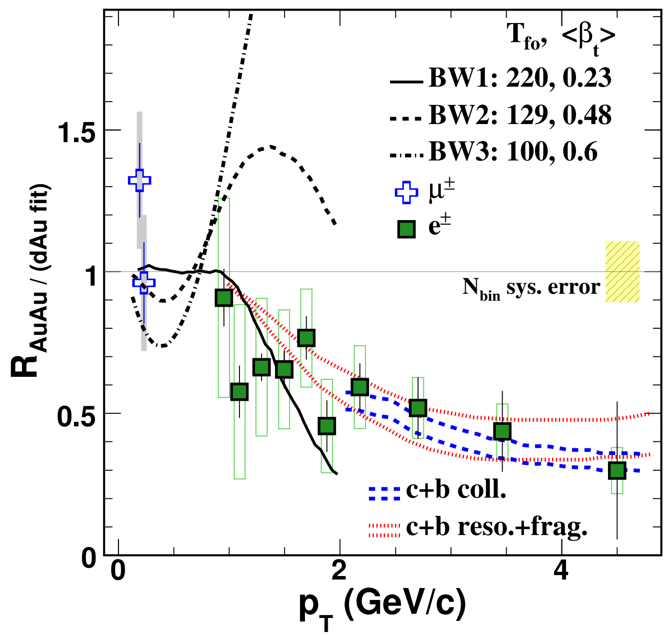

Figure 2.7: Nuclear modification factor, R_{AA} (defined in Section 1.4), as observed in Au–Au 0%-12% central collisions by STAR [62], compared with model calculations. The curves at $p_{\mathrm{t}} \leq 2$ GeV/c indicate blast–wave model with different freeze–out temperatures.

suppression is quantified by the nuclear modification factor R_{AA} defined in Section 1.4. As shown in Fig. 2.8 (left panel), $R_{\mathrm{AA}} \approx 1$ for all centralities (N_{part}) for the $p_{\mathrm{t}} > 0.3$ GeV/c integration region, containing more than a half of the electrons from heavy-flavour decays, in accordance with the binary scaling of the total heavy-flavour yield (see Appendix A). For the higher p_{t} integration regions the R_{AA} decreases with increasing centrality, as expected if heavy quarks lose energy in the medium. In central collisions, Fig. 2.7 and Fig. 2.8 right panel (a), the nuclear modification factor is consistent with 1 at low p_{t} and then reduces at higher p_{t}, reaching, at $p_{\mathrm{t}} \gtrsim 4$ GeV/c, a value similar to that observed for light hadrons like π^0, although a significant contribution from bottom decays is expected at high p_{t}. The dead cone effect is expected to become less important at high p_{t} for charm quark while at RHIC energies it should always affect b quarks.

Collective flows

The large elliptic flow observed for heavy quarks, (right panel in Fig. 2.8), suggests that elliptic flow is built up at partonic stage while radial flow dominantly comes from hadronic scattering at a later stage where charm may have already decoupled. It also indicates that charm relaxation time is comparable to the short time scale of flow development in the produced medium. Theoretical models used to calculate R_{AA} and v_2 simultaneously ([61] and references therein) can reproduce the data with parameters ($\hat{q}$, diffusion coefficient) typical of a strongly coupled, perfect fluid (no viscosity) medium.

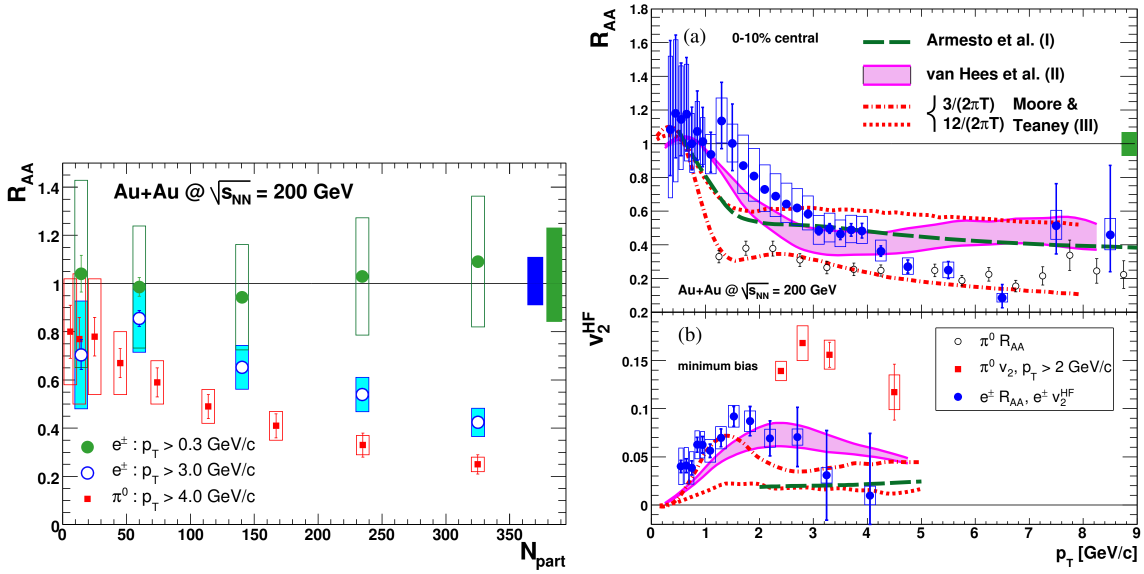

Figure 2.8: PHENIX results, from [61]. Left panel: R_{AA} of heavy-flavour electrons for the integrated p_{t} spectrum ($p_{\mathrm{t}} > 0.3$ GeV/c) and for $p_{\mathrm{t}} > 3$ GeV/c and of π^0 for $p_{\mathrm{t}} > 4$ GeV/c. Right panel (a): R_{AA} of heavy-flavour electrons in 0%–10% central Au–Au collisions compared with π^0 data and model calculations. Right panel (b): v_2 (see elliptic–flow description in Section 1.3.2) of heavy-flavour electrons in minimum bias collisions compared with π^0 data.

The main conclusions that can be drawn from the results obtained at RHIC for the measurement of charm production are the following:

- While there are some discrepancies between STAR and PHENIX concerning the estimated cross–section for charm production (see [60, 91, 92]), it seems rather established that the charm yield scales with the number of binary collisions.
- Non-photonic electron suppression in Au–Au is very large when compared to the expectations from radiative energy loss, which seem to work well for light quark hadrons.
- Non photonic electron v_2 supports the picture of an early thermalization: if the c quark has a collective behaviour, like elliptic flow, it must have been thermalized but its time scale is of the order $\approx 1/M_Q$. Moreover, fitting the data for v_2 to a model based on a diffusion parameter suggests that the matter formed in Au–Au collisions is a near-perfect fluid.

2.5 Strategy for charm production measurements in ALICE through the exclusive reconstruction of charmed hadron decays

The presence of the Inner Tracking System detector will allow ALICE to measure the cross–section for charm quark production in p–p and Pb–Pb collisions via the exclusive reconstruction of the following selected open charm meson/baryon decay channels:

- $D^0 \to K\pi$ [57]
- $D^{*+} \to D^0\pi^+$ with $D^0 \to K^-\pi^+$ [93]
- $D^+ \to K^-\pi^+\pi^+$ [94]
- $D_s^+ \to \pi^+K^+K^-$ [95]
- $D^0 \to K^-\pi^+\pi^-\pi^+$ [96]
- $\Lambda_c \to pK^-\pi^+$ (under study)

The strategy is based on an invariant mass analysis of those combinations of reconstructed tracks ("candidates") that can represent a D meson decayed at a secondary vertex displaced from the primary vertex of interaction. In the following, the main steps in the analyses are summarized.

Raw signal extraction ($N_{sel.}^{reco.}$)

If all the possible candidates were considered, the signal-to-background ratio would be too low, especially in Pb–Pb collisions, to extract the raw signal via an invariant mass analysis. For instance in Pb–Pb central collisions with $dN_{ch}/d\eta|_{|\eta|<0.9} = 6000$ the signal over background ratio is 10^{-6} for the $D^0 \to K^-\pi^+$, 10^{-9} for the $D^+ \to K^-\pi^+\pi^+$ and 10^{-8} for the $D_s^+ \to \pi^+K^+K^-$ assuming an efficient identification of kaons and pions. It is then mandatory to preselect the reconstructed tracks and candidates on the basis of the typical kinematical and geometrical properties characterizing signal tracks and reconstructed vertices. Open charm mesons, decaying weakly, have a relatively long lifetime ($c\tau \approx 123$ μm and $c\tau \approx 312$ μm for the D^0 and the D^+ respectively). Because of this, the presence of tracks displaced from the primary vertex of interaction, is a common signature of all the considered decay channels. Hence, the possibility to resolve the primary and secondary vertices, provided by the high spatial tracking precision of the ITS, is the key–element to reconstruct the above decays exclusively. The invariant mass distribution of the selected candidates is fitted to extract the raw signal yield $N_{sel.}^{reco.}$.

Correction for feed–down from B mesons (f_D)

At LHC energies, a relevant fraction of D mesons comes from the decay of a B meson. On average, the reconstructed tracks coming from these "secondary" D mesons are displaced from the primary vertex, because of the relatively long lifetime of the B mesons (460 − 490 μm). Thus, the selection applied on the reconstructed candidates, further enhances their contribution to the raw signal yield (up to 15%). It is important to subtract this fraction without relying only on MC models that can introduce relevant systematic errors. One possibility is to extract the fraction of prompt D mesons (f_D) exploiting the different shapes of the impact parameter distribution of secondary D mesons, strongly influenced by the B decay length. This approach has been already used by CDF [8] and will be extensively discussed in chapter 7.

Correction for detector acceptance and cuts selection (ϵ)

To recover the number of mesons effectively produced and decayed in a specific channel, (e.g. $N_{tot}^{D^0 \to K^- \pi^+}$) the raw signal yield is divided by an efficiency correction factor (ϵ) that accounts for the use of cuts as well as for the limited detector acceptance. The efficiency factor is estimated from Monte Carlo simulations relying on the good description of the detector response into the simulations themselves. Therefore, it can be one of the main sources of systematic errors.

Cross–section normalization

To get the total number of produced D mesons, the yield obtained for a specific decay channel is divided by the channel branching ratio (BR). Then, the number of produced D mesons must be correctly normalized, by dividing it by the integrated luminosity $\mathcal{L}_{\mathrm{INT}}$, to obtain the cross–section. The integrated luminosity can be calculated in two different ways. The first is based on the direct measurement of the luminosity. In the second the integrated luminosity is estimated as the total number of observed events divided by the total inelastic cross–section, which will be measured by the TOTEM experiment [97].

The cross–section for the production of a given charmed meson is thus calculated with the following formula:

$$\left.\frac{\mathrm{d}^2\sigma(p_{\mathrm{t}}, y)}{\mathrm{d}y\mathrm{d}p_{\mathrm{t}}}\right|_{y=0} = \frac{1}{4}\frac{f_D \cdot N_{\text{sel.}}^{\text{reco.}}(p_{\mathrm{t}})|_{|y|<1}}{\epsilon \cdot \mathrm{BR} \cdot \mathcal{L}_{\mathrm{INT}}} = \frac{1}{4}\frac{f_D \cdot N_{\text{sel.}}^{\text{reco.}}(p_{\mathrm{t}})|_{|y|<1}}{\epsilon \cdot \mathrm{BR} \cdot N_{\text{inel}}^{\text{tot}}}\sigma_{\text{inel}}^{\text{tot}} \; . \tag{2.11}$$

where the factor $1/4$ arises from the rapidity interval $|y| < 1$ in which the measurement is performed and from the fact that both the particle and the relative antiparticle are reconstructed.

Chapter 3

The ALICE detector

Among the LHC experiments ALICE is the one dedicated to heavy-ion collisions. This special role forced a unique design of the apparatus to match the requirements for the study of these collisions. From the detection side the main difference between p–p ad Pb–Pb collisions is determined by the high multiplicity environment created in the latter. Thus the need of a high granularity detector, especially in the region close to the interaction point, to ensure robust tracking [2]. The global design was then dictated by the peculiarities of the physics targets of the experiment. A special request for the ALICE detector is the capability to track and identify particles in a wide transverse momentum range, from more than 100 GeV/c (e.g. for jets physics) down to $\sim$ 100 MeV/c (e.g. for the study of collective phenomena). Precise tracking is required to reconstruct and separate the primary vertex of interaction from secondary vertices from hyperons and heavy-flavoured mesons decays. Both low momentum track reconstruction and precise tracking lead the request of a low material budget detector. As a consequence, the ALICE is a general–purpose detector able to identify and measure the properties of most of the hadrons, leptons and photons produced in the collisions in a wide p_{t} and η range.

In this chapter, after an overview of the global structure and of the main subdetectors, the two main devices relevant for the analyses shown in the following chapters are described, the *Time Projection Chamber* (TPC) and the *Inner Tracking System* (ITS). A fast description of the TOF detector and of its use for particle identification is also given. The event reconstruction procedure and the way it is implemented into the ALICE software framework is then outlined. The procedure for the event-by-event reconstruction of the primary vertex of interaction is also described. All the LHC experiments will produce an unprecedented amount of data: they will be distributed and analysed worldwide using the GRID framework. The ALICE software framework, developed for analysis on the GRID, is introduced in a dedicated section. The chapter focus is on the ITS commissioning and on the cosmic-ray run 2008, described in the last section: cosmic-rays are of fundamental importance for alignment and calibration operations of the detector. The alignment of the ITS, a relevant part of this thesis, is discussed extensively in the next chapters.

3.1 General layout of the ALICE detector

The global ALICE layout is shown in Fig. 3.1. Two main sections can be identified: a central barrel covering the full azimuth in the acceptance region $|\eta| < 0.9$ and a forward

($2.5 < \eta < 4$) muon arm [2]. The ALICE global reference frame is defined with the z axis parallel to the beam direction pointing in the opposite direction than the muon arm and the x and y axes in the plane transverse to the beam direction, the x pointing towards the centre of the LHC ring, the y axis pointing upward (Fig. 3.3, left). The central barrel is devoted to charged hadrons, electrons and photons reconstruction and identification. It includes, from the interaction vertex to the outside: an Inner Tracking System (ITS) composed of six layers of silicon detectors; a Time Projection Chamber (TPC); a Transition Radiation Detector (TRD) for electron identification; a Time Of Flight (TOF) barrel for the particle identification in the intermediate momentum range 0.2 to 2.5 GeV/c; a large acceptance (110° azimuthal coverage in the pseudorapidity range $|\eta| < 0.7$) electromagnetic calorimeter (EMCal) for the measurement of high momentum electrons and photons and to improve jet energy resolution; a small-area ($|\eta| < 0.6$, 57.6° azimuthal coverage) ring imaging Cherenkov detector at large distance for the identification of high-momentum particles (High Momentum Particle Identification Detector, HMPID); an electromagnetic calorimeter consisting of arrays of high density crystals (PHOton Spectrometer, PHOS) covering a 100° region in φ and a pseudorapidity range $|\eta| < 0.12$.

The central detector is embedded in a large solenoidal magnet with a relatively weak field ≤ 0.5 T. The field strength is a compromise between momentum resolution, low momentum acceptance and tracking and trigger efficiency. The momentum cut-off should be as low as possible ($\simeq 100$ MeV/c), in order to study collective phenomena and to detect the decay products of low-p_{t} hyperons. At high p_{t} the magnetic field determines the momentum resolution, which is essential for the study of jet quenching and high-p_{t} leptons. The ideal choice for hadronic physics, maximising reconstruction efficiency, would be around 0.2 T, while for the high-p_{t} observables the maximum field the magnet can produce, 0.5 T, would be the best choice. Since the high-p_{t} observables are limited by statistics, ALICE will run mostly with the higher field option.

The beam pipe is built in beryllium and has an outer radius of 3 cm and a thickness of 0.8 mm, corresponding to 0.3% of X_0. The main aim in the beam pipe construction was the minimisation of the multiple scattering undergone by the particles produced in the collision. Thus, the choice of the material (low atomic number, i.e. low radiation length) and of the smallest possible thickness.

The muon spectrometer was designed to measure the production of the complete spectrum of heavy quarkonia resonances, namely J/ψ and ψ', Υ, Υ' and Υ'' through the reconstruction of $\mu^+\mu^-$ decay channel. It consists of an absorber, positioned very close to the vertex, followed by a spectrometer with a dipole magnet and, finally, an iron wall to select the muons.

The set-up is completed by a forward photon counting detector (Photon Multiplicity Detector - PMD) and a multiplicity detector (Forward Multiplicity Detector - FMD) covering the forward rapidity region, that, in conjunction with the ITS, allows the measurement of the charged multiplicity, in the range $-3.4 < \eta < 5.1$.

A system of scintillators (V0 detector) and quartz counters (T0 detector) provide fast trigger signals.

On both sides of the interaction region, about 90 m downstream in the machine tunnel, two distinct Zero Degrees Calorimeters (ZDC), made respectively of tantalum and brass with embedded quartz fibers, allow the determination of the collision centrality in Pb–Pb interaction through the measurement of the energy (and thus the number) of spectator nucleons[1].

[1]Spectator nucleons propagate along the beam direction after the collision: due to their different Z/A

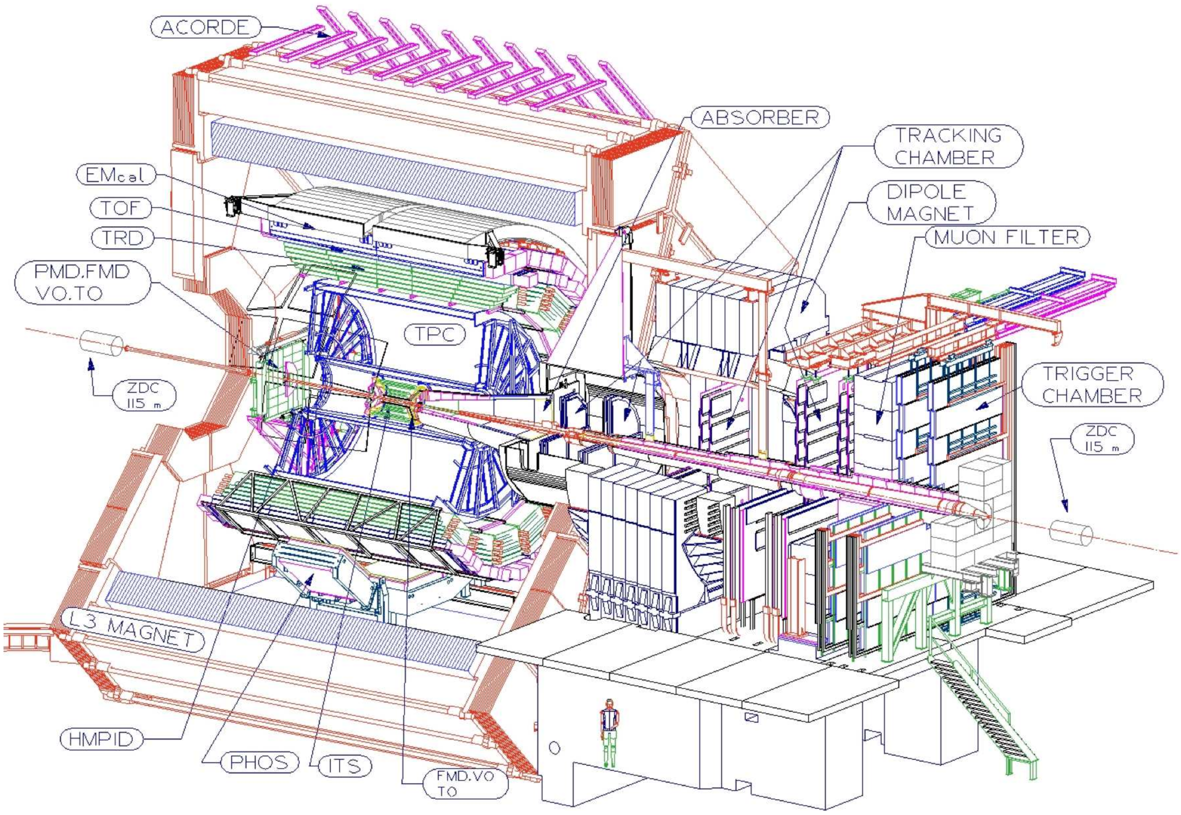

Figure 3.1: Layout of the ALICE detector.

3.1.1 Time Projection Chamber

The TPC is the main tracking device in the ALICE central barrel. It provides track finding, momentum measurement and particle identification through dE/dx measurement. It has a cylindrical shape with an internal radius of 80 cm determined by the maximum acceptable hit density (0.1 cm^{-2}) and an outer radius of 250 cm chosen in order to have an average particle path length in the chamber sufficient to get a dE/dx resolution better than 10%. The total active length of $\sim$ 500 cm in the z direction allows the acceptance in the pseudorapidity range $-0.9 < \eta < 0.9$. The material budget of the TPC is kept as low as possible both for the field cage and for the adopted drift gas to ensure minimal multiple scattering and secondary particle production. The drift gas mixture Ne/CO_2 (90%/10%) is optimized for drift velocity, low electron diffusion and low radiation length.

The TPC readout chambers are multi-wire proportional chambers with cathode-pad readout. The readout planes at the two ends of the large drift volume (88 m^3) are azimuthally segmented in 18 sectors, each covering an angle of 20°. The non-active region between two adjacent sectors is 2.7 cm wide, implying an azimuthal acceptance of $\approx$ 90% for straight tracks originating from the interaction point. The radial thickness of the detector is of 3.5% of X_0 at central rapidity and grows to $\approx$ 40% towards the acceptance edges.

values, it is possible to separate them from the beam particles by means of the first LHC dipole.

3.1.2 Time Of Flight detector (TOF)

The main task of the TOF detector is the particle identification of charged tracks via the measurement of the time of flight over a known distance. It must provide hadron separation (mainly between pions, kaons and protons) in the momentum range from 0.5 GeV/c, where the dE/dx technique is no longer effective, to about 2.5 GeV/c. PID in this momentum range allows the study of the kinematical distributions of the different particles types on an event–by–event basis in heavy ion collisions. Given the large mass of the charm quark, the decay products of D mesons have typical momenta larger than 0.5 GeV/c (of the order of $1-2$ GeV/c): the possibility to exploit the TOF information for K/π separation up to 2.5 GeV/c can be particularly useful for the reconstruction of exclusive decays of D mesons in hadronic channels.

The time of flight is measured using the technology of the Multi–gap Resistive Plate Chambers (MRPC). The RPC is a gaseous detector with resistive electrodes, which quench the streamers so that they do not initiate a spark break–down.

The barrel–like structure of the detector provides full azimuthal coverage; the acceptance in the polar angle is $45° < \theta < 135°$, covering the same pseudo–rapidity range than the TPC and ITS. The MRPC design consists of a double stack with 2×5 gaps. The basic unit is a MRPC pad of size $3.5 \times 2.5\text{cm}^2$; the pads are organised in large modules: the full barrel counts 18 (in $r\varphi$) $\times$ 5 (along z) modules, for a total active area of $\approx 140\text{m}^2$.

Particle Identification with the TOF detector

The measurement of the time of flight t across a known distance L for a track with momentum p (measured in the TPC and in the ITS) allows an estimation of the particle mass as:

$$m = p \cdot \sqrt{\frac{t^2}{L^2} - 1}\,.$$

Fig. 3.2 presents a scatter plot of the measured momenta versus the estimated masses for particles produced in central Pb–Pb collisions generated with HIJING. The points corresponding to electrons, pions, kaons and protons are coloured in red, yellow, blue and green, respectively. The figure, from the TOF Technical Design Report (TDR) [102], is obtained for B=0.4 T assuming an overall time resolution of 150 ps, which underestimates the actual value (120 ps [2]). The association of the time of flight and hence of the mass to a specific reconstructed track is obtained by means of a matching algorithm, that propagates the track from the outer radius of the TPC to the TOF detector and matches it with one of its pads. Tracks matched with a non–active region or with a non–fired (or multi–fired) pad are not assigned a mass. For $0.5 < p < 2 - 2.5$ GeV/c there is a good mass separation for pions, kaons and protons. For lower momenta the matching tends to fail because of multiple scattering and energy loss, while for $p > 2 - 2.5$ GeV/c the separation vanishes, especially between pions and kaons. The association of the particle type to a track (*tagging*) is determined by applying cuts on the momentum-versus-mass plane, as the continuous lines shown in the figure. The cuts values determine the identification efficiency (the ratio of the number of tracks of type i correctly tagged as i divided by the total number of tracks of type i) and the contaminations of the sample (the number of tracks incorrectly tagged as i divided by the total number of tracks tagged as i). For each analysis the cuts must be tuned in order to reach the optimal compromise between efficiency and contamination levels.

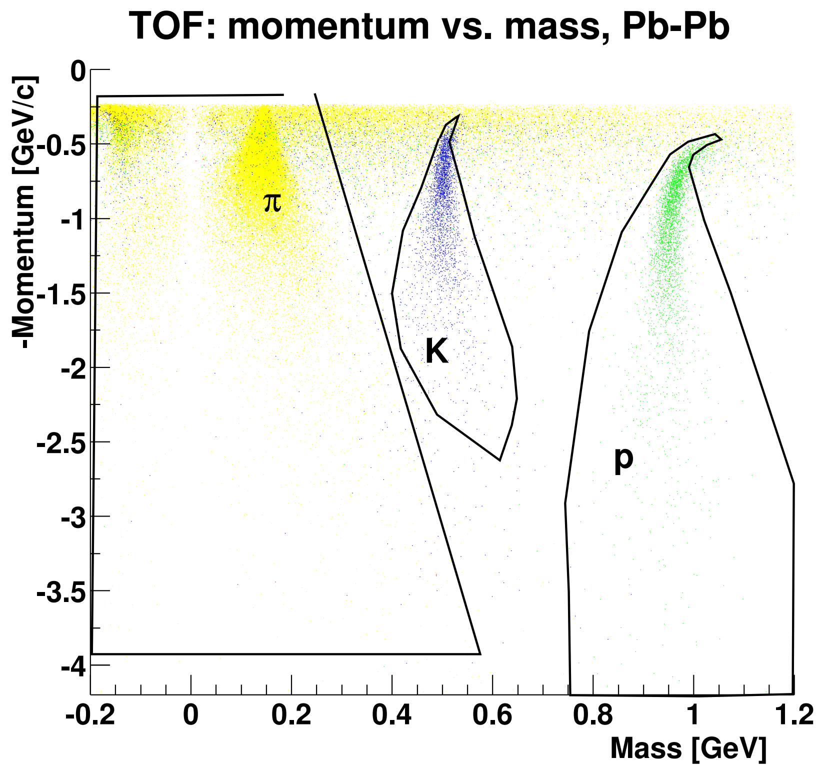

Figure 3.2: Momentum versus mass calculated from TOF for a sample of HIJING Pb–Pb events. The lines correspond to the chosen graphical cuts relative to the selection of pions, kaons and protons. Negative values of the mass are assigned when the reconstructed velocity is larger than the speed of light. Figure from [102].

3.2 Inner Tracking System

The geometrical layout of the ITS layers as it is implemented in the ALICE simulation and reconstruction software framework (AliRoot [103]) is shown in the left-hand panel of Fig. 3.3. The module local reference system (Fig. 3.3, right) is defined with the $x_{\rm loc}$ and $z_{\rm loc}$ axes on the sensor plane and the $z_{\rm loc}$ axis in the same direction as the global z axis. The local x direction is approximately equivalent to the global $r\varphi$ ($\mathrm{d}x_{\rm loc} \approx \mathrm{r d}\varphi$). The alignment degrees of freedom (see Section 4.1) of the module are translations in $x_{\rm loc}$, $y_{\rm loc}$, $z_{\rm loc}$, and rotations by angles $\psi_{\rm loc}$, $\theta_{\rm loc}$, $\varphi_{\rm loc}$, about the $x_{\rm loc}$, $y_{\rm loc}$, $z_{\rm loc}$ axes, respectively[2].

The number, position and segmentation of the ITS layers, as well as the detector technologies, have been optimised in according to the requirements of:

- Efficient track finding in the high multiplicity environment predicted for central Pb–Pb collisions at LHC, which was estimated up to 8000 particles per unit of rapidity at the time of ALICE design. This calls for high granularity in order to keep the system occupancy at the level of a few per cent on all the ITS layers.

[2]The alignment transformation can be expressed equivalently in terms of the degrees of freedom defined in the local or global reference systems.

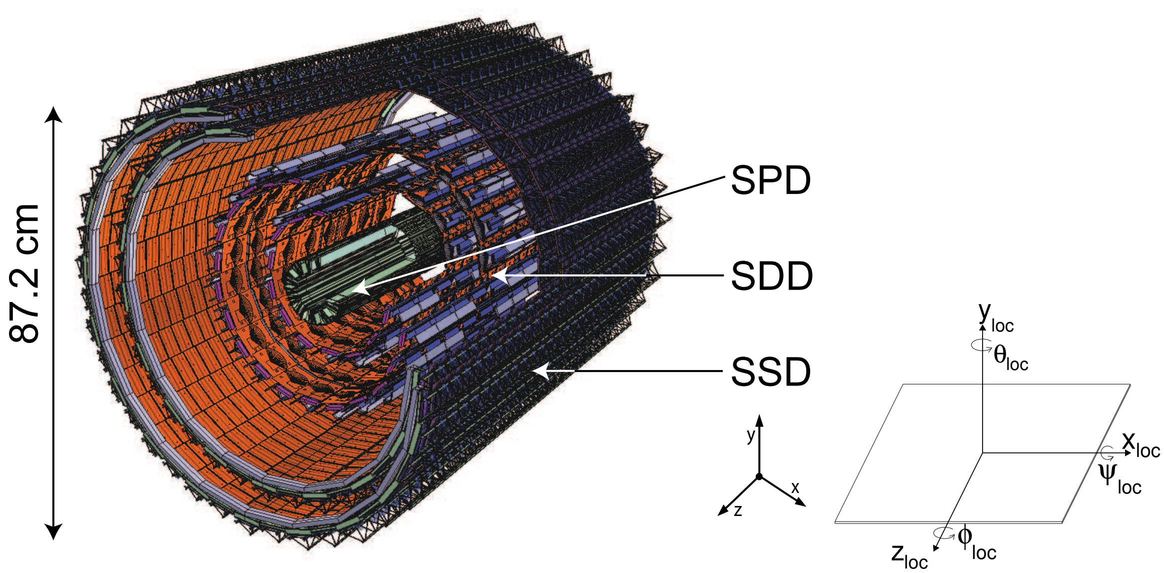

Figure 3.3: Layout of the ITS and definition of the ALICE global (left) and ITS-module local (right) reference systems.

- High resolution on track impact parameter and momentum. The momentum and impact parameter resolution for low-momentum particles are dominated by multiple scattering effects in the material of the detector; therefore the amount of material in the active volume has been kept to a minimum. Moreover, for track impact parameter and vertexing performance, it is important to have the innermost layer as close as possible to the beam axis. The innermost SPD layer is located at a radial distance of 9 mm from the beam vacuum tube.

- Possibility to use the ITS also as a standalone spectrometer, able to track and identify particles down to momenta below 200 MeV/c. For this reason, the four layers equipped with SDD and SSD provide also particle identification capability via dE/dx measurement.

The geometrical parameters of the layers (radial position, length along beam axis, number of modules, spatial resolution, and material budget) are summarised in Table 3.1. As far as the material budget is concerned, it should be noted that the values reported in Table 3.1 account for sensor, electronics, cabling, support structure and cooling for particles crossing the ITS perpendicularly to the detector surfaces. Another 1.30% of radiation length comes from the thermal shields and supports installed between SPD and SDD barrels and between SDD and SSD barrels, thus making the total material budget for perpendicular tracks equal to 7.66% of X_0.

In the following paragraphs, a brief description of the features of each of the three subdetectors (SPD, SDD and SSD) relevant for alignment issues is done, for more details see [1]. In Fig. 3.4, the hierarchical structure of the three subsystems, driving the definition of the alignment procedure (as will be described in Chapter 5), is shown. Each of the objects itemised in Fig. 3.4 is defined as an *alignable volume* in the software geometry and it can be moved, to account for the misalignment, by applying a transformation defined by the

Table 3.1: Characteristics of the six ITS layers.

Layer	Type	r [cm]	$\pm z$ [cm]	Number of modules	Active Area per module $r\varphi \times z$ [mm^2]	Resolution $r\varphi \times z$ [μm^2]	Material budget X/X_0 [%]
1	pixel	3.9	14.1	80	12.8×70.7	12×100	1.14
2	pixel	7.6	14.1	160	12.8×70.7	12×100	1.14
3	drift	15.0	22.2	84	70.17×75.26	35×25	1.13
4	drift	23.9	29.7	176	70.17×75.26	35×25	1.26
5	strip	38.0	43.1	748	73×40	20×830	0.83
6	strip	43.0	48.9	950	73×40	20×830	0.86

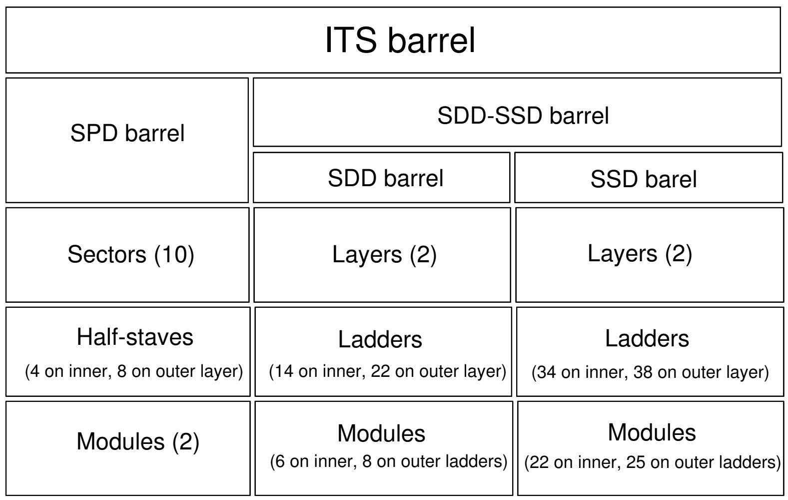

Figure 3.4: Schematic description of the hierarchical structure of the ITS.

six independent alignment degrees of freedom (three translations and three rotations) of the volume [104].

3.2.1 Silicon Pixel Detector

The basic building block of the SPD is a module consisting of a two-dimensional sensor matrix of reverse-biased silicon detector diodes bump-bonded to 5 front-end chips. The sensor matrix consists of 256 $\times$ 160 cells, each measuring 50 μm ($r\varphi$) by 425 μm (z). The active area of each module is 12.8 mm ($r\varphi$) $\times$ 70.7 mm (z), the thickness of the sensor is 200 μm, while the readout chip is 150 μm thick. Two modules are mounted together along the z direction to form a 141.6 mm long half-stave. Two half-staves are attached head-to-head along the z direction to a carbon-fibre support sector, which provides also cooling. Each sector (see Fig. 3.5) supports six staves: two on the inner layer and four on the outer layer. The assembly of half-staves on sectors provides an overlap of about 2% of the sensitive area along $r\varphi$, while there is no sensor overlap along z, where, instead, there is a small gap between the two half–staves. Five sectors are then mounted together to form an half-barrel and finally the two (top and bottom) half-barrels are mounted around the beam pipe to close the full barrel, which is actually composed of 10 sectors. In total, the SPD includes 60 staves, consisting of 240 modules with 1200 readout chips for a total of 9.8×10^6 cells.

The spatial precision of the SPD sensor is determined by the pixel cell size and by the track incidence angle on the detector, as well as by the threshold applied in the readout electronics. The values of resolution along $r\varphi$ and z extracted from beam tests are 12 and 100 μm respectively.

3.2.2 Silicon Drift Detector

The basic building block of the ALICE SDD is a module with a sensitive area of $70.17(r\varphi) \times 75.26(z)$ mm^2 divided into two drift regions where electrons move in opposite directions under a drift field of ≈ 500 V/cm (see Fig. 3.6, right). The SDD modules are mounted on linear structures called ladders. There are 14 ladders with six modules each on the inner SDD layer (layer 3), and 22 ladders with eight modules each on the outer SDD layer (layer 4). Modules and ladders are assembled to have an overlap of the sensitive areas larger than 580 μm in both $r\varphi$ and z directions, so as to provide full angular coverage (Fig. 3.6, left).

The modules are attached to the ladder space frame, which is a lightweight truss made of Carbon-Fibre Reinforced Plastic (CFRP) with a protective coating against humidity absorption, using ryton pins and have their anode rows parallel to the ladder axis (z). During the assembling phase, the positions of the detectors were measured with respect to the reference ruby spheres glued to the ladder feet.

The ladders are mounted on a CFRP structure made of a cylinder, two cones and four support rings. The cones provide the links to the outer SSD barrel and have windows for the passage of the SDD services. The support rings are mechanically fixed to the cones and bear reference ruby spheres for the ladder positioning.

The z coordinate is reconstructed from the centroid of the collected charge along the anodes. The position along the drift (rφ) coordinate is reconstructed starting from the measured drift time with respect to the trigger time. An unbiased reconstruction of the rφ coordinate requires therefore to know with good precision the drift speed and the time-zero (t_0), which is the measured drift time for particles with zero drift distance.

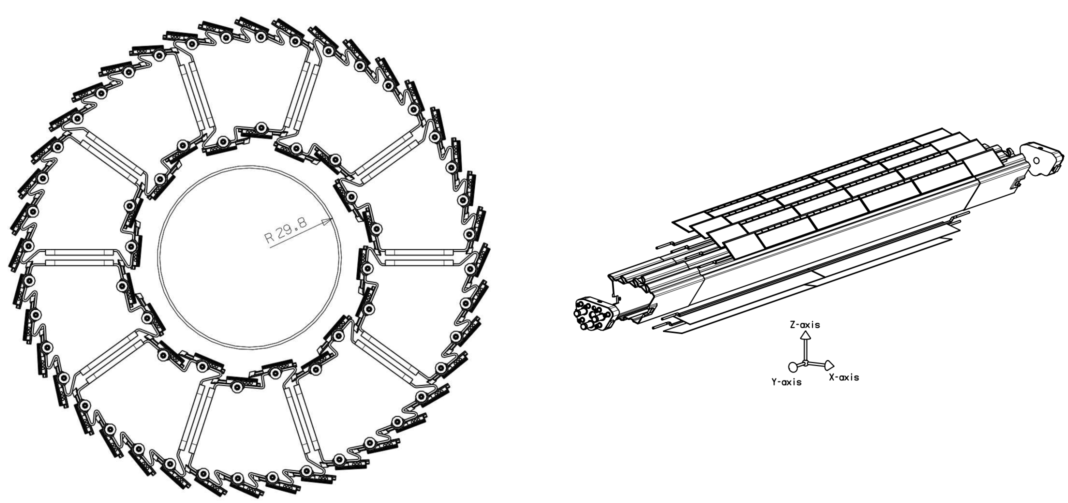

Figure 3.5: SPD drawings. Left: the SPD barrel and the beam pipe (radius in mm). Right: a Carbon Fibre Support Sector.

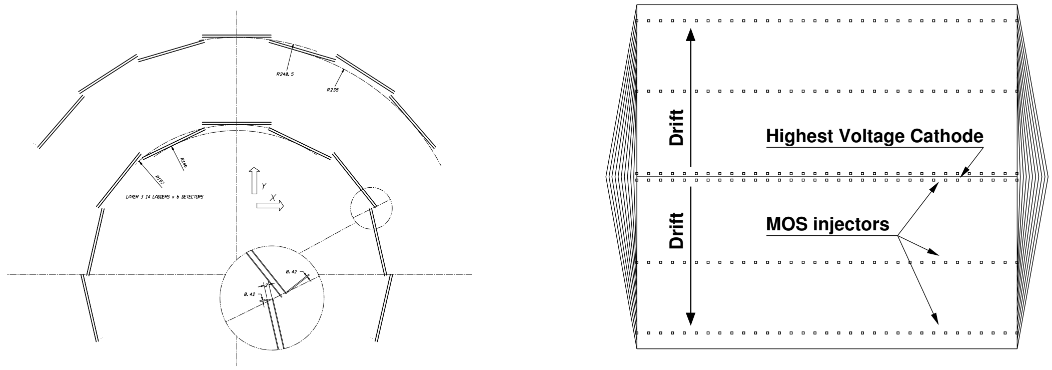

Figure 3.6: Left: scheme of the SDD layers. Right: scheme of an SDD module. Units are millimetres.

The drift speed depends on temperature (as $T^{-2.4}$) and it is therefore sensitive to temperature gradients in the SDD volumes and to temperature variations with time. Hence, it is important to calibrate frequently this parameter during the data taking. For this reason, in each of the two drift regions of an SDD module, 3 rows of 33 MOS charge injectors are implanted at known distances from the collection anodes [105], as sketched in Fig. 3.6 (right). When a dedicated calibration trigger is received, the injector matrix provides a measurement of the drift speed in 33 positions along the anode coordinate for each SDD drift region.

Finally, a correction for non-uniformity of the drift field (due to non-linearities in the voltage divider and for few modules also due to significant inhomogeneities in dopant concentration) has to be applied: it is extracted from measurements of the systematic deviations between charge injection position and reconstructed coordinates that was performed on all the 260 SDD modules with an infrared laser [106].

The space precision of the SDD detectors, as obtained during beam tests of full-size prototypes, is on average 35 μm along the drift direction and 25 μm for the anode coordinate.

3.2.3 Silicon Strip Detector

The basic building block of the ALICE SSD is a module composed of one double-sided strip detector connected to two hybrids hosting the front-end electronics. The sensors are 300 μm thick and have an active area of 73×40 mm^2 along z and $r\varphi$ directions, respectively. Each sensor has 768 strips on each side with a pitch of 95 μm. The stereo angle is 35 mrad which is a compromise between stereo view and reduction of ambiguities resulting from high particle densities. The strips are almost parallel to the beam axis (z-direction), to provide the best resolution in the $r\varphi$ direction. The angle of the strips with respect to the beam axis is +7.5 mrad on one side and −27.5 mrad on the other side. As a result, each strip crosses about 14 strips on the other detector side.

The modules are assembled on ladders of the same design as those supporting the SDD (see Fig. 3.7). The innermost SSD layer (layer 5) is composed of 34 ladders, each of them being a linear array of 22 modules along the beam direction. Layer 6 (the outermost ITS layer) consists of 38 ladders, each of them made of 25 modules. To obtain full pseudo-rapidity

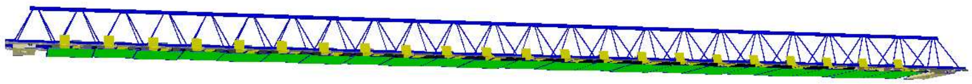

Figure 3.7: View of one SSD ladder (from layer 5) as described in the AliRoot geometry.

coverage, the modules are mounted on the ladders in a way that the active areas of the modules overlap. For a track crossing an overlap region the two clusters measured on the two neighbouring modules are 600 μm apart radially. The 72 ladders, carrying a total of 1698 modules, are mounted on Carbon Fibre Composite support cones in two cylinders. Carbon fiber is lightweight (to minimise the interactions) and, at the same time, it is a stiff material allowing to minimise the bending due to gravity. The ladders are 120 cm long, but the sensitive area amounts to 88 cm on layer 5 and to 100 cm on layer 6. For each layer, the ladders are mounted at two slightly different radii ($\Delta r = 6$ mm) to ensure a full azimuthal coverage. The acceptance overlaps, present both along z and $r\varphi$, amount to 2% of the SSD sensor surface.

The spatial resolution of the SSD system is determined by the 95 μm pitch of the sensor readout strips and by the charge-sharing between those strips. Without making use of the analogue information the r.m.s spatial resolution is 27 μm. Beam tests have shown that a spatial resolution of better than 20 μm in the rφ direction can be obtained by analysing the charge distribution within each cluster. In the direction along the beam the spatial resolution is about 830 μm.

3.3 ALICE Offline software framework

The ALICE collaboration developed a software framework, named AliRoot [103], based on ROOT [107] to allow simulation, reconstruction and analysis of data from both collisions and cosmic events. The main items concerning event simulation and software reconstruction are described in the next sections.

3.4 Track reconstruction and event simulation

In the following, the steps of the simulation and reconstruction chain for collision events, depicted in Fig. 3.8, are outlined.

Event simulation

Collisions are simulated through events generators, like Pythia [108] and HIJING [109]. All the information about the generated particles (e.g. type, momentum, parent particles and production process, decay products) is organised in a *kinematic tree* stored in a file.

Particle transport in the detector: *hits*

The generated particles are propagated to the detector where they can interact with the detector material and be "detected". During this process particles can decay and produce

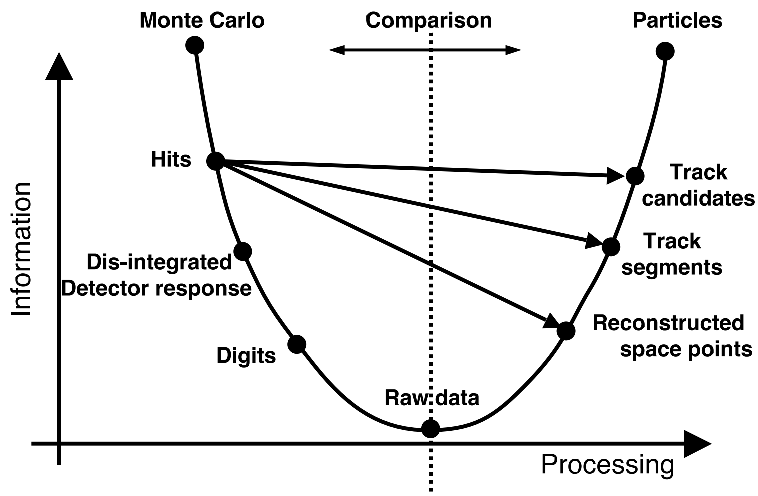

Figure 3.8: Data processing framework [2].

additional particles. Using the ROOT geometrical modeler, the detector shape, structure, position and material are described in the AliRoot framework as realistically as possible, down to the level of all mechanical structures and single electronic components. The specialised programmes for particle transport like Geant3 [110], Geant4 [111] and Fluka [112], by interfacing with the geometry, can reproduce realistic interaction between particles and material. All interactions of particles with sensitive detector parts are recorded as *hits*, containing the position, time and energy deposit of the respective interaction.

Digitization and raw data

For each hit the corresponding digital output of the detector is stored as a *summable digit* taking into account the detector response function. Possible noise is then added to the summable digit and it is stored as a *digit*. The last step consists of the storing of the data in the specific hardware format of the detector, the *raw data*.

The raw data, representing the response of the detector, constitute the minimum of the physical information parabola in Fig. 3.8. They are the starting point of the reconstruction process, which is identical for both simulated and real events and it is divided in the following steps.

Cluster finding

Particles crossing the sensitive part of a detector usually leave a signal in several adjacent detecting elements, for instance adjacent pixels (strips) on the SPD (SSD). These signals are combined into a single *cluster*, which better estimates the position of the traversing particle besides reducing the effect of random noise.

Track reconstruction

As described in [113] tracks reconstruction is performed in the following steps:

1. Primary vertex computation with SPD. The position of the interaction vertex is computed using the correlation of tracklets in the SPD.

2. Track reconstruction in the TPC (inward). Track reconstruction is performed from outside inward by means of a Kalman filtering algorithm [114] using the outermost pad rows and the primary vertex position from the previous step as seed.

3. Track reconstruction in the ITS (inward). TPC reconstructed tracks are matched to the SSD layers and followed down to the innermost SPD layer. Done in two steps: in the first the vertex position is used, to guide track finding and maximise the efficiency for primary tracks while in the second it is not employed to recover also tracks displaced from the collision point.

4. Track back-propagation, to the outermost layer of the ITS and then to the outermost radius of the TPC. Extrapolation and track finding in the TRD. Propagation to the outer layer (TOF, HMPID, PHOS, EMCal) for Particle IDentification (PID).

5. "Refit". Reconstructed tracks are re-fitted inward in TRD, TPC, ITS and are propagated to the primary vertex reconstructed in the first step.

6. Primary vertex recalculation using tracks. The reconstructed tracks are used to determine the primary vertex with optimal resolution.

Tracking efficiency, momentum and spatial resolutions, which are influenced by detector misalignment, are discussed in Section4.2.

The event information

The output of the whole "reconstruction" operation is the Event Summary Data (ESD), which contains all the information about the event, both single track properties (track momentum and trajectory parameters along with their covariance matrix, PID probabilities, etc.) and global properties of the event (e.g. the primary vertex position). Technically, the ESD is a tree with objects of type AliESDEvent stored in AliESD.root files. Since the ESD contains more information than that needed for the analysis, Analysis Object Data (AOD) have been developed to contain only the end user data for analysis. AODs are obtained by filtering ESDs (tracks, vertices,...) or by high level reconstruction based on ESDs or AODs (charmed hadrons, jets, photons, ...). The design of the AOD in AliRoot is equal to the ESD one. The persistent data consists of branches of a tree (aodTree).

The files containing ESD and AOD are distributed worldwide on the GRID, described in the next section.

Figure 3.9: A snapshot of the ALICE VO sites in Europe. A green circle indicates that jobs are running on the sites while red and yellow circles indicate sites with problems.

3.5 ALICE analysis framework on the GRID: an AliEn around the world

After the LHC startup the ALICE detector will produce data at a rate of up to 2PB per year [115]. This huge amount of data makes almost unavoidable the necessity of automatised procedures for the (software) reconstruction of the events and for the first steps of the analysis, with the consequent employ of a large mass of computing resources. The worldwide distributed GRID facilities were designed to provide both the computing power and the disk space needed to face the LHC software challenge. Hence the need of a GRID-oriented analysis code. One of the main advantages in using the GRID is the possibility to analyse a large set of data by splitting a job analysis into many "clone" subjobs, run in parallel on different computing nodes. The ALICE VO (Virtual Organisation) is made of more than 80 sites distributed worldwide (Fig. 3.9 is a snapshot of the sites in Europe). Each site is composed of many worker nodes (WN), which are the physical machines where the software programmes can be run. The Storage Element (SE) is responsible for managing physical files in the site and for providing an interface to mass storage. The Computing Element (CE) service is an interface to the local (WN) batch system and manages the computing resources in the site. The ALICE Collaboration has developed AliEn [116] as an implementation of distributed computing infrastructure needed to simulate, reconstruct and analyse data from the experiment. Alien provides the two key elements needed for large-scale distributed data processing: a global file system (catalogue) for data storage and the possibility to execute the jobs in a distributed environment. The analysis software, the user code and the Aliroot libraries (or par files in the case a development of the code is not deployed on the GRID), needed by each subjob to run must be specified in a JDL (Job Description Language), together with the data sample and the way to split it. The data sample is specified through a XML (eXecutable Machine Language) collection file which contains a list of the Logical File Names (LFN, the entries in the catalogue) of the files to be executed.

Table 3.2: LHC parameters for p–p and Pb–Pb runs at the ALICE IP [2].

Parameter		p–p	Pb–Pb
$\sqrt{s_{NN}}$	[TeV]	14	5.5
$\beta^\star$	[m]	10	0.5
$\sigma_{x,y}^{bunch}$	[μm]	71	16
σ_{z}^{bunch}	[cm]	7.5	7.5
$\sigma_{x,y}^{vertex}$	[μm]	50	11
σ_{z}^{vertex}	[cm]	5.3	5.3
Luminosity	[cm^{-2}s^{-1}]	5×10^{32}	5×10^{26}

3.6 Primary Vertex reconstruction

The beam intersection point (IP) in ALICE has an uncertainty of some centimetres along the beam direction and tens/hundreds micron in the transverse plane. A precise knowledge of the primary vertex position, improving the resolution on the impact parameter and the tracking performances in general, is required by many physical analyses, in particular in heavy flavour physics for the reconstruction of short–lived particles.

3.6.1 Beams and interaction point at the LHC

The two beams accelerated in the LHC will interact in the intersection point, ideally at (0,0,0) in the ALICE global frame. It is possible to define the dispersion of the interaction region as the convolution of the particle distributions in the two intersecting bunches. Assuming that the particles in the bunches have Gaussian distributions along the three coordinate axes with dispersions $\sigma_{x,y,z}^{bunch}$, than the interaction vertex lies in a *diamond* with dimensions:

$$\sigma_{x,y,z}^{vertex} = \sigma_{x,y,z}^{bunch} \Big/ \sqrt{2} \ .$$

The size of the bunches at the IP depends on the *transverse emittance* ϵ (a beam quality parameter) and on the value of the *amplitude function* β at the IP, indicated as $\beta^\star$, which is determined by the accelerator magnet configuration, as:

$$\sigma_{x,y,z}^{bunch} = \sqrt{\frac{\epsilon_{x,y,z}\beta^\star}{\pi}} \, . \tag{3.1}$$

The LHC machine nominal parameters at the ALICE IP for p–p and Pb–Pb collisions are recalled in Table 3.2. For p–p runs the nominal luminosity of 5×10^{32} cm^{-2}s^{-1} will have to be reduced to less than 3×10^{30} cm^{-2}s^{-1}, in order to limit the pile–up in the TPC and in the SDD. Such reduction can be achieved in two ways: either by increasing the value of $\beta^\star$ or by displacing the two beams in the transverse plane to make a collision between the tails of the particle distributions. If the first option is chosen, $\beta^\star$ might be increased up to 100 m; this would broaden of a factor ≈ 3 the transverse size of the interaction diamond, up to ≈ 150 μm. If the second option is necessary, the beams might be displaced to a distance of $\sim 4-5$ $\sigma_{x,y}^{bunch}$ and the collisions would occur in the tails at $4-5$ σ from the centre of the beams: these tails will most likely be non–Gaussian and the transverse size of the interaction diamond may be even larger than 150 μm.

Therefore, a precise reconstruction of the primary vertex position is mandatory especially in p–p collisions.

3.6.2 Vertex finder and vertex fitter

In the following, the main items of primary vertex reconstruction are outlined. A detailed description of the procedures and of the algorithm performances can be found in [113].

Vertex reconstruction can be divided in two distinct tasks:

1. Fast vertex finding and rough determination of its position with SPD "tracklets".
2. Vertex finding and fitting using reconstructed tracks, for the precise reconstruction of the vertex position and the determination of its covariance matrix.

A "tracklet" is built by associating pairs of reconstructed points in the two SPD layers. The vertex information recovered with the SPD is used for track reconstruction (Section 3.4) and as a seed for the vertex position determination in the vertex fitting algorithm. Moreover, the use of "tracklets" instead of reconstructed tracks makes the algorithm very fast, allowing the online monitoring of the beam position and spread along the three coordinates x, y and z. Two vertex finding algorithm are available:

VertexerSPDz. It provides a measurements of the z coordinate assuming that the beam position in the transverse plane is known with an accuracy of the order of 200 μm or better. Tracklets are constructed by matching SPD points in the outer and in the inner layer, within an azimuthal window small enough to reduce the combinatorial background and select high–momentum tracks (better approximated by straight lines) and tracks less affected by multiple scattering effects. The z coordinate is calculated as the weighted average of the tracklet z_i positions at the beam axis.

VertexerSPD3D. The algorithm can be divided in three main steps, which are repeated two times: tracklet finding, tracklet selection and vertex determination. In the first step, tracklet are constructed, requiring that they cross a cylindrical fiducial region. Then, in the second step, tracklets are selected exploiting the distribution of the intersection point of pairs of tracklets. In the third step the three coordinates of the vertex are determined by finding the point of minimum distance among the tracklets. The error considered on the tracklet accounts for the error on the reconstructed SPD points, for curvature effects and for the multiple scattering in the beam pipe and in the inner SPD layer.

As mentioned above, the SPD-based vertexing algorithms provide also a tool to monitor the beam position in the transverse plane and the interaction diamond profile quasi–online. This is achieved by running the local reconstruction (i.e. the cluster finding) on the SPD detectors and successively the vertex finding algorithm quasi–online on a sub–sample of events picked–up by the normal data flow and processed on dedicated machines.

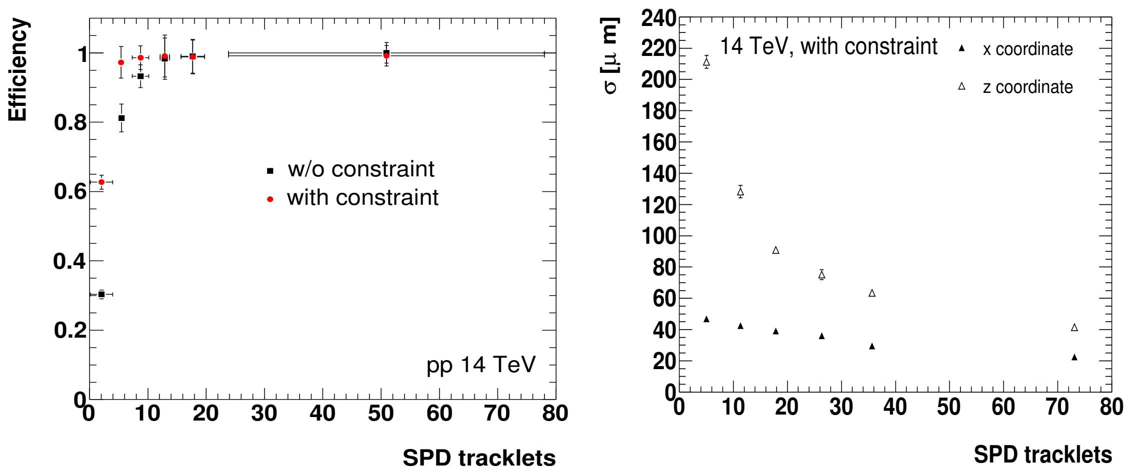

Figure 3.10: On the left: vertex reconstruction efficiency with ITS+TPC tracks for triggered p–p events at 14 TeV, without and with the diamond constraint, as a function of event multiplicity. On the right: resolutions on the x and z coordinates of the vertex reconstructed, with diamond constraint, with ITS+TPC tracks.

Reconstruction of the vertex position with tracks

The use of tracks instead of tracklets improves the resolution on the primary vertex position, especially in the lower-multiplicity environment of p–p collisions. The vertex is reconstructed in three iterations made of three steps each: track selection, vertex finding and vertex fitting. A track selection is needed to reject displaced tracks, that is, far secondaries, e.g. from strangeness decays, and possible fake tracks in the first iteration and close secondaries and particles that undergo large scatterings in the material in the subsequent iteration. In the first iteration, a robust vertex finding algorithm estimates the vertex position as the average of the points of closest approach, that are calculated for all the pairs of the selected tracks in the track straight–line approximation in the vicinity of the vertex[3]. The vertex found is used as a seed in the second iteration. The vertex finding algorithm used in the second and third iterations estimates the vertex position by finding the point of minimum distance among the tracks, taking into account the full covariance matrix of the track parameters in the calculation. The minimization is fast, because of the straight line approximation, used also for this algorithm,.

The determination of the best fit coordinates of the vertex, along with its covariance matrix, is the task of the vertex fitting algorithm. The algorithm used in ALICE has been developed on the basis of the fast vertex fitting method described in [117]. Since the measurement of the different tracks are independent of each other, the χ^2 function to be minimized can be written as a sum over tracks. In the straight–line approximation, in the vicinity of the vertex position, the χ^2 is:

$$\chi^2(\vec{\mathrm{r}}_v) = \sum_i (\vec{\mathrm{r}}_v - \vec{\mathrm{r}}_i)^{\mathrm{T}}\, \mathrm{V}_i^{-1} (\vec{\mathrm{r}}_v - \vec{\mathrm{r}}_i)\,. \tag{3.2}$$

[3]In this approximation a track, modelled as an helix, is propagated to a reference plane, usually related to the actual vertex position and, then, the tangent line to the helix is used in the calculation.

In the above expression, $\vec{\mathrm{r}}_i$ is the vector of the current global position of the track i and V_i^{-1} is its covariance matrix, recovered from the covariance matrix of the track parameters. The vertex is calculated as:

$$\vec{\mathrm{r}}_v = \left(\sum_i \mathrm{W}_i\right)^{-1} \left(\sum_i \mathrm{W}_i \vec{\mathrm{r}}_i\right) , \tag{3.3}$$

with $\mathrm{W}_i = \mathrm{V}_i^{-1}$ and the vertex covariance matrix is defined as

$$\mathrm{C}_v = \left(\sum_i \mathrm{W}_i\right)^{-1} .$$

The information on the diamond can be included as a vertex constraint. If the diamond is defined by the vector $\vec{\mathrm{r}}_d$, defining its centre, and by its covariance matrix C_d, describing the spread of the interaction region, the vertex coordinates and covariance matrix become ($\mathrm{W}_d = \mathrm{C}_d^{-1}$):

$$\begin{aligned} \vec{\mathrm{r}}_v &= \left(\mathrm{W}_d + \sum_i \mathrm{W}_i\right)^{-1} \left(\mathrm{W}_d \vec{\mathrm{r}}_d + \sum_i \mathrm{W}_i \vec{\mathrm{r}}_i\right) \\ \mathrm{C}_v &= \left(\mathrm{W}_d + \sum_i \mathrm{W}_i\right)^{-1} . \end{aligned} \tag{3.4}$$

In Fig. 3.10 (left panel) the efficiency for vertex reconstruction for triggered events, defined as the ratio of the number of events with vertex to the total number of triggered events, is shown as a function of the event multiplicity, estimated from the number of SPD tracklets. At low multiplicity the use of the diamond constraint allows to increase the vertex reconstruction efficiency. In the right panel of the same figure, the resolutions as a function of the event multiplicity is presented for the case in which the diamond constraint is used. In [113] it is shown that the resolutions improve drastically for low multiplicities with the use of the diamond constraint and that the vertex position uncertainties are properly estimated by the algorithm with and without the use of the constraint.

3.7 ITS subdetectors commissioning

The installation of the ITS detectors and the beam pipe in the ALICE cavern was completed in June 2007. A first commissioning run was performed in December 2007 to test the acquisition and the calibration strategy on a fraction of modules for which power supplies and cooling were available. A larger fraction of modules (about 1/2 of the full detector) participated in the February/March 2008 data taking. The installation of services was completed in May 2008. The SPD FastOR was integrated in the Central Trigger Processor and since May 2008 it was used to collect data from cosmic-rays in self-triggering mode as well as to provide the trigger to other detectors. As mentioned in the introduction to this chapter, cosmic-rays are of fundamental importance for alignment and calibration operations of the detector. The task of the commissioning phase is to test and understand the detector functionality from the electronic and cooling system up to the event reconstruction. All the parameters describing the realistic detector response (e.g. electronic parameters as DAC and ADC values, temperature, calibration parameters like drift velocities) and position (i.e. alignment parameters) are stored in the Offline Conditions DataBase (OCDB) and used for event reconstruction.

3.7.1 Cosmic run 2008: data taking and reconstruction

During the 2008 cosmic run, extending from June to October, about 10^5 events with reconstructed tracks in the ITS have been collected. In order to simplify the first alignment round, the solenoidal magnetic field was switched off for most of the run.

Two types of cosmic triggers were available in 2008: a trigger provided by the ACORDE detector (dedicated to the cosmic ray studies), and a trigger provided by the SPD. ACORDE [1] is a large area scintillator array, covering about 20 m^2 of the three upper octants of the ALICE magnet, that provides a relatively high ($\approx$ 100 Hz) cosmic trigger rate. This trigger is useful for the main tracking detector, the TPC, whose geometrical dimension matches well that of ACORDE. On the other hand, for a small inner detector like the ITS, this trigger has a low purity level (below 1%) in terms of the number of events with tracks crossing all the layers of this detector. In addition, the efficiency of the ACORDE trigger for cosmic muons crossing the ITS is lower than 10%, because the scintillators cover about 10% of the surface of the three upper octants of the magnet. For these reasons, using the SPD trigger (described in the following) was much more convenient for the purpose of collecting events for the ITS alignment, and the ACORDE triggered events were not used. The SPD detector has digital, thus fast, readout (100 ns strobe duration). It is, therefore, well suited to be used as a standalone triggering device. The SPD FastOR trigger [1] is based on a programmable hit pattern recognition system at the level of individual readout chips (1200 in total, each reading a sensor area of about 1.4×1.4 cm^2). This trigger system enables a flexible event selection, for example high-multiplicity proton–proton collisions, of special interest in the scope of the ALICE physics program. For the 2008 cosmic run, the trigger logic consisted in selecting events with at least one hit on the upper half of the outer SPD layer and at least one on the lower half of the same layer. This trigger condition enhances significantly the probability of selecting events in which a cosmic muon, coming from above (the dominant component of the cosmic-ray particles reaching the ALICE cavern placed below $\approx$ 30 m of rock), traverses the full ITS detector. This cosmic trigger is very efficient (better than 99%) and has purity (fraction of events with a reconstructed track having points in both SPD layers) reaching about 30–40%, mainly determined by the fact that the trigger ensures only that a particle has crossed the outer layer, whose average radius is about 7/4 the radius of the inner layer. For the FastOR trigger, typically 77% of the chips (i.e. about 90% of the active modules) could be configured and used. The trigger rate was about 0.18 Hz. The average SPD FastOR trigger rate scales geometrically quite well with the ACORDE trigger rate and is also in agreement with the known cosmic-muon flux in ALICE, as measured by the previous LEP experiment L3 [118], situated in the same cavern.

The following procedure, fully integrated in the AliRoot framework [103], is used for track reconstruction:

- the event reconstruction starts from the cluster finding in the ITS (hereafter, we will refer to the clusters as "points");
- a pseudo-primary vertex is created using the reconstructed points in the two SPD layers; this is done by looking for a set of at least three points lying on a straight line and defining as vertex the middle point of the segment between the two points that belong to the same layer; in this way the rest of the reconstruction can proceed in a similar way as for interactions occurring inside the beam pipe; if there are less than the required three points in SPD, also SDD and SSD points can be used for the vertex construction;

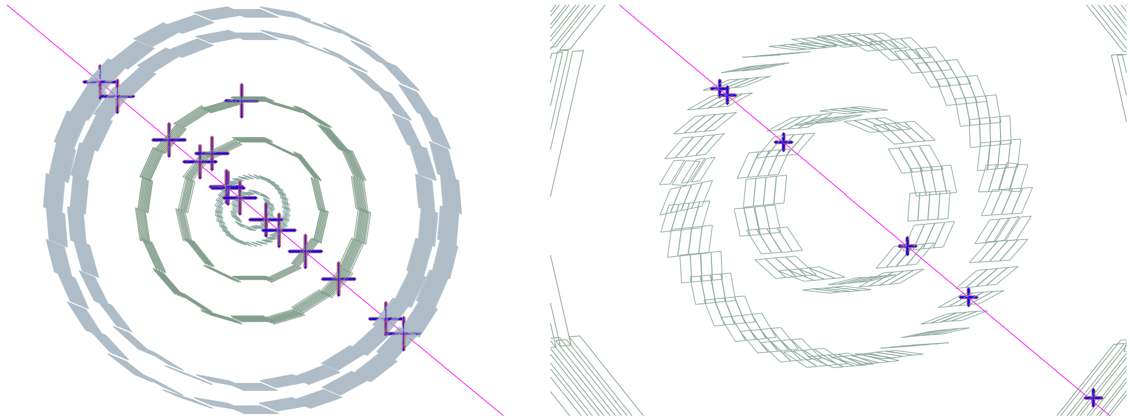

Figure 3.11: (colour online) A clean cosmic event reconstructed in the ITS (left), as visualised in the ALICE event display. The zoom on the SPD (right) shows an "extra" point in one of the $r\varphi$ acceptance overlaps of the outer layer.

- the track reconstruction is performed using the ITS standalone tracker (as described in [3]), which finds tracks in the outward direction, from the innermost SPD layer to the outermost SSD layer, using the previously found pseudo-primary vertex as a seed; all tracks found in this way are then refitted using the standard Kalman-filter fit procedure implemented in the default ITS tracker.

During the track refit stage, when the already identified ITS points are used in the Kalman-filter fit in the inward direction, to obtain the track parameters estimated at the pseudo-primary vertex, "extra" points are searched for in the ITS module overlaps. For each layer, a search road for these points in the neighbouring modules is defined with a size of about seven times the current track position error. Currently, the "extra" points are not used to update the track parameters, thus they can be exploited as a powerful tool to evaluate the ITS alignment quality.

A "clean" cosmic event consists of two separate tracks, one "incoming" in the top part of the ITS and one "outgoing" in the bottom part. Their matching at the reference median plane ($y = 0$) can be used as another alignment quality check. These two track halves are merged together in a single array of track points, which is the single-event input for the track-based alignment algorithms. A typical such event, as visualised in the ALICE event display, is shown in Fig. 3.11.

The uncorrected zenith-azimuth 2D distribution of the (merged) tracks with at least eight points in the ITS is shown in Fig. 3.12, where the azimuth angle is defined starting from the positive side of the z global axis. The modulations in the azimuthal dependence of the observed flux are due to the presence of inhomogeneities in the rock above the ALICE cavern, mainly the two access shafts. These show up as the structures at zenith about 30° and azimuth about 180° (large shaft) and about 270° (small shaft). On top of these structures, the effect of the SPD outer layer geometrical acceptance is visible: the azimuthal directions perpendicular to the z axis (around 90° and 270°) have larger acceptance in the zenith angle.

Figure 3.13 shows the coverage of the ITS modules for the sample of cosmic events used for alignment: number of track points in (φ, z) plane, where each cell corresponds approximately

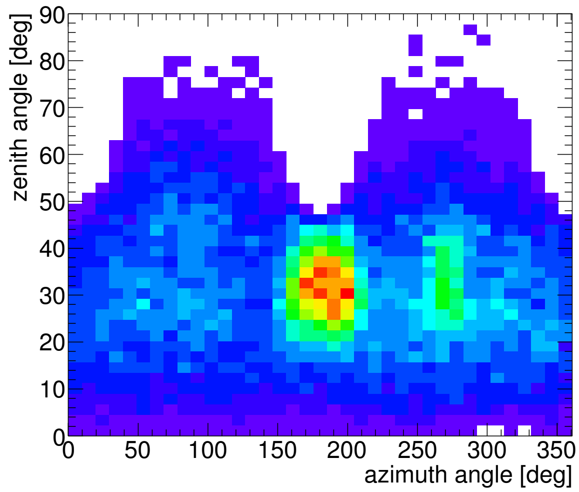

Figure 3.12: (colour online) Uncorrected distribution of the zenith-azimuth angles of the cosmic tracks reconstructed in the ITS.

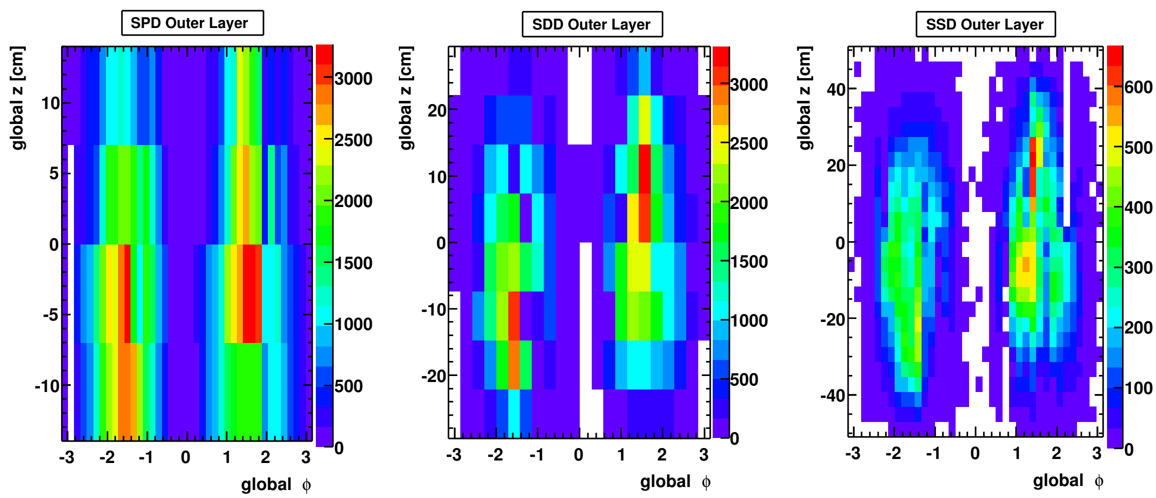

Figure 3.13: (colour online) 2008 cosmic sample, B = 0: total number of points associated to tracks per module, for the outer layers of SPD, SDD, and SSD.

to a module, for the outer layers of SPD, SDD, SSD. The figure illustrates the limits of the usage of cosmic-ray tracks for the alignment of a cylindrical detector like the ITS: too small occupancy of the side modules, especially in case of the outer detector, SSD. This weakness in the use of cosmic–rays in an alignment perspective is counter-balanced by the unique feature of such events, that provide a direct correlation of the upper and lower half-barrel modules, impossible with tracks originating from collisions occurring inside the beam pipe.

3.7.2 ITS commissioning with cosmic

In this section an overview of the commissioning of the ITS subdetectors is presented. For a more detailed description of the detector calibration see [119] and [120]. The ITS alignment is fully described in chapters 4 and 5.

SPD. The detector performance was optimised tuning several 8-bit DACs integrated in the front-end electronics and taking dedicated calibration runs to verify the pixel response. The calibration procedure is fully integrated in the ALICE calibration framework. It is based on detector algorithms which determine the proper values of the DACs by analysing data from dedicated runs, using either the on chip test-pulse or particles crossing the detector. In particular, for each of the 1200 front-end chips the pixel-matrix response and the minimum threshold have been optimised in order to maximise the efficiency and minimise the number of noisy pixels. A typical threshold value is about 2800 electrons. The remaining individual noisy pixels, corresponding to less than 0.15%, are masked and the information is stored in the Offline Conditions DataBase (OCDB) to be used in the offline reconstruction. The high power dissipation (1.32kW) mainly generated by the front-end chips requires an efficient cooling system to maintain an operating temperature around 30°C. The performance of the C_4F_{10} based evaporative cooling has been studied in detail. Before the winter shutdown, 212 modules out of 240 could be stably operated for data taking and trigger purpose. The SPD was operational during the LHC beam injection tests since June 2008 and provided relevant information to study the level of background induced in ALICE by the LHC monitoring equipments.

SDD. 246 out of 260 SDD modules were included during summer 2008 in the cosmic-rays run data taking. The SDD calibration strategy is based on three types of standalone runs, collected periodically during the data taking and analysed by dedicated quasi-online algorithms that store the obtained calibration parameters in the OCDB. The first type is the pedestal run which allows to measure, for each of the 133k anodes, the values of baseline and noise as well as to tag the noisy channels ($\approx$ 0.5%). The baselines are then equalised to a common value in the front-end analog memory buffers [121]. In the pulser runs, a test pulse is sent to the pre-amplifiers to measure the gain and to tag the dead channels ($\approx$ 1%). Finally, injector runs provide a measurement of the drift speed in 33 positions along the anode coordinate for each SDD module by exploiting the MOS charge injectors integrated on the detector surface [105]. This is a crucial element for the detector calibration since the drift speed depends on temperature (as $T^{-2.4}$) and is therefore sensitive to temperature gradients in the SDD volumes and to temperature variations with time. A correction for non-uniformity of the drift field (due to non-linearities in the voltage divider and, for few modules, also to significant inhomogeneities in dopant concentration) is applied: it is extracted from measurements of the systematic deviations between charge injection position and reconstructed coordinates that was performed on all the 260 SDD modules with an infrared laser [106].

SSD. 1477 out of 1698 SSD modules took data in summer 2008. The fraction of bad strips was $\approx$1.5%. The SSD gain calibration has two components: overall calibration of ADC values to energy loss and relative calibration of the P and N sides. This charge matching is a strong point of double sided silicon sensors and helps to remove fake clusters. Both calibrations relied on cosmic. The calibration constants were determined already in the laboratory, using cosmic on a spare ladder. This was refined during the cosmic runs with the SPD FastOR trigger. The resulting normalised difference in P- and N-charge has a FWHM of 11%. The gains have proved to be stable during data taking. In any case, since the signal-to-noise ratio is $\approx$ 20–40 [122], the detecting efficiency does not depend much on the details of the gain calibration. The absolute calibration matches within 5% with the standard values for energy loss from the literature.

Chapter 4

Introduction to ITS alignment

As described in Section 3.2, the Inner Tracking System (ITS) is a barrel-type silicon tracker that surrounds the interaction region. It consists of six cylindrical layers, with radii between 3.9 and 43 cm, covering the pseudo-rapidity range $|\eta| < 0.9$. The two innermost layers are equipped with Silicon Pixel Detectors (SPD), the two intermediate layers are made of Silicon Drift Detectors (SDD), while Silicon Strip Detectors (SSD) are mounted on the two outermost layers. The main task of the ITS is to provide precise track and vertex reconstruction close to the interaction point. In particular, the ITS was designed in order to improve the position, angle, and momentum resolution for tracks reconstructed in the Time Projection Chamber (TPC), to recover particles that are missed by the TPC (due to either dead regions or low-momentum cut-off), to reconstruct the interaction vertex with a resolution better than 100 μm and to identify secondary vertices from the decay of hyperons and heavy flavoured hadrons [3]. The separation, from the interaction vertex, of the decay vertices of heavy flavoured hadrons, which have mean proper decay lengths $c\tau \sim$ 100–500 μm, requires a resolution on the track impact parameter (distance of closest approach to the vertex) well-below 100 μm. The ITS was designed to fulfil this requirements: the micro-metric intrinsic resolutions of the sensor modules together with the low material budget and the layout of the layers allow to reach a $\sim$ 10 μm resolution on the track impact parameter at high transverse momentum ($p_{\rm t} \gtrsim 10$ GeV/c). However, when considering the real detector, as installed in the experiment, the resolution is in general significantly degraded by *misalignment*. The ITS is an assembly of thousands of separate modules, whose positions are displaced, with respect to the ideal case, during the assembly and the integration of the different components. These displacements, if not taken into account, degrade the tracking performance of the detector, thus the physics performance. Therefore, it is mandatory to align the detector, that is, to measure the displacements (translations and rotations), so that they can be properly taken into account during track reconstruction. The ITS alignment procedure starts from the positioning survey measurements performed during the assembly, and is refined using tracks from cosmic-ray muons and from particles produced in p–p collisions. Two independent methods, based on tracks-to-measured-points residuals minimisation, are considered. The first method uses the Millepede approach [5], where a global fit to all residuals is performed, extracting all the alignment parameters simultaneously. The second method performs a (local) minimisation for each single module and accounts for correlations between modules by iterating the procedure until convergence is reached.

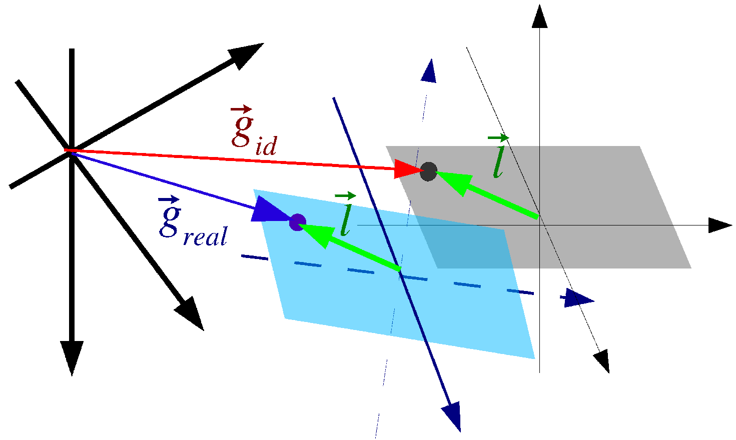

Figure 4.1: The grey rectangle represents the module plane in the ideal geometry while the light blue represents its real position and orientation in space. The 2-D green vectors lying on the module planes represent the local coordinates of a cluster. The black axes define the global reference frame.

In this chapter the ITS alignment problem is introduced. After an outline of the main consequences on tracking performance arising from the ITS misalignment, the target and strategy adopted for the ITS re–alignment are defined. In the last sections, the methods and the results obtained using cosmic–ray tracks for the validation of the survey measurements done during SSD assembly are presented. The description of the two alignment algorithms along with the results achieved after the 2008 cosmic-ray run (Section 3.7.1) is postponed to the next chapter.

4.1 ITS alignment degrees of freedom

Each of the six silicon layers composing the ITS is formed by many planar-shape modules. The response of a silicon detector (or at least of the three kinds of silicon detector technologies employed in the ITS) to the passage of a particle through the sensor can be represented as a "cluster", which gives a two dimensional information on the point where the particle crossed the module plane. For each module, a local reference system naturally anchored to the module itself is defined (Fig. 3.3, right) and the cluster can be identified with two local coordinates which are actually directly measured[1]. The reconstruction of a track is performed by a fit to the clusters produced in different modules: it is thus unavoidable to work in a global reference frame. To get the three dimensional position of the clusters in the global frame the position and orientation of the module planes in this frame must be known. A module is misaligned when its position and orientation differ from those by design, that is, from those defined in the "ideal" geometry. In the sketch in Fig. 4.1, the local information is represented by the green vector lying on the module plane. The grey rectangle represents the module plane in

[1]This is not completely true for the SDD where the anodic coordinate and the drift time are measured: the remaining coordinate is recovered by the drift time and the drift velocity.

the ideal geometry, while the light blue represents its real position and orientation in space. For each module k the relations between the local vector and the global vectors in the two cases can be expressed as:

$$\vec{g}_{\mathrm{id}} = G_k^{id}\vec{l} \tag{4.1}$$

$$\begin{aligned}\vec{g}_{\mathrm{real}} = G_k^{real}\vec{l} &= \Delta_k^{gl} G_k^{id}\vec{l} = \Delta_k^{gl}\vec{g}_{\mathrm{id}} \\ &= G_k^{id}\Delta_k^{loc}\vec{l}\end{aligned} \tag{4.2}$$

In the relations above G_k^{id} and G_k^{real} are the roto-translations between the module local reference system and the global reference system, in the ideal and misaligned geometry respectively, that allow to reconstruct the point positions in the global frame. We define the

- *global delta-transformation* Δ^{gl}, that is the transformation to be applied to the ideal global coordinates of a point to recover the real global coordinates.
- *local delta-transformation* Δ^{loc}, that is the transformation to be applied to the local "measured" vector to get the real coordinates of the point in the ideal local reference frame.

From Eq. 4.1 the relation between local and global delta transformations is simply $\Delta_k^{loc} = G_k^{id\ -1}\Delta_k^{gl}G_k^{id}$. The task of the alignment is to determine the global (or local) delta-transformation for all the ~ 2000 modules the ITS is made of. Since each roto-translation is determined by six parameters, three for the translations and three angles for the rotation, this implies the recovering of more than 13000 parameters.

The convention adopted for the angles defining the rotational part of the roto-translations, described in [104], is now briefly recalled. A general rotation in three-dimensional space can be decomposed into and represented by three successive rotations around three orthogonal axes. The three angles characterising the three rotations are called Euler angles. There are several conventions for the Euler angles, depending on the axes around which the rotations are carried out, right/left handed systems, (counter)clockwise direction of rotation, order of the rotation. The convention adopted in the ALICE alignment framework is the *'xyz convention'* also known as *pitch-roll-yaw* convention. Each rotation is represented as a composition of a rotation around the z-axis (yaw) with a rotation around the y-axis (pitch) with a rotation around the x-axis (roll). The matrices representing the three rotations are:

$$\mathcal{D} = \begin{pmatrix} c_\phi & -s_\phi & 0 \\ s_\phi & c_\phi & 0 \\ 0 & 0 & 1 \end{pmatrix} \qquad \mathcal{C} = \begin{pmatrix} c_\theta & 0 & s_\theta \\ 0 & 1 & 0 \\ -s_\theta & 0 & c_\theta \end{pmatrix} \qquad \mathcal{B} = \begin{pmatrix} 1 & 0 & 0 \\ 0 & c_\psi & -s_\psi \\ 0 & s_\psi & c_\psi \end{pmatrix} \tag{4.3}$$

where the c_i and s_i denote $\cos(i)$ and $\sin(i)$ respectively. For very small rotations, like those to be applied in the alignment (i.e. the rotational part of the delta-transformations), the sines can be approximated by the angles and the cosines by 1. Moreover if only the term linear in the sines are kept, the product of the matrices above is commutative and the order of the product does not matter. Therefore the general form of the rotation for a delta transformation is:

$$\mathcal{A} = \mathcal{BCD} = \begin{pmatrix} 1 & -\delta\phi & \delta\theta \\ \delta\phi & 1 & -\delta\psi \\ -\delta\theta & \delta\psi & 1 \end{pmatrix}, \tag{4.4}$$

where a δ has been added to the angles names to remark that the angles are small.

Average point displacements from local rotations

Point displacement due to local module rotations depends on the point position on the module. The displacement, small for a point close to the rotation axis, increases linearly with the distance between the point and the rotation axis, as it is clear in the following equation expressing the point coordinates in the ideal geometry local reference system as transformed by the matrix $\mathcal{A}$.

$$\begin{pmatrix} x' \\ y' \\ z' \end{pmatrix} = \begin{pmatrix} x - \delta\phi\, y + \delta\theta\, z \\ y + \delta\phi\, x - \delta\psi\, z \\ z - \delta\theta\, x + \delta\psi\, y \end{pmatrix} \tag{4.5}$$

It is useful to estimate the average point displacements caused by rotations for the different sub–detector modules. Rotations in the local delta-transformation are defined around axes that are also symmetry axes for the module and the average displacement is zero. It is thus convenient to estimate the RMS, as:

$$\mathrm{RMS}^2 = \int_\Sigma p(x,z)(\nu' - \nu)^2 \mathrm{d}x\mathrm{d}z\,,$$

with Σ the module surface, $\nu = x, y, z$ and $p(x,z)$ representing the probability to observe a cluster at position (x,z) (local $y = 0$). For a uniform distribution $p(x,z)$ is simply $1/\Sigma = 1/\mathrm{L}_z\mathrm{L}_x$, with $\mathrm{L}_z, \mathrm{L}_x$ the module dimensions. Thus,

$$\mathrm{RMS}_x = \frac{\delta\theta\, \mathrm{L}_z}{\sqrt{12}} \tag{4.6}$$

$$\mathrm{RMS}_y = \frac{\delta\phi\, \mathrm{L}_x + \delta\psi\, \mathrm{L}_z}{\sqrt{12}} \tag{4.7}$$

$$\mathrm{RMS}_z = \frac{\delta\theta\, \mathrm{L}_x}{\sqrt{12}}\,. \tag{4.8}$$

The maximum displacement is $\sim \sqrt{3}$ times the RMS. In Table 4.1 the RMS obtained when all the rotations are 10 mdeg are reported for the ITS sub–detectors. In the global delta–transformations, rotations are applied to point vectors in global coordinates. Their effect thus depends on the module position and can be very large if compared to the effect of a local rotation of the same magnitude simply because of the larger numbers entering Eq. 4.5. This derives only from the different definition of the degrees of freedom used in the two transformations to describe the same physical module displacement: the rotations in the two cases describe different movements and are not properly comparable. For instance, the rotation around the z–axis ($\delta\phi$ angle) in global coordinates implies a rigid movement of the module basically along the local–x direction ($\Delta x_{\mathrm{loc}} \approx r\delta\phi$, r is the detector radius) and is therefore

Table 4.1: RMS of local displacements obtained from Eq. 4.6 with $\delta\psi = \delta\theta = \delta\phi$=10 mdeg for the three ITS sub–detectors. Values are in μm.

	RMS_x	RMS_y	RMS_z
SPD	3.5	4.2	0.6
SDD	3.8	7.3	3.5
SSD	2.0	5.7	4.7

strongly correlated to the local x translation in the local delta–transformation. The radii are of the order of $3.9 - 43$ cm and, with $\delta\phi$ =10 mdeg, the displacements are ~ 7 μm for the inner SPD layer and ~ 75 μm for the outer SSD layer.

Finally, it is important to remark that the reported RMS correspond to the RMS of the distance of the very same reconstructed cluster positioned in two different positions defined by the ideal and misaligned geometries: this is not fully representative of the RMS of the residuals between the reconstructed cluster local coordinates (in the real, i.e. misaligned, geometry) and the local coordinates that would be observed if the real geometry corresponds to the ideal one. These residuals, which constitute the information exploited by the alignment algorithms described in the next chapter[2], are determined also by the track direction: the same cluster local coordinates are recovered if the module is displaced along the track direction. Hence, displacements along the global y–axis (cosmic–rays preferential direction) and radial movements do not broaden the residuals distributions observed with cosmic–rays and tracks from collisions respectively.

4.2 Effect of misalignment on tracking efficiency and spatial resolution

As anticipated in the introduction to this chapter, misalignment can degrade detector performances if not properly corrected for. In this section, possible effects on tracking efficiency and on spatial and transverse momentum resolutions are shown.

Tracking efficiency

Tracking efficiency can be spoiled by misalignment effects if tracking algorithms are not designed to cope with possible displacements of the points from their real positions. As explained in Section 3.4, starting from a seed (e.g. a segment constructed using two points), the tracking algorithm looks, among the reconstructed clusters, for points to be added to a track into a given *search road* determined by the uncertainty on the track extrapolation at a given detector plane and on the intrinsic cluster position uncertainty at the same plane. For each point inside the search road a χ^2 prevision is done and the compatible clusters are attached to the track. The uncertainty on the track extrapolation, besides the errors on the track parameters, accounts for multiple scattering effects in the material budget of the detector. The latter contribution is $p_{\rm t}$ dependent. The uncertainty on the cluster position is determined by the $p_{\rm t}$–independent intrinsic detector resolution that induces an uncertainty on the measured point position in the local (i.e. module) reference system. A realistic uncertainty on the cluster position should account for an additional contribution deriving from a possible misalignment of the module: the tracker works in a global reference frame[3] and a displacement of the module where the cluster lies causes a *mispositioning* of the point in the global reference frame. This can spoil the tracking efficiency because a cluster which

[2]The alignment algorithms use the residuals between the measured clusters position and the tracks extrapolation to the module planes defined in the geometry used for track reconstruction (can be the ideal or the latest alignment result).

[3]The reference system used by the tracker algorithm is track dependent and does not coincide with the global ALICE reference system: they differ for a rotation in the $r\varphi$ plane to get the y axis as a radial coordinate, that is, pointing towards the track direction in the $r\varphi$ plane.

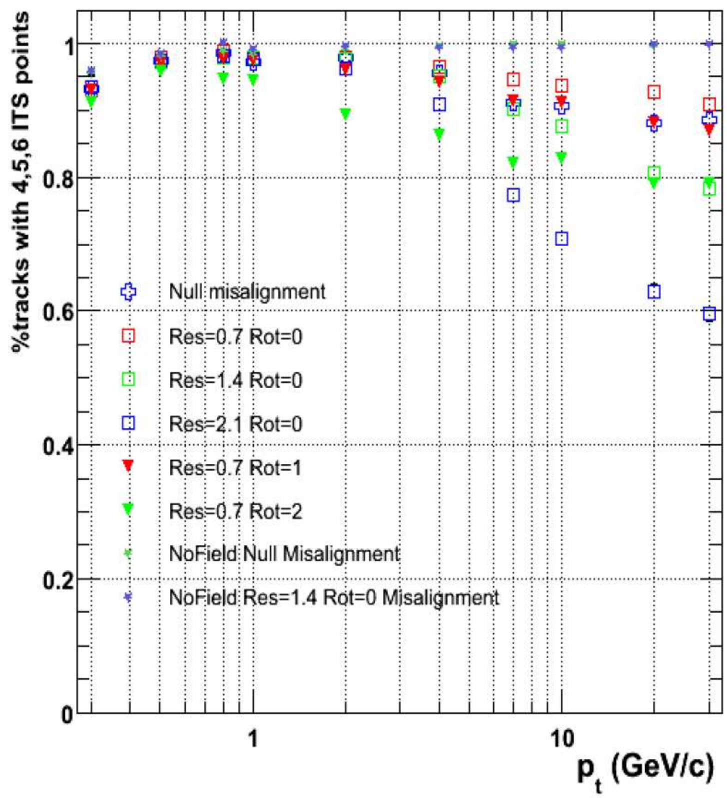

Figure 4.2: ITS tracking efficiency as a function of transverse momentum in different misalignment scenarios. 500 events have been simulated with a box generator producing 10 charged pions per each of the ten p_t bins chosen. For all misalignment scenarios but the two identified by star-like points the magnetic field was on (B=0.5 T). The "Res" and "Rot" factors in the legend indicate the level of misalignment considered. The misalignment parameters of the modules are extracted randomly from Gaussian distributions with sigma "Res" times the detector local resolutions for the x and z local translations while for the local rotations the sigma is calculated in order to displace the points on the modules "Rot" times the detector resolution on average.

actually belongs to a track can be placed outside of the search road or be rejected since the χ^2 prevision is above the limits for accepting it. In Fig. 4.2 the tracking efficiency trend is shown in different misalignment scenarios. The data used for this analysis consists of 500 events simulated with a box generator set to produce 10 charged pions per each of the ten p_t bins chosen. The effect is particularly relevant at high transverse momentum where multiple scattering effects are small and the misalignment contribution to the spatial resolutions can be the dominant one. To correct for this effect (which was expected) it has been sufficient to increase the size of the search road and to tune the criteria to attach a point to a track. As shown in the figure (star-like points), in the absence of magnetic field the efficiency is always close to 100%: since the transverse momentum cannot be measured, a "most probable" p_t ($\sim$ 300GeV/c) is assigned to all tracks so that, for higher momentum tracks, the multiple

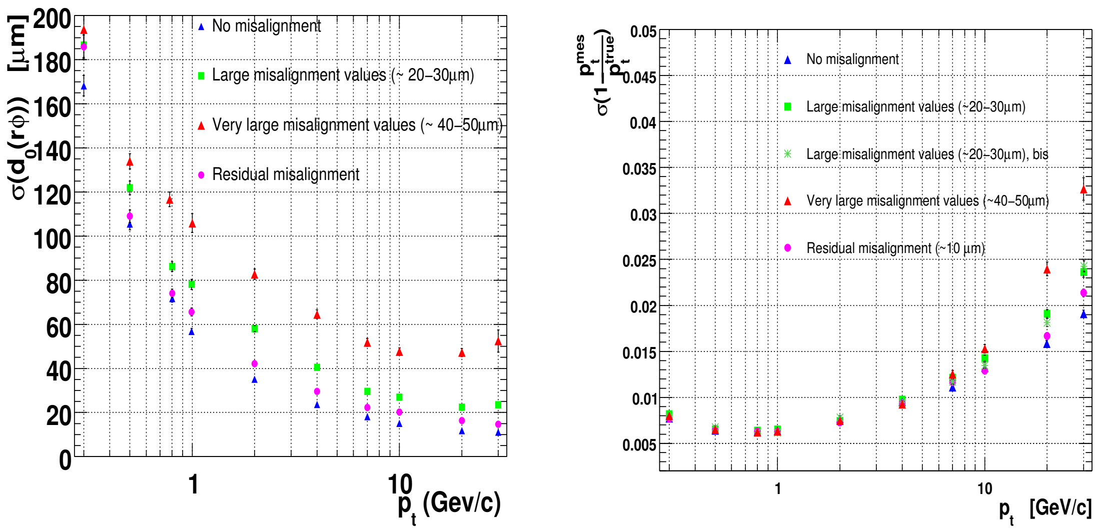

Figure 4.3: Impact parameter resolution (left) and transverse momentum resolution (right) as a function of transverse momentum in different misalignment scenarios. For both studies 500 events have been simulated with a box generator producing 10 charged pions per each of the ten p_{t} bins chosen. For all misalignment scenarios the magnetic field set to 0.5 T. The level of misalignment is indicated in the legend as the average displacement of the points. A different seed for the generation of the random misalignment values has been set for the two "Large misalignment" cases shown in the right panel.

scattering contribution in the χ^2 previsions mentioned above is always overestimated. As a consequence the search road is always large enough to include also displaced points.

Impact parameter and momentum resolution

If the misalignment of the modules are not correlated, the effect of the mispositioning of the points reveals as a deterioration of the track parameter resolution, comparable to what would happen with a worse intrinsic detector resolution. In fact, an *effective* detector resolution $\sigma^{2\ \mathrm{eff}}_{\mathrm{det}}$ accounting for both the intrinsic detector resolution and for the misalignment can be considered. In a simplified picture, the residuals between the true and reconstructed cluster positions in global coordinates can be described by a probability function p_{res} which is the convolution of an intrinsic detector resolution term g_{det} and a function Δ_{mis} describing the probability that the reconstructed cluster position is displaced of a given quantity due to misalignment:

$$p_{res}(x^{\mathrm{rec}}_{\mathrm{mis}} - x^{\mathrm{true}}) = \int \Delta_{mis}(x^{\mathrm{rec}}_{\mathrm{mis}} - x^{\mathrm{rec}}) g_{det}(x^{\mathrm{rec}} - x^{\mathrm{true}}). \tag{4.9}$$

Actually the function Δ_{mis} would not depend only on the distribution of the misalignments of the modules but also on the number of tracks passing through the modules themselves. In the hypothesis that the statistics is "equalized" among modules with different misalignments and that the misalignments values follow a Gaussian distribution with variance σ^2_{Δ}, the Δ_{mis}

function coincides with this distribution and qualitatively the effective detector resolution can be written as:

$$\sigma^{2\ \mathrm{eff}}_{\mathrm{det}} \approx \sigma^{2\ intr}_{\mathrm{det}} + \sigma^2_{\Delta} \tag{4.10}$$

Thus, globally, misalignment affects the detector resolution and accordingly the track impact parameter[4] and transverse momentum resolutions. In Fig. 4.3 (left panel) the impact parameter resolution in the $r\varphi$ plane is shown for different misalignment scenarios. The same generator utilised for the study of the efficiencies has been used for this analysis. The resolution worsening due to misalignment is larger at high transverse momentum even if the effect survives at low p_{t} where it is supposed to become negligible with respect to multiple scattering effects. The misalignment cases considered correspond to realistic scenarios possible after the ITS alignment. The "Residual" case in the figure corresponds to the target set for the alignment procedures, described in the following section. The impact parameter is a fundamental variable for all heavy–flavour physics analyses used to separate tracks coming from the primary vertex of interaction from tracks coming from unstable particles decays at secondary vertices displaced from the primary vertex. The better the resolution on the track impact parameter is, the higher the possibility to resolve secondary and primary vertices is. For all physics analyses it is of fundamental importance to estimate the residual misalignment and the effective detector resolution directly on the data and to tune the simulation in order to reproduce the realistic tracking performance of the detector. Many examples of how this can be done will be shown through this and the following chapter.

The measurement of the track sagitta allows the determination of the track curvature and thus of the transverse momentum. The sagitta is measured mainly with the TPC (Section 3.1.1) but the ITS points improve the transverse momentum resolution, especially at high momentum ([3]). As shown in Fig. 4.3 (right panel) the transverse momentum resolution is not too much affected by ITS misalignment at low p_{t} while degrades from $\sim 2\%$ to $\gtrsim 3\%$ at high p_{t} in the worse misalignment scenario considered.

4.3 Alignment target and strategy

For silicon tracking detectors, the 'standard' target of the alignment procedures is the achievement of a level of precision and accuracy such that the resolution on the reconstructed track parameters (in particular, the impact parameter and the curvature, which measures the transverse momentum) is degraded by at most 20% with respect to the resolution expected in case of the ideal geometry without misalignment. This standard is adopted by all four LHC experiments.

The resolutions on the track impact parameter and curvature are both proportional to the space point resolution, in the limit of negligible multiple scattering effect (large momentum). If the residual misalignment is assumed to be equivalent to random Gaussian spreads in the six alignment parameters of the sensor modules Eq. 4.10 holds. Then a 20% degradation in the effective space point resolution (hence 20% degradation of the track parameters in the large momentum limit) is obtained when the misalignment spread in a given direction is $\sqrt{120\%^2 - 100\%^2} \approx 70\%$ of the intrinsic sensor resolution along that direction. With reference

[4] The impact parameter is defined as: $d_0(r\phi) \equiv q[r - \sqrt{(x_v - x_c)^2 + (y_v - y_c)^2}]$, with q the sign of the particle charge, r and (x_c, y_c) the radius and the centre of the projection of the track helix in the transverse plane and (x_v, y_v) the primary vertex coordinates.

to the intrinsic precisions listed in Table 3.1, the target residual misalignment spreads in the local coordinates on the sensor plane are: for SPD, 8 μm in $x_{\rm loc}$ and 70 μm in $z_{\rm loc}$; for SDD, 25 μm in $x_{\rm loc}$ and 18 μm in $z_{\rm loc}$; for SSD, 14 μm in $x_{\rm loc}$ and 500 μm in $z_{\rm loc}$. Since also the misalignment in the $\theta_{\rm loc}$ angle (rotation about the axis normal to the sensor plane) impacts directly on the effective spatial precision, the numbers given above should be taken as effective spreads including also the effect of the $\theta_{\rm loc}$ rotation. In any case, these target numbers are only an indication of the precision that is requested to the alignment procedures.

The other alignment parameters ($y_{\rm loc}$, $\psi_{\rm loc}$, $\varphi_{\rm loc}$) describe movements of the modules in the radial direction. These have a small impact on the effective resolution, for tracks with a small angle with respect to the normal to the module plane, a typical case for tracks coming from the interaction region. However, they are related to the so-called *weak modes*: correlated misalignments of the different modules that do not affect the reconstructed tracks fit quality (χ^2), but bias systematically the track parameters. A typical example is radial expansion or compression of all the layers, which biases the measured track curvature, hence the momentum estimate. Also correlated misalignments for the parameters on the sensor plane can determine weak modes. These misalignments are, by definition, difficult to determine with collision tracks, but can be tackled using physical observables [123] (e.g. looking for shift in invariant masses of decay particles) and cosmic-ray tracks. These offer a unique possibility to correlate modules that are never correlated in case of tracks from the interaction region, and to have a broad range of track-to-module-plane incidence angles that help to constrain also the $y_{\rm loc}$, $\psi_{\rm loc}$ and $\varphi_{\rm loc}$ parameters, thus improving the sensitivity to weak modes.

As already mentioned in the introduction to this chapter, the sources of alignment information that we use are the survey measurements and the reconstructed space points from cosmic-ray and collision particles. These points are the input for the software alignment methods, based on global or local minimisation of the residuals. The strategy for the ITS first alignment is outlined as follows:

1. Validation of the SSD survey measurements with cosmic-ray tracks.

2. Alignment of SPD and SSD with cosmic-ray tracks, without magnetic field. The initial alignment is more robust if performed with straight tracks (no field), which help to avoid possible biases that can be introduced when working with curved tracks (e.g. radial layer compression/expansion).

3. Use of the already aligned SPD and SSD to confirm and refine the initial time-zero calibration of SDD, obtained with SDD stand-alone methods.

4. Validation of the SDD survey measurements with cosmic-ray tracks.

5. Alignment of the full detector (SPD, SDD, SSD) with cosmic-ray tracks, including also data collected with magnetic field B = 0.5 T. These data are extremely useful also to study the track quality and precision as a function of the measured track momentum, which allows to separate the detector resolution and residual misalignment from the multiple scattering effect.

6. Relative alignment of the ITS and the TPC, when both detectors are already internally aligned and calibrated.

7. Alignment with tracks from pp collisions, with both B = 0 and B = 0.5 T. Cosmic-ray tracks have a dominant vertical component and the sides of the barrel layers have limited

statistics. In addition, most of the tracks crossing the side modules, which are close to vertical, have small incident angles with respect to the module plane. We reject tracks with incident angle below 30°, because the precision of the corresponding space points is much worse than for other tracks and it is quite difficult to evaluate and account for. For this reason, tracks from pp collisions are essential to complete the alignment of the full detector. They will also be used to routinely monitor the quality of the alignment during data taking, and refine the corrections if needed.

In this work of thesis the status of the ITS alignment after the second step is presented and some hints for step3. However many of the analysis and the tools developed for these first steps can be used for the next ones.

4.4 Validation of the survey measurements

The SDD and SSD were surveyed during the assembling phase using a measuring machine. The survey, very similar for the two detectors, was carried out in two stages: the measurement of the modules positions on the ladders and the measurement of the positions of the ladder endpoints on the support cone.

In the first stage, for SDD for example, the three-dimensional positions of six reference markers engraved on detector surface were measured for each module with respect to a reference system defined from ruby spheres fixed to the support structure. The precision of the measuring machine was of 5 μm in the coordinates on the ladder plane and of about 10 μm in the direction orthogonal to the plane. The deviations of the reference marker coordinates on the plane with respect to design positions showed an average value of 1 μm and a r.m.s. of 20 μm. In the second stage, the positions of the ladder endpoints with respect to the cone support structure were measured with a precision of about 10 μm. However, for the outer SSD layer, the supports were dismounted and remounted after the survey; the precision of the remounting procedure is estimated to be around 20 μm in the $r\varphi$ direction [1].

The results for the validation of the SSD survey measurements with comics data are described in the following. Three different methods have been used [6]: the first, using "extra" clusters in the module overlaps, is sensitive only to relative misalignments of neighbouring modules, the others, using point–to–track and track–to–track residuals, are sensitive also to ladders misalignmnents.

The validation of the SDD survey will be performed after completion of the detector calibration.

4.4.1 Read-out clock synchronisation effect

As explained in [2, 6], the SSD is readout serially with a 10 MHz clock. Analog signals are sent from by the front-end electronics (on the module and in the endcaps on the ladders) to digitiser cards (FEROMs) over long cables. The time between sending the data request command and the start of digitisation in the FEROM has to be adjusted to take into account the signal transit time over the cables between the FEROMs and the ladders.

Before the cosmic data taking in summer 2008, the hold-delay time was adjusted for the A and C side of the detector separately. In subsequent studies, it was realised that the read-out clock had to be adjusted for each DDL (9 FEROMs). This adjustment was performed on 13 September 2008. It also turned out, however, that in some cases different FEROMs which were connected to a single DDL had different cable lengths, making it impossible to set a correct timing for all FEROMs (half ladders).

The cable lengths were made uniform for every DDL in the winter shutdown 2008/2009 and the final timings are set for the cosmic run in 2009.

Incorrectly set read-out clock times cause a shift by one strip number in opposite directions on the two sensor sides. The resulting coordinate of the crossing point is approximately correct in the x direction, but off-by-one in the z direction, leading to an apparent shift of up to 4 mm in z. The read out clock time can be set in 16 ns increments, which is 1/6 of the period of the serialised signal from the front-end. As a result, shifts by a fraction of a strip width can also occur, but the exact magnitude of such shifts depends on details of the shaping of the transmitted signal and this has not been studied in detail.

4.4.2 Double points in SSD module overlaps

The modules are mounted with a small (2 mm) overlap in both the longitudinal (z, modules on a single ladder) and transverse direction ($r\varphi$, adjacent ladders) (see Section 3.2.3). These overlaps allow us to verify the relative position of neighbouring modules using double points produced by the same particle on the two modules. More in detail, they allow to estimate the effective spatial resolution of the sensor modules, i.e. the combination of the intrinsic spatial resolution and the relative misalignment of the two adjacent modules. Since the two points are very close in space and the amount of material crossed by the particle in-between the two points is very limited, the multiple scattering can be neglected.

The distance Δx_{loc} between the two points in the local x direction on the module plane ($\approx r\varphi$) is calculated by projecting, along the track direction, the point of one of the two modules on the other module plane.

Figure 4.4 shows the Δx_{loc} distributions without and with the survey corrections, for the two SSD layers. When the survey corrections are applied, the spread of the distributions, obtained from a gaussian fit, is $\sigma \approx 25.5$ μm. This arises from the combined spread of the two points, thus the effective position resolution for a single point is smaller by a factor $1/\sqrt{2}$, i.e. ≈ 18 μm, which is compatible with the expected intrinsic spatial resolution of about 20 μm. This indicates that the residual misalignment after applying the survey is compatible with zero, or, better, it is negligible with respect to the intrinsic spatial resolution. This is compatible with the expected precision of the survey measurements of ≈ 5 μm.

This validation procedure was verified using Monte Carlo simulations of cosmic muons in the detector without misalignment, which give a spread in Δx_{loc} of about 25 μm, in agreement with that obtained from the data.

4.4.3 Track-to-point residuals in SSD

The second test that was performed uses two points in the outer SSD layer to define a straight track (no magnetic field) and inspects the residuals between points on the inner layer and the track. The residuals are calculated using the position along the track corresponding to the minimum of the weighted (dimensionless) distance to the point[5]. Figure 4.5 shows the distribution of the $r\varphi$ (left-hand panel) and z residuals (right-hand panel) between tracks through

[5]The different expected resolutions in $r\varphi$ and z have been taken into account in the calculation of the distance of closest approach, by dividing the deviations by the expected uncertainties, i.e. making use of a dimensionless distance measure.

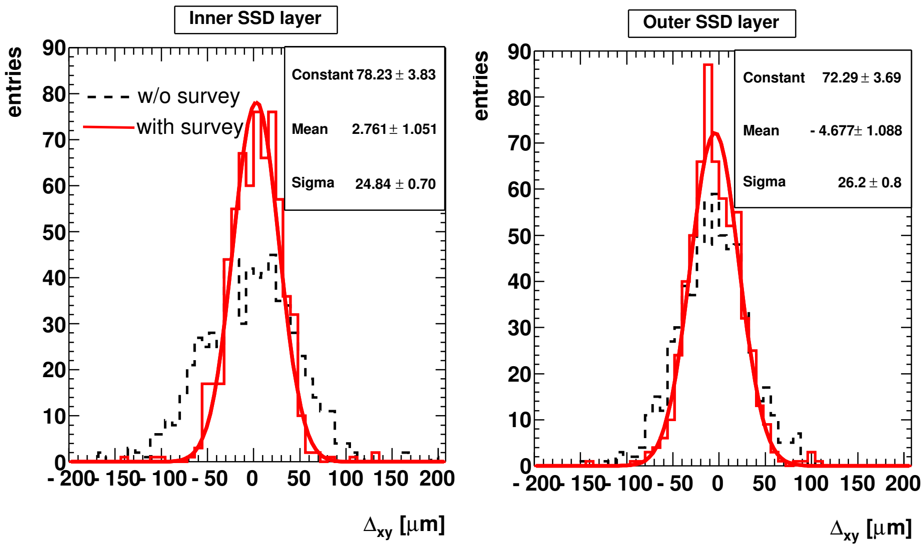

Figure 4.4: Distribution of Δx_{loc}, the distance between two points in the module overlap regions along z on the same ladder, for the two layers of the SSD.

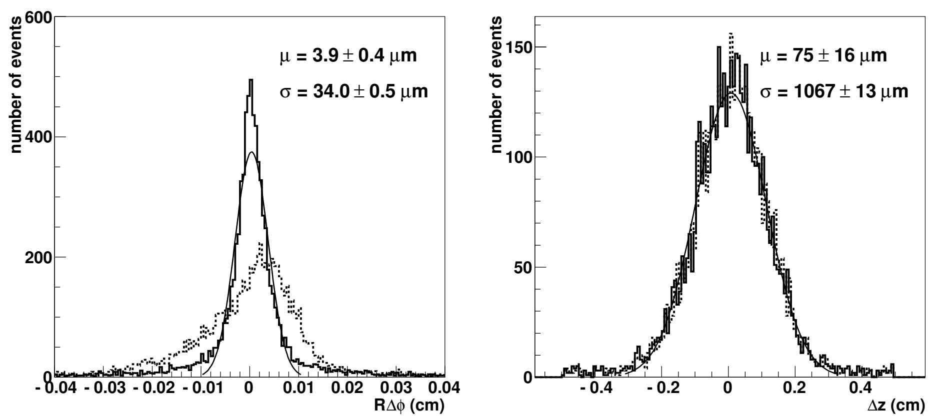

Figure 4.5: Distribution of the $r\varphi$ (left panel) and z (right panel) residuals between tracks through layer 6 and points on layer 5. A gaussian fit truncated at $3\,\sigma$ (thin line) was used to determine the spread σ and mean μ.

layer 6 and points on layer 5. The width of the distributions is quantified by performing a gaussian fit truncated at $3\,\sigma$ (thin line in Fig. 4.5), giving $\sigma_{r\varphi} = 34\ \mu$m and $\sigma_z = 1073\ \mu$m. The tails in the distribution are mostly due to combinatorial background from noise clusters. The spreads contain a contribution from the uncertainty in the track trajectory due to the uncertainties in the points on the outer layer. Assuming the same resolution on the outer and inner layer and taking into account the geometry of the detector, the effective single point resolution spread is $1/\sqrt{1.902}$ times the overall spread [6], so 25 μm and 778 μm in $r\varphi$ and z, respectively.

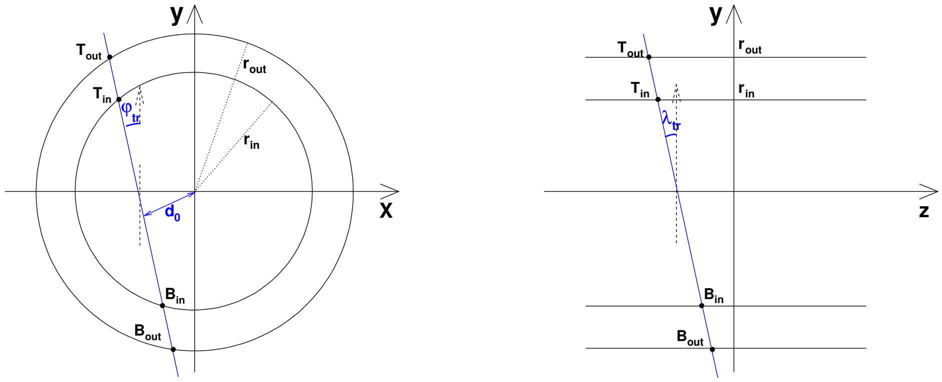

Figure 4.6: Schematic view of the projection of a track: in the xy plane on the left and in the yz plane on the right.

The effective resolution of the points in z is well within the expected uncertainty, indicating that no significant additional misalignment is present. For the $r\varphi$ direction, the obtained spread of 25 μm is larger than the intrinsic resolution of 20 μm. Multiple scattering of low-momentum tracks is expected to contribute to the broadening of the distribution, but no quantitative estimate of this effect was carried out. We can therefore not rule out that additional misalignments with an r.m.s. up to about 20 μm are present in the SSD. The mean residual is also non-zero, (3.9 ± 0.4) μm, which suggests that residual shifts at the 5–10 μm level could be present. These misalignments would have to be at the ladder level to be compatible with the result from the study with sensor module overlaps.

4.4.4 Track-to-track matching

High momentum tracks ($p \gtrsim 2$ GeV/c), for which multiple scattering effects are negligible, can be well approximated as straight lines, in the absence of magnetic field. A cosmic-ray track passing through the SSD can be represented as a straight line matching four points as it is schematically drawn in Fig. 4.6. It is possible to split the track in two parts and to construct two segments with two points each as depicted in Fig. 4.7 and in Fig. 4.8. Two different possibilities are considered:

- "Up–To–Down" : the two points in the upper part ($y > 0$) are used to construct the first segment and the two in the lower part ($y < 0$) are used for the second one (see Fig. 4.7 and 4.8, left panel).

- "Inner–To–Outer" : the two points on the outer layer are used to construct the first segment and the two points on the inner layer are used for the second one (see Fig. 4.7 and 4.8, right panel).

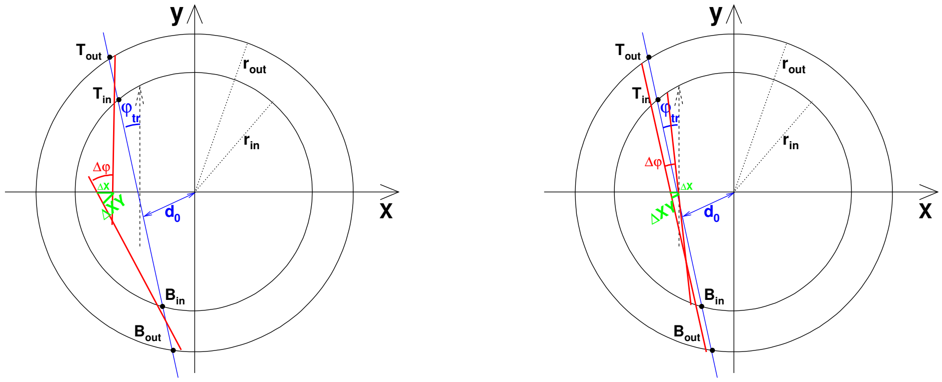

Figure 4.7: The two ways the track segments are constructed in the xy plane. On the left, the "Up–To–Down" case: a segment ($\overline{T_{in}T_{out}}$) is made of the two points in the upper ($y > 0$) part of the detector, the other ($\overline{B_{in}B_{out}}$) is made of the two point in the lower part. On the right, the "Inner–To–Outer" case: the two segments are $\overline{T_{in}B_{in}}$ and $\overline{T_{out}B_{out}}$. In both cases the drawn points represent the real position of the points and the true track trajectory is represented by the blue line matching all the four points. To represent the effect of the misalignment (and detector resolution too) the red segments, representing the reconstructed segments, do not match the points. The $\Delta xy|_{y=0}$ variable is defined as the Δx at $y = 0$ plane corrected for a track inclination factor $\cos\varphi_{\rm tr}$.

The positions and directions of the two track segments are compared and used to determine an effective resolution on the position of the points used to construct the segments. The recovered effective resolution includes the intrinsic detector resolution and a contribution due to misalignment. The following variables are used for the comparison:

- $\Delta xy|_{y=0}$: the distance in the transverse plane (xy) between the two straight line extrapolations at $y = 0$. The distance is measured along a line perpendicular to the line through the four points.

- $\Delta z|_{y=0}$: the difference between the z coordinates of the extrapolations at the $y = 0$ plane of the two straight lines.

- $\Delta\varphi_{\rm tr}$: the difference between the azimuthal angles $\varphi_{\rm tr}$ of the two straight lines.

- $\Delta\lambda^*_{\rm tr}$: the difference between the angles $\lambda_{\rm tr}$ between the y axis and the projections of the segments in the yz plane corrected for a geometry factor (see Section 4.4.5).

As shown in Section 4.4.5, these variables can be directly related to effective resolutions in the local x and z coordinates. A broadening of the distributions is expected if the modules are misaligned but there are no correlations among the misalignments of different modules. A misalignment at the level of the layers, like a movement of one layer with respect to the other, is equivalent to a correlation between the misalignments of all the modules on one layer. This would cause a displacement of the mean values of the distributions. Misalignments at the level

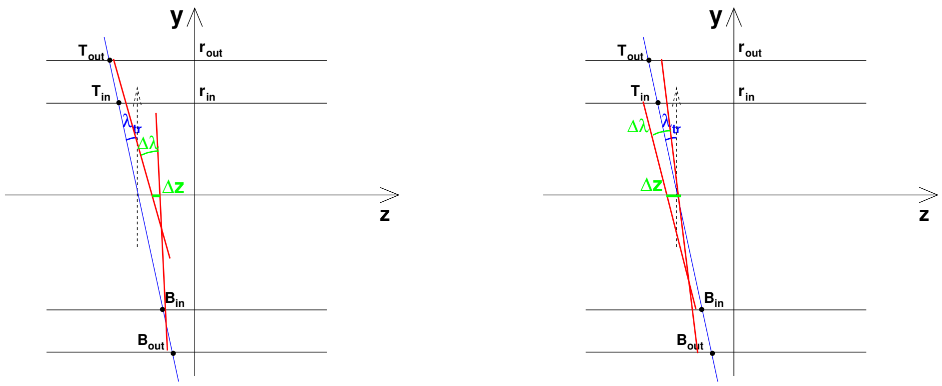

Figure 4.8: The two ways the track segments are constructed in the yz plane. On the left, the "Up–To–Down": a segment ($\overline{T_{in}T_{out}}$) is made of the two points in the upper ($y > 0$) part of the detector, the other ($\overline{B_{in}B_{out}}$) in made of the two points in the lower part. On the right, the "Inner–To–Outer" case: the two segments are $\overline{T_{in}B_{in}}$ and $\overline{T_{out}B_{out}}$. In both cases the drawn points represent the real position of the points and the true track trajectory is represented by the blue line matching all the four points. To represent the effect of the misalignment (and detector resolution too) the red segments, representing the reconstructed segments, do not match the points.

of ladders, if randomly distributed, would cause a broadening of the distributions without any displacement of the mean values because the number of ladders per layer is large.Therefore it is not possible to disentangle between misalignments at the ladder level and those at the module level with this kind of analysis.

Up–To–Down case

As it is clear from Fig. 4.7 (left panel) the difference between the azimuthal angles φ_{tr} of the two tracks is more sensitive to a relative translation in the xy plane between the two layers while it is almost unaffected by a relative rotation around the z axis. Conversely, the difference between the impact parameter ($\Delta xy|_{y=0}$) is more sensitive to a relative rotation of the layers around the z axis while it is unaffected by a relative translation in the xy plane. Similar considerations are applicable to the yz plane (Fig. 4.8): the difference between the λ_{tr} track angles is more sensitive to a relative translation of the layers in the yz plane while the $\Delta z|_{y=0}$ variable is more sensitive to a relative rotation of the layers around the x axis. The following equations (see Section 4.4.5), relate the variances of the observed distributions to

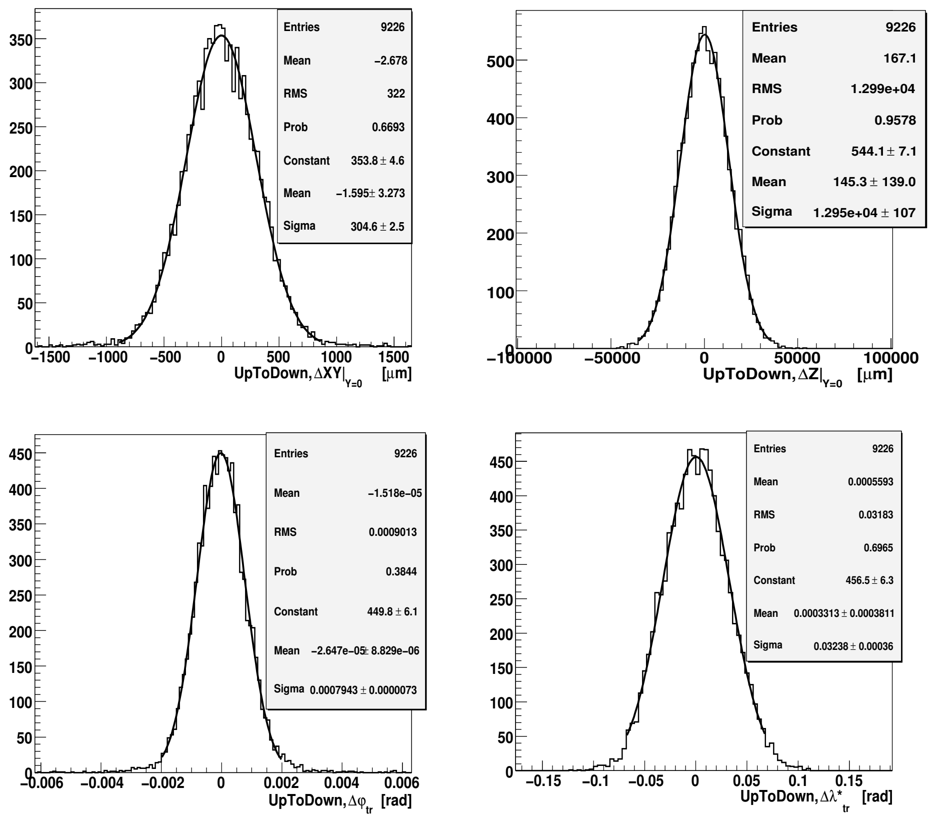

Figure 4.9: "Up–To–Down" case, simulation data. Starting from panel on top left in clockwise order: $\Delta xy|_{y=0}$,$\Delta z|_{y=0}$, $\Delta\lambda^*_{\rm tr}$ and $\Delta\varphi_{\rm tr}$ distributions (defined in the text) obtained with a simulation of about 10000 cosmic events without any misalignment in the geometry.

the effective resolutions on the position of the points in local coordinates:

$$\sigma^2(\Delta xy|_{y=0}) \approx 2\ (\sigma^{\rm eff}_{{\rm loc}\,x})^2 \cdot \frac{r^2_{\rm out}+r^2_{\rm in}}{(r_{\rm out}-r_{\rm in})^2} \tag{4.11}$$

$$\sigma^2(\Delta z|_{y=0}) \approx 2\ (\sigma^{\rm eff}_{z})^2 \cdot \frac{r^2_{\rm out}+r^2_{\rm in}}{(r_{\rm out}-r_{\rm in})^2} \tag{4.12}$$

$$\sigma^2(\Delta\varphi_{\rm tr}) \approx \frac{4\ (\sigma^{\rm eff}_{{\rm loc}\,x})^2}{(r_{\rm out}-r_{\rm in})^2} \tag{4.13}$$

$$\sigma^2(\Delta\lambda^*_{\rm tr}) \approx \frac{4\ (\sigma^{\rm eff}_{z})^2}{(r_{\rm out}-r_{\rm in})^2} \tag{4.14}$$

The validity of these relations has been checked on a simulation of $\approx$ 10000 cosmic tracks in the absence of any misalignment. As shown in Fig. 4.9 the mean values of all the distributions are compatible with zero. The local effective resolutions calculated with the above relations are reported in Table 4.2. The agreement between the observed and the expected values is satisfactory.

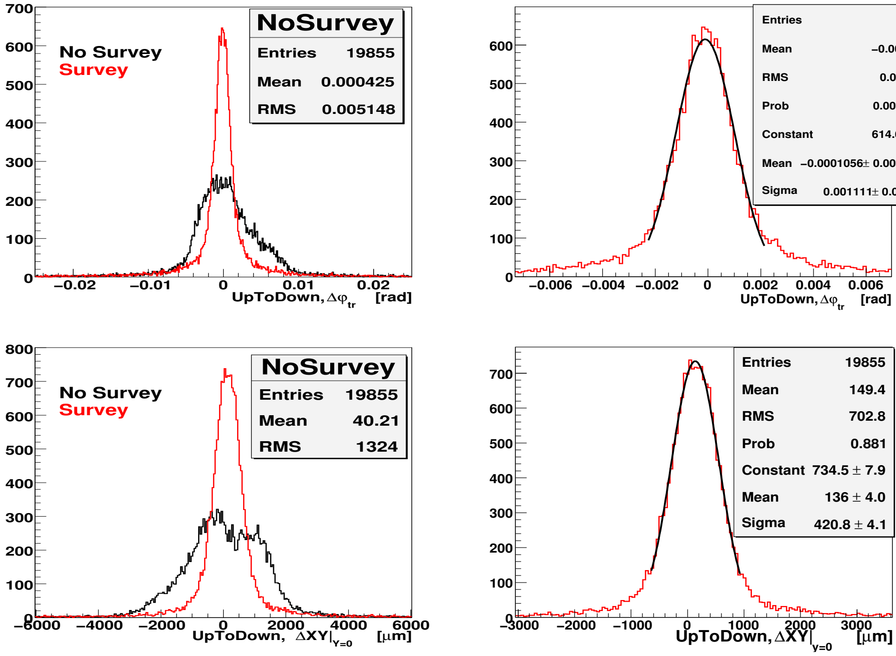

Figure 4.10: "Up–To–Down" case, 2008 cosmic-ray run data. Top-left: $\Delta\varphi_{\mathrm{tr}}$ distributions. Top-right: gaussian fit to the histogram obtained with the survey information. Bottom-left: $\Delta xy|_{y=0}$ distributions. Bottom-right: gaussian fit to the histogram obtained with the survey information.

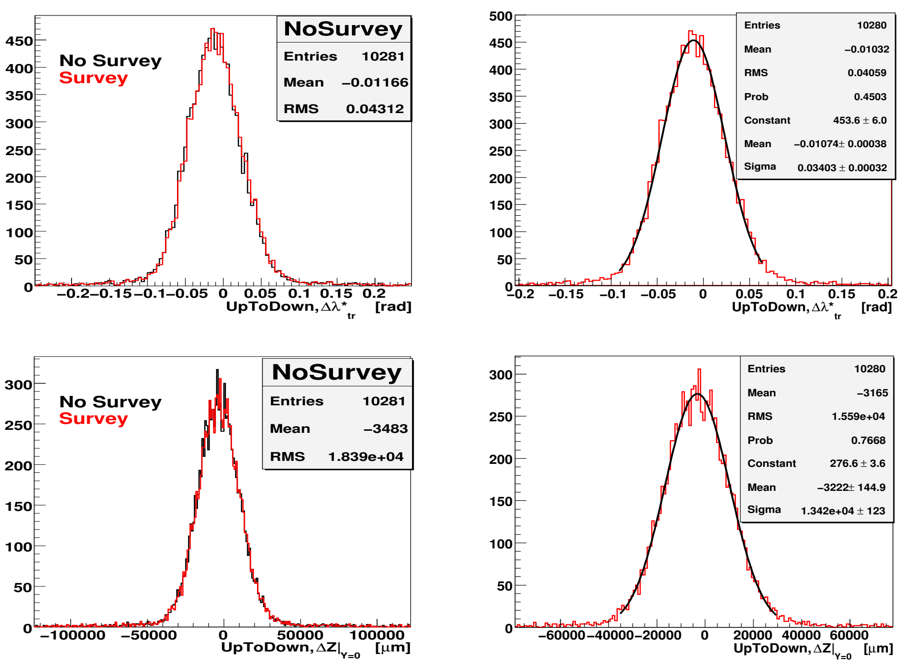

Figure 4.11: "Up–To–Down" case, 2008 cosmic-ray run data. Top-left: $\Delta\lambda^{*}_{\mathrm{tr}}$ distributions. Top-right: gaussian fit to the histogram obtained with the survey information. Bottom-left: $\Delta z|_{y=0}$ distributions. Bottom-right: gaussian fit to the histogram obtained with the survey information.

In Fig. 4.10 and Fig. 4.11 the distributions obtained with cosmic-ray data are shown. The black histograms refer to the ideal geometry case (no survey information employed), while for the red ones the survey information is used. Due to the cable-length differences in the readout described in Section 4.4.1 only the subset of data collected after 13 September 2008 (time of the hardware fix) is employed for the study of the $\Delta z|_{y=0}$ and $\Delta\lambda^*_{\mathrm{tr}}$ distributions: these variables are related to the measurement of the local z coordinate, which is the most affected by the problem. It has been checked that the $\Delta xy|_{y=0}$ and $\Delta\varphi_{\mathrm{tr}}$ distributions, recovered from the entire data sample and from only the data collected after the hardware fix show no significant differences. Hence, the results obtained using the entire data sample are presented for these variables.

The means of the $\Delta xy|_{y=0}$ and the $\Delta\varphi_{\mathrm{tr}}$ distributions are not compatible with zero within errors, indicating that there are residual misaligments in the SSD after survey. The values are small, however, making it difficult to further investigate whether the displacements are dominantly translations or rotations at the layer level.. Also the means of the $\Delta z|_{y=0}$ and $\Delta\lambda^*_{\mathrm{tr}}$ distributions are incompatible with zero. Because of the cable-length differences in the readout it is not possible to argue whether the displacement of the means is caused by a relative translation or rotation in the yz plane between the layers. As expected the widths of the distributions are larger with respect to the simulation with the ideal geometry due to misalignments on the ladders and modules positions. With the use of the survey information the observed widths are much closer to the ideal ones. In Table 4.3 the effective resolutions on the local x and z coordinates obtained from the variances of the observed distributions by using Eq. 4.11 are reported. In the same table, average values for the misalignment affecting

Table 4.2: "Up–To–Down" case, simulation data: test for the formula (4.11). The observed variances refer to the distributions in Fig. 4.9 obtained with a simulation of $\approx$ 10000 cosmic-ray events without any misalignment.

Variable	Observed Sigma	Eff. Loc. Resol. [μm]	Nominal Resol. [μm]
$\Delta xy\|_{y=0}$	305 μm	18.7	18.5
$\Delta\varphi_{\mathrm{tr}}$	0.79 mrad	19.7	18.5
$\Delta z\|_{y=0}$	12950 μm	792	750-790
$\Delta\lambda^*_{\mathrm{tr}}$	32.4 mrad	808	750-790

Table 4.3: "Up–To–Down" case, 2008 cosmic-ray run data. Effective local resolutions and residual misalignment estimated for the "Up–To–Down" case using about 20000 cosmic-ray tracks for the $\Delta xy|_{y=0}$ and $\Delta\varphi_{\mathrm{tr}}$ distributions and about 10000 cosmic-ray tracks for the $\Delta\lambda^*_{\mathrm{tr}}$ and $\Delta z|_{y=0}$.

Variable	Observed Sigma		Eff. Loc. Resol. [μm]			Misal. [μm]	
	No Surv	Surv	Ideal	No Surv	Surv	Initial	Residual
$\Delta xy\|_{y=0}$	1355	421 μm	18.5	84	25.8	82	18
$\Delta\varphi_{\mathrm{tr}}$	3.6	1.1 mrad	18.5	91	27.4	89	20.2
$\Delta z\|_{y=0}$	13440	13420 μm	750-790	822	821	$\approx 230-330$	$\approx 230-330$
$\Delta\lambda^*_{\mathrm{tr}}$	34	34 mrad	750-790	848	848	$\approx 310-395$	$\approx 310-395$

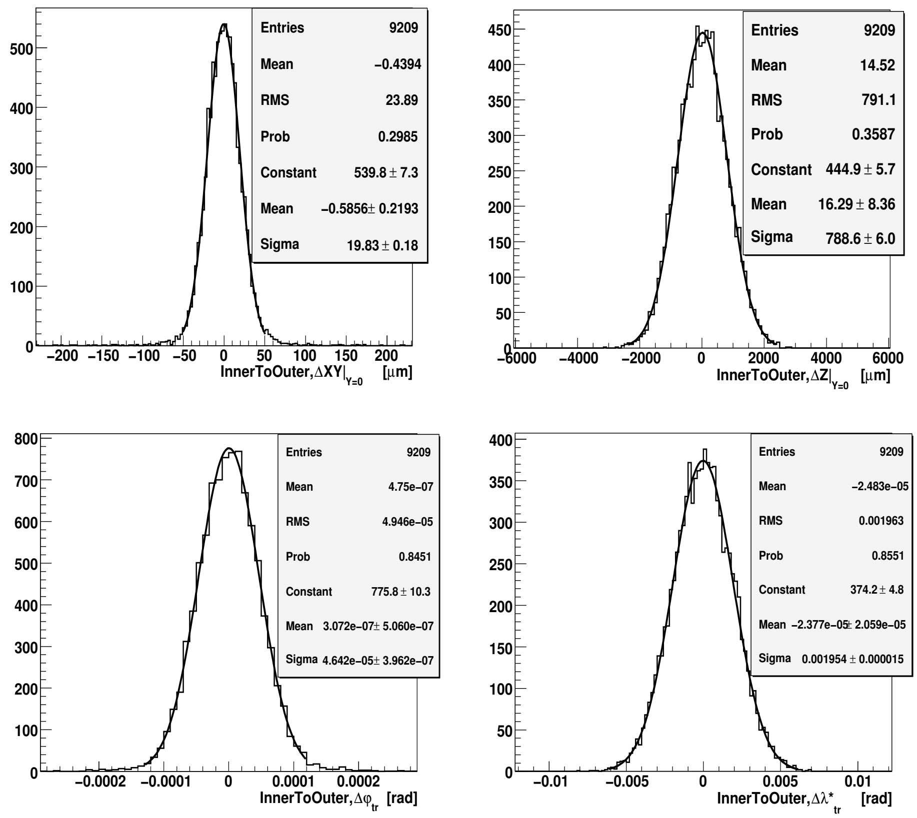

Figure 4.12: "Inner–To–Outer" case, simulation data. Starting from panel on top left in clockwise order: $\Delta xy|_{y=0}$,$\Delta z|_{y=0}$, $\Delta\lambda^*_{\rm tr}$ and $\Delta\varphi_{\rm tr}$ distributions (defined in the text) obtained with a simulation of about 10000 cosmic events without any misalignment in the geometry.

the SSD at the level of ladders and of modules are estimated, by considering:

$$\sigma^2_{\rm eff}(\mathrm{loc}\, x[z]) = \sigma^2_{\rm ideal}(\mathrm{loc}\, x[z]) + \sigma^2_{\rm misal}(\mathrm{loc}\, x[z]) \tag{4.15}$$

Only a rough estimate is possible if the survey information is not used because of the clearly not gaussian shapes of the distributions. With the survey, the effective resolutions in the xy plane improves from $\approx$ 84 μm to $\approx$ 27 μm, the latter value being compatible with a residual misalignment of $\approx$ 20μm. The effective resolution on the z coordinate is practically unchanged, $\sigma_z^{\rm eff} \approx 830$ μm, compatible with a residual misalignment of $\approx$ 220 μm. The latter value can be affected by the cable-length differences in the read-out.

Inner–To–Outer case

As it is clear from Fig. 4.7 (right panel) the $\Delta\varphi_{\rm tr}$ variable is sensitive to a relative rotation of the layers around the z axis while the $\Delta xy|_{y=0}$ is sensitive to a translation of one layer with respect to the other. The $\Delta\lambda^*_{\rm tr}$ is sensitive to a relative rotation of the layers around the x axis and the $\Delta z|_{y=0}$ is sensitive to a relative translation in the yz plane. The following equations (see Section 4.4.5) relate the variances of the observed distributions to the effective resolutions on the position of the points in local coordinates:

$$\sigma^2(\Delta xy|_{y=0}) \approx (\sigma^{\text{eff}}_{\text{loc }x})^2 \tag{4.16}$$

$$\sigma^2(\Delta z|_{y=0}) \approx (\sigma^{\text{eff}}_{z})^2 \tag{4.17}$$

$$\sigma^2(\Delta\varphi_{\text{tr}}) \approx \frac{(\sigma^{\text{eff}}_{\text{loc }x})^2}{2} \cdot \left(\frac{1}{r^2_{\text{out}}} + \frac{1}{r^2_{\text{in}}}\right) \tag{4.18}$$

$$\sigma^2(\Delta\lambda^*_{\text{tr}}) \approx \frac{(\sigma^{\text{eff}}_{z})^2}{2} \cdot \left(\frac{1}{r^2_{\text{out}}} + \frac{1}{r^2_{\text{in}}}\right) \tag{4.19}$$

Also in this case, the validity of these relations has been checked on a simulation of ≈ 10000 cosmic-ray tracks in the absence of any misalignment. As shown in Fig. 4.12, the mean values of all the distributions are compatible with zero. The local effective resolutions calculated with the above relations are reported in Table 4.4. The agreement between the observed and the expected values is satisfactory.

In Fig. 4.13 and Fig. 4.14 the distributions obtained with cosmic data are shown. The selection applied on the cosmic tracks is the same as in the "Up–To–Down" case. The black histograms refer to the ideal geometry case (no survey information applied), while for the red ones the survey information is used. As in the "Up–To–Down" case, the means of the $\Delta xy|_{y=0}$ and $\Delta\varphi_{\text{tr}}$ distributions are not compatible with zero within errors: their values are however very close to zero and it is not possible to conclude that the displacement is due to a relative translation or rotation in the xy plane between the layers. The means of the $\Delta z|_{y=0}$ and $\Delta\lambda^*_{\text{tr}}$ distributions in the yz planes are not compatible with zero, as in the "Up–To–Down"

Table 4.4: "Inner–To–Outer" case: test for the formula (4.16). The observed variances refer to the distributions in Fig. 4.12 obtained with a simulation of ≈ 10000 cosmic-ray events without any misalignment applied to the geometry.

Variable	Observed Sigma	Loc. Eff. Resol. [μm]	Nominal Resol. [μm]
$\Delta xy\|_{y=0}$	19.8 μm	19.8	18.5
$\Delta\varphi_{\text{tr}}$	0.046 mrad	18.6	18.5
$\Delta z\|_{y=0}$	789 μm	789	750-790
$\Delta\lambda^*_{\text{tr}}$	1.95 mrad	789	750-790

Table 4.5: Effective local resolutions and residual misalignment estimated for the "Inner–To–Outer" case obtained using about 20000 cosmic-ray tracks for the $\Delta xy|_{y=0}$ and $\Delta\varphi_{\text{tr}}$ distributions and about 10000 cosmic-ray tracks for the $\Delta\lambda^*_{\text{tr}}$ and $\Delta z|_{y=0}$.

Variable	Observed Sigma		Eff. Loc. Resol. [μm]			Misal. [μm]	
	No Surv	Surv	Ideal	Surv	No Surv	Initial	Residual
$\Delta xy\|_{y=0}$	65-90	27 μm	18.5	65-90	27	62-88	19.7
$\Delta\varphi_{\text{tr}}$	0.18	0.065 mrad	18.5	73	26.5	71	20
$\Delta z\|_{y=0}$	856	852 μm	750-790	856	852	$\approx 320-400$	$\approx 320-400$
$\Delta\lambda^*_{\text{tr}}$	2.02	2.02 mrad	750-790	817	817	$\approx 210-320$	$\approx 210-320$

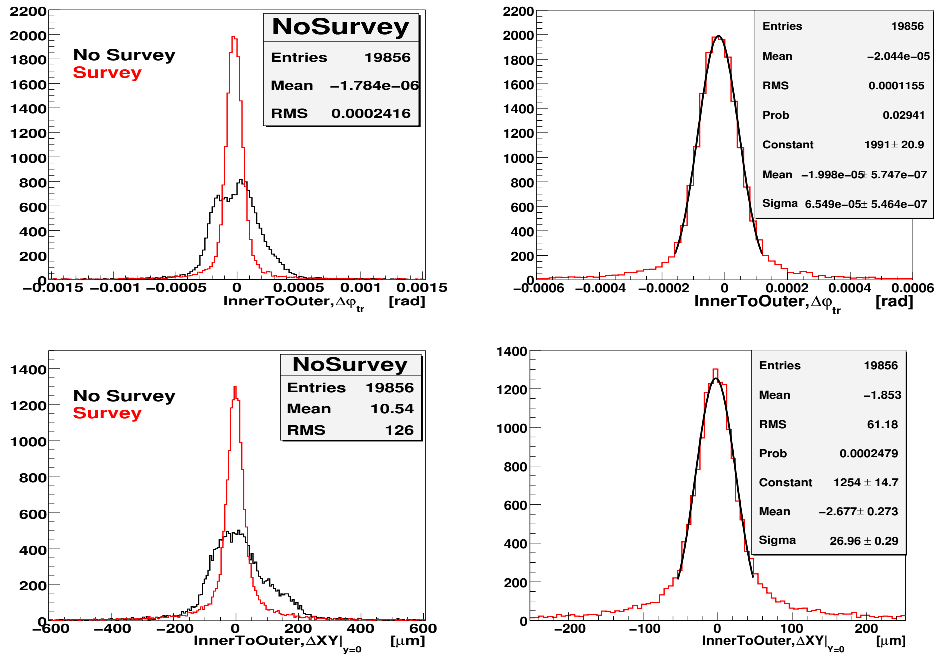

Figure 4.13: "Inner–To–Outer" case, 2008 cosmic-ray run data. Top-left: $\Delta\varphi_{\mathrm{tr}}$ distributions. Top-right: gaussian fit to the histogram obtained with the survey information. . Bottom-left: $\Delta xy|_{y=0}$ distributions. Bottom-right: gaussian fit to the histogram obtained with the survey information.

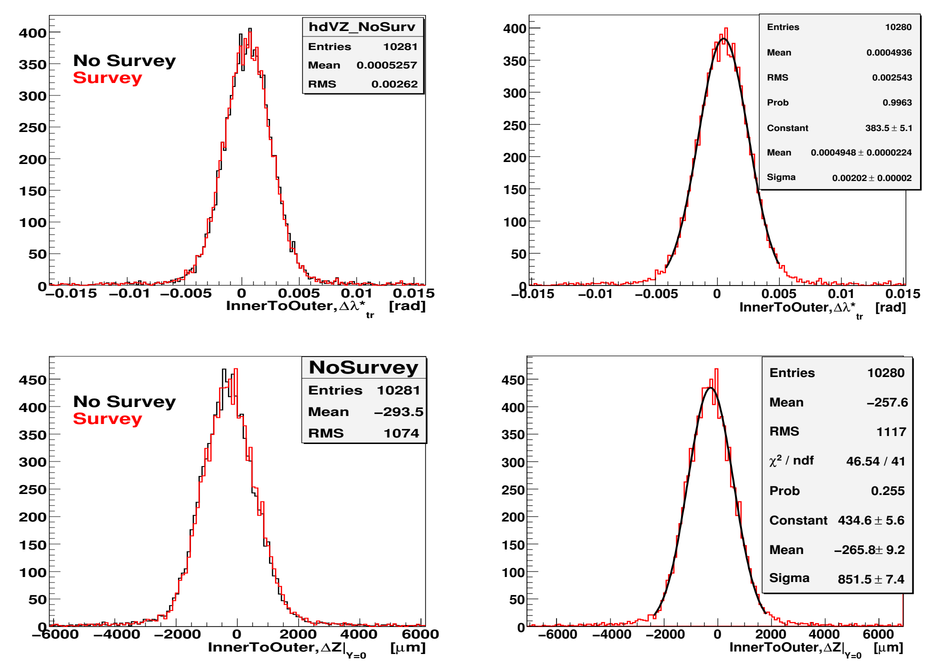

Figure 4.14: "Inner–To–Outer" case, 2008 cosmic-ray run data. Top-left: $\Delta\lambda^*_{\mathrm{tr}}$ distributions. Top-right: gaussian fit to the histogram obtained with the survey information. Bottom-left: $\Delta z|_{y=0}$ distributions. Bottom-right: gaussian fit to the histogram obtained with the survey information.

case. This might be related to the cable-length differences in the readout (Section 4.4.1). In Table 4.5 the effective resolutions on the local x and z coordinates obtained from the variances of the observed distributions by using Eq. 4.16 are reported, along with the estimated average values for the residual misalignment affecting the SSD at the ladder and module levels. A window of possible values is reported for the variance of the $\Delta xy|_{y=0}$ distribution in the case the survey information is not used since the shape is clearly not gaussian and the extracted variance is strongly dependent on the fit range. The obtained values are consistent with those found in the "Up–To–Down" case. With the survey, the effective resolution in the xy plane improves from $\approx 65-90$ μm to ≈ 27 μm, compatible with a residual misalignment of ≈ 20 μm. No significant differences can be appreciated with the use of the survey for the $\Delta z|_{y=0}$ and $\Delta\lambda^*_{\mathrm{tr}}$ distributions. The resolution on the z coordinate is practically unchanged, $\sigma_z^{\mathrm{eff}} \approx 830$ μm, compatible with a residual misalignment of ≈ 220 μm. The latter value can be affected by residual cable-length differences in the read-out.

4.4.5 Estimation of effective detector resolutions from track-to-track residuals

In this section the formula in Eq. 4.11 and 4.16 relating the track-to-track residuals spreads to the effective local resolutions are derived. The full error propagation on the considered variables is done even if the same approach outlined in the Appendix A of [6] to derive the geometrical factors used in section 4.4.3 could be applied. In the following, the xy plane is often referred to as the $r\varphi$ plane.

The straight line fitting two points is unequivocally determined and can be parametrised as follows:

$$x(y) = \frac{x_2 - x_1}{y_2 - y_1}\left(y - \frac{y_2 + y_1}{2}\right) + \frac{x_2 + x_1}{2}\,, \tag{4.20}$$

The y coordinate is chosen as the free parameter. The two SSD layers can be represented as two concentric cylinders whose projections in the xy plane are two concentric circles. The azimuthal angle in the xy plane defined as the angle (clockwise) between a vector and the y-axis is indicated with φ . A track pointing towards the center of the detector crosses these circles being perpendicular to the tangent lines at the hitting points. The projection in the xy plane is then perpendicular to the modules planes, since the sensor modules a layer consists of can be roughly represented as planes tangent to a cylinder. The hitting point position of a track is measured with a finite precision determined by the detector resolution, $\sigma_{\mathrm{loc}\,x} = 20$ μm $\equiv \sigma_{r\varphi}$ in the xy plane and $\sigma_z \simeq 770$ μm along the z coordinate. In the local reference frame this error is described by the covariance matrix of the measured cluster:

$$\mathrm{cov}(\vec{x}_{\mathrm{loc}}) = \begin{pmatrix} \sigma^2(x_{\mathrm{loc}}) & 0 & 0 \\ 0 & 0 & 0 \\ 0 & 0 & \sigma^2(z_{\mathrm{loc}}) \end{pmatrix} \tag{4.21}$$

with $\sigma(x_{\mathrm{loc}}) = \sigma_{r\varphi}$ and $\sigma(z_{\mathrm{loc}}) = \sigma_z$. In the global reference frame this matrix is:

$$\mathrm{cov}(\vec{x}_{glob}) = R^T_{g\to l}\mathrm{cov}(\vec{x}_{loc})R_{g\to l} = \tag{4.22}$$

$$= \begin{pmatrix} \cos^2(\varphi_{\mathrm{rot}})\sigma^2(x_{\mathrm{loc}}) & \cos(\varphi_{\mathrm{rot}})\sin(\varphi_{\mathrm{rot}})\sigma^2(x_{\mathrm{loc}}) & 0 \\ \cos(\varphi_{\mathrm{rot}})\sin(\varphi_{\mathrm{rot}})\sigma^2(x_{\mathrm{loc}}) & \sin^2(\varphi_{\mathrm{rot}})\sigma^2(x_{\mathrm{loc}}) & 0 \\ 0 & 0 & \sigma^2(z_{\mathrm{loc}}) \end{pmatrix} \tag{4.23}$$

$R_{g\to l}$ is the rotation matrix which enters the transformation of the coordinates from the global to the local system, written, for the SSD, as:

$$R_{g\to l} = \begin{pmatrix} -\cos(\varphi_{\mathrm{rot}}) & -\sin(\varphi_{\mathrm{rot}}) & 0 \\ -\sin(\varphi_{\mathrm{rot}}) & \cos(\varphi_{\mathrm{rot}}) & 0 \\ 0 & 0 & -1 \end{pmatrix}$$

φ_{rot} is the angle of the rotation around the z axis defined as the angle that rotates the global y axis onto the local one. For the SSD the rotation angle is equal to the azimuth φ of the center of the module. As explained in the preivous section, it is useful to split a track made of four points in two segments and to compare their directions in the xy plane identified by the angle:

$$\varphi_{\mathrm{tr}} = \arctan\left(\frac{x_2 - x_1}{y_2 - y_1}\right) \tag{4.24}$$

For a track almost parallel to the y-axis (vertical direction) and pointing towards the origin, $\varphi_{\mathrm{tr}} \approx 0$ and it is possible to approximate $\tan\varphi_{\mathrm{tr}}$ with φ_{tr}. The azimuth φ of the two points is small and it is possible to neglect the error on the y coordinate and to approximate $y_i = r_i\cos(\varphi_i)$ for points with global $y > 0$ and $y_i = -r_i\cos(\varphi_i)$ for points with global $y < 0$. The variances on the measured angles for the two "Inner–To–Outer" and "Up–To–Down" cases are recovered by simple error propagation:

$$\text{“Up – To – Down''} : \sigma^2(\varphi_{\mathrm{tr}}) \approx \frac{2\sigma^2_{\mathrm{r}\varphi}}{(r_{out} - r_{in})^2} \tag{4.25}$$

$$\text{“Inner – To – Outer''} : \sigma^2(\varphi_{trout[in]}) \approx \frac{2\sigma^2_{\mathrm{r}\varphi}}{(2\ r_{out[in]})^2} \tag{4.26}$$

If the track is pointing towards the origin but with an angle φ_{tr} far from 0, it is possible to repeat the above considerations in a reference frame rotated around the z axis by an angle $\varphi_{ref} \approx \varphi_{\mathrm{tr}} \approx \varphi_{\mathrm{pts}}$. In this frame $\varphi'_{\mathrm{tr}} = \varphi_{\mathrm{tr}} - \varphi_{ref} \approx 0$ and it is still possible to approximate the tangents with the angles. Since $\sigma(x') \approx \sigma_{\mathrm{r}\varphi}$ and $\sigma(y') \approx 0$, the error on φ_{tr} is given by the formula above. The next step is to consider a more general case, with tracks not pointing towards the origin. As depicted in Figure 4.15, the angles α_2,α_1 between the track and the lines tangent to the layers at the hitting points will differ from 90^o. With simple geometrical arguments it is possible to show that:

$$r_{out}\sin\alpha_{out} = r_{in}\sin\alpha_{in} = d_0 \tag{4.27}$$

d_0 is the impact parameter with respect to the origin. Since the trigger for cosmic-ray events is given by the SPD2, it is possible to estimate the maximum angle α_1 for the detected cosmic-ray tracks. The maximum impact parameter is equal to the outer SPD layer radius and

$$\alpha_1^{Max} = \arcsin\left(\frac{r_{SPD2}}{r_{SSD1}}\right) \approx 0.2rad = 12^o \tag{4.28}$$

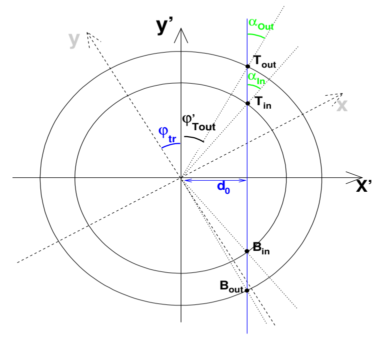

Figure 4.15: Sketch of a track in the rotated reference system where $\varphi'_{\rm tr} \approx 0$

To estimate the error on $\varphi_{\rm tr}$ in the "Inner–To–Outer" case a reference frame rotated around the z axis by an angle $\varphi_{ref} \approx \varphi_{\rm tr}$ is considered. In this frame $\varphi_{\rm pts}$ is equal to α_1 and it could be possible to approximate $\tan(\varphi'_{\rm tr}) \approx \varphi'_{\rm tr}$. However for completeness the whole error propagation is reported and approximations are done at the end. Taking into account also the error on the y' coordinate each point contributes to the error on the track direction with

$$\frac{(y'_2 - y'_1)^2}{(x'_2 - x'_1)^2 + (y'_2 - y'_1)^2} \cdot \left[\sigma^2_{y'} \left(\frac{x'_2 - x'_1}{(y'_2 - y'_1)^2}\right)^2 + \sigma^2_{x'} \left(\frac{1}{y'_2 - y'_1}\right)^2 - 2\mathrm{cov}(x', y') \frac{x'_2 - x'_1}{(y'_2 - y'_1)^3}\right] \tag{4.29}$$

Since the modular shape of the detector is neglected (that is equivalent to consider as infinitesimal the dimension of the modules) the angle $\varphi_{\rm rot}$ in the formula (4.22) can be identified with the $\varphi'_i = \alpha_i$ of the points to get the point covariance matrices in this reference frame. Thus, the formula (4.29) can be rewritten as:

$$\frac{\sigma^2_{\mathrm{loc}\,x}}{\Delta x'^2 + \Delta y'^2} \cdot \left[\cos \alpha_i - \frac{\Delta x'}{\Delta y'} \sin \alpha_i\right]^2 \tag{4.30}$$

The coordinates of the points are:

$$x' \approx d_0 \tag{4.31}$$

$$y' \approx \pm\sqrt{r_{out[in]^2 - d_0^2}} \tag{4.32}$$

where the positive sign is for points in the upper part of the detector (T_{out}, T_{in}) while the negative sign is for points in the lower part (B_{out}, B_{in}). By neglecting the second term, which is negligible due to the choice of the frame and the smallness of α_i, by using $\cos \alpha_i = |y_i|/r_i$, and after summing the contributions of the two points of each segment, the following relation is recovered for the "Inner–To–Outer" case:

$$\text{“Inner–To–Outer”}: \ \sigma^2(\varphi_{tr\ in[out]}) \approx \frac{\sigma^2_{\mathrm{loc}\,x}}{2r^2_{in[out]}} \cdot \frac{1}{\sqrt{1-(\frac{d_0}{r_{in[out]}})^2}} \tag{4.33}$$

$$\begin{aligned} \sigma^2(\Delta\varphi_{\mathrm{tr}}) &\approx \frac{\sigma^2_{\mathrm{loc}\,x}}{2}\left[\frac{1}{r^2_{out}\sqrt{1-(\frac{d_0}{r_{out}})^2}} + \frac{1}{r^2_{in}\sqrt{1-(\frac{d_0}{r_{in}})^2}}\right] \\ &\approx \frac{\sigma^2_{\mathrm{loc}\,x}}{2}\left[\frac{1}{r^2_{out}-\frac{d_0{}^2}{2}} + \frac{1}{r^2_{in}-\frac{d_0{}^2}{2}}\right] \end{aligned} \tag{4.34}$$

The last two equations reduced to the relation in Eq. 4.16 for tracks with zero impact parameter or in the limit $d_0/r_i \to 0$.

The same approximations in the "Up–To–Down" case lead to:

$$\text{“Up–To–Down”}: \ \sigma^2(\varphi_{tr\ Up[Down]}) \approx \frac{2\sigma^2_{\mathrm{loc}\,x}\cdot(\cos^2(\alpha_{in})+\cos^2(\alpha_{out}))}{(r_{out}\cos(\alpha_{out})-r_{in}\cos(\alpha_{in}))^2} \tag{4.35}$$

$$\sigma^2(\Delta\varphi_{\mathrm{tr}}) \approx \frac{4\sigma^2_{\mathrm{loc}\,x}\cdot(\cos^2(\alpha_{in})+\cos^2(\alpha_{out}))}{(r_{out}\cos(\alpha_{out})-r_{in}\cos(\alpha_{in}))^2} \tag{4.36}$$

Eq.4.11 is recovered when $\cos(\alpha_i) \to 1$.

The relation between the variance of the $\Delta xy|_{y=0}$ distribution and the effective local resolution can be recovered repeating the same steps done for the $\Delta\varphi_{\mathrm{tr}}$ distribution. For tracks hitting the detector on top at small global x and pointing towards the origin (a likely case for cosmic-ray tracks when the trigger is given by the SPD2), $\varphi_{\mathrm{tr}} \simeq \varphi_{mod} \approx 0$ and the error on the global y (Eq. 4.22) is negligible with respect to $\sigma(x_{glob}) \approx \sigma_{r\varphi}$. By error propagation on Eq. (4.20) it follows:

$$\sigma^2(x(y=0)) \approx \sigma^2_{r\varphi} \cdot \frac{y_2^2+y_1^2}{(y_2-y_1)^2} \tag{4.37}$$

The error on the difference between the extrapolation for the upward part of a track and the downward one, $\Delta x(y=0) \simeq x(y=0)^{\mathrm{up}} - x(y=0)^{\mathrm{down}}$ gets an extra factor 2 and by approximating the layers to cylinders, $y_{1(2)} = r_{1(2)}\cos(\varphi_{\mathrm{tr}})$, the previous equation is rewritten as:

$$\sigma^2(\Delta x(y=0)) \approx 2\sigma^2_{r\varphi} \cdot \frac{r_2^2+r_1^2}{(r_2-r_1)^2} \tag{4.38}$$

For tracks pointing towards the center of the detector but with a $\varphi_{\mathrm{tr}} \neq 0$ it is convenient to rotate the global reference system in such a way that the new y axis coincides with the real (unknown) track direction in the xy plane. In this system all the previous approximations still hold. The relation between the $\Delta x(y=0)$ in this frame and in the standard global one is:

$$\Delta x'(y'=0) = \cos(\varphi_{\mathrm{tr}})\Delta x(y=0) \equiv \Delta xy|_{y=0} \tag{4.39}$$

Since the distribution of the $\Delta x(y=0)$ in the standard reference system is φ_{tr} dependent the $\Delta xy|_{y=0}$ is considered. This variable is actually the difference between the two segments impact parameters with respect to the origin. For tracks with small impact parameter the angle between the tracks and the planes of the modules is small and Eq. (4.38) holds also for the $\Delta xy|_{y=0}$ variable. In the case a track is not pointing towards the origin the formula (4.38) is only an approximation. To get an insight into this the full error propagation is reported. The first[second] point contribution to the variance of the extrapolation of the track at the $y = 0$ plane in the chosen reference frame is:

$$\sigma_x^2 \left(\frac{\pm y_{2[1]}}{y_2 - y_1}\right)^2 + \sigma_y^2 (x_2 - x_1)^2 \left(\frac{\mp y_{2[1]}}{(y_2 - y_1)^2}\right)^2 - \operatorname{cov}(x, y) \frac{y_2^2 (x_2 - x_1)}{(y_2 - y_1)^3} \tag{4.40}$$

In the equation above only the first term is relevant, the others are suppressed due to the small value of $\frac{x_2 - x_1}{y_2 - y_1}$ in the chosen reference frame. As depicted in Figure 4.15, $|y_i| = \cos \alpha_i r_i$ and $\sigma_{x,i} = \sigma^2_{\mathrm{loc}\,x} \cos \alpha_i$. Hence the variance for the $\sigma^2(\Delta xy|_{y=0})$ is:

$$\text{“Up–To–Down”}: 2\sigma^2_{\mathrm{r}\varphi} \left[\cos^2 \alpha_{\mathrm{out}} \cos^2 \alpha_{\mathrm{in}} \frac{r^2_{out} + r^2_{in}}{(r_{out} \cos \alpha_{out} - r_{\mathrm{in}} \cos \alpha_{in})^2}\right] \tag{4.41}$$

$$\text{“Inner–To–Outer”}: \sigma^2_{\mathrm{r}\varphi} \left[\frac{\cos \alpha^2_{out} + \cos \alpha^2_{\mathrm{in}}}{2}\right] \tag{4.42}$$

The square of the cosine in the equation above should be kept as a mean value, since an average over all tracks is implied to get the observed variances. The relations in Eq. (4.11) and in Eq. (4.16) are recovered in the approximation $\cos^2 \alpha_i \approx 1$. For 12^o (the maximum incident angle) the deviation is $\sim 3\%$.

To recover the $\sigma(\Delta\lambda^*_{\mathrm{tr}})$ and $\sigma(\Delta z|_{y=0})$ relation to $\sigma_{\mathrm{loc}\,z}$ the same steps done in the xy plane are repeated in the yz plane. A track made of two points can be parametrised in the yz plane as:

$$z(y) = \frac{z_2 - z_1}{y_2 - y_1} \left(y - \frac{y_2 + y_1}{2}\right) + \frac{z_2 + z_1}{2} \tag{4.43}$$

While in the xy plane the error on the local x is basically the error on the azimuthal coordinate φ ($\sigma^2(\varphi) \approx \frac{\sigma^2(\mathrm{loc}\,x)}{r^2}$), in the yz plane the error on the z coordinate of the points affects directly the tangent $\tan \lambda$ and not the angle λ. To be independent from the track direction, the variable $\Delta\lambda^*_{\mathrm{tr}} \equiv \Delta\lambda_{\mathrm{tr}} \cos \varphi_{\mathrm{tr}} / \cos^2(\lambda_{\mathrm{tr}})$ is considered instead of $\Delta\lambda$. This choice derives from the fact that λ_{tr} is calculated as $\arctan(\Delta z/\Delta y)$ and that, for tracks pointing towards the origin, $y_i \approx \cos \varphi_i r_i$, thus:

$$\sigma^2(\lambda_{\mathrm{tr}}) \approx \frac{\sigma^2(\Delta z/\Delta y)}{\cos^4(\lambda)} \approx \frac{\cos^2(\varphi) \sigma^2(\Delta z/\Delta r_i)}{\cos^4(\lambda)} \tag{4.44}$$

where $r_i = \pm r_{\mathrm{IN/OUT}}$ depending on the point.

By simple error propagation and neglecting the error on y whose effect is always negligible with respect to $\sigma(z)$, is straightforward to recover the relation in Eq. 4.16 and Eq. 4.11. For the $\Delta z|_{y=0}$ distribution all extra factors to account for the dependence on the track direction cancel out and the variance for this variable can be recovered as for the $\Delta xy|_{y=0}$, at least for tracks pointing towards the origin. To avoid the approximations deriving by the impact parameter dependence it is sufficient to calculate the $\Delta z|_{y=0}$ and $\Delta\lambda^*_{\mathrm{tr}}$ variables directly in the track reference system, obtained with a rotation of the global reference system around the z–axis by an angle φ_{tr} (the new y–axis is parallel to the track direction in the transverse plane). In this system $y'_i = r_i = \pm r_{\mathrm{IN/OUT}}$ by construction and none residual approximations due to the track impact parameter are left in the Eq. 4.16 and 4.11 for $\Delta z|_{y=0}$ and $\Delta\lambda^*_{\mathrm{tr}}$ distributions. This has been checked on a toy–model simulation. A dependence on the impact parameter might arise because of a detector response dependence on the track incident angle on the module plane.

4.4.6 Conclusions on SSD survey validation

With the cosmic-ray run 2008 it was possible to validate the survey measurements performed during SSD assembly and mounting phase. Three different methods were employed.

The SSD survey measurements have been validated with three different methods using tracks from cosmic–rays (2008 run).

The first method uses extra clusters in the module overlap regions and is therefore only sensitive to the relative positioning of neighboring modules. For neighboring modules on the same ladder, the single-point resolution is found to be 15 μm in x, indicating that the relative survey precision is better than ≈ 5 μm.

The other two methods use pairs of points to form tracks and then investigate track-to-point residuals and track-to-track residuals. The effective single point resolutions obtained by both methods are in reasonable agreement and are ≈ 30 μm in local x ($r\phi$ direction) and ≈ 800 μm in z. The expected intrinsic resolution of the detector in x is 18 μm, so the derived survey accuracy is 10–20 μm in x. The intrinsic resolution of the detector in z is around 800 μm: it can thus be concluded that the survey precision in z is significantly better than the intrinsic resolution of the detector.

The usable cosmic track sample for this analysis was limited, because read-out time adjustments were made late in the cosmic runs. In addition, some ladders needed a hardware intervention which was performed after the cosmic run. As a result, the conclusions above are only strictly tested for a subset of ladders. The obtained results for the survey precision should be representative for the entire detector. The final goal is to align the detector further using larger samples of collision data. The alignment results should show displacements which are in the range of the survey precision.

The absence of misalignment at the level of the modules positioning within the ladder is very important in view of the software alignment using the alignment algorithms mentioned in the introduction to this chapter. The number of modules the SSD is made of is very large and it is very difficult to collect the minimal statistics required by the algorithms to work properly for each module. However if the relevant misalignments are at the ladder level it is no more necessary to align the modules and ladders can enter the algorithms as rigid blocks with a consequently large reduction of the degrees of freedom. Moreover, since there are 22 (25) modules per ladder in the inner (outer) layer, it is much easier to collect the statistics required to align a ladder rather than a module. Besides this, due to the good alignment status after the survey, the SSD can serve as a reference for the other ITS sub-detectors, especially concerning the fits of the tracks which are much affected by misalignment effects.

Chapter 5

The ITS alignment with track-based algorithms

Two track-based methods are used for the ITS alignment. The main one is based on the Millepede algorithm [5], while the second is based on a module-by-module iterative approach. Similar algorithms are used by all LHC experiments [124, 125, 126]. In this chapter, after a description of the algorithms, the results obtained for the ITS alignment using about 10^5 charged tracks from cosmic-rays are shown. An important part of this work of thesis was devoted to the development of the iterative algorithm and to test it on simulated data first and on data from cosmic-rays later. Comparable results are achieved, with the two alignment methods, in terms of alignment quality and of alignment parameters recovered (as it is shown in a dedicated section). A summary of the results and of the status of the ITS alignment in view of proton–proton collisions concludes the chapter.

5.1 Generalities on methods based on residual minimisation

In general, the task of track-based alignment algorithms is the determination of the set of geometry parameters minimizing a global χ^2 of the track-to-point residuals:

$$\chi^2_{\mathrm{global}} = \sum_{\mathrm{modules,\,tracks}} \vec{\delta}^{\,\mathrm{T}}_{t,p}\,\mathbf{V}^{-1}_{t,p}\,\vec{\delta}_{t,p}\,. \tag{5.1}$$

In this expression, the sum runs over all the detector modules and all the tracks in a given dataset; $\vec{\delta}_{t,p} = \vec{r}_t - \vec{r}_p$ is the residual between the data point $\vec{r}_p$ and the reconstructed track extrapolation $\vec{r}_t$ to the module plane; $\mathbf{V}_{t,p}$ is the covariance matrix of the residual. Note that, in general, the reconstructed tracks themselves depend on the assumed geometry parameters.

5.1.1 Observables to check alignment quality

The same variables employed for the validation of the SSD survey with cosmic–ray tracks (Section 4.4) are considered to check the alignment quality after the track–based alignment methods are used. Before entering into the details of the algorithms, the two main observables, used through this chapter, are recalled here, pointing out the differences arising from the peculiar shape of the SPD outer layer.

For the first observable, the cosmic-ray track is split into the two track segments that cross the upper ($y > 0$) and lower ($y < 0$) ("Up–To–Down" configuration) halves of the ITS barrel, and the parameters of the two segments are compared at $y = 0$. The main variable is $\Delta xy|_{y=0}$, the track-to-track distance at $y = 0$ in the (x, y) plane transverse to beam-line. This observable, accessible only with cosmic-ray tracks, provides a direct measurement of the resolution of the track transverse impact parameter d_0; namely, $\sigma_{\Delta xy|_{y=0}}(p_t) = \sqrt{2}\,\sigma_{d_0}(p_t)$. When a single sub–detector is used and the tracks are straight lines (no magnetic field), the spread of the $\Delta xy|_{y=0}$ distribution can be related (Eq. 4.11) to an effective spatial resolution $\sigma^{\mathrm{eff}}_{\mathrm{loc}x}$ accounting for both the intrinsic sensor resolution and for the residual misalignment. Eq. 4.11 is valid for tracks with a small incidence angle with respect to the modules plane. This is particularly relevant for the SPD because the modules on the outer layer are not orthogonal to the radial direction. Eq. 4.11 for the SPD is better written as:

$$\sigma^2_{\Delta xy|_{y=0}} \approx 2\,\frac{(r^2_{\mathrm{SPD1}}\sigma^{2\,\mathrm{eff}}_{\mathrm{loc}x,\mathrm{SPD1}} + r^2_{\mathrm{SPD2}}\sigma^{2\,\mathrm{eff}}_{\mathrm{loc}x,\mathrm{SPD2}})}{(r_{\mathrm{SPD1}} - r_{\mathrm{SPD2}})^2} \approx 2\,\frac{r^2_{\mathrm{SPD1}} + r^2_{\mathrm{SPD2}}}{(r_{\mathrm{SPD1}} - r_{\mathrm{SPD2}})^2}\,\sigma^{2\,\mathrm{eff}}_{\mathrm{loc}x}\,, \tag{5.2}$$

where the inner and outer SPD layers are indicated as SPD1 and SPD2, respectively. An average over the different effective SPD resolutions on the two layers, due to the different average angle between tracks and modules, is implicit in the last approximation. The effective resolution $\sigma^2_{\mathrm{loc}x}$ recovered via the above formula is realistic only for tracks passing close to the beam line, thus with an incidence angle on the modules planes small enough to keep the difference between the resolutions on the two layer of the order of 2 μm. Hence, only tracks with an impact parameter smaller than 1 cm are used to construct this distribution. With this cut, tracks with a similar topology as those produced in collisions are selected. The relation above neglects the effect of multiple scattering in the pixels and in the beam pipe, which is certainly one of the reasons why the $\Delta xy|_{y=0}$ distribution is in general not gaussian outside the central region, most likely populated by the high-momentum component of the cosmic muons.

To check the alignment of a single sub–detector, it is also useful to split the track in the "Inner–To–Outer" configuration described in Section 4.4.4 for the SSD.
The second alignment quality observable is the Δx_{loc} distance between points in the region where there is an acceptance overlap between two modules of the same layer. Because of the short radial distance between the two overlapping modules (a few mm), the effect of multiple scattering is negligible. However, in order to relate the spread of Δx_{loc} to the effective resolution, the dependence of the intrinsic sensor resolution on the track-to-module incidence angle has to be accounted for. In particular, for SPD, due to the geometrical layout of the detector (Fig. 3.5, left), the track-to-module incidence angles in the transverse plane are in general not equal to 90° and different for two adjacent overlapping modules crossed by the same track. If Δx_{loc} is defined as described in section 4.4.2, the error on Δx_{loc} can be related to the effective spatial resolution of the two points, $\sigma_{\mathrm{spatial}}$, as:

$$\sigma^2_{\Delta x_{\mathrm{loc}}} = \sigma^{2\,\mathrm{eff}}_{\mathrm{loc}x}(\alpha_2) + \sigma^{2\,\mathrm{eff}}_{\mathrm{loc}x}(\alpha_1)\cos^2(\varphi_{12}) \tag{5.3}$$

where the 1 and 2 subscripts indicate the two overlapping points, α_i is the incidence angle of the track on the module plane, and φ_{12} is the relative angle between the two module planes, which is 18° and 9° on the inner and outer SPD layer, respectively. Note that, for SSD overlaps on the same ladder, $\alpha_1 = \alpha_2 \simeq 90°$ (in the transverse plane) and $\varphi_{12} = 0$; therefore, $\sigma_{\Delta x_{\mathrm{loc}}} = \sqrt{2}\,\sigma_{\mathrm{spatial}}$, which is the relation used in section 4.4.2.

5.2 The iterative module-by-module algorithm

The local module-by-module algorithm assumes that the misalignments of the modules crossed by a given track are uncorrelated and performs the minimization of the residuals independently for each module. The core of the method consists of the following steps:

- Select a module to be aligned.
- Fit each track passing through it without using the cluster lying on it.
- Propagate the tracks to the module plane and, for each track, calculate the residual between the extrapolated point and the measured cluster.
- Minimize the χ^2 function in Eq. 5.5 of the alignment parameters of the module.
- Go to the next module.

The track parameters recovered are not influenced by the misalignment affecting the selected module but are influenced by the misalignment affecting the modules employed in the fit.To reduce the residual correlation between the alignment parameters obtained for the different modules, the procedure is iterated until the parameters converge. This method is expected to work at best if two conditions are fulfilled: the correlation between the misalignments of different modules is small and the tracks used to align a given module cross as many other modules as possible. In order to limit the bias that can be introduced by modules with low statistics, for which the second condition is normally not met, the modules are aligned following a sequence based on the number of points registered on the modules: the modules with higher statistics are aligned first. This prevents that the results for the modules with lower statistics are influenced by the misalignment of the modules with higher statistics. To further reduce the correlations, especially between modules close in space, the fraction of tracks available for the alignment of a selected module and crossing another module is limited to 5%. This, along with a proper selection on the residuals (see Section 5.2.2), reduces also possible biases due to module with noisy sensor elements.

5.2.1 Minimization algorithm

The alignment parameters of the modules are written together in a 6-dim vector $\vec{a} = (\vec{a}_{\rm tra}, \vec{a}_{\rm rot})$ with $\vec{a}_{\rm tra} = (\delta x, \delta y, \delta z)$ being the vector for the translation correction and $\vec{a}_{\rm rot} = (\delta\psi, \delta\theta, \delta\phi)$ the three angles for the correction of the orientation of the module plane embodied in a rotation matrix $\mathbf{A}_{\rm rot}$. The angles are defined according to the convention described in Section 4.3. The alignment correction is supposed to be small, so that the rotation matrix can be approximated as the unity matrix plus a matrix linear in the angles:

$$\mathbf{A}_{\rm rot} = \begin{pmatrix} 1 & \delta\phi & -\delta\theta \\ -\delta\phi & 1 & \delta\psi \\ \delta\theta & -\delta\psi & 1 \end{pmatrix} = \mathbf{1}_3 + \epsilon \equiv \mathbf{1}_3 + \sum_{i=1}^{3} \vec{a}_{\rm rot}^{\,\rm i}\epsilon_{\rm i} \, .$$

ϵ^i are three antisymmetric matrices. For each $k^{\rm th}$ track, the observed residual between the cluster point and the track extrapolation to the module plane, i.e. the 3D difference between the coordinates of the two points

$$\vec{\delta}^{\rm k}_{t,p} \equiv \vec{r}^{\,\rm k}_t - \vec{r}^{\,\rm k}_p \, ,$$

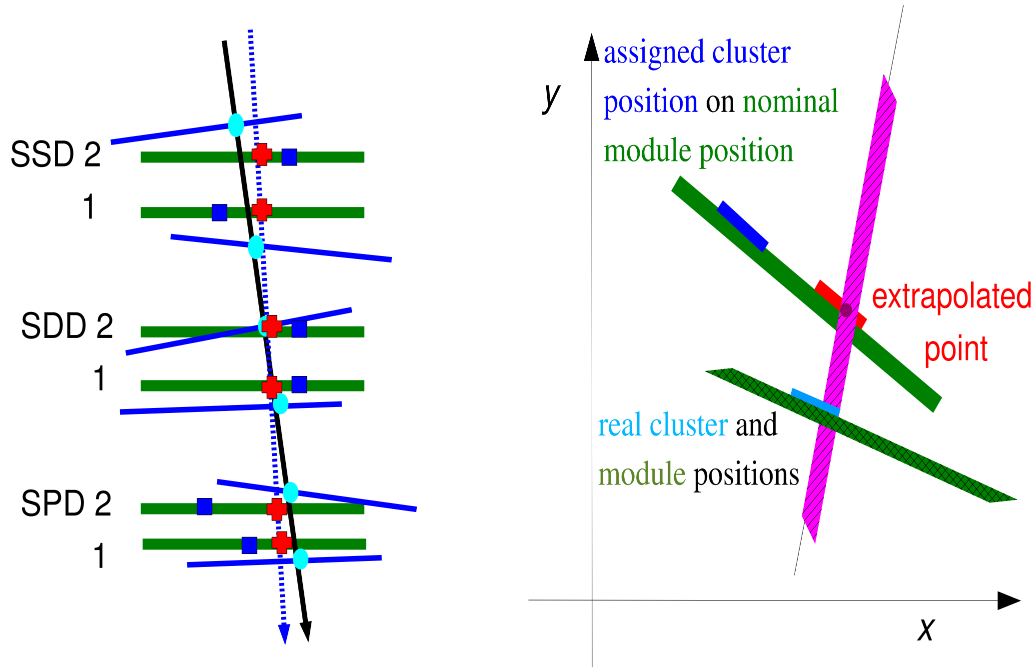

Figure 5.1: On the left. Schematic view of a track crossing 6 modules. The green rectangles represents the modules in the ideal geometry while the blue lines represents the modules in the real geometry, displaced from the ideal positions because of misalignment. The filled arrow represents the true track trajectory intersecting the modules in the cyan circles. The assigned point positions are the small blue rectangles while the red crosses represent the intersection between the reconstructed track (dotted line) and the modules in the ideal geometry. On the right. The real (unknown) position of the module is represented by the cross-hatched shadowed green rectangle. In the iterative method the track is extrapolated to the plane of the module as defined in the ideal geometry (upper green rectangle). A large error along the track direction (purple cross-hatched rectangle) is assigned to the extrapolation point (small red bar) to account for this.

is parametrized as:

$$\vec{\delta}^{\star\,\mathrm{k}}_{t,p} \equiv \vec{a}_{\mathrm{tra}} + \sum_{i=1}^{3} \vec{a}^{\,\mathrm{i}}_{\mathrm{rot}} \epsilon_{\mathrm{i}} \vec{r}^{\,\mathrm{k}}_{p} \equiv \mathbf{J}^{\mathrm{k}}_{p} \vec{a}\,. \tag{5.4}$$

$\mathbf{J}^{\mathrm{k}}_{p}$ is the 3×6 Jacobian matrix expressing the derivative of the residual with respect to the alignment parameters:

$$\left[\mathbf{J}^{\mathrm{k}}_{p}\right]_{ij} = \frac{\partial_i \vec{\delta}^{\star\,\mathrm{k}}_{t,p}}{\partial \vec{a}_j} = \begin{bmatrix} 1 & 0 & 0 & 0 & -z_p & y_p \\ 0 & 1 & 0 & z_p & 0 & -x_p \\ 0 & 0 & 1 & -y_p & x_p & 0 \end{bmatrix}$$

where (x_p, y_p, z_p) are the measured point coordinates.

The χ^2 function of the alignment parameters of a single module minimized by the iterative method is:

$$\chi^2(\delta\vec{t}, \mathbf{A}_{\mathrm{rot}}) = \sum_{\mathrm{k}} \left(\vec{r}_t^{\,\mathrm{k}} - \mathbf{A}_{\mathrm{rot}}\vec{r}_p^{\,\mathrm{k}} - \vec{a}_{\mathrm{tra}}\right)^{\mathrm{T}} \left(\mathbf{V}_t^{\mathrm{k}} + \mathbf{V}_p^{\mathrm{k}}\right)^{-1} \left(\vec{r}_t^{\,\mathrm{k}} - \mathbf{A}_{\mathrm{rot}}\vec{r}_p^{\,\mathrm{k}} - \vec{a}_{\mathrm{tra}}\right) \tag{5.5}$$

$$= \sum_{\mathrm{k}} \left(\vec{\delta}_{t,p}^{\mathrm{k}} - \vec{\delta}_{t,p}^{\star\mathrm{k}}\right)^{\mathrm{T}} \left(\mathbf{V}_t^{\mathrm{k}} + \mathbf{V}_p^{\mathrm{k}}\right)^{-1} \left(\vec{\delta}_{t,p}^{\mathrm{k}} - \vec{\delta}_{t,p}^{\star\mathrm{k}}\right) . \tag{5.6}$$

The index k runs over the tracks passing through the module, $\vec{r}_p^{\,\mathrm{k}}$ is the position of the measured point on the module while $\vec{r}_{\mathrm{k}}^{\,t}$ is the crossing point on the module plane of the k$^{\mathrm{th}}$ track fitted with all points but $\vec{r}_p^{\,\mathrm{k}}$. $\mathbf{V}_t^{\mathrm{k}}$ and $\mathbf{V}_p^{\mathrm{k}}$ are the covariance matrices of the crossing point and of the measured point, respectively. The six alignment parameters enter this formula in the vector $\vec{a}_{\mathrm{tra}}$, the alignment correction for the position of the centre of the module, and in the rotation matrix $\mathbf{A}_{\mathrm{rot}}$ defined above, the alignment correction for the orientation of the plane of the module. The rotation matrix in Eq. 5.2.1 is linear in the angles, thus the χ^2 is a quadratic form of the alignment parameters and the minimization can be performed by simple inversion.

By imposing the derivative of the χ^2 function with respect to the alignment parameters equal to 0 the following equation is recovered:

$$\sum_{k} \left(\mathbf{J}^{\mathrm{k}}\right)_p^{\mathrm{T}} \left(\mathbf{V}_t^{\mathrm{k}} + \mathbf{V}_p^{\mathrm{k}}\right)^{-1} \mathbf{J}_p^{\mathrm{k}}\,\vec{a} = \sum_{k} \mathbf{J}_p^{\mathrm{k}} \left(\mathbf{V}_t^{\mathrm{k}} + \mathbf{V}_p^{\mathrm{k}}\right)^{-1} \vec{\delta}_{t,p}^{\mathrm{k}}$$

The alignment parameters are obtained from the previous equation, along with their covariance matrix $\mathbf{W}$:

$$\vec{a} = \left(\sum_{k} \mathbf{J}_p^{\mathrm{k\,T}} \left(\mathbf{V}_t^{\mathrm{k}} + \mathbf{V}_p^{\mathrm{k}}\right)^{-1} \mathbf{J}_p^{\mathrm{k}}\right)^{-1} \sum_{k} \mathbf{J}_p^{\mathrm{k}} \left(\mathbf{V}_t^{\mathrm{k}} + \mathbf{V}_p^{\mathrm{k}}\right)^{-1} \vec{\delta}_{t,p}^{\mathrm{k}} \tag{5.7}$$

$$\mathbf{W} \equiv \left(\sum_{k} \mathbf{J}_p^{\mathrm{k\,T}} \left(\mathbf{V}_t^{\mathrm{k}} + \mathbf{V}_p^{\mathrm{k}}\right)^{-1} \mathbf{J}_p^{\mathrm{k}}\right)^{-1} \tag{5.8}$$

Points and residuals coordinates are expressed in the global reference system and the algorithm output is thus a global-delta transformation (Section 4.1). The χ^2 function in Eq. (5.5) can be written in the same way also for a set of modules considered as a rigid block. The track parameters are not affected by the misalignment of the module under study, because the point is not used in the fit, while the positions of the crossing points are affected, because the tracks are propagated to the plane of the module defined in the ideal geometry. This is taken into account by adding a large error along the track direction to the covariance matrix of the extrapolated point, as depicted in Fig. 5.2. Because of this, the interpretation of $\mathbf{W}$ as a realistic error matrix for the alignment parameters is not straightforward.
A selection is performed on the normalized residuals (that is, residuals divided by the error) to reduce the effect of the outliers. Module-by-module residuals larger than two times the RMS of the residuals distribution are rejected.

The χ^2 function (5.5) can be minimized also numerically. It has been verified that no differences are present among the parameters recovered with the numerical and with the analytic minimization. For both the options the possibility to fix a subset of degrees of freedom has been implemented, useful in the case the available statistics is low.

5.2.2 Track fit and point covariance matrix enlargement

The track-to-point residuals, used to construct the χ^2 function, are calculated using a parametric straight line $\vec{r}(t) = \vec{a} + \vec{b}\,t$ or helix $\vec{r}(t) = \{a_x + r\,\cos(t+\varphi_0), a_y + r\,\sin(t+\varphi_0), b_z\,t\}$ track model, depending on the presence of the magnetic field. In this chapter, if not specified, all the results refer to the case without magnetic field and, therefore, of the straight line fitter is used. The full error matrix of the measured points is accounted for in the track fit, while multiple scattering is ignored, since it has no systematic effect on the residuals. The straight line fitter is based on a Kalman filter like algorithm. As explained in Section 4.2 the misalignment spoils the detector resolution. The point covariance matrix, based on the cluster properties determined on the module plane, does not account for this by default. Points with a higher spatial precision have a larger influence in the determination of the track parameters. The fitter can work properly only if realistic errors, including the misalignment contribution, are assigned to the points. It is particularly important that detectors with high intrinsic spatial resolution but with possibly large misalignments do not bias the fit results. To account for this, the points covariance matrices are properly modified. This can be done in two ways. It is possible to simply enlarge the local variances by tuning the values for each subdetector. Another possibility, the one adopted for the local iterative method, consists in propagating the alignment parameters error on the point position uncertainty. The error on the alignment parameters are chosen looking at some global observable, like the $\Delta xy|_{y=0}$ variable introduced in Section 4.4.4, before the first iteration, then the covariance matrix $\mathbf{W}$ is used. As explained in the previous section, the latter matrix is affected by the large error assigned to the extrapolation points: it has been checked that this bias behaves like a global factor and none negative consequences arise from the usage of $\mathbf{W}$ to enlarge the covariance matrices of the points used in the track fit. Thus the point covariance matrix $\mathbf{V}_p$ is modified as:

$$\mathbf{V}\,'_p = \mathbf{J}_p^{\mathrm{k}} \mathbf{V}_p \mathbf{J}_p^{\mathrm{k}\,\mathrm{T}}$$

5.2.3 Parameter initialization and constraint from survey measurement

The survey measurements are used as the starting point of the algorithm, to initialize the modules parameters, and as a constraint to the recovered parameters. If the difference between the latter and the survey parameters exceeds the survey spatial precision by a given factor the results are rejected and the parameters of the module are reinitialized to the survey ones. The survey measurements must be validated independently before the use of alignment algorithms. In Section 4.4 the validation of the SSD survey with cosmic-ray tracks is discussed. The survey spatial precision used to constrain the alignment parameters is not the mechanical precision characterizing the survey operation but the effective detector spatial resolution, accounting for misalignment effects, estimated by the survey validation. In the absence of survey measurement, as for the SPD case, "reasonable" boundaries are set as well to reject outliers that could cause the algorithm to fail.

5.2.4 Tests on simulation

The performance of the method has been checked on different simulation samples and with various misalignment scenarios. The analyses shown in this section refer to a sample of about $6 \cdot 10^4$ cosmic-ray tracks simulated with the same trigger condition used for the cosmic–run 2008 (Section 3.7.1). The statistics considered is also comparable to that obtained in the

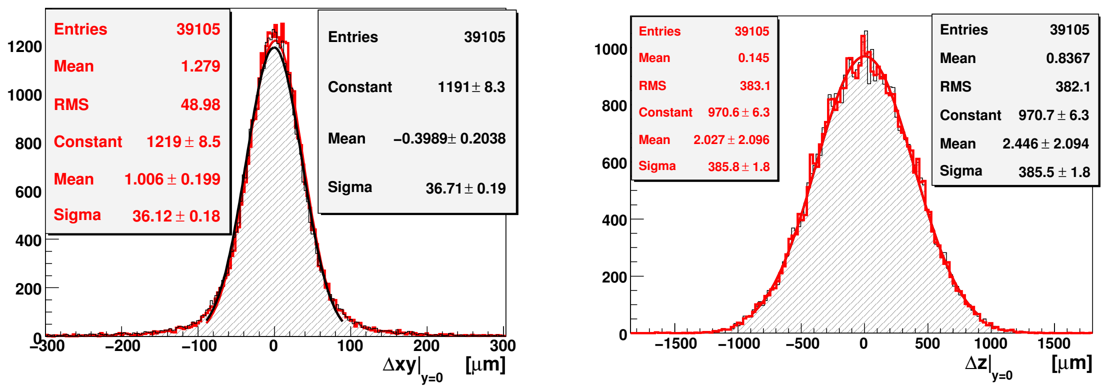

Figure 5.2: On the left: distribution of $\Delta xy|_{y=0}$ from a simulated sample of about $6 \cdot 10^4$ tracks from cosmic-rays with the ideal geometry. The alignment parameters recovered by aligning this sample are used for the dashed histogram, while the thick red line represent the ideal result (no real misalignment, no influence of the re-alignment results). On the right: the same for the $\Delta z|_{y=0}$ variable.

cosmic–run 2008. The incidence angle between tracks and modules planes is required to be smaller than 60^o.

Tests with the ideal geometry and general observations

In Fig. 5.3 the parameters obtained when the real geometry corresponds to the ideal geometry, are shown for the inner SPD layer (on top) and for the outer SPD layer (on bottom). The parameters are expressed in local coordinates, that is, they represent the local-delta transformation introduced in Section 4.1. The interpretation of the alignment parameters in terms of displacements of the points is more transparent looking at the local delta transformation since the rotations are referred to the local axes and the effect of a given rotation is similar for all the modules. For instance, rotations around the local z-axis (ϕ angle) and around the local x-axis imply mainly movements along the local y-axis, as it is evident looking at the following expression of the point coordinates $\vec{r}_p'$ after a delta-rotation:

$$\vec{r_p}\,' = \vec{r}_p + \begin{pmatrix} -\delta\theta z_p + \delta\phi y_p \\ \delta\psi z_p - \delta\phi x_p \\ -\delta\psi y_p + \delta\theta x_p \end{pmatrix} \xrightarrow[\text{loc.}y=0]{\text{loc. coord.}} \begin{pmatrix} x_p - \delta\theta z_p \\ \delta\psi z_p - \delta\phi x_p \\ z_p + \delta\theta x_p \end{pmatrix}$$

The average points displacements caused by delta–rotations for the three ITS sub–detectors has been described in Section 4.1. As explained in Section 4.3, due to the cylindrical shape of the detector, $y_{\rm loc}$, $\psi_{\rm loc}$, $\varphi_{\rm loc}$ describe movements of the modules in the radial direction that have a small impact on the effective resolution for tracks with a small angle with respect to the normal to the module plane. This is a typical case for tracks coming from the interaction region. However, tracks from cosmic-rays are selected by requiring the incidence angles on the module planes to be smaller than $60\circ$ degrees and, moreover, the trigger is provided by the SPD (also for the simulated samples): thus most of the tracks have small incidence angles and the above degrees of freedom have small influence on the residuals also for cosmic tracks. In Fig. 5.3 the RMS of the local δx, the movement along the local x–axis, is about 5 μm and

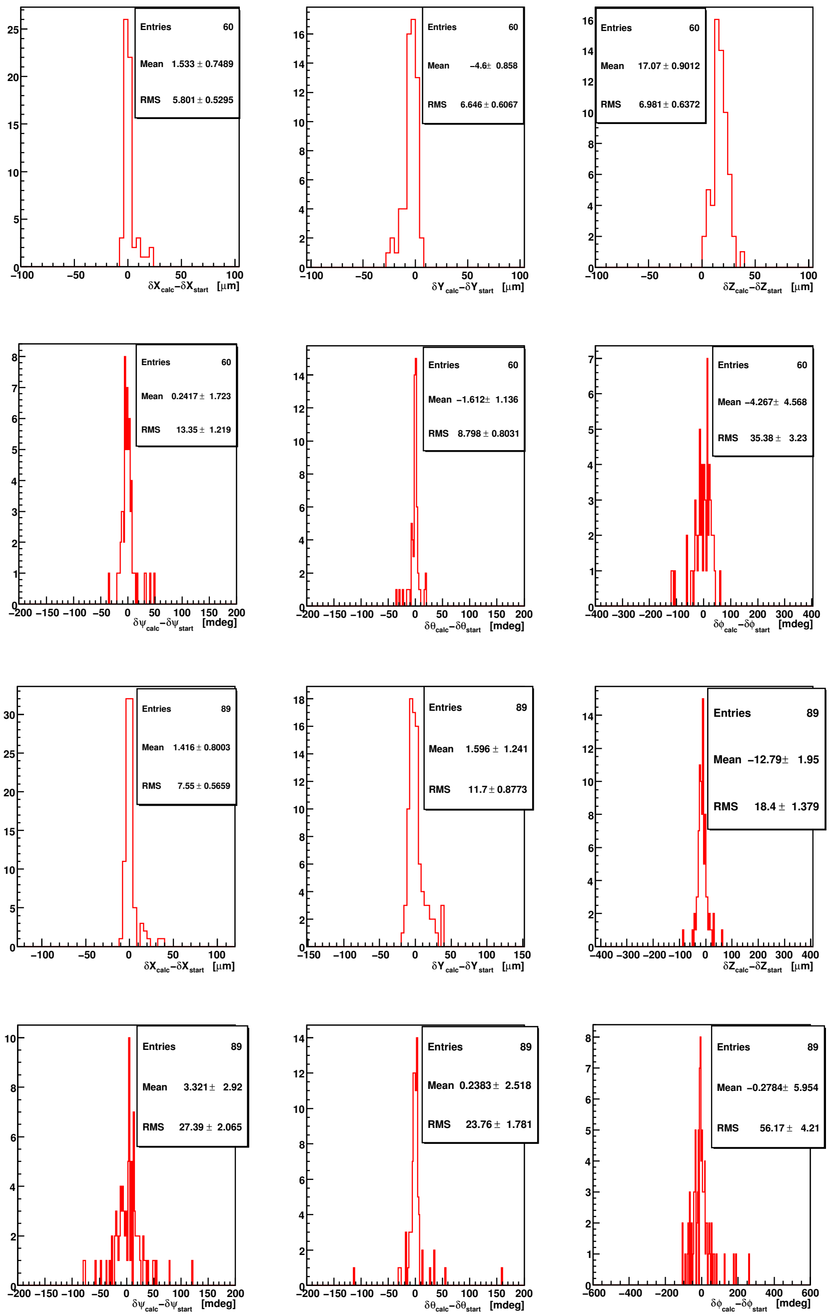

Figure 5.3: Distributions of the parameters recovered with the iterative method when the real geometry corresponds to the ideal geometry for the inner (six upper panels) and outer (six lower panels) SPD layers. See the RMS reported in Table 4.1 to get an estimate of the average points displacements corresponding to the recovered rotations parameters.

the $\delta\theta$ correction would imply an average movement of about $3-5$ μm. However it is not straightforward to get a quantitative estimate of the average displacement by, for instance,

adding the squares of the average displacements deriving from single parameters, because the recovered delta-rotations and delta-translations are in general correlated. It is possible to look at the global observable variables defined in Section 5.1.1 to get more information on the global effect of the residual misalignment. Figure 5.2, left panel, shows that there are no relevant differences between the "Up–To–Down" $\Delta xy|_{y=0}$ distribution with SPD points only before and after the "alignment".
In Fig. 5.3 the mean value of the δz significantly differs from zero. The algorithm is not sensitive to a global roto-translation of all the modules, that is, to a rototranslation of the whole ITS. This can be interpreted as a change of the global reference system and is the most trivial example of the *weak modes* mentioned in Section 4.3. The determination of the position and orientation of the whole ITS requires an external information and cannot of course be determined by aligning the modules that compose it. A global rototranslation of the whole set of aligned modules is in general always present, independently on the algorithm employed. However the global reference system can always be determined (or fixed by convention) *a posteriori*: thus, this is a harmless weak mode without any physical consequences, as confirmed by looking at the $\Delta z|_{y=0}$ distribution in Fig. 5.2 (right panel).

Tests with randomly generated misalignments

A misaligned geometry with random misalignments applied to the modules position and orientation is now considered. The displacements are generated randomly from uniform distributions chosen to have misalignments significantly larger than each sub-detector resolution, at least for the local x coordinate. The widths of the distributions are:

- SPD. local x,y: 77 μm   local z: 100 μm
- SDD. local x,y,z: 150 μm
- SSD. local x,y: 100 μm, local z: 510 μm
- SPD, SDD, SSD. All local rotations: 90 mdeg

The RMS of the distributions can be calculated by dividing the width by $\sqrt{12}$. The average points displacements corresponding to the applied rotations can be estimated as 9 times the RMS reported in Table 4.1. In Fig. 5.4 the "Up–To–Down" $\Delta xy|_{y=0}$ and $\Delta z|_{y=0}$ distributions using SPD points only are shown before and after the alignment. After the alignment, the distribution is very similar to that obtained with the ideal geometry (Fig. 5.2). The distributions of the "Inner–To–Outer" $\Delta xy|_{y=0}$ and $\Delta z|_{y=0}$ variables using SSD points only (described in Section 4.4.4) are shown in Fig. 5.5. In the $r\varphi$ (left panel) plane an improvement is clearly visible after the alignment, though the ideal result (Section 4.4.4) is not recovered. We recall that in the "Inner–To–Outer" case the variance of the $\Delta xy|_{y=0}$ distribution corresponds to the local effective sigma that accounts also for the misalignment contribution. Since the intrinsic detector resolution is ≈ 18.5 μm the residual misalignment is ≈ 31 μm, while a reference value for the initial misalignment is 62 μm. The effect of the alignment on the effective local z coordinate (Fig. 5.5, right panel) is not evident because of the relative small misalignment applied on the local z coordinate with respect to the local z intrinsic detector resolution. In Fig. 5.6, 5.7, 5.8, 5.9 the differences between the input and output alignment parameters in local coordinates are shown for the SPD1, SPD2, SDD2 and SSD1 layers. Due to the topology of the cosmic-ray tracks and to the SPD trigger the two SPD

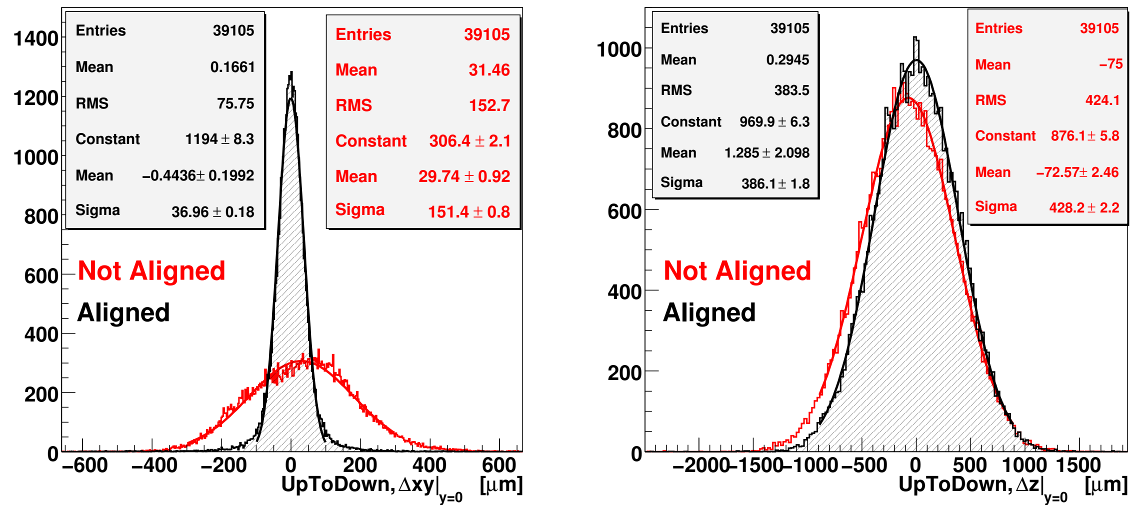

Figure 5.4: On the left: distribution of "Up–To–Down" $\Delta xy|_{y=0}$ using only SPD points from a simulated sample of about $6 \cdot 10^4$ tracks from cosmic-rays with a misaligned geometry. The modules displacements are randomly generated from uniform distributions (see text) of ~ 100 μm width (≈ 30 μm RMS). The dashed histogram is the distribution after the alignment while the thick red line is before the alignment. On the right: the same for the $\Delta z|_{y=0}$ variable.

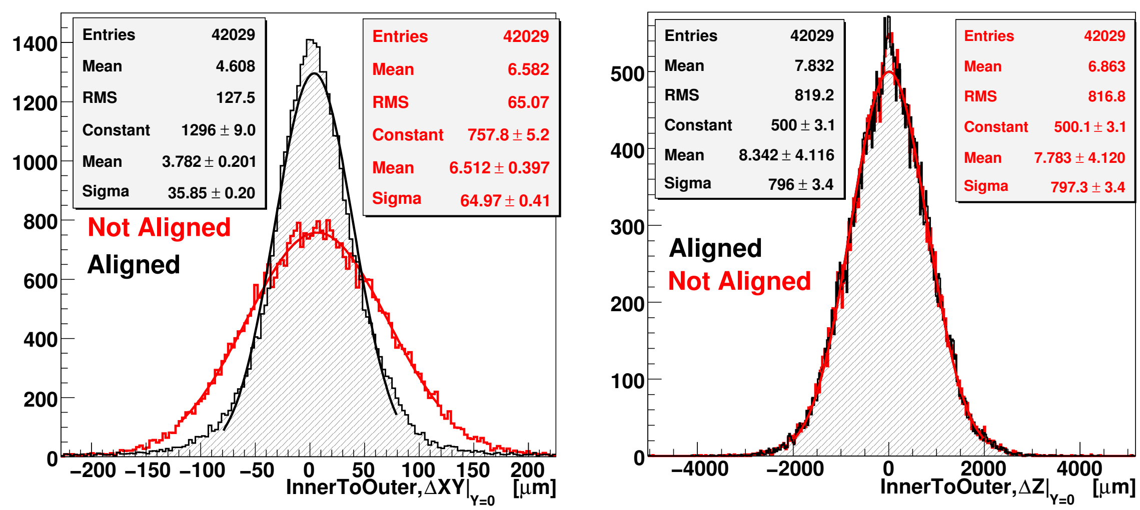

Figure 5.5: On the left: distribution of "Inner–To–Outer" $\Delta xy|_{y=0}$ using only SSD points from a simulated sample of about $6 \cdot 10^4$ tracks from cosmic-rays with a misaligned geometry. The modules displacements are randomly generated from uniform distributions (see text) of ~ 100 μm width (≈ 30 μm RMS) in $r\varphi$ and ~ 500 μm width (≈ 145 μm RMS) in local z. The dashed histogram is the distribution after the alignment while the thick red line is before the alignment. On the right: the same for the $\Delta z|_{y=0}$ variable.

layers are those better aligned while the statistics is rather poor to align the SSD at module level. As already mentioned, for tracks orthogonal to the module planes the residuals are

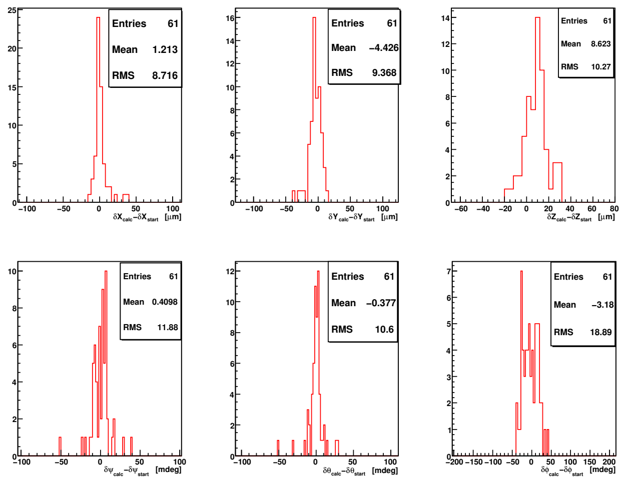

Figure 5.6: Inner SPD layer: distributions of the difference between the local parameters recovered with the iterative method and the input parameters. The modules misalignments are generated randomly from uniform distributions (see text) of $\sim 100\ \mu$m width ($\approx 30\ \mu$m RMS). See the RMS reported in Table 4.1 to get an estimate of the average points displacements corresponding to the differences observed for rotations.

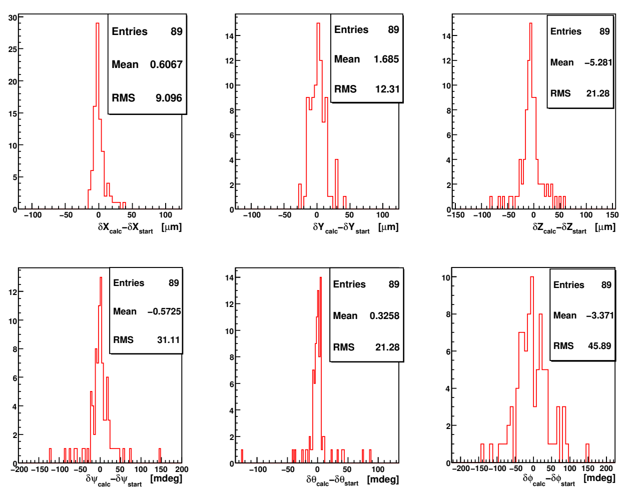

Figure 5.7: Outer SPD layer: distributions of the difference between the local parameters recovered with the iterative method and the input parameters. The modules misalignments are generated randomly from uniform distributions (see text) of $\approx 100\ \mu$m width ($\approx 30\ \mu$m RMS).

sensitive to the local x, z and $\delta\theta$ degrees of freedom. These are better recovered than the y, $\delta\psi$ and $\delta\phi$ ones especially for the outer layers. In Fig. 5.10 the correlation between the output and input local parameters is shown for the inner SPD layer. The red line corresponds to the case the parameters are exactly recovered. It is possible to see that the difference between the output and input parameters is not dependent on the magnitude of the latter, that is,

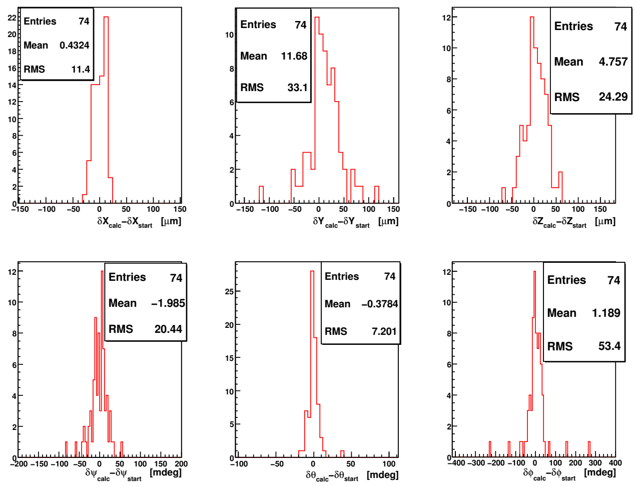

Figure 5.8: Outer SDD layer: distributions of the difference between the local parameters recovered with the iterative method and the input parameters. The modules misalignments are generated randomly from uniform distributions (see text) of $\approx 100\ \mu$m width ($\approx 30\ \mu$m RMS).

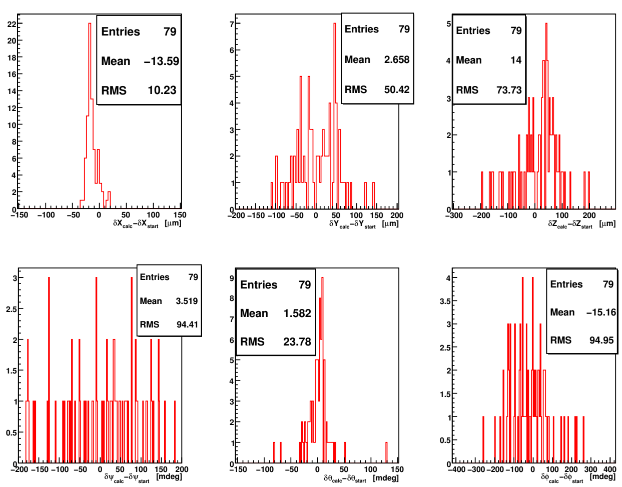

Figure 5.9: Inner SSD layer: distributions of the difference between the local parameters recovered with the iterative method and the input parameters. The modules misalignments are generated randomly from uniform distributions (see text) of $\approx 100\ \mu$m width ($\approx 30\ \mu$m RMS) in $r\varphi$ and $\approx 500\ \mu$m width ($\approx 145\ \mu$m RMS) in local z.

not dependent on the magnitude of the misalignment. In Fig. 5.11 the difference between the recovered and input local δx is shown module-by-module for the inner SPD layer. Cosmic-ray tracks have a preferential direction and the modules at $\varphi \approx \pm\pi/2$ are those with the higher statistics and, as a consequence, better results can be obtained. A couple of modules close to $\varphi \approx -\pi/2$ could not be aligned because they were switched off in the simulation to simulate

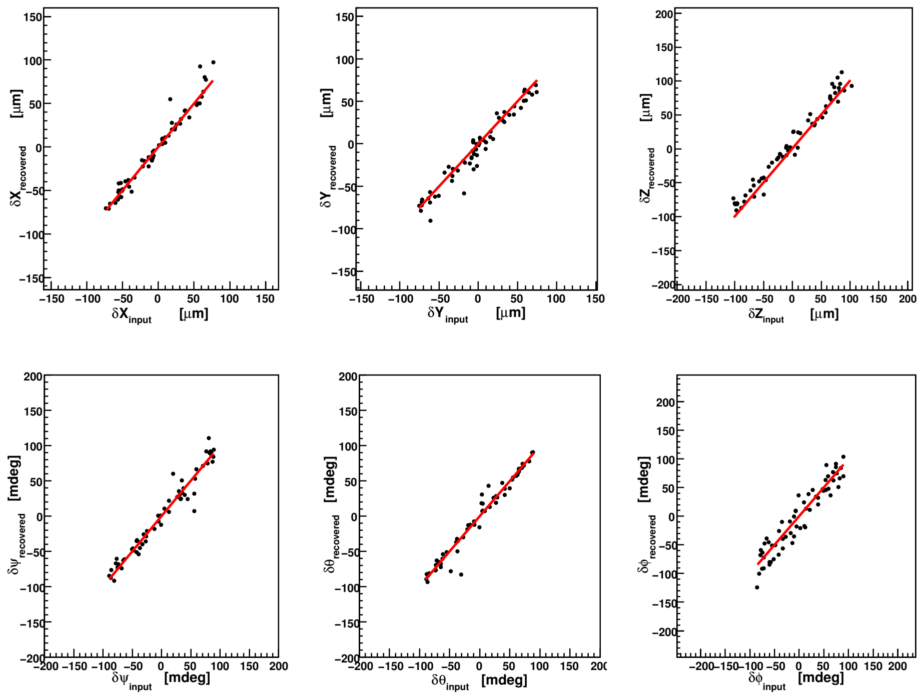

Figure 5.10: Inner SPD layer: correlation between the input misalignment parameters (horizontal axis) and the alignment parameters recovered with the iterative method (vertical axis).

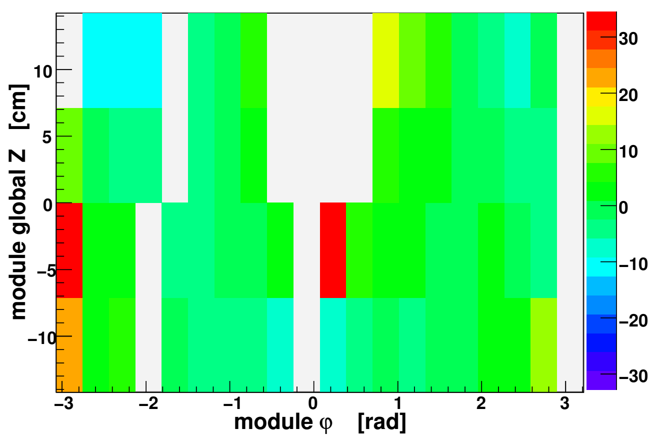

Figure 5.11: Inner SPD layer: module-by-module difference between the recovered and input local δx parameter. Each cell correspond to a module, identified by the global coordinates of the module centre. White cells correspond to modules not aligned because of the too poor statistics or because they were switched off to simulate the presence of dead–zones in the detector.

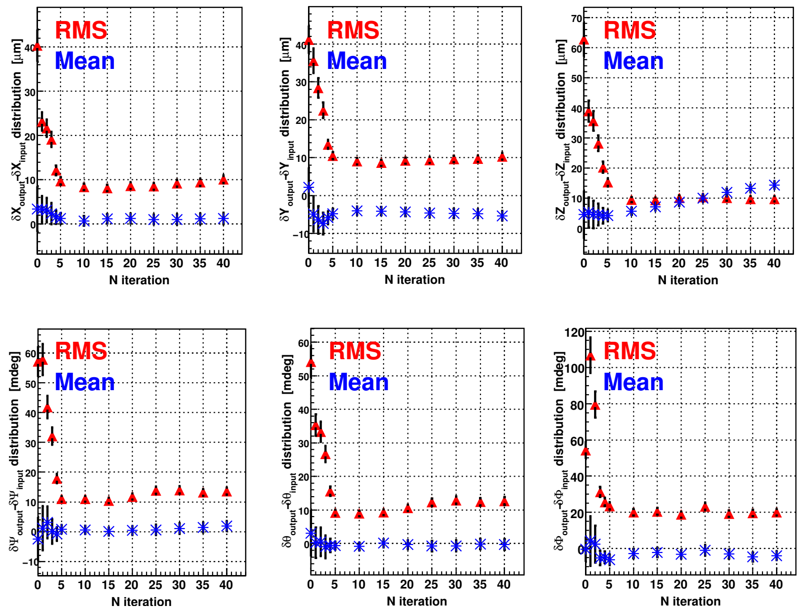

Figure 5.12: Example of the convergence of the iterative method for the inner SPD layer on simulated cosmic-muon events with randomly distributed misalignments with local translations in a range of ± 100 μm, and local rotations that give equivalent mean shifts (see text). The mean (star markers) and r.m.s. (triangle markers) of the distribution of the residuals, for all SPD modules, between the true and estimated value of the six local alignment parameters (three translations in the upper row and three rotations in the lower row) are shown.

the presence of dead-zone in the detector.

As shown in Fig. 5.12 and 5.13 acceptable results are obtained in 5 to 10 iterations for the SPD layers. For the outer layers (Fig. 5.14) more iterations might be necessary, especially to recover those degrees of freedom that have a minor effect on the residuals.

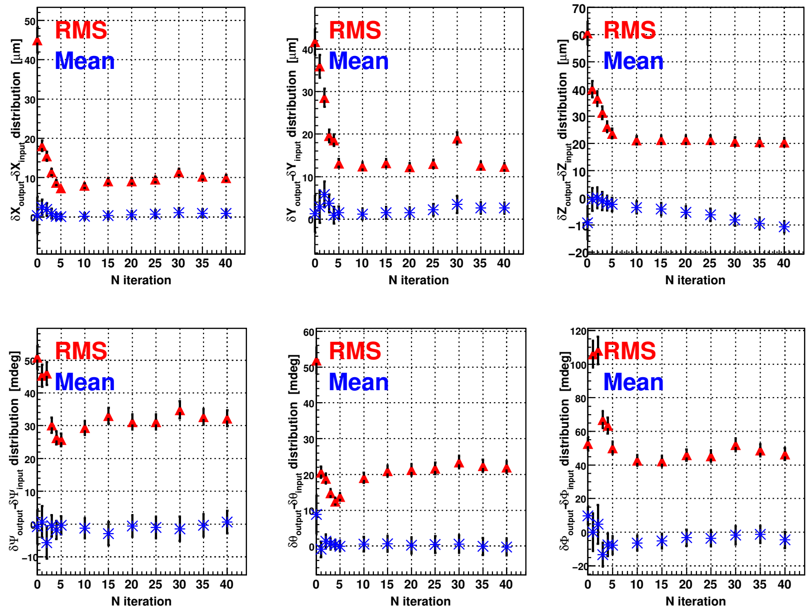

Figure 5.13: Same as for Fig. 5.12 but for the outer SPD layer.

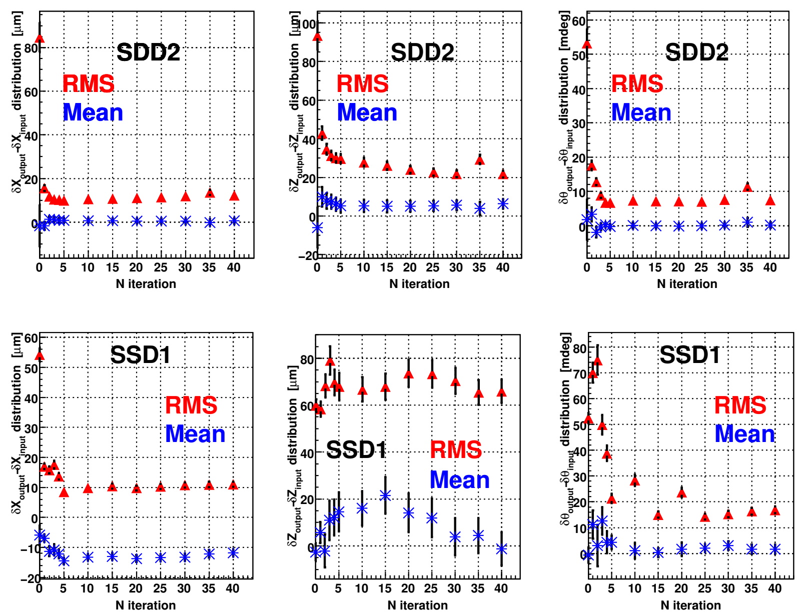

Figure 5.14: Same as for Fig. 5.12 for the outer SDD layer (upper panels) and for the inner SSD layer (lower panels). Only the most important degrees of freedom that can be recovered with cosmic-ray tracks collected with the SPD trigger (local δx, δz and $\delta\theta$), are shown.

5.3 ITS alignment with Millepede

The main algorithm used for ITS alignment is Millepede [5, 127]. This section describes the general idea behind this method and its implementation for the ITS case.

5.3.1 General principles of the Millepede algorithm

Millepede belongs to *global least squares minimization* type of algorithms and it aims at determining the set of alignment parameters by minimizing the residuals of a large amount of pre-reconstructed tracks. It assumes that the residual of a given track t to a specific point p (measured with precision σ) can be represented in a linearized form:

$$\delta_{t,p} = \vec{a} \cdot \partial\delta_{t,p}/\partial\vec{a} + \vec{\alpha}_t \cdot \partial\delta_{t,p}/\partial\vec{\alpha}_t$$

where $\vec{a}$ is the vector of the (global) parameters describing the alignment of the detector (dimension $6 \times M$, with M the number of volumes to be aligned while 6 are the degrees of freedom per module) and $\vec{\alpha}_t$ are the (local) parameters of the track. The corresponding $\chi^2 = \sum_{t,p} \delta^2_{t,p}/\sigma^2_{t,p}$ equation for n tracks with ν local parameters per track and N global parameters leads to a huge set of $N + \nu n$ normal equations. These can be written in the following partitioned matrix equation form:

$$\begin{pmatrix} \mathbf{C} & \mathbf{G}_1 & \dots & \dots & \mathbf{G}_n \\ \mathbf{G}_1^{\mathrm{T}} & \mathbf{\Gamma}_1 & 0 & \dots & 0 \\ \vdots & \vdots & \vdots & \vdots & 0 \\ \mathbf{G}_n^{\mathrm{T}} & 0 & \dots & 0 & \mathbf{\Gamma}_n \end{pmatrix} \begin{pmatrix} \vec{a} \\ \vec{\alpha}_1 \\ \vdots \\ \vec{\alpha}_n \end{pmatrix} = \begin{pmatrix} \vec{b} \\ \vec{\beta}_1 \\ \vdots \\ \vec{\beta}_n \end{pmatrix} \tag{5.9}$$

The sub-matrices $\mathbf{C}$ involve the derivatives of the residuals only over the global parameters (in the local frame of the sensor, where the covariance matrix of the points are diagonal), $\mathrm{C}_{ij} = \sum_{t,p} \sigma_p^{-2} \partial\delta_{t,p}/\partial a_i \; \partial\delta_{t,p}/\partial a_j$, $\mathbf{\Gamma}_t$ depends only on the track t parameters ($\Gamma_{t,ij} = \sum_p \sigma_p^{-2} \partial\delta_{t,p}/\partial\alpha_{t,i} \; \partial\delta_{t,p}/\partial\alpha_{t,j}$) and $\mathbf{G}_t$ is for the local parameters of the track t and the global parameters ($\mathrm{G}_{t,ij} = \sum_p \sigma_p^{-2} \partial\delta_{t,p}/\partial a_i \; \partial\delta_{t,p}/\partial\alpha_{t,j}$). Similarly, the right-hand side of Eq. (5.9) is grouped to $b_i = \sum_{t,p} \sigma_p^{-2} \delta_{t,p} \; \partial\delta_{t,p}/\partial a_i$ and $\beta_{t,i} = \sum_p \sigma_p^{-2} \delta_{t,p} \; \partial\delta_{t,p}/\partial\alpha_{t,i}$.

The idea behind the Millepede method is to consider the local $\vec{\alpha}$ parameters as nuisance parameters which are eliminated using the Banachiewicz identity [128] for partitioned matrices:

$$\left(\begin{array}{c|c} \mathbf{C}_{11} & \mathbf{C}_{12} \\ \hline \mathbf{C}_{12} & \mathbf{C}_{22} \end{array}\right)^{-1} = \left(\begin{array}{c|c} \mathbf{B} & -\mathbf{B}\mathbf{C}_{12}\mathbf{C}_{22}^{-1} \\ \hline -\mathbf{C}_{22}^{-1}\mathbf{C}_{12}^{\mathrm{T}}\mathbf{B} & \mathbf{C}_{22}^{-1} + \mathbf{C}_{22}^{-1}\mathbf{C}_{12}^{\mathrm{T}}\mathbf{B}\mathbf{C}_{12}\mathbf{C}_{22}^{-1} \end{array}\right) \tag{5.10}$$

with $\mathbf{B} = \left(\mathbf{C}_{11} - \mathbf{C}_{12}\mathbf{C}_{22}^{2}\mathbf{C}_{12}^{\mathrm{T}}\right)^{-1}$. In fact, the full matrix of all the $N + \nu n$ parameters is not built explicitly: using Eq. (5.9) the set of N normal equations for the global parameters is constructed by subtracting from $\mathbf{C}$ and $\vec{b}$ the contributions related to the local parameters. If needed, linear constraints on the global parameters can be added using the Lagrange multipliers. Historically, two versions, Millepede and Millepede II, were released. The first one, written in Fortran, was performing the calculation of the residuals, the derivatives and the final matrix elements as well as the extraction of the exact solution in one single step, keeping all necessary information in computer memory. The large memory and CPU time needed to extract the exact solution of a $N \times N$ matrix equation effectively limited its use to $N < 10,000$ global (alignment) parameters. This limitation was removed in the second

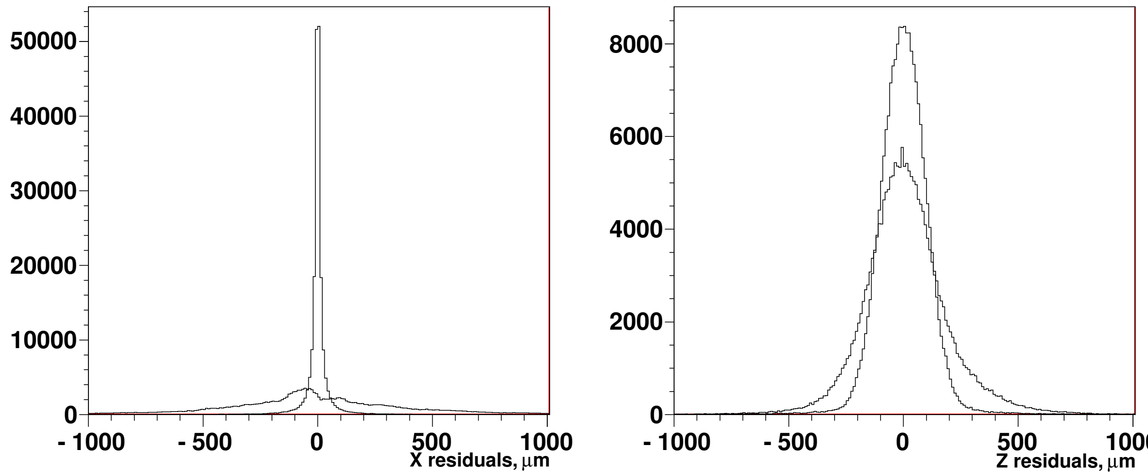

Figure 5.15: Example of Millepede residuals in the local reference frame of the SPD modules before and after the alignment.

version, Millepede II. Software-wise the algorithm is split in two parts: the first one (available in C and Fortran) stores in an intermediate file the residuals, derivatives and constraints provided by the user, while the second one (in Fortran) processes these data, builds the necessary matrices (optionally in sparse format, to save memory space) and solves them using advanced iterative methods, much faster and robust than the exact methods.

5.3.2 Millepede for the ALICE ITS

Following the development of Millepede, ALICE had its own implementation of both versions, hereafter indicated as MP and MPII, within the AliRoot framework [103, 7]. All the results shown in this chapter are obtained with MPII. The track-to-point residuals, used to construct the global χ^2, are calculated using the same tracks models described in Section 5.2.2 for the iterative method.

Special attention was paid to the possibility to account for the complex hierarchy of the alignable volumes of the ITS, shown in Fig. 3.4, in general leading to better description of the material budget distribution after alignment. This is achieved by defining explicit parent–daughter relationships between the volumes corresponding to mechanical degrees of freedom in the ITS. The alignment is performed simultaneously for the volumes on all levels of the hierarchy, e.g. for the SPD the corrections are obtained in a single step for the sectors, the half-staves within the sectors and the modules within the half-staves. Obviously, this leads to a degeneracy of the possible solutions, which should be removed by an appropriate set of constraints. The possibility to constrain either the mean or the median of the corrections for the daughter volumes of any parent volume has been implemented. The relative movement δ of volumes for which the survey data is available (e.g. SDD and SSD modules) can be restricted to be within the declared survey precision σ_{survey} by adding a set of gaussian constraints $\delta^2/\sigma^2_{\text{survey}}$ to the global χ^2.

A few example figures to illustrate the bare output results from Millepede II for the alignment of the SPD detector (in this case) are reported here, while the analysis of the alignment quality is presented in the next section. Figure 5.15 shows an example of the

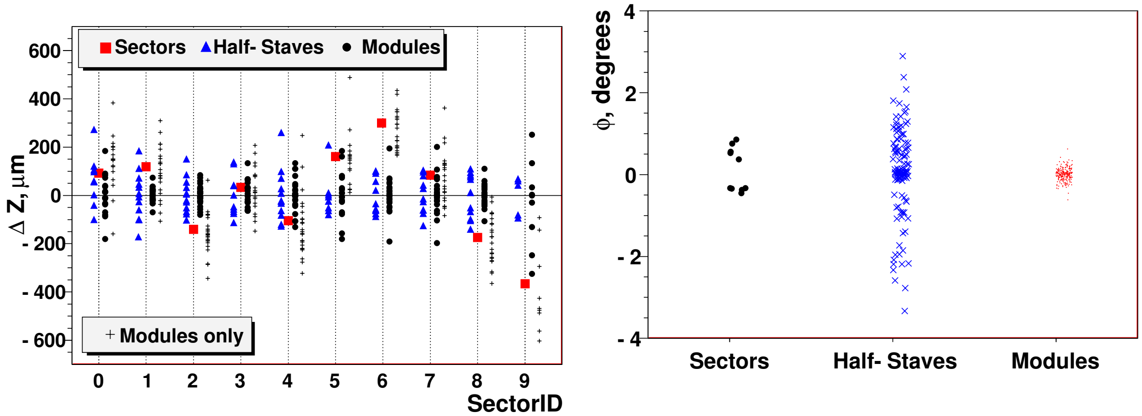

Figure 5.16: (colour online) Example of hierarchical SPD alignment. Left: corrections for the z coordinate of the SPD volumes as a function of the sector number. Crosses: results from the alignment with all misalignments attributed to the module degrees of freedom. Hierarchical alignment resolves the corrections in contributions from sectors (squares), half-staves (triangles) and module (circles) misalignments. Right: corrections to the φ_{loc} angle obtained in the hierarchical alignment.

residuals in SPD (in the local reference frame of the modules) before and after alignment. Figure 5.16 (left) shows an example of the corrections obtained for the local z coordinate of the alignable volumes in SPD: the corrections are distributed among the different levels of hierarchy (sectors, half-staves, modules). For comparison, the cross markers show the result of the non-hierarchical alignment —modules only (smallest alignable volumes) are aligned. Figure 5.16 (right) shows, instead, the obtained corrections for the φ_{loc} angle (rotation of the volume with respect to its z_{loc} axis), indicating that the largest misalignments are at the level of the half-staves with respect to the carbon fiber support sectors.

5.4 Alignment results with 2008 cosmic-ray data

In this section the main results achieved with the two algorithms presented in this chapter using tracks from cosmic-ray events collected in 2008 (Section 3.7.1) are shown.

5.4.1 Results on alignment quality with the Millepede algorithm

The SPD detector was first aligned using about 5×10^4 cosmic-ray tracks, with two points in the inner layer and two points in the outer layer, collected in 2008 with the magnetic field switched off. As described in the previous section, the hierarchical alignment procedure consisted in (cfr. Fig. 3.4): aligning the ten sectors with respect to each other, the twelve half-staves of each sector with respect to sector and two modules of each half-stave with respect to half-stave.

Figure 5.17 (left) shows the distribution of $\Delta xy|_{y=0}$ at the successive steps of the hierarchical SPD alignment, from the uncorrected data to the final step with the corrections for sectors, half-staves and modules applied. The two track segments are required to have a point in each of the SPD layers and to pass, in the transverse plane, within 1 cm from the origin (see Section 5.1.1). The figure indicates that the main alignment improvement

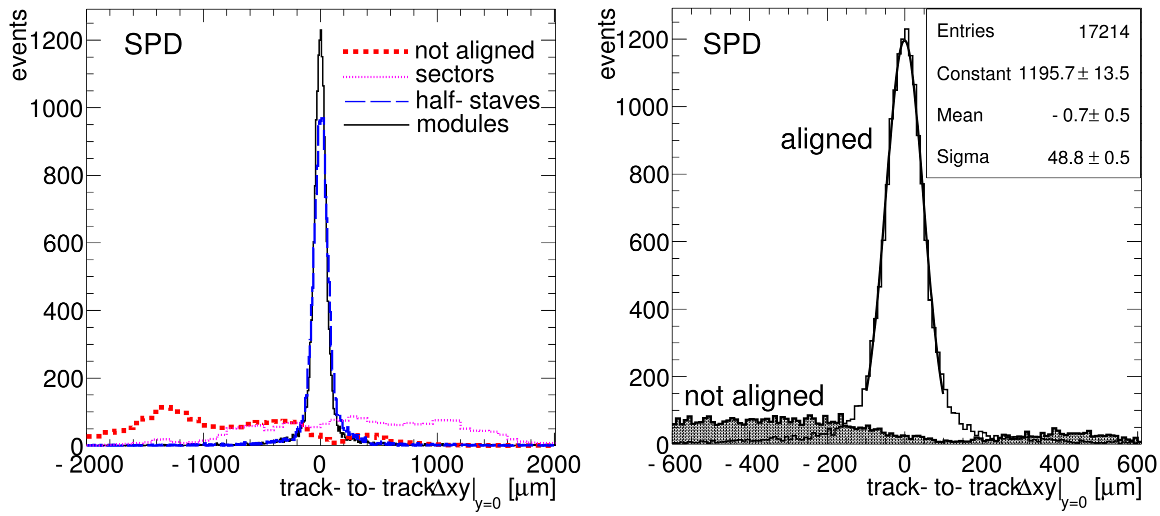

Figure 5.17: (colour online) Left: distribution of $\Delta xy|_{y=0}$ in the successive hierarchical steps used for the SPD alignment. Right: fit of the $\Delta xy|_{y=0}$ distribution for the final step.

is obtained when applying the corrections at the level of the half-staves, as also shown by Fig. 5.16 (right). A gaussian fit to the final distribution in the range $[-100\ \mu\text{m}, +100\ \mu\text{m}]$, shown in Fig. 5.17 (right), gives a centroid compatible with zero and a spread $\sigma \approx 50\ \mu$m. For comparison, a spread of 38 μm is obtained from a Monte Carlo simulation, with the ideal geometry of the ITS (without misalignment), of comic-muons generated according to the momentum spectrum measured by the ALICE TPC in cosmic runs with magnetic field on. Using the fit result, $\sigma_{\Delta xy|_{y=0}} \approx 50\ \mu$m, obtained in the central region $[-100\ \mu\text{m}, +100\ \mu\text{m}]$, the value $\sigma_{\text{spatial}} \approx 14\ \mu$m is estimated, not far from the intrinsic resolution of about 11 μm extracted from simulations. However, a precise estimation of the effective spatial resolution with this method requires the measurement of the track momentum, to account properly for the multiple scattering contribution. The statistics collected in 2008 with magnetic field on did not allow a momentum-differential analysis.

The next step in the alignment procedure is the inclusion of the SSD detector. As shown in section 4.4, the survey measurements already provide a very precise alignment, with residual misalignment levels of the order of less than 5 μm for modules on the ladder and of about 20 μm for ladders. Because of the limited available statistics ($\approx 2\times10^4$ tracks with four points in SPD and four points in SSD), the expected level of alignment obtained with Millepede on single SSD modules is significantly worse than the level reached with the survey measurements. For this reason, Millepede was used only to align the whole SPD barrel with respect to the SSD barrel and to optimize the positioning of large sets of SSD modules, namely the upper and lower halves of layers 5 and 6. For this last step, the improvement on the global positioning of the SSD layers was verified by comparing the position and direction of the pairs of SSD-only track segments built in both the “Up–To–Down” and “Inner–To–Outer” configuration. As reported in Table 5.1, all mean values are compatible with zero after the alignment. These must be considered only as preliminary results: further studies are needed to understand whether the recovered alignment parameters describe physical displacements or are just the best “average” to minimize misalignments which are indeed at ladder level.

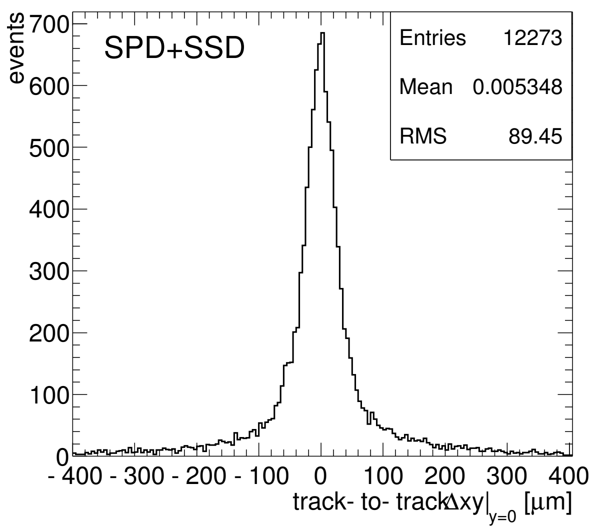

Figure 5.18: Distribution of the distance in the transverse plane ($\Delta xy|_{y=0}$) for track segments reconstructed in the upper and lower parts of SPD+SSD layers. SSD survey and Millepede alignment corrections are applied.

Figure 5.18 shows the distribution of $\Delta xy|_{y=0}$ for pairs of track segments, each reconstructed with two points in SPD and two in SSD, i.e. the merged cosmic-ray track has eight points in SPD+SSD. It can be seen that, when the SSD survey and the Millepede alignment are applied, the distribution is centred at zero and very narrow (FWHM $\approx$ 60 μm), but it shows non-gaussian tails, most likely due to multiple scattering. A more precise alignment of the SSD using tracks will be performed with the cosmic-ray and proton–proton data.

In Fig. 5.19 (left), the track-to-point distance $\Delta x_{\rm loc}$ for the SPD "extra" points in the transverse plane, before and after the Millepede alignment is shown. The extra points are not used in the alignment procedure. The spread of the distribution is $\sigma \approx 18$ μm, to be compared to $\sigma \approx 15$ μm from a Monte Carlo simulation with ideal geometry. An analysis of the $\Delta x_{\rm loc}$ distance as a function of the α incidence angle has been performed: five windows on the sum ($\alpha_1 + \alpha_2$) of the incidence angles on the two overlapping modules have been considered. These cuts sample increasing ranges of incidence angles from 0° to 50°. Figure 5.19 (right) shows the spread of the $\Delta x_{\rm loc}$ distribution for the different incidence angle selections: a clear dependence of the spread (hence of the spatial resolution) on the incidence angle can be seen.

Table 5.1: Mean values of the distributions of the linear ($\Delta xy|_{y=0}$) and angular ($\Delta\varphi|_{y=0}$) SSD track-to-track distances in the transverse plane for the Top–To–Down and Inner–To–Outer configurations, before and after Millepede alignment. The survey corrections are always applied.

Configuration	Variable	Mean before alignment	Mean after alignment
top–to–down	$\Delta xy\|_{y=0}$ [μm]	120±7	-5±6
top–to–down	$\Delta\varphi\|_{y=0}$ [mdeg]	4±1	-1±1
inner–to–outer	$\Delta xy\|_{y=0}$ [μm]	-1.8±0.6	0.5±0.6
inner–to–outer	$\Delta\varphi\|_{y=0}$ [mdeg]	-1±0.1	0.0±0.1

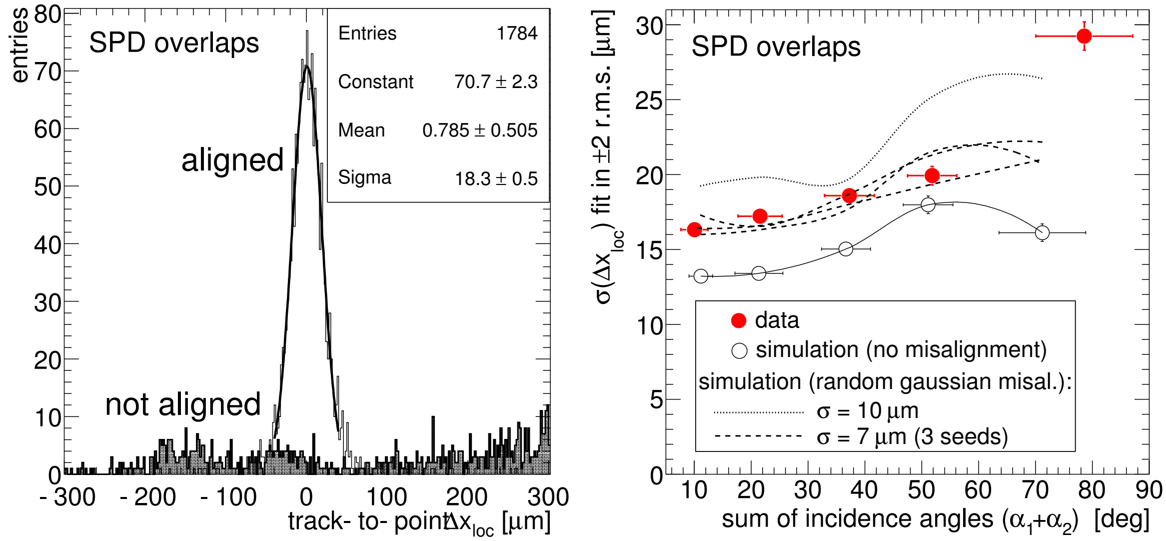

Figure 5.19: SPD double points in acceptance overlaps. Left: track-to-point $\Delta x_{\rm loc}$ for "extra" points before and after alignment. Right: σ of the $\Delta x_{\rm loc}$ distributions as a function of the track-to-module incidence angle selection; 2008 cosmic-ray data are compared to the simulation with different levels of residual misalignment. See text for details.

This dependence was already observed in SPD test-beam measurements [129, 130], which were used to tune the detector response implementation in the AliRoot software. In the same figure, Monte Carlo simulation results are reported for comparison: simulation with ideal geometry (open circles) and with a misaligned geometry obtained using a random gaussian residual misalignment (dashed lines: misalignments with $\sigma = 7$ μm and three different seeds; dotted line: misalignments with $\sigma = 10$ μm). The 2008 data are well described by the simulation with a random residual misalignment with $\sigma \approx 7$ μm, a value compatible with the alignment target defined in Sect 4.3. However, this conclusions is based on the assumption that the intrinsic resolution is the same in the real detector and in the simulation. Since the intrinsic resolution can slightly vary depending on the working conditions of the detector (e.g. the settings used for the bias voltage and for the threshold), the value of 7 μm for the residual misalignment should be taken only as an indication. Furthermore, this is an equivalent random misalignment, while the real misalignments are likely non-gaussian and to some extent correlated among different modules.

The robustness and the stability of the obtained results have also been studied. First, the data sample has been divided in two parts, one ("even" tracks) used to align the SPD and the other ("odd" tracks) to check the alignment quality. The corresponding $\Delta xy|_{y=0}$ distribution is presented in the left-hand panel of Fig. 5.20: the distribution is centred at zero and has the same $\sigma \approx 50$ μm as in the case of aligning with all tracks. In the right-hand panel of the same figure, Fig. 5.20, we address the stability in time of the alignment results by plotting the $\Delta xy|_{y=0}$ distribution for three subsamples roughly corresponding to July 08, August 08, and September-October 08. The full statistics was used to obtain the alignment. The alignment quality was stable in time during the whole 2008 run.

Finally, the data with the 0.5 T magnetic field switched-on have been used (a few thousand

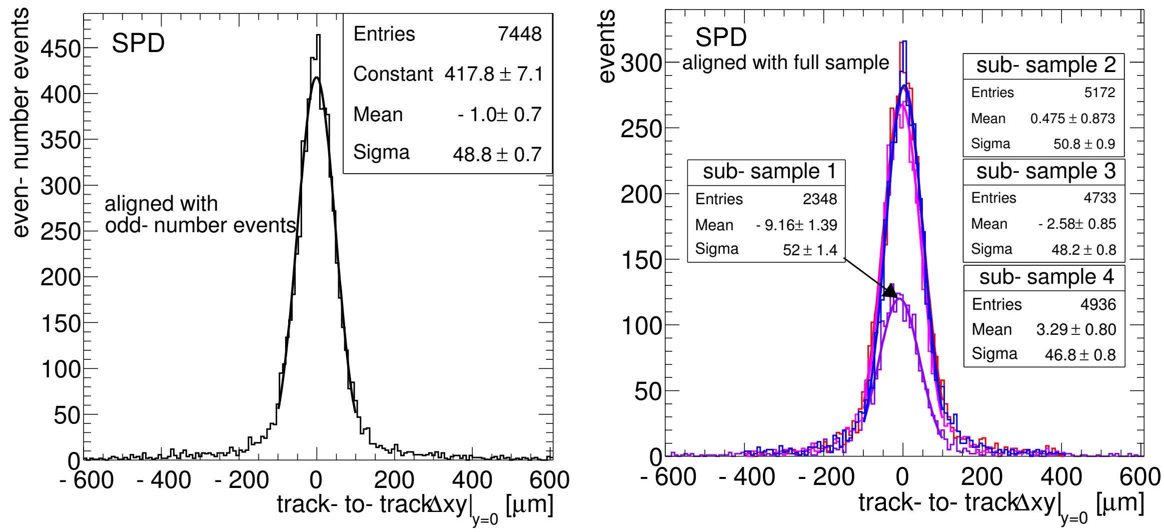

Figure 5.20: SPD alignment stability tests. Left: distribution of the $\Delta xy|_{y=0}$ distance obtained when aligning with every second track and checking the alignment with the other tracks. Right: $\Delta xy|_{y=0}$ distribution for three successive subsamples collected in 2008 (July, August, September-October).

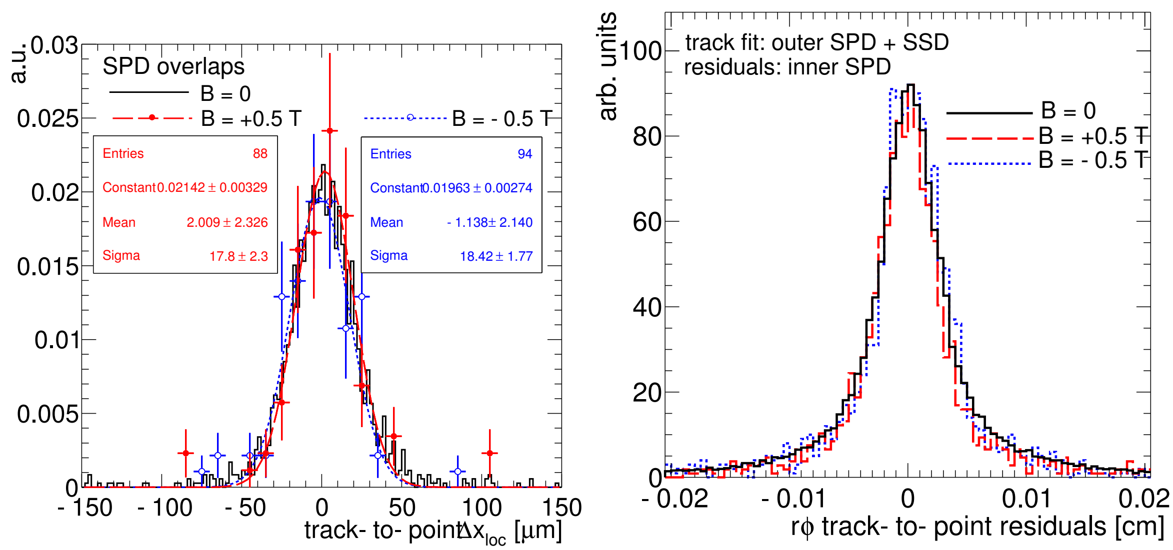

Figure 5.21: (colour online) Alignment validation checks with magnetic field switched on. Left: track-to-point distance for extra points in SPD acceptance overlaps. Right: track-to-point residuals in the inner SPD layer (track fit in outer SPD layer and in the two SSD layers).

events collected at the end of the 2008 cosmic run) to perform dedicated checks to evaluate a possible effect of the field on the alignment. The alignment correction extracted from data with B = 0 has been applied to data with B = ±0.5 T. In the left-hand panel of Fig. 5.21

the track-to-point distance for extra points in SPD acceptance overlaps is reported for B = 0, +0.5 T and −0.5 T data. The fitted widths of the distributions with field on and field off (Fig. 5.19, left) are compatible. Also the track-to-point residuals have been checked, calculated by fitting the tracks in the SSD layers and the outer SPD layer and evaluating the residuals in the inner SPD layer. In Fig. 5.21 (right) the comparison between the residuals without magnetic field, with +0.5 T and with −0.5 T is shown. Also in this case the distributions without field and with the two field polarities are compatible.

5.4.2 SDD minimum drift-time calibration and prospects for SDD inclusion in the Millepede procedure

The alignment of SDD detectors for the $x_{\rm loc}$ coordinate (reconstructed from the drift time) is complicated by the interplay between the geometrical misalignment and the calibration of drift speed and t_0 (defined in section 3.2.2). The t_0 parameter accounts for the delays between the time when a particle crosses the detector and the time when the front-end chips receive the trigger signal. Two methods have been developed in order to obtain a first estimate of the t_0 parameter. The first and simpler method consists in extracting the t_0 from the minimum measured drift time on a large statistics of reconstructed SDD points. In practice, the distribution of measured drift times is built and the sharp rising part of the distribution at small drift times is fitted with an error function. The t_0 value is then calculated from the fit parameters. The second method measures the t_0 from the residual distributions along the drift direction ($x_{\rm loc}$) between tracks fitted in SPD and SSD layers and the corresponding points reconstructed in the SDD. These distributions, in case of mis-calibrated t_0, show two opposite-signed peaks corresponding to the two separated drift regions of each SDD module where electrons move in opposite directions (see Fig. 3.6, right). The t_0 can be calculated from the distance of the two peaks and the drift speed. This second procedure has the advantage of requiring smaller statistics because it profits from all the reconstructed tracks, with the drawback of relying on SDD calibration parameters (the drift speed and possibly the correction maps). moreover, being based on track reconstruction, it might be biased by SPD and/or SSD misalignments.

Depending on the available statistics, the t_0 determination with these two methods can be done at the level of SDD barrel, SDD ladders or SDD modules. The t_0 parameter needs actually to be calibrated individually for each of the 260 SDD modules, because of differences in the overall length of the cables connecting the DAQ cards and the front-end electronics. In particular, a significant difference is expected between modules of A ($z > 0$) and C sides ($z < 0$), due to the ≈6 m difference in the length of the optical fibres connecting the ITS ladders to the DAQ cards. With the first 2000 tracks, it is possible to determine the t_0 from track-to-point residuals for 4 sub-samples of modules, i.e. separating sensors connected to sides A and C of layers 3 and 4. An example of residual distributions for the left and right drift sides of the modules of layer 4 side C is shown in Fig. 5.22. The Millepede alignment corrections for SPD and SSD are applied in this case, and it has been checked that, if they are not applied, the centroid positions in this figure are not affected significantly, while the spread of the distributions increases, as it could be expected. A difference of ≈35 ns between sides A and C of each SDD layer has been observed, in agreement with the ≈6 m difference in fibre lengths (the propagation time of light in optical fibres is 4.89 ns/m). With larger statistics (≈ 35,000 tracks), it is possible to extract the t_0 for each half-ladder, which requires building 36(ladders)×2(A/C sides) pairs of histograms like the ones shown in Fig. 5.22. Since

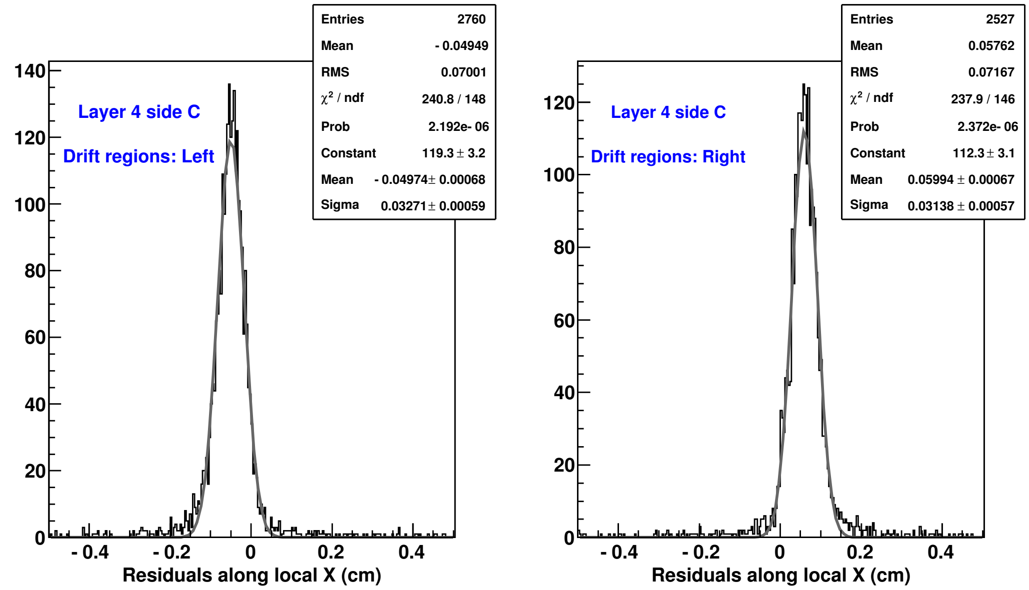

Figure 5.22: Distribution of track-to-point residuals in the two drift regions for the SDD modules of layer 4 side C ($z < 0$).

the spread on optical fibres length among half-ladders connected to the same (A or C) side is ≈ 1.5 m, the effect on the half-ladder t_0 is expected to be below 7 ns. This fact, however, could not be verified with the cosmic data collected in 2008, because only few ladders (the ones close to the vertical) were illuminated enough to allow the t_0 determination. A systematic difference on the t_0 is finally expected among modules connected to the same ladder, due to the different length of the cables connecting the front-end chips with the electronic boards located at the end of the ladder. The maximal difference amounts to ≈ 15 cm on layer 3 and 22 on layer 4, corresponding to less than 1 ns effect on t_0. It should be noted that given the ≈ 6.5 μm/ns of drift speed, a bias of 1 ns on the t_0 can lead to a significant effect on the reconstructed position along the drift coordinate $x_{\rm loc}$.

After a first calibration with these methods, a refinement of the t_0 determination is obtained by running the Millepede minimization with the t_0 as a free global parameter for each of the 260 SDD modules. Similarly, the drift speed is considered as a free parameter for those SDD modules with mal-functioning injectors. This allows to assess at the same time geometrical alignment and calibration parameters of the SDD detectors. An example is shown for a specific SDD module in Fig 5.23, where the $x_{\rm loc}$ residuals along the drift direction are shown as a function of $x_{\rm loc}$. In the left panel, the result obtained using only the geometrical rotations and translations as free parameters in the Millepede minimization is shown. The clear systematic shift between the two drift regions ($x_{\rm loc} < 0$ and $x_{\rm loc} > 0$) is due to both mis-calibrated t_0 and biased drift speed (this is a module with non-working injectors). In the right panel, where the residuals with geometry and calibration parameters fitted by Millepede are shown, these systematic effects are no longer present. It should be pointed out that the width of the SDD residual distributions shown in Figs. 5.22 and 5.23 does not correspond to the expected resolution on SDD points along drift coordinate because of the jitter between the time when the muon crosses the detectors and the asynchronous SPD FastOR trigger, which has a readout time of 100 ns.

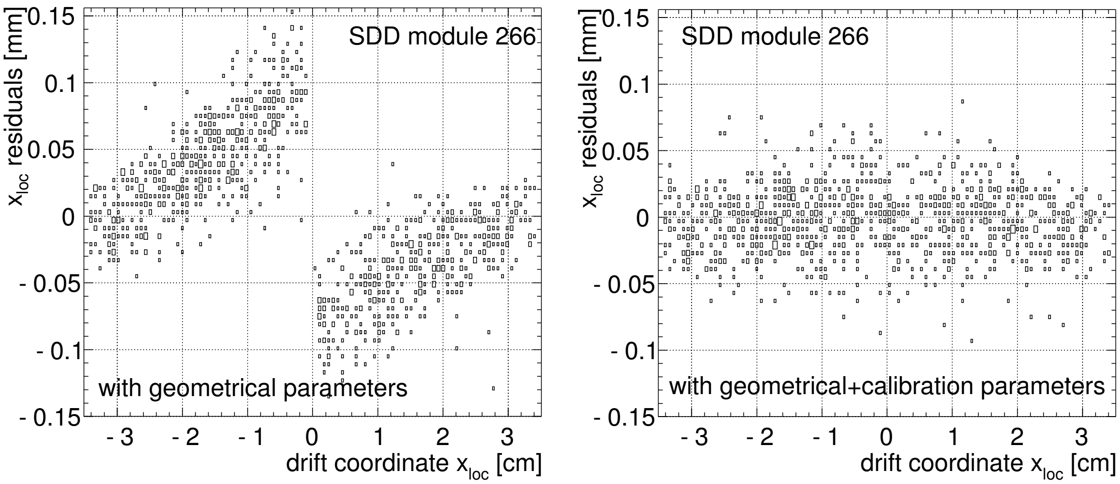

Figure 5.23: Residuals along the drift coordinate for one SDD module as a function of drift coordinate after Millepede re-alignment with only geometrical parameters (left) and with geometrical+calibration parameters (right).

5.5 SPD alignment with the iterative method

For the ITS alignment using the 2008 cosmic-ray data, only the SPD modules have been aligned using the iterative method because the statistics collected was too poor to align the SSD at module or ladder level and the SDD detector needed to be calibrated first.

As for Millepede, a "hierarchical" approach was adopted. Given the excellent precision of the SSD survey measurements, the SSD layers have been used as a reference. The SPD is aligned following this sequence:

1. Whole SPD barrel with respect to the SSD (using only SSD points in the fit of the tracks).
2. The two SPD half-barrels with respect to the SSD.
3. The SPD sectors with respect to the SSD.
4. The SPD modules with respect to the SSD.
5. The SPD sensor modules using both SPD and SSD points in the fit the tracks.

The top–bottom track-to-track $\Delta xy|_{y=0}$ distribution obtained using only the SPD points for the raw data and after steps 3, 4 and 5 is shown in Fig. 5.24. Figure 5.25, left-hand panel, shows the same distribution when only the SPD modules tagged as "aligned" by the algorithm are used. In the (right-hand panel) the track-to-point Δx_{loc} for the double points in acceptance overlaps is shown after alignment. Both distributions are compatible (mean and sigma from a gaussian fit) with the corresponding distributions after Millepede alignment. Thus we concluded that the iterative module-by-module approach can be used for a cross-check with the Millepede algorithm, in order to further confirm the Millepede results and, since the two methods are in many aspects independent, to check the presence of possible systematic trends in the extracted alignment parameters. To further confirm the reliability of

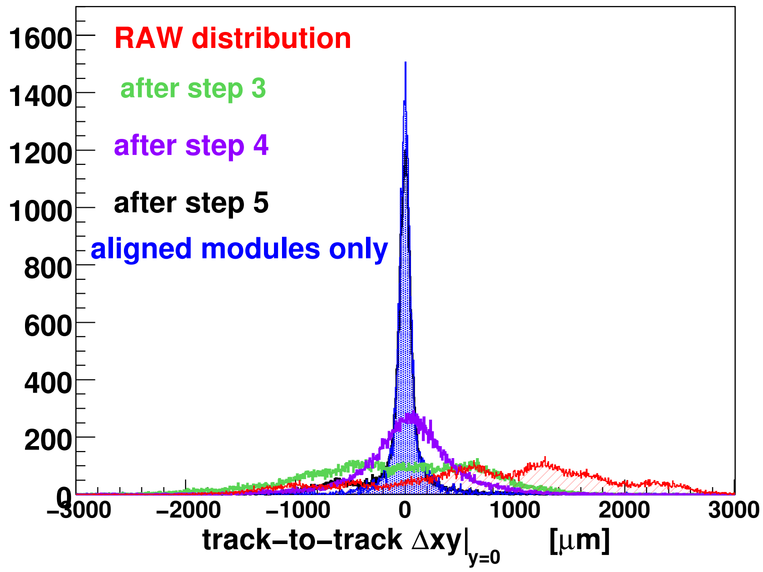

Figure 5.24: Track-to-track $\Delta xy|_{y=0}$ distribution defined in section 5.4.1 using only SPD points after the "hierarchy" steps defined in the text. For the blue distribution only the modules tagged as aligned by the algorithm are employed: the obtained distribution is scaled to get the same integral of the others.

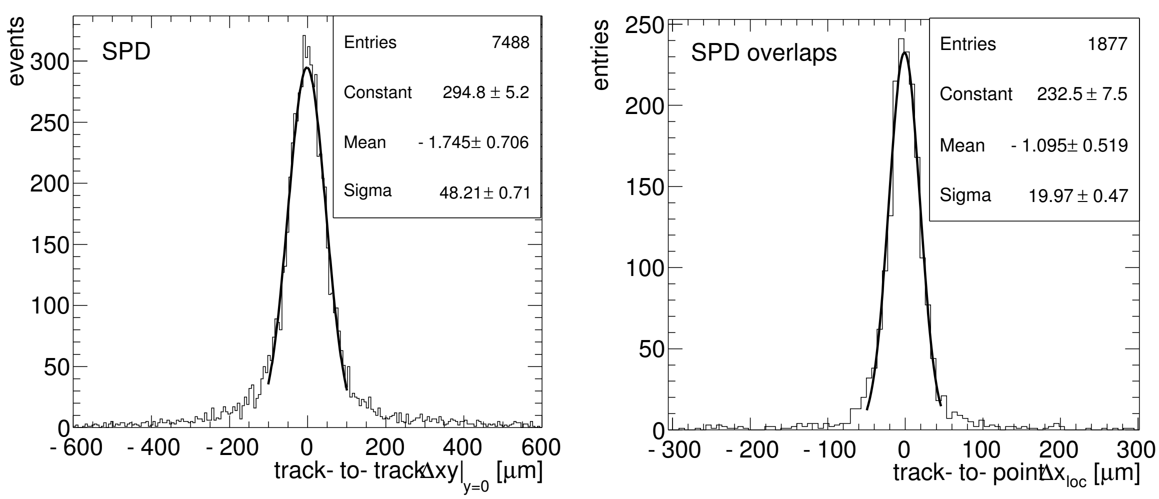

Figure 5.25: SPD alignment quality results for the iterative local method. Left: track-to-track $\Delta xy|_{y=0}$ distribution defined in section 5.4.1 using only SPD points. Right: track-to-point Δx_{loc} distribution for extra points in acceptance overlaps.

the iterative method we checked that if the parameters obtained from the analysis of cosmic-ray data are used to misalign the ideal geometry they are recovered by repeating the same alignment procedure on a sample of simulated cosmic-ray events. In Fig. 5.26 the correlation

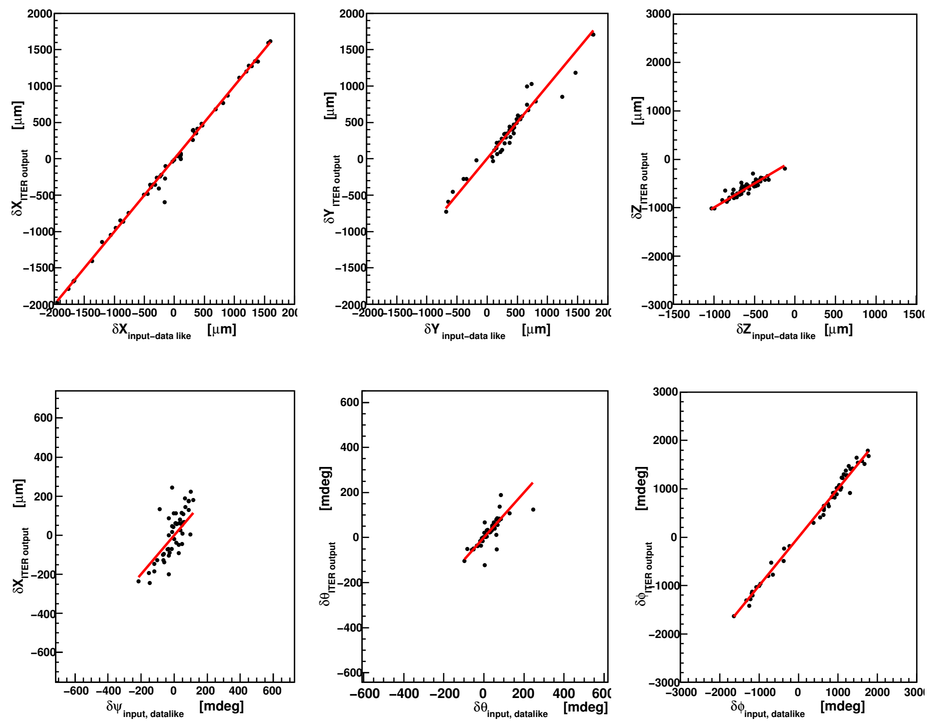

Figure 5.26: Simulated data, inner SPD layer: correlation between the input misalignment parameters (horizontal axis) and the alignment parameters recovered with the iterative method (vertical axis). The parameters obtained from the analysis of 2008 cosmic-ray run data are used to misalign the geometry.

between the input and recovered parameter in global coordinates is shown for the inner SPD layer. A correction was applied to account for a possible global roto-translation of the whole ITS, which, as explained in Section 5.2.4 does not affect the quality of the alignment.

5.5.1 Comparison with the results obtained with the Millepede algorithm

In Fig. 5.27 and 5.29 the values of the parameters recovered with the iterative method are plotted as a function of those recovered with Millepede for the inner and outer SPD layer respectively. A correction was applied to account for a possible global roto-translation of the whole ITS, which does not affect the quality of the alignment and can be different for the two methods. Most of the modules are clustered along the diagonal lines, that correspond to the situation in which the parameters from the two methods are exactly the same. There are some outlier modules, that are far from the ideal result. However, the plots of the difference between the two parameter values as a function of the statistics on the module (Fig. 5.28) show that the outliers mostly correspond to modules with low statistics (sides of the SPD barrel). Tracks from collisions will be needed to check whether this is only a statistical effect or is due to a possible negative feature of the iterative method: as mentioned in Section 5.2, the influence of the misalignment of the modules where the tracks are fitted is not directly taken into account in the algorithm to minimize the results for a given module, thus the modules

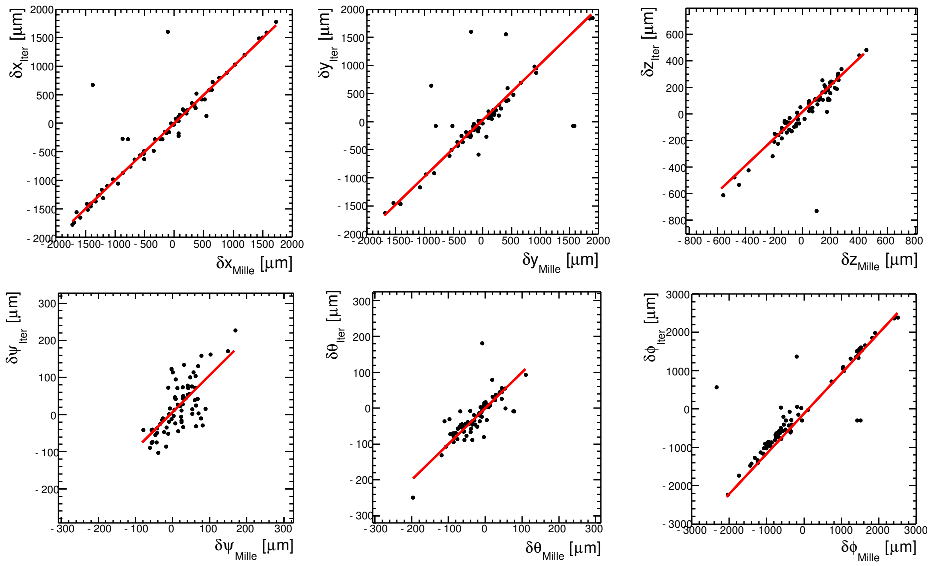

Figure 5.27: Correlation between the alignment parameters obtained from Millepede (vertical axis) and the iterative method (horizontal axis), for the inner SPD layer modules.

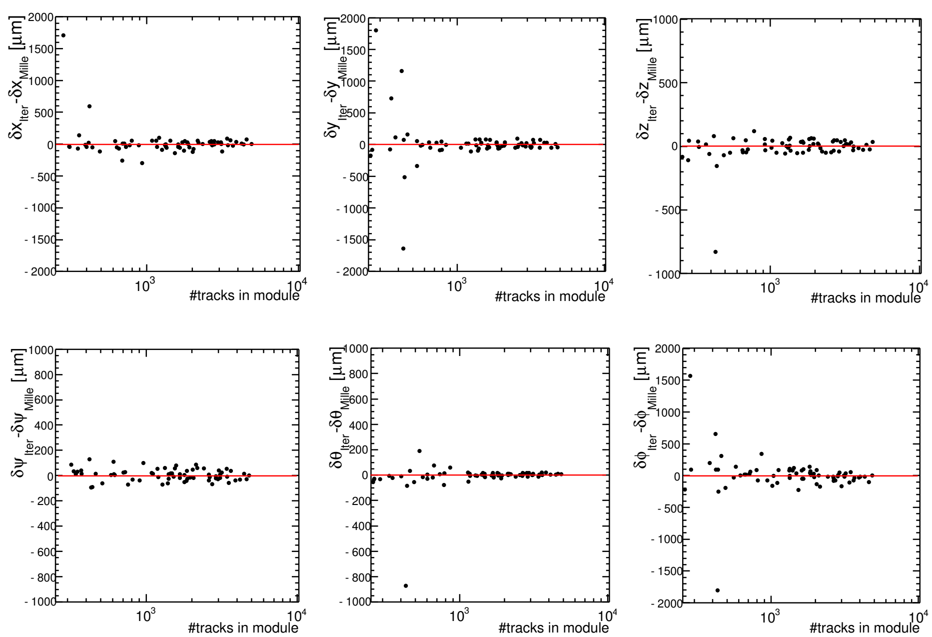

Figure 5.28: Difference between the alignment parameters obtained from Millepede and the iterative method, for the inner SPD layer modules, as a function of the points statistics on the module.

with the highest statistics can "drive" the results of the modules with a poorer statistics. To reduce this effect the tracks used for the fits are sampled by setting a limit on the number of

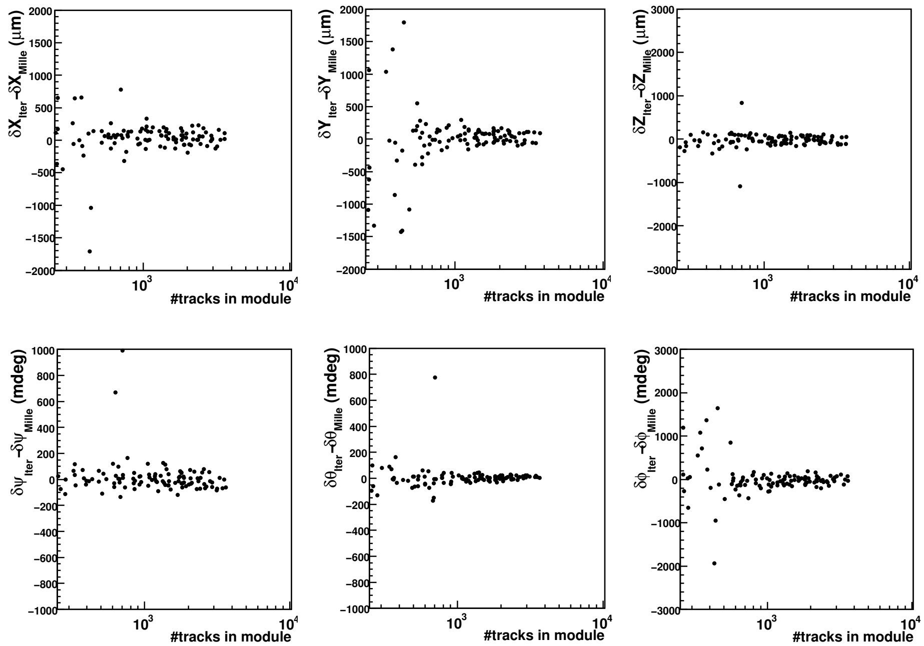

Figure 5.29: Difference between the alignment parameters obtained from Millepede and the iterative method, for the outer SPD layer modules, as a function of the points statistics on the module.

tracks passing through each modules. The Millipede algorithm, minimizing all the alignment and tracks parameters in a single step, is less affected by this effect.

5.6 ITS alignment status before proton–proton collisions

The procedure adopted for the ITS alignment and the results achieved with the cosmic-ray tracks, collected in 2008 are here summarized.

The initial step of the alignment procedure consisted in the validation of the survey measurements for the SSD. The three methods applied to this purpose indicate that the residual misalignment for modules on ladders is within 5 μm, i.e. negligible with respect to the intrinsic resolution of this detector in the most precise direction, while the residual misalignment for the ladders with respect to the support cones amounts to about 20 μm. These values do not account for possible global deformations related to the “weak modes” mentioned in Section 4.3.

The procedure continues with track-based software alignment performing residuals minimization. Two algorithms were employed. The main method exploits the Millepede algorithm, which minimizes a global χ^2 of residuals for all alignable volumes and a large set of tracks. The second method iteratively minimizes a set of local module-by-module χ^2 functions. Both methods align the SPD in a hierarchical approach, from the largest mechanical structures (10 support sectors) to the 240 single sensor modules. The SSD coverage provided by the cosmic-ray tracks is insufficient to align the SSD at the level of ladders, especially for the ladders close to the horizontal plane $y = 0$. For the time being the SSD has been aligned only at the level of large sets of ladders with the Millepede algorithm.

The two intermediate ITS layers, the Silicon Drift Detectors, represent a special case, because the reconstruction of one of the two local coordinates requires dedicated calibration procedures (drift velocity and drift time zero extraction), which are to some extent related to the alignment. Indeed, one of the approaches that we are developing for the time zero calibration is based on the analysis of track residuals in a standalone procedure, initially, and then directly within the Millepede algorithm. Once these procedure will become stable and robust, the SDD will be included in the standard alignment chain. For all six layers, the completion of the alignment for all modules will require tracks from proton–proton collisions; a few 10^6 events (collected in a few days) should allow us to reach a uniform alignment level, close to the target, over the entire detector.

Two observables are mainly used to assess the quality of the obtained alignment: the matching of the two half-tracks produced by a cosmic-ray particle in the upper and lower halves of the ITS barrel, and the residuals between double points produced in the geometrical overlaps between adjacent modules. For the SPD, both observables indicate an effective space point resolution of about $13--14$ μm in the most precise direction, to be compared to about 11 μm extracted from the Monte Carlo simulation without misalignments. This $\approx 25\%$ difference(from 11 to 14 μm) is already quite close to the 20%, which is the final target of the alignment. In addition, the measured incidence angle dependence of the spread of the double points residuals is well reproduced by Monte Carlo simulations that include random residual misalignments with a gaussian sigma of about 7 μm. A similar alignment quality is obtained with the two algorithms employed. Further confidence on the robustness of the results is provided by the comparison of the Millepede alignment parameters to those from the iterative method.

Using the present data set with magnetic field off, since the track momenta are not known, the multiple scattering effect, which is certainly not negligible, cannot be disentangled from the residual misalignment effect. Therefore, a more conclusive statement on the SPD residual misalignment will be possible only after the analysis of cosmic-ray data collected with magnetic field switched on. The same applies for combined tracking with SPD, SDD and SSD points: in this case, the momentum-differential analysis of the transverse distance between the two half-tracks (upper and lower half-barrels) will allow us to measure the track transverse impact parameter resolution, which is a key performance figure in view of the ALICE heavy flavour physics program.

Chapter 6

Charm production measurement in the $D^0 \to K^-\pi^+$ channel

The measurement of the cross–section for charm production in p–p collisions at the LHC is a fundamental reference to understand medium properties in heavy–ion collisions as well as an important test of perturbative QCD predictions in a new energy domain (see Chapter 2). ALICE will measure charm production at central rapidity via the exclusive reconstruction of selected D meson decay channels. This strategy relies on the high spatial resolution provided by the ITS, thus on the quality of the ITS alignment, discussed in the last two chapters. In this chapter, the strategy and the analysis preparation for the $D^0 \to K^-\pi^+$ channel are presented. In the first section the adopted strategy is recalled. Then the decay topology is shown and the variables used to increase the signal–to–background ratio are described. The details of the invariant mass analysis and of the efficiency correction, which accounts for the finite detector acceptance and the cut selection are discussed in a dedicated section. From the statistical significance, obtained with the invariant mass analysis, the statistical error affecting the recovered yield of produced D^0 decayed in the $D^0 \to K^-\pi^+$ channel can be estimated. The exclusive reconstruction of D mesons is characterised by a very low signal–to–background ratio: the analysis of large data sample to extract a raw signal yield with an acceptable significance is thus required. The software strategies and solutions, developed within the ALICE Grid Computing framework (see Sec. 3.5), are described. In the last section the main sources of systematic errors are listed and briefly discussed: the next chapter is entirely dedicated to the correction for the feed down from B mesons.

6.1 Strategy for D^0 cross–section measurement

As explained in Section 2.5, a common strategy has been planned for the reconstruction of all the open charmed meson decay channels that will be analyzed.In this section, after a short review of the global strategy for the $D^0 \to K^-\pi^+$ channel reconstruction, each analysis step is described in detail. The analysis strategy is based on an invariant mass analysis of those combinations of reconstructed tracks (“candidates”) that can represent a D^0 meson decayed at a secondary vertex displaced from the primary vertex of interaction. The cross–section is calculated from the raw signal yield extracted with the invariant mass analysis via the following formula:

$$\left.\frac{\mathrm{d}^2\sigma^{D^0}(p_\mathrm{t},y)}{\mathrm{d}y\mathrm{d}p_\mathrm{t}}\right|_{y=0} \approx \frac{1}{4}\frac{f_D \cdot N^{\text{reco.}}_{\text{sel.}}(p_\mathrm{t})\big|_{|y|<1}}{\epsilon \cdot \mathrm{BR} \cdot \mathcal{L}_{\mathrm{INT}}} = \frac{1}{4}\frac{f_D \cdot N^{\text{reco.}}_{\text{sel.}}(p_\mathrm{t})\big|_{|y|<1}}{\epsilon \cdot \mathrm{BR} \cdot N^{\text{tot}}_{\text{inel}}}\,\sigma^{\text{tot}}_{\text{inel}}\,. \tag{6.1}$$

The different terms in the above equation are described in the following along with the analysis steps.

Secondary vertex reconstruction

For each pair of tracks with opposite charges a secondary vertex is computed as the point of closest approach between the two reconstructed tracks.

Raw signal extraction ($\mathbf{N}^{\text{reco.}}_{\text{sel.}}$)

In p–p central collisions, if all the possible pairs are considered as possible "candidates" D^0, the signal over combinatorial background ratio is $\sim 10^{-4}$. It is then mandatory to preselect the reconstructed tracks and candidates on the basis of the typical kinematical and geometrical properties characterizing the signal tracks and reconstructed vertices. The D^0 decays weakly in a relatively long lifetime ($c\tau \approx 123$ μm): the high tracking spatial precision provided by the ITS (see Section 3.2) allows the reconstruction of the primary vertex position and the extrapolation of the track position at the primary vertex with sufficient precision to tag as "displaced" tracks with an impact parameter of few tens of micron. The possibility to resolve the D^0 decay vertices and the primary vertex is the key–element to select signal candidates among the huge number of combinatorial background candidates. The variables used to enhance the signal–to–background ratio are described in the following section. Besides geomtrical cuts, Particle IDentification (PID) information can be used to select signal candidates. As explained in Section 6.5 we decided to avoid the use of the PID information for the reconstruction of the $D^0 \to K^-\pi^+$ decay; in the same section some details for the inclusion of this possibility in the analysis are given.

Fit to invariant mass distribution

The invariant mass distribution obtained in the previous step is fitted to extract the raw signal yield $N^{\text{reco.}}_{\text{sel.}}$. The fitting function comprises a gaussian term describing the signal invariant mass distribution and an exponential/polynomial function modelling the background.

Correction for feed–down from B mesons (f_D)

At LHC energies, a relevant fraction of D^0 mesons comes from the decay of a B meson. On average, the reconstructed tracks coming from those "secondary" D^0 are rather displaced from the primary vertex, because of the relatively long lifetime of the B mesons ($c\tau \sim 460 - 490$ μm). Thus, the selection applied on the reconstructed candidates, further enhances their contribution to the raw signal yield (up to 15%). It is important to subtract this fraction without relying only on MC models that can introduce relevant systematic errors. One possibility is to extract the fraction of "direct" D^0 mesons (f_D) exploiting the different shapes of the impact parameter distribution of secondary D^0, strongly influenced by the B decay length. This approach has been already used by CDF [8] and will be extensively discussed in the next chapter. The main alternatives to this option consist in relying on Monte Carlo estimates based on pQCD calculations first and, then, on the measurement of beauty production, which is one of the main target of the ALICE heavy–flavour physics program.

Efficiency corrections for detector acceptance and cuts selection (ϵ)

To recover the total number of D^0 mesons effectively produced and decayed in the $D^0 \to K^-\pi^+$ channel, ($N_{\rm tot}^{D^0\to K^-\pi^+}$) the raw signal yield is divided by an efficiency correction factor (ϵ) that accounts for the use of cuts and for the limited detector acceptance. The efficiency factor, estimated from Monte Carlo simulations, relies on a realistic description of the detector response into the simulation itself.

Cross–section normalization

The raw yield corrected for the efficiency is divided by the decay channel branching ratio (BR($D^0 \to K^-\pi^+$) $= 3.80 \pm 0.09\%$ [58]) to get the total number of produced D^0 mesons $N_{\rm tot}^{D^0}$. The latter number is divided by the integrated luminosity $\mathcal{L}_{\rm INT}$ to obtain the cross–section for D^0 meson production. A factor 1/4 must be considered because both D^0 and $\bar{D}^0$ mesons are reconstructed and the measurement is performed in two rapidity unities.

6.1.1 Simulation samples analyzed

Three different datasets of simulated p–p collision events at $\sqrt{s} = 10$ TeV are used in this and the following chapters:

- A minimum bias sample ($\sim$ 59M events). Charm and beauty quarks are generated in four $p_{\rm t}$–hard bins[1]. The relative abundances in the bins are such that the $p_{\rm t}$-differential cross–section reproduces the one resulting from MNR calculations (see Section 2.2). The fraction of events with a $c\bar{c}$ pair is $N^{c\bar{c}}$/ev.(10 TeV) ≈ 0.1188, while the fraction of events with a $b\bar{b}$ pair is $N^{b\bar{b}}$/ev.(10 TeV) ≈ 0.0061.

- A "charm enriched" collection ($\sim$5.1M events). A $c\bar{c}$ pair is required in each event and D^0 mesons are forced into $D^0 \to K^-\pi^+$ (BR=3.8%) and $D^0 \to K^-\pi^+\pi^-\pi^+$ (BR=8.1%) decay channels. 357M minimum bias events would be necessary to generated an equivalent number of D^0 from c–quarks decaying in the $D^0 \to K^-\pi^+$ channel. [2]

- A "beauty enriched" collection ($\sim$0.6M events). A $b\bar{b}$ pair is required in each event and D mesons are forced into hadronic decay channels as in the "charm enriched" collection. 870M events would produce the same statistics of D^0 from B mesons decaying in the $D^0 \to K^-\pi^+$ channel.

The PDF, the fragmentation functions and the hard–processes allowed are the same in the three samples. The detector response is simulated in order to reproduce realistic detector properties (dead zones, noise, misalignment) as expected at the end of 2009. The production was done using the ALICE Grid Computing framework and lasted three months. The events were stored in the GRID within the Physics Data Challenge 2009 (PDC09) productions. Part of the analyses shown in this chapter were performed while the production of the minimum bias sample was still in progress, and thus they refer to a subsample of $\sim 3.8 \cdot 10^7$ events.

[1]The $p_{\rm t}$–hard is the quark transverse momentum in the rest frame of the hard process.

[2]$N_{MB} = \frac{N_{c\bar{c}}^{D\to h}}{N^{c\bar{c}}/ev \times ({\rm BR}(D^0\to K^-\pi^+)+{\rm BR}(D^0\to K^-\pi^+\pi^-\pi^+))}$

6.2 Raw signal yield extraction

In this section the topological properties of the $D^0 \to K^-\pi^+$ decay channel are described along with the variables used to enhance the signal–to–background ratio. The kinetic of the decay is depicted in Fig. 6.1. The impact parameter, defined as the distance between the projection of a track in the plane transverse to the beam direction and the primary vertex of interaction, is used to identify tracks displaced from the primary vertex of interaction. As shown in the figure, a typical signature of the $D^0 \to K^-\pi^+$ decay channel is the presence of two opposite charged tracks with an impact parameter not compatible with zero. The pointing angle θ_{point} is defined as the angle between the sum of the reconstructed track momenta and the flight line of the candidate D^0, the latter being the flight line joining the primary vertex and the hypothetical secondary vertex. The θ^* angle is the angle between the kaon trajectory in the D^0 centre of mass system (c.m.s.) and the D^0 flight line taken as the boost direction. In the ultra–relativistic limit ($E \approx p$) the typical impact parameter of a particle coming from the two body decay of a mother particle with a decay length $c\tau$ is $\approx c\tau$ [131], due to the kinematics of the decay. In Fig. 6.2 (right) the $D^0 \to K^-\pi^+$ case is depicted. From here on, variables labelled with a star refer to quantity defined in the D^0 centre of mass system.

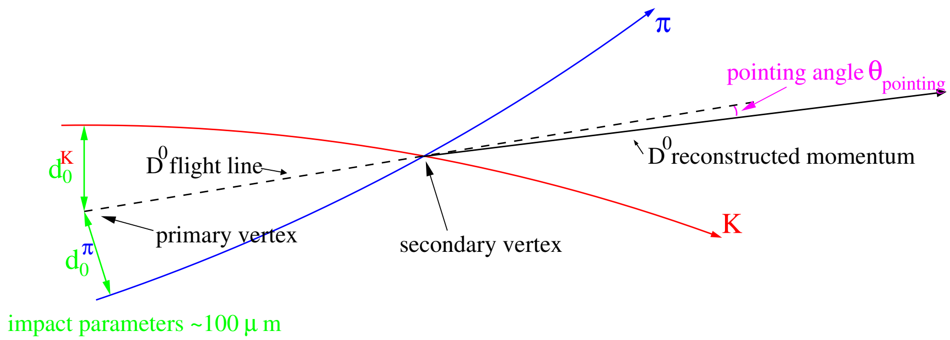

Figure 6.1: Schematic view of a D^0 decay in the $D^0 \to K^-\pi^+$ channel.

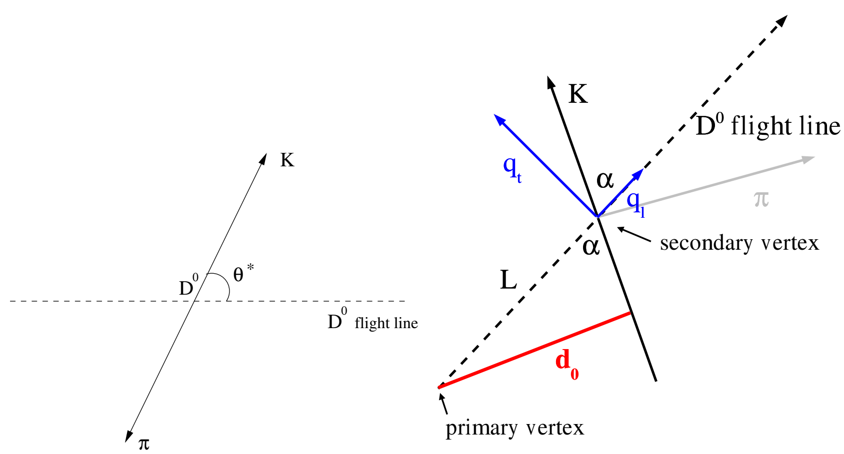

Figure 6.2: Schematic view of a D^0 decay in the $D^0 \to K^-\pi^+$ channel in the D^0 (left) and detector (right) reference systems. q_l and q_t are the momentum projections along the D^0 flight line and in the plane transverse to it.

Neglecting the curvature due to the magnetic field of the detector, the impact parameter of a daughter can be estimated as

$$d_0 = L \sin\alpha \,,$$

where $L = ct^*\beta\gamma$ is the distance covered by the D^0 meson decaying in a proper time t^* and α is the angle between the chosen particle (the kaon in the figure) and the D^0 straight line. To highlight the effect of the boost, the special case in which the decay plane (identified by the two daughter momentum vectors) corresponds to the transverse plane and the θ^* angle is $\pi/2$ is considered. Then,

$$\sin\alpha = \frac{q_\mathrm{t}}{\sqrt{q_\mathrm{t}^2 + q_\mathrm{l}^2}} = 1 \Bigg/ \sqrt{1 + \left(\frac{q_\mathrm{l}}{q_\mathrm{t}}\right)^2} \,.$$

In the relativistic limit $p^\star \simeq E^\star$:

$$\frac{q_\mathrm{l}}{q_\mathrm{t}} = \frac{\gamma(p^\star \cos\theta^\star + \beta E^\star)}{p^\star \sin\theta^\star} \simeq \frac{\beta\gamma p^\star}{p^\star} = \beta\gamma.$$

Hence the impact parameter is given by:

$$d_0 = ct^\star\beta\gamma \Big/ \sqrt{1 + (\beta\gamma)^2} = ct^\star \Bigg/ \sqrt{1 + (M_{D^0}/p_{D^0})^2} \,. \tag{6.2}$$

The proper time distribution follows the exponential decay law ($N_{D^0}(t^\star) = N_{D^0}(0)e^{-t^\star/\tau}$) and, from the above equation, a similar trend is expected for the impact parameter, whose mean value can be estimated as:

$$\langle d_0 \rangle = c\tau \Bigg/ \sqrt{1 + (M_{D^0}/p_{D^0})^2} = 123\ \mu\mathrm{m} \Bigg/ \sqrt{1 + (M_{D^0}/p_{D^0})^2} \,. \tag{6.3}$$

In Fig. 6.3 the trend of the average impact parameter as a function of the D^0 transverse momentum is shown. The average impact parameter for pions and kaons coming from the

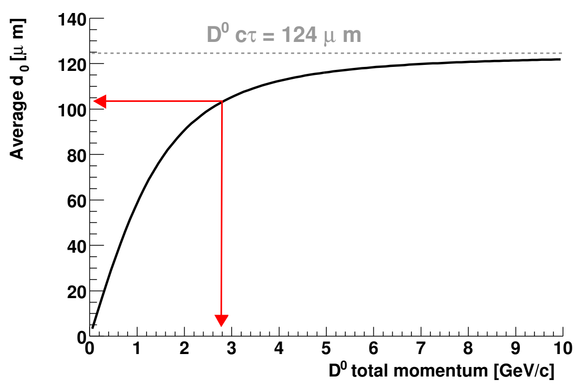

Figure 6.3: Mean impact parameter in the transverse plane for the D^0 kaon and pion decay products as a function of the momentum [57]. The arrows indicate the average momentum expected at LHC energies in a rapidity range $|y| < 1$.

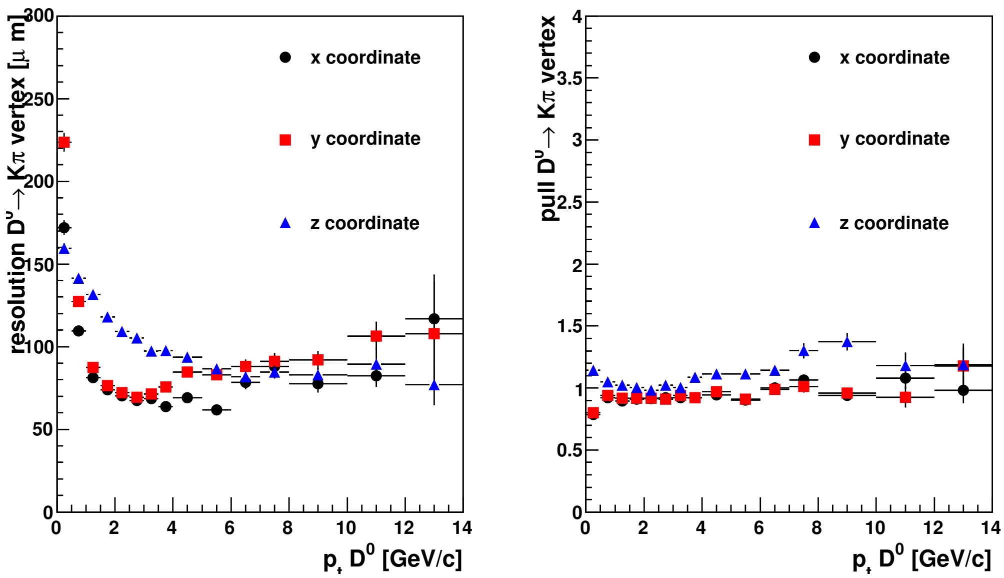

Figure 6.4: On the left: $D^0 \to K^-\pi^+$ secondary vertex resolution as a function of D^0 transverse momentum. On the right: the sigma of the pull distribution. From [132].

decay of a D^0 is ≈ 100 μm at LHC energies. Therefore, the spatial resolution on the impact parameter and on the primary vertex position must be of the order of tens of microns to disentangle between primary and secondary tracks and resolve the secondary and primary vertices.

6.2.1 Secondary vertex reconstruction

For each pair of tracks a secondary vertex is defined as the point of closest approach (PCA) between the two reconstructed tracks. The PCA is calculated along the segment minimizing the distance between the two helices, taking into account the error on the helix parameters, thus the different spatial precision on the track trajectories. Tracks with higher momentum are usually better reconstructed because of the smaller multiple scattering in the beam pipe and in the detector material. Because of this the PCA is on average closer to the track with the highest momentum. In Fig. 6.4 (left plot) the resolutions on the three secondary vertex coordinates are shown as a function of the D^0 transverse momentum. The resolution at very low $p_{\rm t}$ is better for the z coordinate because the two tracks are back to back in the transverse plane and the vertex position along the tracks direction cannot be well determined. The resolution worsen at high momentum because, even if in the D^0 c.m.s. the two particles are produced back–to–back isotropically, the boost in the laboratory frame forces them towards the D^0 direction. It is thus difficult to determine the secondary vertex coordinate along the D^0 flight line. The resolution for the y coordinate is worse than for the x due to geometrical effects: there are more dead regions in the SPD (the innermost ALICE sub-detector) in the horizontal plane, hence more reconstructed mesons are directed along y than along x. In the plots on the right, the sigma of the distribution of the pulls (defined as the residuals divided by their errors) are shown. If the errors are correctly described, the sigma of the pull

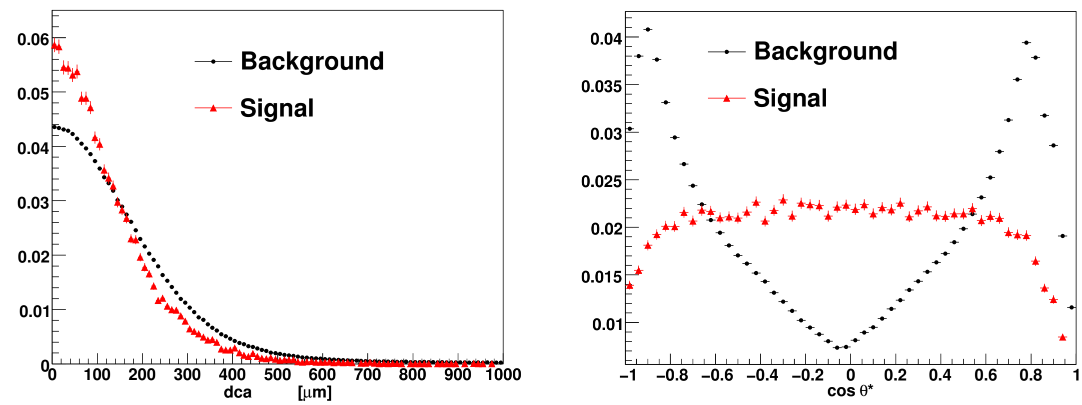

Figure 6.5: Distance of closest approach (dca, left panel) and $\cos\theta^{\star}$ (right panel) and distributions for background (black circles) and signal (red triangles) candidates. The different error bar sizes are due to the smaller number of signal than background candidates. The variables are defined and described in the text.

distributions should be equal to one. This is the case (within 5%) for the x and y coordinates except at very low p_{t}. Conversely the error on the z coordinate seems to be underestimated, especially at high transverse momentum.

6.2.2 Selection cut variables

Two kinds of variables are used to enhance the signal–to–background ratio: single track variables and pair variables. The firsts, related to single track properties, are the impact parameter with respect to the primary vertex and the transverse momentum. A cut on the minimum impact parameter could reduce the number of primary tracks coming from the primary vertex of interaction. However, especially at low p_{t}, the impact parameter of particles coming from D^0 decays is determined mainly by the detector resolution rather than by the D^0 lifetime. Conversely, a cut on the maximum impact parameter can reject tracks coming from decays of particles with long lifetime, as strange and bottom hadrons, or produced by the interaction of primary particles with the detector material. Most of the background are low p_{t} primary tracks and a cut on the minimum transverse momentum rejects a fraction of them.
In the following, the pair–variables used to enhance the signal–to–background ratio are described.

Distance of closest approach between kaon and pion tracks

The distance of closest approach (dca) between the two tracks is the length of the segment minimizing the distance between the two track helices. For tracks coming from a common point, like a decay vertex or the primary vertex of interaction (ideal dca=0), the observed dca is determined by the detector spatial resolution on the track position. In Fig. 6.5, left panel, the dca distributions for background and signal pairs are shown. Most of the background is made of primary track pairs: their dca distribution is strongly correlated to the impact parameter resolution, thus to the tracks transverse momenta. On average, tracks coming

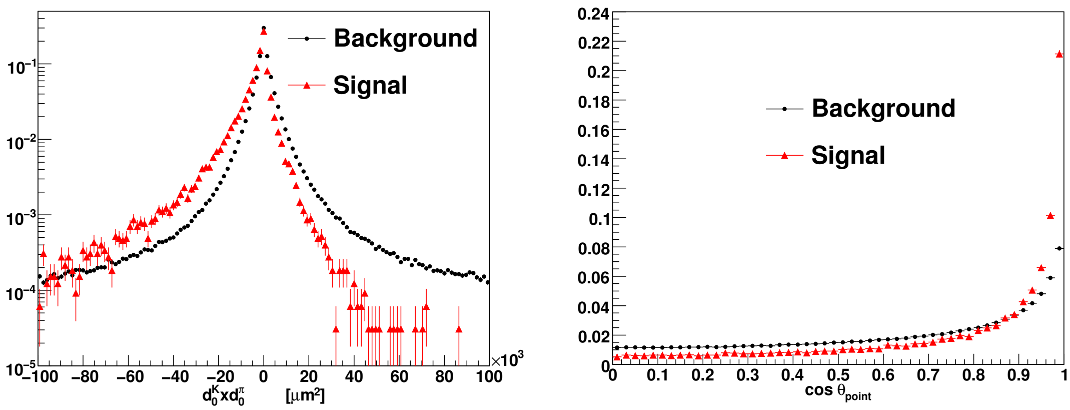

Figure 6.6: Product of daughter impact parameters ($d_0^K \times d_0^\pi$, left panel) and $\cos\theta_{\mathrm{point}}$ distributions for background (black circles) and signal (red triangles) candidates. The different error bar sizes are due to the smaller number of signal than background candidates. A cut $\cos\theta_{\mathrm{point}} > 0$ was applied already at the level of candidates reconstruction: the background distribution shape is almost flat in the entire range [3]. The variables are defined and described in the text.

from the decay of a D^0 meson are reconstructed with a higher spatial precision because of the higher average transverse momentum. With a cut on the minimum transverse momentum, background pairs made of primary tracks with relatively high momentum are selected and the background dca distribution is similar to the signal one. Therefore, the dca is effective in rejecting background pairs only if a cut on the minimum impact parameter is applied. In this way background pairs including a secondary track are rejected.

Cosine of the decay angle

In the D^0 reference system the pion and the kaon are emitted isotropically with three–momenta $\vec{p}^\star$ of equal magnitude $p^\star$ and opposite direction, as depicted in Fig. 6.2 (left panel). The decay angle in the c.m.s. $\theta^\star$ is defined as the angle between the kaon momentum and the D^0 flight line, which is also taken as the boost direction. For each candidate two values are calculated, one per each mass hypothesis (the $D^0[\bar{D}^0]$ hypothesis forces the negative[positive] track to be interpreted as the kaon). As it is shown in Fig. 6.5 (right panel), due to the isotropic production in the c.m.s., the $\cos\theta^\star$ distribution for signal pairs is almost flat[3]. Conversely, the background distribution peaks close to ± 1. The depletion at $|\cos\theta^\star| \approx 1$ is related to the cuts applied in the candidate reconstruction ($p_{\mathrm{t}} > 0.3$ GeV$/c$ and $\cos\theta_{\mathrm{point}} > 0$) and to detector effects: if the particles are emitted parallel to the D^0 momentum, one of the two is boosted at very low momenta and can go out of the geometrical acceptance.

Cosine of the pointing angle $\cos\theta_{\mathrm{point}}$

The pointing angle, already defined in Section 6.2 is the angle between the D^0 flight line and the total momentum of the two daughter tracks. For background pairs there is no correlation

[3] It is possible to represent each decay in the c.m.s. with a point on a sphere of radius $p^\star$. Taking the $z^\star$–axis along the D^0 flight line and introducing spherical coordinates $(\theta^\star, \phi^\star)$ ($\theta^\star$ is the polar angle while $\phi^\star$ is the azimuth), then the isotropy of the decay implies: $const = \frac{dN}{d\Omega} = \frac{dN}{d\phi^\star\, d\cos\theta^\star} \to \frac{dN}{d\cos\theta^\star} = 2\pi\, const.$

between the momentum direction and the reconstructed flight line, because most of the pairs are composed of primary tracks and the secondary vertex position is determined only by the finite spatial tracking resolution. For any flight line associated to a background pair the possible total three-momentum is distributed isotropically. This implies that the distribution of the cosine of the polar angle with respect to the flight line (that is, the cosine of the pointing angle) is flat. Conversely, for a signal pair the flight line direction is effectively determined by the D^0 three–momentum direction and the cosine of the pointing angle distribution is expected to peak at 1. The distributions of $\cos\theta_{\rm point}$ for the signal and background are shown in Fig. 6.6 (right panel).

Product of track impact parameters

The typical impact parameters for a pion and a kaon track coming from a D^0 decay is of the order of ~ 100 μm (Section 6.2) and have opposite signs. Ideally, their product would be negative. Due to detector resolution the observed distribution (Fig. 6.6, left panel) shows both positive and negative values but it is strongly asymmetric with respect to zero. For background pairs, composed mainly of randomly associated primary tracks with opposite charges, the distribution is symmetric.

6.2.3 Selection of the cut variable values

The values of the variables used as cuts are chosen in order to reject as much background as possible without losing too much signal. The adopted criterion is to maximize the statistical significance, defined as:

$$\mathcal{S} \equiv \frac{\rm S}{\sqrt{\rm S+B}} = \sqrt{\rm S}\frac{1}{\sqrt{1+\frac{1}{r}}}\,. \tag{6.4}$$

with S and B the signal and background candidates after cuts and $r = {\rm S/B}$ the signal–to–background ratio, which depends on the effectiveness of the cuts. The significance quantifies how much the signal emerges above the fluctuations of the background. It is possible to rewrite it as:

$$\mathcal{S} = \epsilon_{\rm S}\sqrt{\frac{r_0 n^{\rm ev}_{\rm D^0} N^{\rm ev}}{\epsilon_{\rm B} + r_0\epsilon_{\rm S}}}\,, \tag{6.5}$$

where r_0 is the signal–to–background ratio before the cuts, $\epsilon_{\rm S[B]}$ is the cut efficiency for the signal[background], that is, the fraction of signal[background] pairs surviving the cuts, $n^{\rm ev}_{\rm D^0}$ is the signal per event (the number of $D^0 \to K^-\pi^+$ decays per event) and $N^{\rm ev}$ is the total number of events. The values of the cuts have already been optimised in previous studies using simulation data: the cut values were varied in a n–dimensional grid defined in the cut variable space (n depending on the study) and, for each set of values, the significance was calculated [3, 133]. The set maximizing the significance was selected as the optimal one. The two most "powerful" cut variables are the cosine of the pointing angle and the product of the impact parameters. In Fig. 6.7 a projection of the significance trend in the two–dimensional space ($\cos\theta_{\rm point}, d_0^K \times d_0^\pi$) is shown. The high correlation between the two variables for signal candidates results in a very efficient cut of background pairs. The development of an automatised procedure to optimize the cuts on "real" data is in progress. The main idea is to repeat the same procedure adopted on Monte Carlo data and to calculate the significance from the amount of background (B) and signal (S) estimated with the fit to the invariant

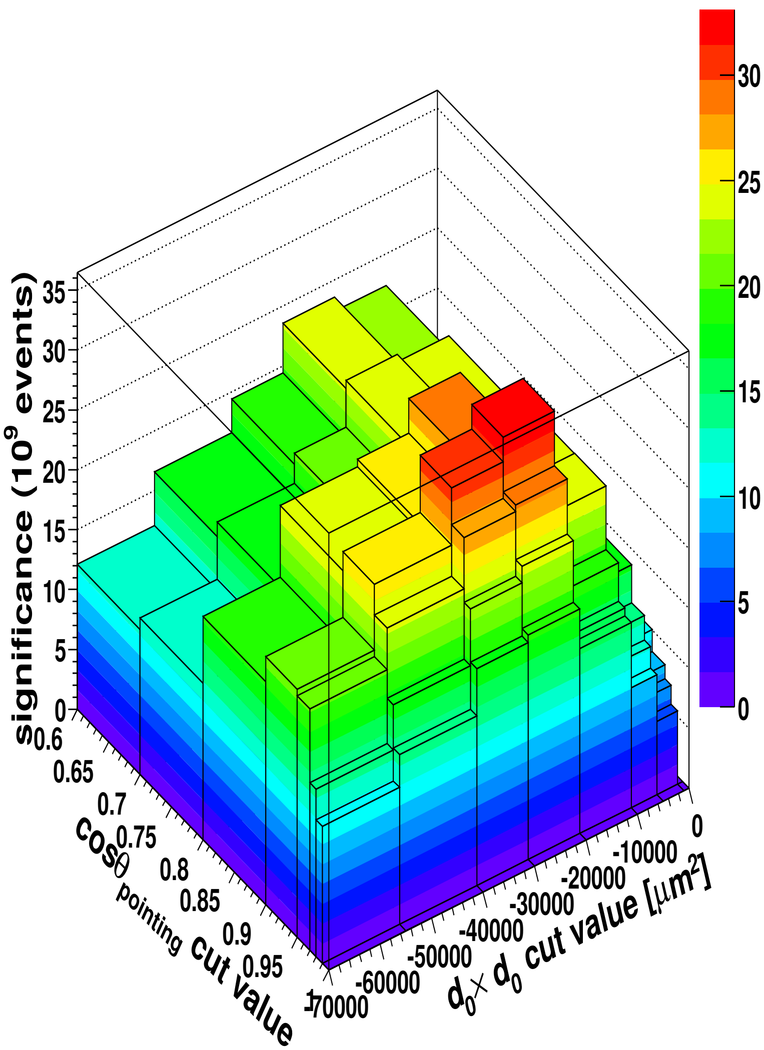

Figure 6.7: Significance trend in the two–dimensional space ($\cos\theta_{\rm point}, d_0^K \times d_0^\pi$) in the interval $2 < p_{\rm t}^{D^0} < 3{\rm GeV}/c$. Figure from [133].

mass distribution.

Two different sets of cuts were used in the analyses shown in this chapter: "looser" cuts (Table 6.2), with values similar to previous studies on larger size samples [3], are used to analyze the "charm–enriched" sample while "tighter" (Table 6.1) cuts are used in the analysis of the minimum bias sample, to increase the otherwise poor statistical significance.

6.2.4 Invariant Mass Resolution

It is important to know the invariant mass resolution in the D mesons mass region, since the better the resolution, the smaller the statistics needed to extract a signal with a good significance. It is also important to check that there are not discrepancies between the resolution observed using Monte Carlo generated events and the variances recovered with the Gaussian fit to the invariant mass peak obtained from real data. A similar discrepancy would affect the efficiency correction and would be a source of systematic errors. The invariant mass of the (K, π) pair can be expressed as:

Table 6.1: Set of "tighter" cuts

p_t[GeV/c] bin	$p_t^{K,\pi}$ [GeV/c]	$\lvert d_0^{K,\pi}\rvert$ [cm]	dca [cm]	$\cos\theta^\star$	$d_0^K \times d_0^\pi$ [cm^2]	$\cos\theta_{\rm point}$
$0 < p_t < 1$	> 0.5	< 0.05	< 0.04	< 0.8	< -0.00025	> 0.7
$1 < p_t < 2$	> 0.7	< 0.1	< 0.02	< 0.8	< -0.00025	> 0.8
$2 < p_t < 3$	> 0.7	< 0.1	< 0.02	< 0.8	< -0.00025	> 0.8
$3 < p_t < 5$	> 0.7	< 0.05	< 0.02	< 0.8	< -0.00015	> 0.8
$p_t > 5$	> 0.7	< 0.05	< 0.02	< 0.8	< -0.00015	> 0.9

Table 6.2: Set of "looser" cuts

p_t[GeV/c] bin	$p_t^{K,\pi}$ [GeV/c]	$\lvert d_0^{K,\pi}\rvert$ [cm]	dca [cm]	$\cos\theta^\star$	$d_0^K \times d_0^\pi$ [cm^2]	$\cos\theta_{\rm point}$
$0 < p_t < 1$	> 0.5	< 0.05	< 0.04	< 0.8	< -0.0002	> 0.5
$1 < p_t < 2$	> 0.6	< 0.05	< 0.03	< 0.8	< -0.0002	> 0.6
$2 < p_t < 3$	> 0.6	< 0.05	< 0.03	< 0.8	< -0.0002	> 0.6
$3 < p_t < 5$	> 0.7	< 0.05	< 0.02	< 0.8	< -0.0001	> 0.8
$p_t > 5$	> 0.7	< 0.05	< 0.02	< 0.8	< -0.00005	> 0.6

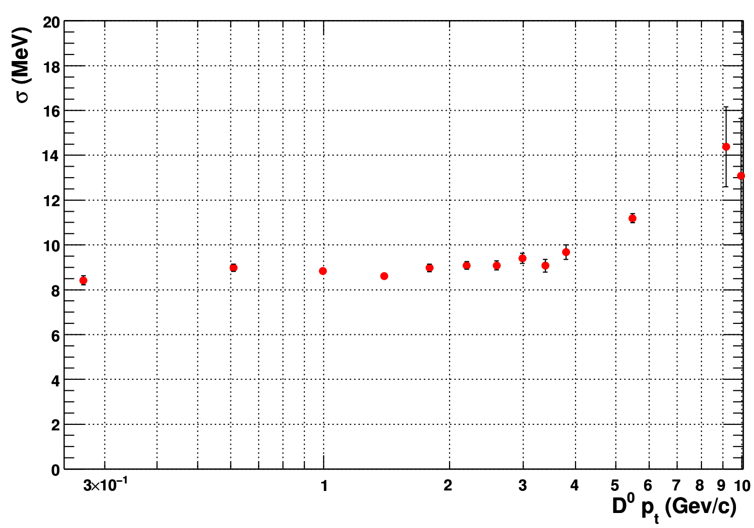

Figure 6.8: Sigma of the invariant mass distribution of D^0 as a function of p_t. The sigma is obtained with a gaussian fit to the invariant mass residual $(M_{reco} - M_{true})$ distribution in each p_t bin. The error bars in the x axis represent the momentum ranges of each bin.

$$
\begin{aligned}
P_K &= (E_K, \vec{p}_K)\ ,\ P_\pi = (E_\pi, \vec{p}_\pi) \\
P^2_{D^0} &= M^2_{D^0} = (P_K + P_\pi)^2 = (E_K + E_\pi)^2 - (p_K^2 + p_\pi^2 + 2p_K p_\pi \cos\alpha) = \\
&\quad m_K^2 + m_\pi^2 + 2(E_K E_\pi - p_K p_\pi \cos\alpha)
\end{aligned} \tag{6.6}
$$

where P is used to indicate four–momenta, p for the module of the three–momenta and α is the angle between the pion and kaon three–momenta. In the relativistic limit, where the masses are neglected ($p \simeq E$), the invariant mass can be approximated as:

$$M^2_{D^0} \simeq 2p_K p_\pi (1 - \cos\alpha) \tag{6.7}$$

From the last equation, if the error on the angle are considered negligible with respect to those affecting the momenta and the relative uncertainty on the momentum is approximated to a constant (see Fig. 4.3), it is possible to estimate the expected error on the invariant mass as:

$$\frac{\sigma(M)}{M} \approx \frac{1}{\sqrt{2}} \frac{\sigma(p)}{p} \tag{6.8}$$

Using a reference value $\sigma(p)/p \approx \sigma(p_{\rm t})/p_{\rm t} \approx 0.7\%$, $\sigma(M)/M \approx 5/1000$ and $\sigma(M) \approx 1865 \times 0.005 \approx 9.3$ MeV is expected in the D^0 mass region. In Fig. 6.8, the sigma of Gaussian fits to the residuals between the reconstructed invariant mass for signal candidates and the true D^0 mass are shown as a function of the reconstructed D^0 transverse momentum. As it is clear from the figure the obtained sigma are close to the expected resolution, slightly increasing with transverse momentum, following the slope of $\sigma(p)/p$.

6.2.5 Invariant mass fit

The raw signal yield $N^{\rm reco.}_{\rm sel.}$ is extracted by fitting the invariant mass distribution of the selected pairs. As already mentioned, the fitting function comprises a Gaussian term describing the

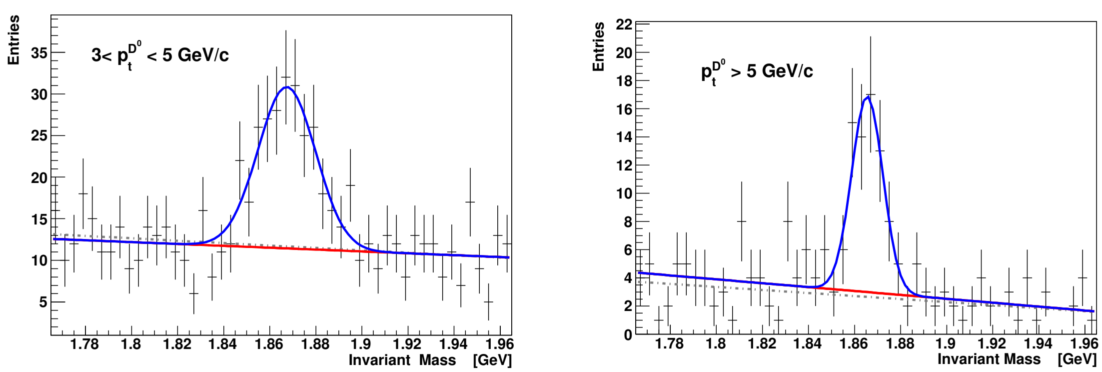

Figure 6.9: Fit to the invariant mass distributions obtained with a sample of $\sim 9 \cdot 10^6$ minimum bias events in two different $p_{\rm t}$ intervals after the selection described in Table. 6.2. The cross–hatched line is the background fit after the first step of the invariant mass fit procedure (see text) extrapolated under in the peak region. The blue continuous line is the final fit function, the background term represented by the red continuous line.

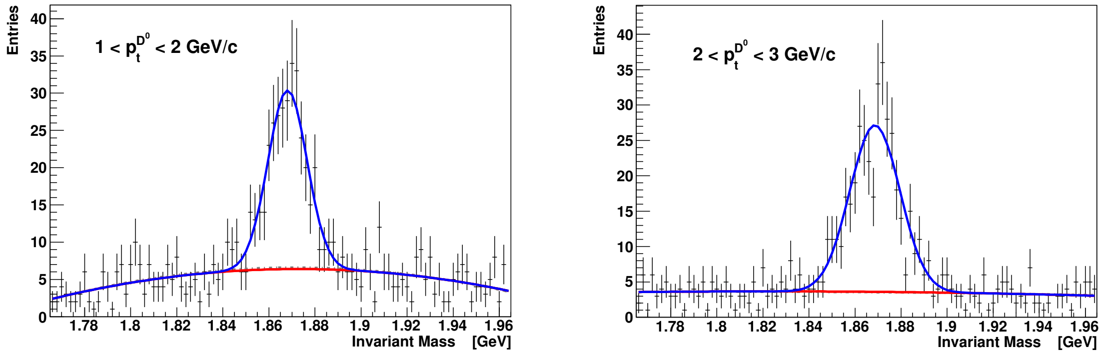

Figure 6.10: Fit to the invariant mass distributions obtained with a sample of $\sim 5.5 \cdot 10^6$ events from the "charm enriched" collection (see Section 6.1.1) in two different p_t intervals after the selection described in Table. 6.1. The cross–hatched line is the background fit after the first step of the invariant mass fit procedure (see text), extrapolated in the peak region. The blue continuous line is the final fit function, the background term is represented by the red continuous line.

signal invariant mass distribution and an exponential/polynomial (1^{st} or 2^{nd} order) function modelling the background. If a candidate is selected as a D^0 and as a $\bar{D}^0$, two invariant mass values are considered, one of the hypotheses ("reflection") being of course wrong. The reflected signal consists of a Gaussian–like distribution characterized by a much larger sigma with respect to the signal one. It is possible to add a Gaussian term in the fitting function to account for this component. However, it has been checked that, at low statistics, the amount of reflected signal under the signal Gaussian peak is very small and its variance large enough to be accounted for in the background function. The fit is done in two steps:

1. Fit of the "sidebands". The region outside the Gaussian peak ($3\sigma(M) < |M - M_{D^0}| < 5\sigma(M)$) is fitted with the chosen background function (exponential, linear, parabolic) and a first estimation of the total amount of background (B_0) and of the other background function parameters is done.

2. Fit of the whole distribution with a Gaussian function for the signal (weighted by the signal amount S) and the background function used in the previous step, weighted by the background amount B, which is initially taken equal to B_0. The amount of S and B, along with their errors, are extracted from the fit parameters.

In Fig. 6.9 some examples of invariant mass distributions obtained from the analysis of $\sim 3.8 \cdot 10^7$ minimum bias events with the cuts defined in Table 6.2 are shown. The results are summarized in Table 6.3. In Fig. 6.10 some examples of invariant mass distributions obtained from the analysis of $\sim 5.5 \cdot 10^6$ events from the "charm enriched" sample (see Section 6.1.1) with the cuts defined in Table 6.1 are shown.

Background subtraction methods

Fitting the invariant mass distribution requires the modelling of the background distribution shape with an appropriate function. This can be a source of systematic error affecting directly

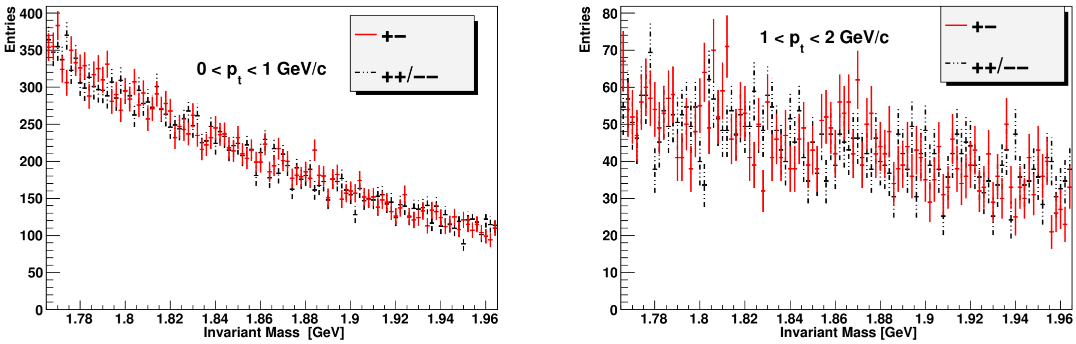

Figure 6.11: Invariant mass distributions for like–sign pairs (black cross–hatched crosses) and opposite–sign (red full line crosses) candidates after cuts selection in two different interval of candidate transverse momentum.

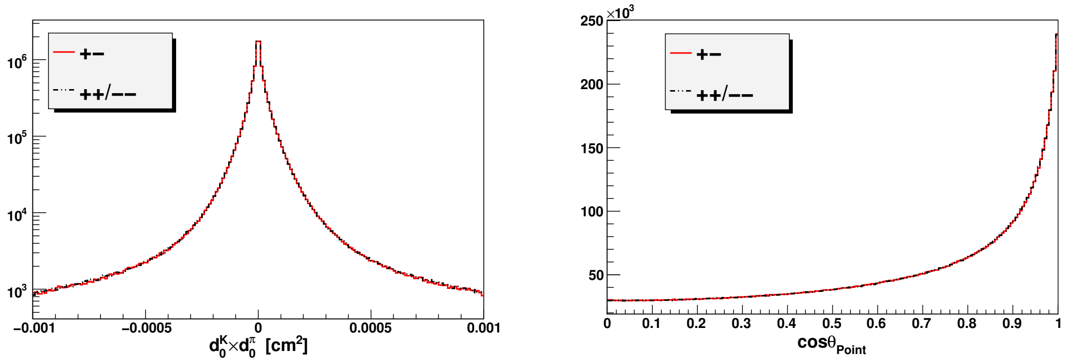

Figure 6.12: Product of daughter impact parameters ($d_0^K \times d_0^\pi$, left panel) and $\cos\theta_{\mathrm{point}}$ distributions for like–sign pairs (black cross–hatched crosses) and opposite–sign (red full line crosses) candidates after cuts selection.

the estimated amount of signal. In fact, while the signal distribution is supposed to be quite well described by a Gaussian function because is directly related to the resolution on the track momenta, the shape of the background distribution is strongly influenced by the cut selection. Instead of assuming a suitable function to describe it, it is possible to recover its shape from the analysis of a pure background sample. A background sample must be composed of pairs of uncorrelated tracks, not coming from a $D^0 \to K^-\pi^+$ decay. Three methods, based on three distinct approaches, are under study:

- Like–sign pairs: the pairs are made of reconstructed tracks with the same charge.
- Event mixing: the pairs are constructed taking the tracks from different events.
- "Rotated" pairs: in each event the positive (or negative) tracks are rotated by 180° around the event z-axis (the z-axis translated to match the reconstructed primary vertex).

In Fig. 6.11 a comparison of the shapes of the invariant mass distributions obtained from like–sign pairs and from a pure-background sample of opposite–sign pairs are compared. The same

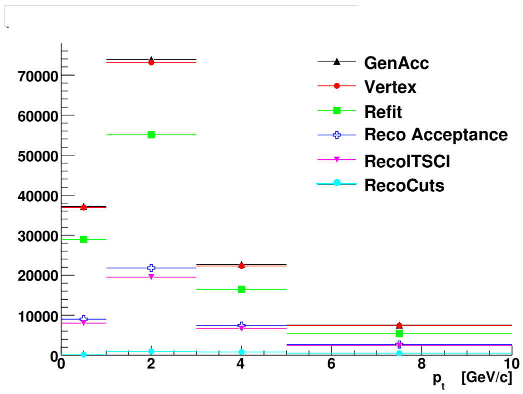

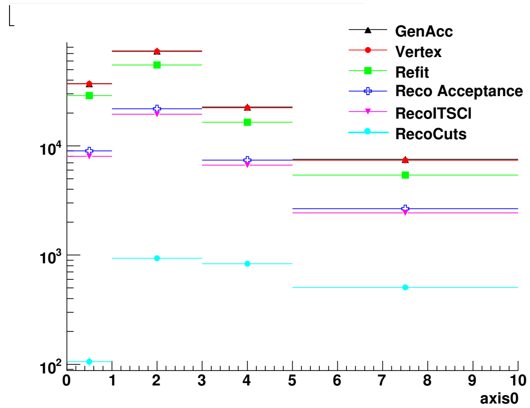

Figure 6.13: On the right: number of D^0 mesons at each step of the simulation/reconstruction/analysis chain as a function of the D^0 transverse momentum. The upper black triangles refers to the generated D^0s, the lowest cyan filled circles refers to the D^0 reconstructed and selected with the cuts. The other steps are described in the text. On the left, same numbers shown in log scale. The MC sample used is from the "charm–enriched" collection (Section 6.1.1).

cuts have been applied to the pairs. It is possible to directly subtract the like–sign invariant mass distribution, properly normalized to match the expected amount of background pairs, to the whole invariant mass distribution obtained from the opposite–sign sample. However, it is essential that the background sample reproduces correctly not only the invariant mass shape of the "true" background but also the shape of the distribution of all the other variables used as cuts. In Fig. 6.12 the distributions of the cosine of the pointing angle and of the product of the impact parameters are shown for like–sign and pure-background opposite–sign pairs.

6.3 Correction for the efficiency

The raw signal yield extracted from the invariant mass study $N^{reco.}_{sel.}$ is a small fraction of the total number of D^0 mesons produced, due to the limited detector acceptance, to the primary vertex and track reconstruction efficiencies and to the cut selection on the candidates. It is then necessary to correct $N^{reco.}_{sel.}$ in order to recover the total yield. This is achieved using Monte Carlo p–p collision events. The D^0 mesons generated and decayed in the $D^0 \to K^-\pi^+$ channel are counted ($N^{D^0}_{\mathrm{gen}}$) and are "monitored", along with their daughter kaon and pion particles along the simulation/reconstruction/analysis chain. An efficiency factor can be calculated at each step of the chain itself. The most important steps are:

1. Generated: the number of generated D^0 mesons coming from a c–quark and decaying in the the $D^0 \to K^-\pi^+$ channel.

2. Generated in acceptance: both the kaon and pion are in the detector acceptance ($|\eta_{MC,prod}| < 0.9$,$p_{\mathrm{t}}^{MC,prod} > 0.1$ GeV/c, the label *MC,prod* highlights that the values are taken at the D^0 decay point).

3. Primary vertex reconstruction.

4. Daughter "tracking quality" check (*refit*): it is checked that the kaon and pion are reconstructed and the respective tracks cover at least the TPC and the ITS detectors and are not rejected after the re–fit step during track reconstruction (see Section 3.4).

After this step the D^0 mesons can be considered "reconstructable", that is, the secondary vertex reconstruction algorithm should match the daughter kaon and pion track to make up a possible pair. However, as explained in Section 6.6.2, a further minimal selection is applied to the pairs to consider them as candidates. Thus, the number or reconstructed candidate is smaller than the number obtained in the last step. The successive steps consists of the "data–like" selection. The MC information is not accessed anymore and the reconstructed candidates are selected according to the same criteria adopted in the data analysis:

5. Reconstructed: the number of D^0 reconstructed as candidate D^0.

6. Tracks acceptance & ITS cluster–map check: the daughter tracks are required to stay in the acceptance ($|\eta| < 0.9$,$p_{\rm t} > 0.1$ GeV/c). This is a different check with respect to step number 2 because due to detector effect (e.g. interaction with material) the reconstructed tracks can go out of acceptance even if they are in the acceptance at the MC level. Moreover, the tracks should contain at least one cluster on each SPD layer and at least 5 clusters on the ITS, that is, the track can lack only one cluster on the SDD and SSD layers.

7. Analysis cut selection: the number of reconstructed D^0 mesons that survived the cut selection.

The number of reconstructed D^0 at the end of the chain divided by $N_{\rm gen}^{D^0}$ gives the global efficiency factor ϵ. The efficiency factor may depend on D^0 properties ($p_{\rm t}, \eta$) and on a series of variables, like event properties (primary vertex position, event multiplicity, azimuthal particle distribution) and detector properties (dead zones, material budget). Due to this, a non-realistic description in the simulation at the level of D^0 production and decay kinematics as well as at the level of detector response may cause systematic errors to arise, as it will discuss in Section 6.7. The efficiency factor is calculated for different D^0 $p_{\rm t}$ bins (the same intervals considered to construct the invariant mass histograms). In Fig. 6.13 the number of D^0 mesons after the main steps are reported as a function of the D^0 transverse momentum. As expected, larger gaps are observed after step number 4, 5, and 7. The "refit" requirement rejects kaons and pions that decay before going out of the TPC and those soft pions which are bad reconstructed or go out from the acceptance because of the interaction with the detector material. If the primary vertex is far from the origin ($z_{\rm vtx} \gtrsim 1$ cm) the $|\eta| < 0.9$ cut does not correspond to the real detector acceptance and the pion and the kaon can be reconstructed only for a short track in the detector (while most of the tracks out of the TPC acceptance because of the too small helix radius are rejected from the $p_{\rm t}^{MC,prod} > 0.1$ GeV/c selection). The drop after step number 5 ("Reconstructed") is caused by the rejection of low $p_{\rm t}$ pions ($p_{\rm t} > 0.3$ GeV/c).

The figure is obtained using data of the "charm–enriched" MC sample (Section 6.1.1). It has been checked that the reported efficiencies are compatible within errors with those calculated using a minimum–bias sample. This is important both for the study of systematic errors and both for software computational reasons, allowing the calculation of the efficiencies on a relatively small–size sample. A study of the systematic errors affecting the efficiency factor requires to calculate it many times starting from different initial conditions at the level of Monte Carlo generators as well as of detector status (e.g. alignment and calibration), with the consequent employment of large amount of disk–space and computing time.

6.4 Estimate of the statistical error on the produced D^0 yield

In Table 6.3 the results obtained with the invariant mass analysis of $3.8 \cdot 10^7$ minimum bias events are reported. The signal and background recovered by the fit are always compati-

Table 6.3: Minimum bias collection ($\sim 3.8 \cdot 10^7$ events): signal (S), background (B), signal–to–background ratio, significance ($\mathcal{S}$) recovered from the invariant mass analysis. The signal and background estimated from the fit are compared to the Monte Carlo values. The significance extrapolation to the reference number of events expected for ≈ 1 year data taking is shown.

p_t[GeV/c] bin	S [MC S]	B [MC B]	S/B	$\mathcal{S}$	$\mathcal{S}(10^9$ev.)
$1 < p_t < 2$	65 ± 22 [37]	341.1 ± 7.3 [375]	0.2	3.2 ± 1.1	16.4 ± 5.6
$2 < p_t < 3$	43 ± 10 [37]	60.6 ± 2.2 [60]	0.7	4.2 ± 1.0	21.5 ± 5.1
$3 < p_t < 5$	112 ± 15 [98]	80.1 ± 4.5 [86]	1.4	8.1 ± 1.1	41.6 ± 4.8
$p_t > 5$	45.2 ± 6.8 [42]	12.0 ± 1.5 [7]	3.8	6.0 ± 1.0	30.8 ± 4.2

ble within errors with the real amount of signal and background. Compatible results were achieved with preliminary tests on the whole $\sim 5.9 \cdot 10^7$ minimum bias event sample. It is possible to estimate the statistical relative error on the produced D^0 yield as the inverse of the statistical significance:

$$\sigma^2(\mathrm{S}) = \sigma^2(T - B) \approx T + \sigma^2(B) \approx S + B \tag{6.9}$$

$$\rightarrow \frac{\sigma(S)}{S} = \frac{1}{\mathcal{S}} \tag{6.10}$$

In the above relation, the error on the background, $\sigma^2(B)$, corresponds to the error on the background estimated with the invariant mass fit and it is usually negligible with respect to the total number of observed candidates. The same approximation holds if the background is estimated from a pure background sample (e.g. like–sign candidates) and subtracted. As

Table 6.4: Estimation of the statistical error on the raw signal yield extracted from the invariant mass analysis of the minimum bias collection ($\sim 3.8 \cdot 10^7$ events). The error on the signal as estimated from the fit is reported in the second column while in the third and fourth columns the inverse of the statistical significance is used.

p_t[GeV/c] bin	$\sigma_{\mathrm{S}}^{\mathrm{fit}}$/S (%)	$1/\mathcal{S}$ (%)	$1/\mathcal{S}$ (%)(10^9ev.)
$1 < p_t < 2$	34	31	6.1
$2 < p_t < 3$	23	24	4.7
$3 < p_t < 5$	13	12	2.4
$p_t > 5$	15	17	3.2

shown in Table 6.4, the statistical error calculated in this way (third column) is compatible with the signal error from the invariant mass fit (second column). If the significance is extrapolated to 10^9 events ($\sim$1 year data taking) the estimated statistical error is of the order of few percents. The relative statistical error on the total yield $N_{\rm tot}^{D^0\to K^-\pi^+}$ is calculated as

$$\frac{\sigma(N_{\rm tot}^{D^0\to K^-\pi^+})}{N_{\rm tot}^{D^0\to K^-\pi^+}} = \frac{\sigma(S/\epsilon)}{S/\epsilon} = \sqrt{\frac{\sigma^2(S)}{S^2} + \frac{\sigma^2(\epsilon)}{\epsilon^2}}\,. \tag{6.11}$$

The relative statistical error on the efficiency correction is of the order

$$\frac{\sigma(\epsilon)}{\epsilon} \approx \frac{1}{\sqrt{N_{\rm reco}^{\rm Corr.Sample}}}\,,$$

where $N_{\rm reco}^{\rm Corr.Sample}$ is the number of D^0 reconstructed in the analysis for the calculation of the efficiency correction factor. The error is thus directly proportional to the size of the correction sample. For the analysis performed on the $3.8\cdot10^7$ minimum bias events sample, the statistical error on the efficiency correction is negligible and the relative error on the raw signal yield well approximates the relative statistical error on the total yield $N_{\rm tot}^{D^0\to K^-\pi^+}$. The efficiency factor can be estimated from the "charm–enriched" sample: as it is shown in Fig. 6.13 the number of reconstructed D^0 is above 500 in each $p_{\rm t}$ interval. Thus, the contribution to the total relative error in Eq. 6.11 is $\lesssim 0.002$ to be compared with the square of the statistical error on the signal $\gtrsim 0.017$. Conversely, the effect of the efficiency factor statistical error would not be negligible with respect to the $\approx 3\%$ statistical error extrapolated for a 10^9 events sample. However, the statistics used for the efficiency correction must be always larger than the size of data sample analysed.

6.4.1 Misalignment consequences on the statistical error

In Fig. 6.14 the statistical significance for the D^0 reconstruction extrapolated to 10^9 events is shown as a function of $p_{\rm t}$ in different misalignment scenarios expected after alignment. The simulation sample used is an old one: however no larger differences are expected for the purpose of evaluating the misalignment effect on the statistical significance. At low $p_{\rm t}$ a significance drop due to misalignment is visible (up to 10%).

6.5 Prospects for the use of the TOF PID information

The possibility to exploit the Particle IDentification (PID) information for the reconstruction of the $D^0 \to K^-\pi^+$ decay channel has been already considered in previous studies [3, 133, 57]. We decided to not include it in the analyses presented in this thesis mainly for two reasons. First of all, the PID can help to reject background pairs, at low momenta (below 2 GeV/c), in particular pairs of primary pions: however these are efficiently rejected by the geometrical cuts. The second, most important, reason derives from the correction for the efficiency related to the use of the PID. As all the other corrections, it requires a tuning of the simulation aimed at reproducing a realistic detector response as well as a correct treatment of the PID information. This can not be achieved with cosmic-rays beacuse they mostly consists of muons. The tuning of the simulation requires p–p data and will be done in the first phases of the experiment. Therefore, the PID information will not be used for the D^0 analysis in the first stages of the experiment. In the following, an outline of the strategy for the future inclusion

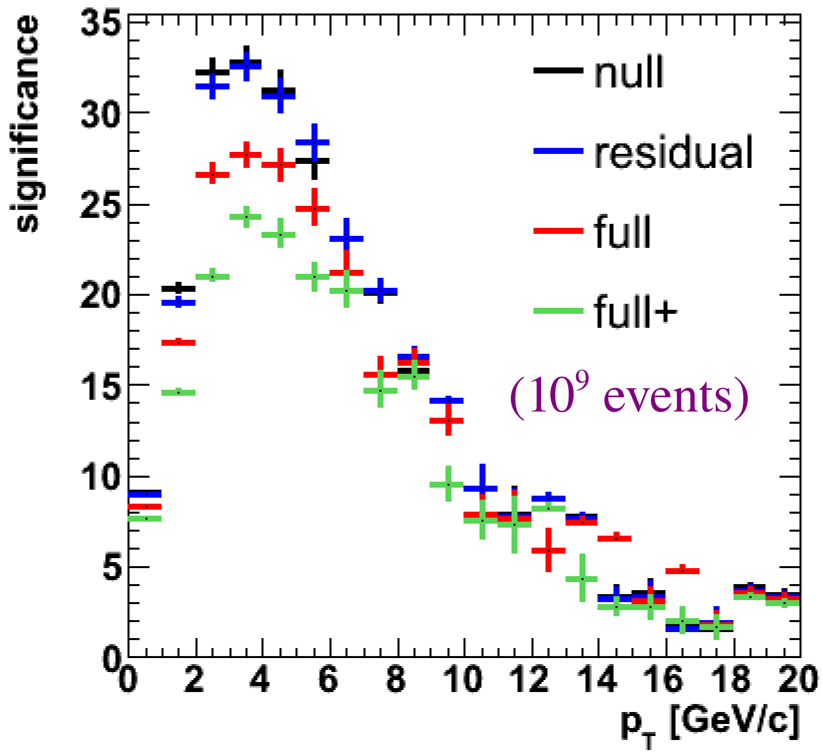

Figure 6.14: Statistical significance as a function of D^0 transverse momentum in different misalignment scenarios: in the residual misalignment scenario the ITS modules are displaced randomly accordingly to Gaussian distribution in order to get a 20% worsening of the detector resolution. In the "full" and "full+" scenario the sigma of the Gaussian distribution are 2 and 3 times than in the residual case.

of the PID in the analysis is given.

For pions and kaons with momenta $p > 0.5$ GeV/c the dE/dx can not provide a mass information efficiently. Therefore, the main source of PID for this analysis is provided by the TOF, which measures the time of flight of a particle across a known distance (Section 3.1.2). The TOF response can be used to tag efficiently pions, kaons and protons in the range $0.5 < p < 2 - 2.5$ GeV/c. For the purposes of the $D^0 \to K^-\pi^+$ reconstruction it is convenient to divide the set of reconstructed tracks into four samples: those identified as pions ($\pi_{\rm tag}$), as kaons ($K_{\rm tag}$), as protons ($p_{\rm tag}$) and non–identified ($?_{\rm tag}$). As described in [3], four complementary samples are defined for the pairs:

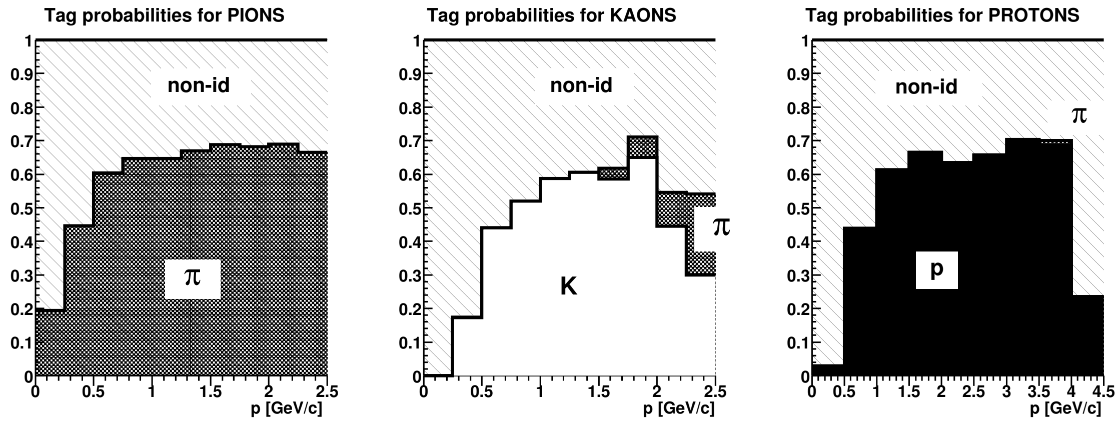

Figure 6.15: PID tag probabilities for reconstructed pions (left), kaons (centre) and protons (right) in p–p collisions with the TOF detector (from [57]).

A:$(K_{\rm tag}, \pi_{\rm tag}) + (K_{\rm tag}, ?_{\rm tag})$. The kaon is identified while the other track is identified as pion or not identified.

B:$(\pi_{\rm tag}, ?_{\rm tag})$. Only one of the two tracks is identified as a pion.

C:$(?_{\rm tag}, ?_{\rm tag})$. Both tracks are not identified.

D. All other combinations, such as $(\pi_{\rm tag}, \pi_{\rm tag})$. The latter, which constitute the most of background pairs are rejected.

If the pion from a D^0 decay is correctly identified while the kaon is misidentified as a pion, the candidate falls in sample D and is lost. Therefore, for open charm detection, the PID strategy has to be optimised in order to minimise the number of kaons tagged as pions, while tagging correctly a large fraction of the pions. In Fig. 6.15, from [57], an example of the PID tag probabilities obtained with the TOF detector is shown for reconstructed pions, kaons and protons in p–p collisions. In the figure, the probability to misidentified a kaon as a pion is almost negligible for momenta smaller than ~ 1.5 GeV/c. For each pair, the probability to fall into one of the samples above as a D^0 or a $\bar{D}^0$ is calculated. If this is indicate as $w^i_{D^0}[w^i_{\bar{D}^0}]$ $(i = A, B, C, D)$, then:

$$2 = w_{\rm T} = w_{D^0} + w_{\bar{D}^0} = \left(\sum_i w^i_{D^0}\right) + \left(\sum_i w^i_{\bar{D}^0}\right) \qquad (6.12)$$
$$w_{D^0} = w_{\bar{D}^0} = 1.$$

These probabilites are used as weights when filling the invariant mass histogram: for instance, if it is chosen to reject candidates in sample D (thus to accept the sample ABC), the two invariant mass hypotheses calculated for a given pair are assinged a weight $1 - w^D_{D^0}$ and $1 - w^D_{\bar{D}^0}$. In this way, the signal estimated by the fit to the invariant mass distribution should correspond to the number of D^0 and $\bar{D}^0$ correctly identified.

6.6 Software strategy for multi–channel charm production analysis of large sets of data using the GRID

The use of the GRID is particularly convenient for the exclusive reconstruction of charmed meson decays in hadronic channels. The analysis strategy (Section 2.5) adopted for most of the considered decay channels goes through the computation, event by event, of a "candidate" decay vertex for each possible pair (triplet, quadruplet for channels with three, four daughters) of reconstructed tracks. Especially in Pb–Pb collisions the number of possible combinations can be huge ($\sim 10^{-6}$ for the $D^0 \to K^-\pi^+$ case) with consequent relevant time consumption. Even if cuts are applied to enhance the signal-to-background ratio, most of the combinations are background. Thus, a relatively high statistics is needed to extract a raw signal yield with an acceptable significance. The employ of the ALICE GRID analysis framework is essential to analyse large data samples in a reasonable time. Part of this work of thesis was devoted to contribute to the realization of the analysis train dedicated to the reconstruction and analysis of heavy flavoured mesons decay channels and test it on the GRID [132].

6.6.1 Charmed hadrons search with an analysis train

To fully exploit the GRID features, the software analysis tools must be designed in a GRID-oriented fashion. Different analyses need to analyse the same set of events stored in the GRID: it is then convenient to exploit the possibility to organise them in a common structure, called an analysis "train". An analysis train is an assemble from a list of modules/tasks (the "wagons") that are sequentially executed by a common analysis manager that provides the connection between the input data, the user analysis and the output.
From the software point of view there are two main steps in the analysis. The first step, consists of the reconstruction of the possible decay vertices and candidates at the same time for all the decay channels. A first selection on the candidates is done already at this level. The vertices and the candidates produced by a dedicated task are collected into an AOD "friend" tree (see Section 3.3), which is stored into a separate "delta" file, AliAOD.VertexingHF.root (one delta file per AOD file). In the second step the analysis dedicated to the different decay channels (invariant mass study, extraction of efficiency correction factors, feed-down from B, etc.) are performed independently as wagons of a second analysis train (see Section 6.6.3) which takes as an input both the AliAOD.root and the AliAOD.VertexingHF.root files produced in the first step.

6.6.2 Software aspects for secondary vertices reconstruction

For each decay channel, all the possible candidates, that is, all the possible combinations of tracks (pairs, triplets, quadruplets), are considered and the related secondary vertices are computed in order to identify secondary vertices displaced from the primary vertex.

A selection is done to reduce the huge number of combinatorial background candidates and enhance the signal-to-background ratio. The kinematic and topological cut variables used to this purpose can be applied at the level of single tracks (e.g. transverse momentum, impact parameter with respect to the primary vertex), pairs of tracks (e.g. product of impact parameters), triplets (D^+ decay vertex properties) and quadruplets. In general, they are peculiar to the decay channel under study but in many cases different analysis can profit from the same selection on the tracks. A common feature of the lower state open charmed mesons under study is that they decay weakly and have a relatively long lifetime ($c\tau \approx 123\ \mu$m and $c\tau \approx 312\ \mu$m for the D^0 and the D^+ respectively): a signature of all the decay channels under study is the presence of tracks displaced from the primary vertex of interaction, that is, tracks with a large impact parameter.

Therefore, the request of a minimum transverse momentum (0.3 GeV/c) and of a minimum impact parameter ($> 50\ \mu$m) are found to be an efficient choice to enhance the signal-to-background ratio in all the decay channels considered. The first because the particles coming from heavy flavor decays produce relatively high $p_{\rm t}$ tracks. The second request enhances the fraction of tracks coming from a displaced vertex, especially for high transverse momentum tracks. The impact parameter resolution improves with increasing momentum (lower multiple scattering) and it is unlikely that a primary high momentum track has a large impact parameter. It is then easier to distinguish primary tracks from secondaries at high momentum. A special treatment is needed for the D^{+*} reconstruction which requires to associate a D^0 meson candidate to a "soft", low momentum, pion coming from the primary vertex. The selection flow has been organised to minimize time and disk space consumption by matching as far as possible the requests of each decay channel analysis. Both the values of the cuts and the physical quantities stored for each candidate affect the size of the AOD, the former determining the number of selected candidates, the latter determining the size of the candidate objects. Therefore, the values of the cuts and the physical quantities stored for each candidate have been chosen in order to reach a compromise between the information requested by the successive analysis and the need to keep the disk space demand as small as possible. The average size of the AOD for p–p collisions at $\sqrt{s} = 10$ TeV is of the order of 1 Kb/event while the candidate information are contained in $\sim$ 0.1 Kb/event.

Candidate information

For each candidate, the reconstructed decay vertex and the properties of the daughter tracks, like the momentum, the impact parameter with respect to the primary vertex and the particle identification probabilities are stored. The main information stored for each secondary vertex consists of the reconstructed position, its covariance matrix and the χ^2 of the vertex fit, the number of prongs, along with references to the daughter particles and a reference to a (possible) parent particle. The secondary vertex and candidate information are stored in distinct arrays: for each candidate a reference to the related vertex is provided. It is possible to set a primary vertex specific of the candidate, obtained by excluding the daughter tracks from the calculation of the primary vertex position. This is important because high momentum tracks, which suffer low multiple scattering, are usually better reconstructed and enter the primary vertex reconstruction algorithm with a small error (thus with a large weight). Due to this, they "pull" the vertex position towards them. As a consequence the impact parameter with respect to the primary vertex is underestimated. In Fig. 6.16 the resolution on the track impact parameter with respect to the default primary vertex (computed using all tracks) can be compared to the resolution on the impact parameter with respect to the true primary vertex. This bias can be partially corrected for by recalculating the vertex position excluding the track for which the impact parameter is evaluated (black circles in Fig. 6.16).

The distance between the reconstructed primary and secondary vertices can be reduced by the above effect, because particles coming from the decay of heavy-flavour mesons have usually high momentum. A possible solution is to recalculate, candidate by candidate, the primary vertex position excluding the tracks involved in the candidate construction. If this is

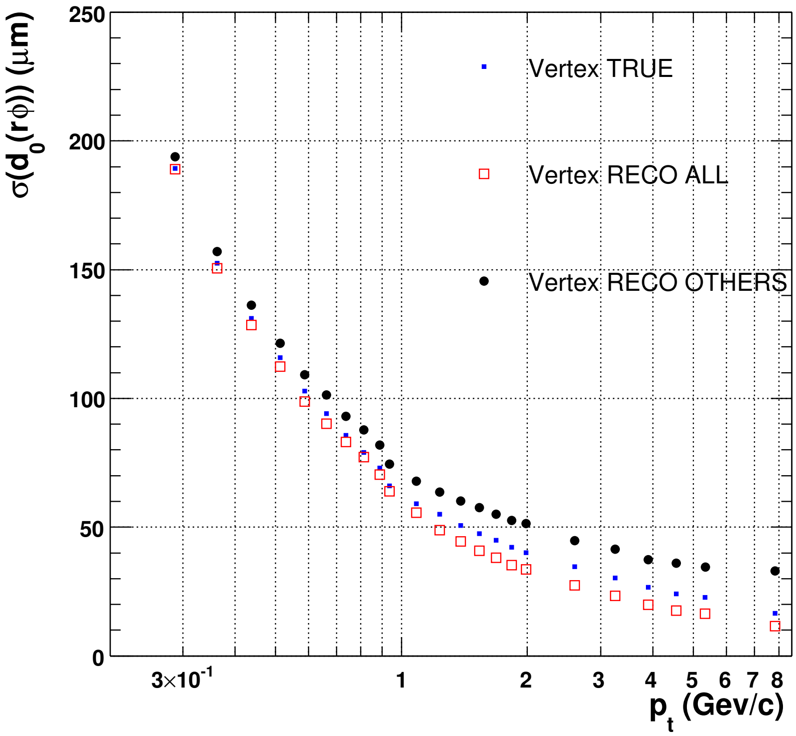

Figure 6.16: Impact parameter resolution using three distinct primary vertex, the true vertex position (blue circle), the vertex reconstructed using all tracks (red boxes) and the vertex reconstructed excluding the track for which the impact parameter is computed (black circle).

done, the distribution of the product of the impact parameters of the π and K coming from a $D^0 \to K^-\pi^+$ decay broadens and is slightly shifted towards negative values, that is, towards the region where the background and the signal differ, as shown in Fig. 6.17.

The selection flow

The candidates are constructed, event by event, in a series of "hierarchical" loops on the reconstructed tracks and stored into arrays (one per analysis channel). As already mentioned, the secondary vertices are stored in an independent array and the connection between candidates and secondary vertices is provided through references, allowing vertex sharing among candidates (useful, for instance, for the $D^0 \to K^-\pi^+$ and $D^{+\star} \to K^-\pi^+\pi^-_{\rm soft}$ channels). The cut values of the selection variables are not fixed and can be configured by means of a configuration file. The number of candidates in a channel is roughly proportional to N^{np}, with np being the number of prongs and N the number of reconstructed tracks in an event: the "hierarchy" in the application of the cuts starts from single-track cuts, then cuts on the pairs are considered, then on the triplets and finally on the quadruplets. The selection flow is depicted in Fig. 6.18. As a first step, two distinct sets of cuts are considered for the single–track variables: "displaced–track" cuts ($p_{\rm t} > p_{\rm t}^{cut}$ and impact parameter $|d_0^{r\phi}| > d_0^{cut}$), to

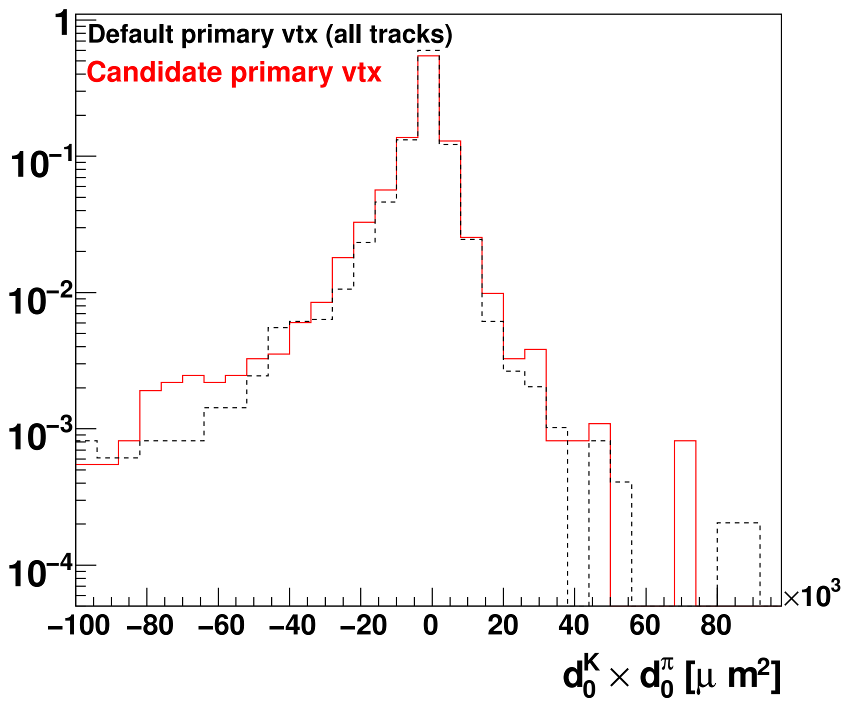

Figure 6.17: Product of the daughters impact parameters for $D^0 \to K^-\pi^+$ signal candidates in the range $1 < p_t(D^0) < 2\mathrm{GeV}/c$. The dotted line refers to the case the primary vertex is reconstructed using all tracks while the solid line refers to the case the D^0 daughters are excluded from the primary vertex position computation.

select tracks coming from secondary vertices and "soft pion" cuts ($p_t < p_t^{\mathrm{cutsoft}}$ and impact parameter $|d_0^{r\phi}| < d_0^{\mathrm{cutsoft}}$), to select primary tracks that could come from the soft pion of the $D^{+*} \to D^0\pi^+$ decay. Tracks incompatible with both kinds of cuts are rejected. The second step consists of the construction of all the possible pairs of "displaced" tracks. Opposite-charged (+,-) pairs as well as *like-sign* pairs are considered, the latter for the study of the background and of its properties. For each pair a secondary vertex is computed. The selection is then split in two steps. In the first step, the pairs are treated as representatives of tracks coming from a two prong decay (from D^0 or J/Ψ mesons). Specific cuts for the $J/\Psi \to e^+e^-$, $D^0 \to K^-\pi^+$ reconstructions, and special cuts for D^0 from a D^{+*} ($\equiv D^0 \leftarrow D^{+*}$) are sequentially applied. The pairs surviving the J/Ψ cuts are stored as J/Ψ candidates. If a pair survives the special cuts for the $D^0 \leftarrow D^{+*}$, it is matched to the "soft pion" tracks and, according to a selection based on specific cuts for the $D^{+*} \to K^-\pi^+\pi^+$ channel, D^{+*} candidates are created. A pair is stored as a D^0 candidate if it survives the cuts for the $D^0 \to K^-\pi^+$ or/and it survives the special cuts for the $D^0 \leftarrow D^{+*}$ and at least one D^{+*} candidate is found. In the second step, the pairs constitute the base for the construction of the triplets. A loop is performed on all "displaced" tracks and with each triplet a three–prong candidate is constructed. Specific cuts are then applied for the $D^+ \to K^-\pi^+\pi^+$ and $D_s^+ \to K^-K^+\pi^+$ decay channels and D^+ and D_s^+ candidates are stored. The last step is the construction of the

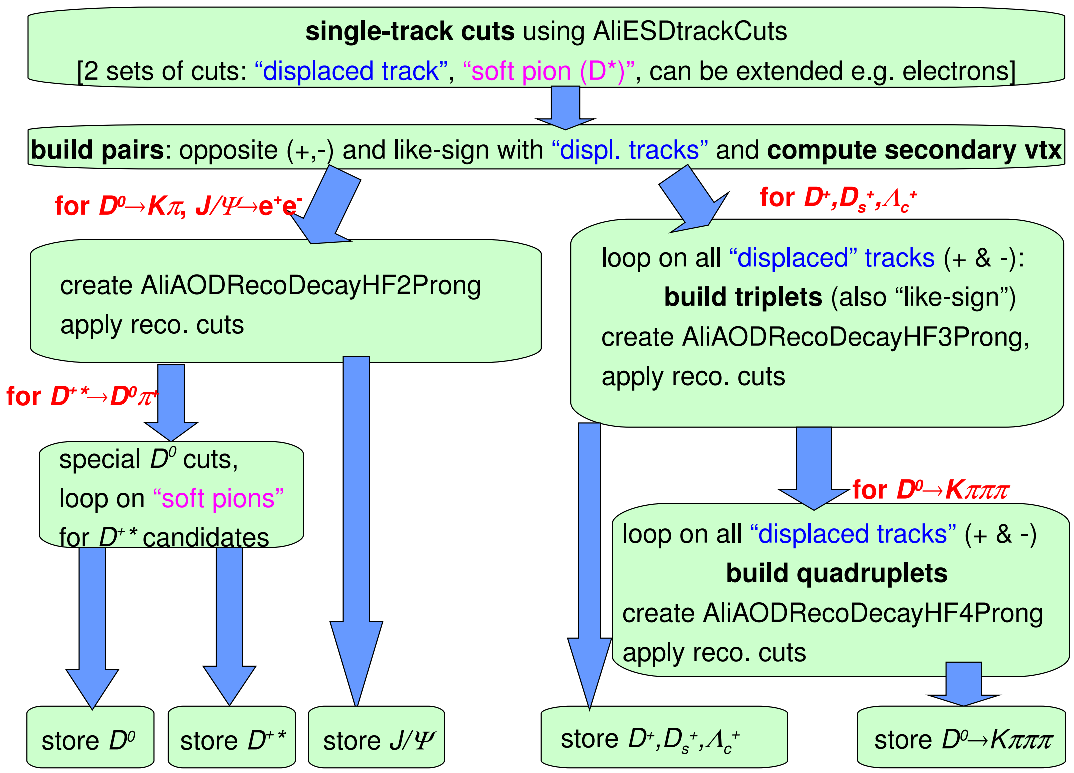

Figure 6.18: Selection and reconstruction flow for secondary vertices (from [132]). AliAODRecoDecayHF2Prong, AliAODRecoDecayHF3Prong, AliAODRecoDecayHF4Prong are the names of the software objects representing candidate pairs, triplets and quadruplets.

quadruplets for the $D^0 \to K^-\pi^+\pi^-\pi^+$ channel These are created starting from the triplets, in a further loop on all “displaced” tracks. The quadruplets surviving the specific selection for this channel are stored.

6.6.3 Analysis of the reconstructed candidates on the CAF/GRID

The analysis of secondary vertices and the study of the produced candidates, is performed via a dedicated “analysis train” that can analyze files stored on the GRID, on CAF as well as on a local computer. Each of the following analysis corresponds to a different task (wagon) that can be added to the train:

- Secondary vertex resolution analysis.
- Invariant mass analysis for the $D^0 \to K^-\pi^+$ channel.
- Invariant mass analysis for the $D^+ \to K^-\pi^+\pi^-$ channel.
- Analysis of secondary J/Ψ from $B \to XJ/\Psi, J/\Psi \to e^+e^-$.
- Invariant mass analysis of like-sign candidates for the J/Ψ decay channel.

- Invariant mass analysis of the like sign candidates for D^0 decay in two prongs
- Correction Framework for calculation of efficiency correction factors.
- Analysis of secondary D^0 mesons coming from B mesons.

More details on the structure of the train can be found in [132]. Most of the figures presented in this and the following chapter have been produced using the heavy–flavour train.

6.7 Main sources of systematic errors

As explained in Section 6.1, a number of corrections are applied to extract the cross–section from the raw yield signal. Each of them can introduce systematic errors. In Table 6.5 the main corrections and the expected systematic errors introduced are listed. In Table 6.6 the relative systematic errors expected (from [3]) are reported.

Efficiency correction

The efficiency factor may depend on D^0 properties (p_t, η) and on other variables, like event properties (primary vertex reconstruction, event multiplicity, azimuthal particle distribution) and detector properties (dead zones, material budget). A "differential" correction accounting for the efficiency dependence on all the variables would require the analysis of a very large samples because the invariant mass analysis should be performed with the same "granularity". In the ALICE software framework, the possibility to construct an efficiency map in a n–dimensional space of selected variables has been developed. The efficiency correction is usually done only for the subset of D^0 variables related to the target measurement: if the (p_t, y) differential cross–section is under study both the invariant mass analysis and the efficiency correction calculation are performed in intervals of rapidity and transverse momentum. It is however important that simulations produce realistic distributions for all the relevant variables used in D^0 analysis and that detector properties are properly accounted for. The recovered efficiency can be formally written as

$$\epsilon(x_0^{D^0}, ..., x_m^{D^0}; y_0^{\text{det.}}, ..., y_j^{\text{det.}}, y_{j+1}^{\text{anal.}}, ..., y_k^{\text{anal.}}) = g(z_0^{D^0}, ..., z_m^{D^0}) \otimes \mathcal{T}_{\text{det.}}^{\text{reco.}}(x_0^{D^0}, ..., x_m^{D^0}; y_0^{\text{det.}}, ..., y_j^{\text{det.}}) \cdot \epsilon^{\star}(x_0^{D^0}, ..., x_m^{D^0}; y_{j+1}^{\text{anal.}}, ..., y_k^{\text{anal.}}) . \tag{6.13}$$

Table 6.5: Main corrections and related systematic errors.

	Correction	*Systematic error*
1)	Feed-down from beauty	Uncertainty on $b\bar{b}$ production at LHC
2)	Reconstruction efficiency	Tracking efficiencies and resolutions
3)	Acceptance	Geometrical detector acceptance
4)	From $D^0 \rightarrow K^-\pi^+$ to $D^0 \rightarrow X$	Error on branching ratio $D^0 \rightarrow K^-\pi^+$
5)	cross–section normalization	Pb–Pb: error on centrality selection and number of binary collisions pp: error on inelastic cross–section

Table 6.6: Expected relative systematic uncertainties for the measurement of $\mathrm{d}\sigma(D^0)/\mathrm{d}y$ in $|y| < 1$ and $p_\mathrm{t} > p_\mathrm{t}^\mathrm{min}$.

System	p–p $p_\mathrm{t}^\mathrm{min} = 0.5$ GeV/c
Correction for b feed-down	8%
Monte Carlo corrections	10%
Branching ratio	2%
Cross–section normalization	5%
Systematic error	**14%**

g is the probability that a $D^0 \to K^-\pi^+$ decay happens with properties specified by the set of variables z^{D^0}; g is convoluted with a detector term $\mathcal{T}_\mathrm{det}^\mathrm{reco}$ to express the probability that the decay is reconstructed with observed variables x^{D^0} (that may refer also to event properties like the event multiplicity); $\epsilon^\star$ represents a selection term describing the cut-variable space region allowed by the analysis selection.

The calculation of the efficiency correction for a subset of $j < m$ variables (e.g. only as a function of p_t) can formally be seen as the integration of the efficiency ϵ in the $j - m$ dimensional space of the other variables.

Systematic errors arise when g and/or $\mathcal{T}_\mathrm{det}^\mathrm{reco}$ in the MC differ from the real ones. It is reasonable to assume that these uncertainties will initially amount to about 10% [3]. However, experience from other experiments suggests that this kind of systematic error can be reduced after few years of running as the understanding of the detector response improves.

Chapter 7

Feed–down from B mesons

At LHC energies, a significant fraction of D^0 mesons comes from the decay of B mesons. The cross–section for B meson production is basically determined by the cross–section for $b\bar{b}$ production reported in Table 2.2. Most of the B meson decay channels includes a $D^0(\bar{D}^0)$ or a $D^\star$, $\mathrm{BR}(b_{\mathrm{hadr.}} \to D^0 X) = 61.0 \pm 3.1\%$, $\mathrm{BR}(b_{\mathrm{hadr.}} \to D^\star X) = 17.3 \pm 2.0\%$, for $B^\pm/B^0/B^0_s/b-$ baryon admixture [58]. In order to recover the cross–section for the production of primary charmed mesons[1], this contribution must be estimated and properly subtracted from the raw signal yield obtained with the invariant mass analysis. The chapter focuses on the possibility to extract the fraction of "direct" D^0 mesons (f_D in Eq. 6.1) exploiting the different shapes of the impact parameter distributions of primary and secondary D^0 mesons, the latter strongly influenced by the B decay length. This approach has been already used by CDF [8]. The main alternatives to this option consist in relying on Monte Carlo estimates based on pQCD calculations first and, then, on the measurement of beauty production, which is one of the main target of the ALICE heavy–flavour physics program.

7.1 Feed–down from B mesons

The correction for the B feed–down is one of the main sources of systematic errors (see Table 6.6). In Fig. 7.2, left panel, the normalized p_{t} spectra for primary and secondary (from B mesons decays) D^0 are shown. The average p_{t} for secondary D^0 is 2.45 GeV/c. Even if the D^0 shares the B energy with more than one particle on average (Fig. 7.2, right panel), due to the large B meson mass the p_{t} spectrum is harder for secondary than for primary D^0. As it is clear from Fig. 7.3 (left panel), a strong correlation is present between the D^0 and the parent B hadron transverse momenta. The D^0 retains a large fraction of the B momentum and the angle between the two momenta is small on average (Fig 7.3, right panel). As depicted in Fig. 7.1, reconstructed tracks coming from "secondary" D^0 mesons are, on average, rather displaced from the primary vertex because of the relatively long lifetime of B mesons ($c\tau \approx 460 - 490$ μm). The selection applied on the reconstructed candidates, aimed at finding secondary vertices displaced from the primary vertex, further enhances their contribution to the raw signal yield (Fig. 7.4, described in the next section). In principle, it could be possible to tune the cut values in order to minimize this contribution. For instance, a cut on the track maximum impact parameter $|d_0| < 500$ μm reduces the fraction of D^0 from B.

[1] Through the chapter D^0 coming from the primary vertex are referred as "primary" or "direct" D^0 while those coming from B decay are referred as "secondary" D^0.

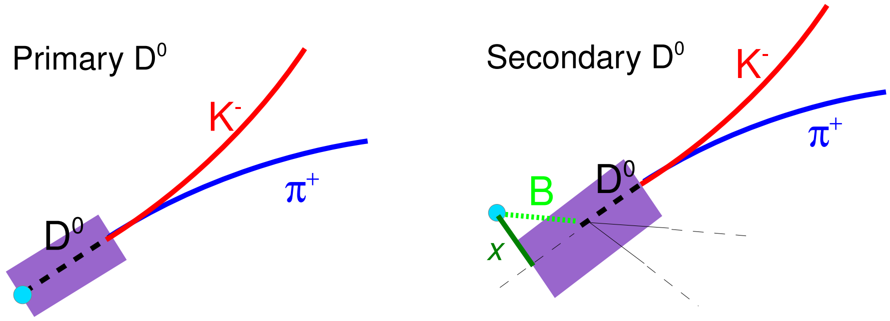

Figure 7.1: Schematic representation of a $D^0 \to K^-\pi^+$ decay for primary (left) and secondary (right) D^0. The light blue circle represents the primary vertex. The (purple) rectangle represents the contribution of the detector charm impact parameter resolution function to the observed D^0 impact parameter (see text). The (light green) thin dashed line is the B meson flight line while x, the (dark green) continuous line, is the true impact parameter of the secondary D^0.

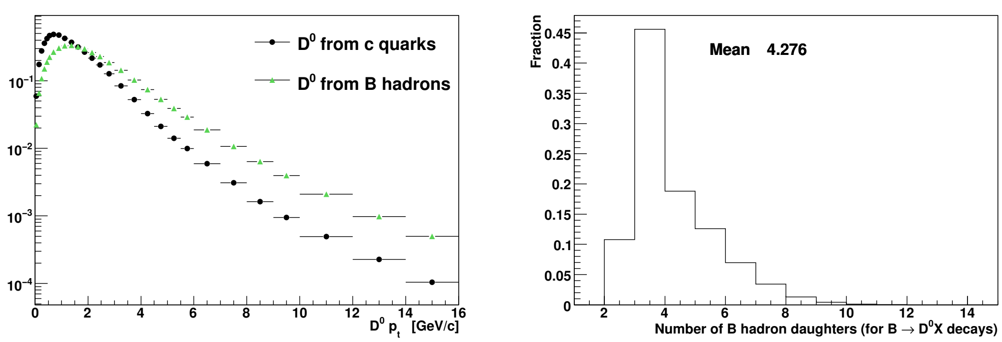

Figure 7.2: p_{t} spectra for primary D^0 and for D^0 from B mesons decays (left panel) and number of B meson daughters for $B(\to D^\star X) \to D^0 X$ decays. No selection is applied and all generated particles are considered (there is not a selection for the detector acceptance).

Nevertheless, this would still require the subtraction of the residual fraction of secondary D^0 on the basis of Monte Carlo simulations. The possibility to estimate the fraction of prompt D^0 directly from data can reduce the systematic error deriving from Monte Carlo models used to simulate beauty production. CDF attained this by estimating the fraction of "direct" D^0 mesons (f_D) via the analysis of the impact parameter distribution of the reconstructed candidate D^0 [8] . In this section the possibility to use the same method for the ALICE case is investigated.

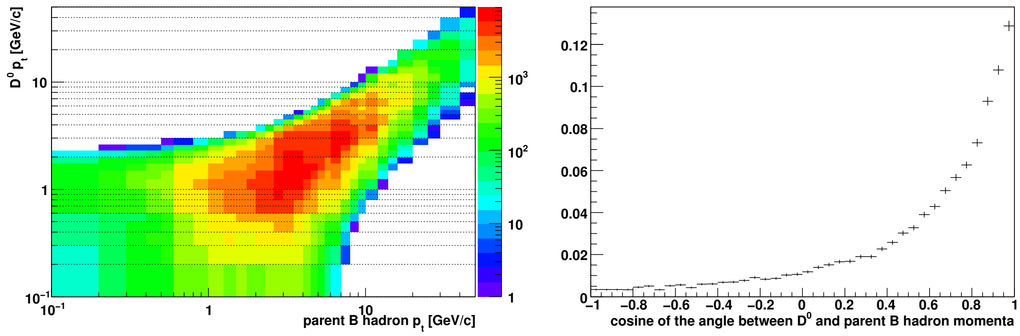

Figure 7.3: On the left, D^0 p_t as a function of the parent B hadron p_t. On the right: distribution of the cosine of the angle between the D^0 and B hadron momenta. No selection is applied and all generated particles are considered (there is not a selection for the detector acceptance).

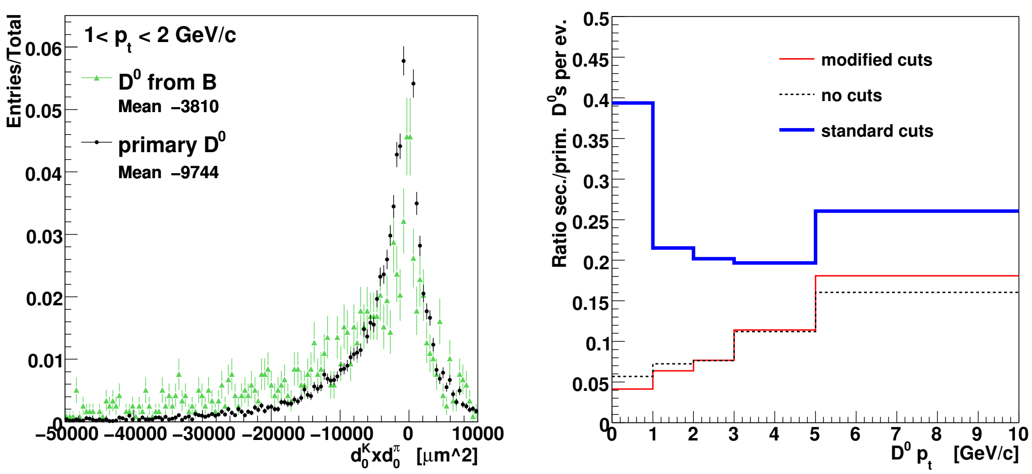

Figure 7.4: Left panel: product of kaon and pion track impact parameter distribution for primary and secondary D^0. Right panel: ratio between secondary and primary D^0 produced per event without cuts (dashed line), with the modified set of cuts (continuous line) and with the standard set of cuts (thicker continuous line) described in the text.

7.1.1 D^0 meson impact parameter distribution function

The impact parameter (d_0) distribution for D^0 mesons is parametrized as follows:

$$F_{d_0} = f_D F_{\mathrm{det}}(d_0) + (1 - f_D) \int F_B(x) F_{\mathrm{det}}(d_0 - x) \mathrm{d}x \,. \tag{7.1}$$

F_{det} is the *detector resolution impact parameter function for charm*, describing the impact parameter distribution of primary charm, that is determined mainly by the detector resolution on the daughter track positions and momenta. f_D is the fraction of primary charm. The integral term is the convolution of the *true impact parameter distribution function* for D^0

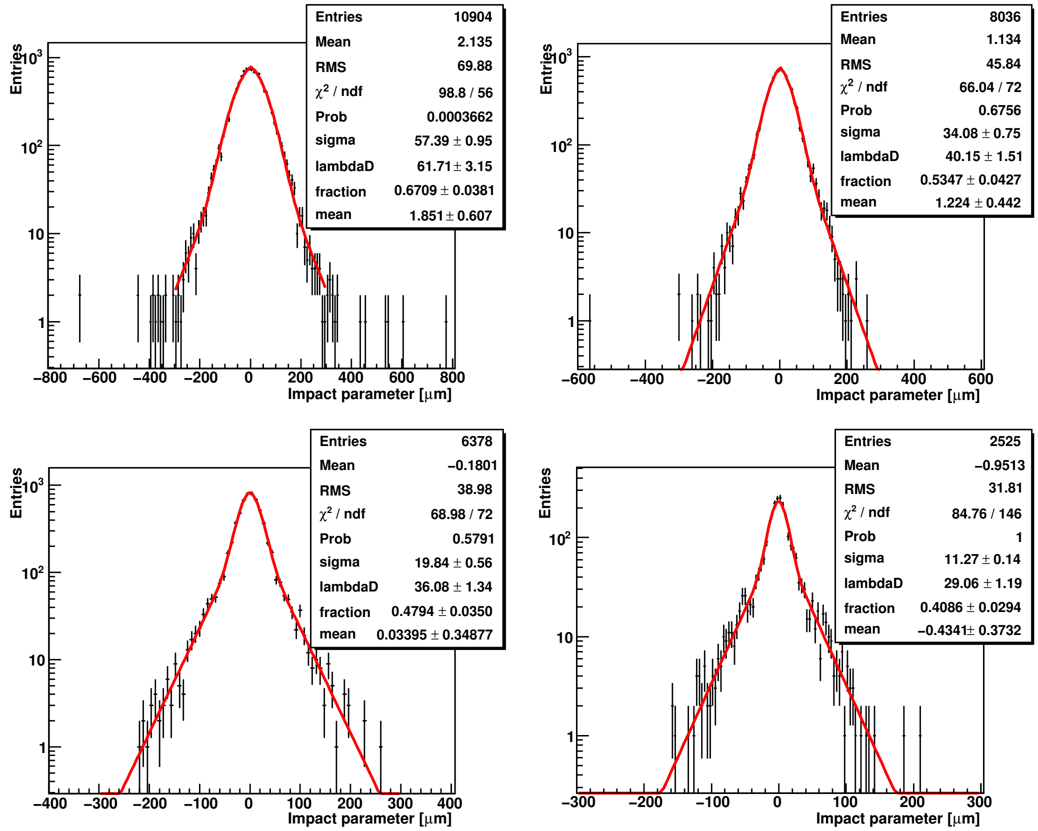

Figure 7.5: "Reconstructed" impact parameter distribution for primary D^0 mesons in different p_t intervals. The continuous lines is the fit to the distribution peak done with a Gaussian function plus exponential tails (Eq. 7.2). The momentum intervals are (from upper panel on the left, clockwise order): $1 < p_\mathrm{t} < 2$ GeV/c, $2 < p_\mathrm{t} < 3$ GeV/c, $3 < p_\mathrm{t} < 5$ GeV/c, $p_\mathrm{t} > 5$ GeV/c.

coming from B mesons (F_B) with F_det: it expresses the probability to observe an impact parameter d_0 if the true impact parameter (x) distribution is described by F_B. By properly modelling each term, Eq. 7.1 can be used to fit the impact parameter distribution of the reconstructed candidate D^0 and recover f_D, treated as a fit parameter.

Cut selection

An implicit assumption in Eq. 7.1 is that the "detector" contribution f_D is really a "resolution" term, equal for primary and secondary D^0, that is, it does not depend on the true D^0 impact parameter. This hypothesis can be violated by the use of cut variables correlated with the impact parameter of the reconstructed candidates and operating differently on secondary and primary D^0. Special care is needed if the single track impact parameter as well as the product of the kaon and pion impact parameters are used as cut variables, for this method to work properly. The 500 μm selection on the single track impact parameter in the "standard cuts" set reduces the fraction of secondary D^0 but also biases the impact parameter distribution of the residual fraction. Conversely the selection on the product of the pion and kaon track

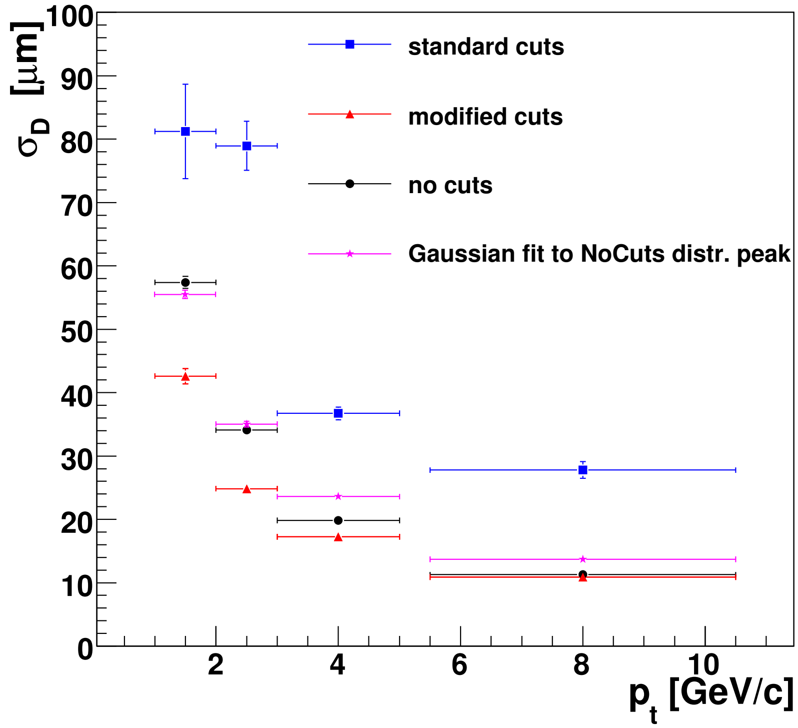

Figure 7.6: Sigma obtained from the fit of the impact parameter distributions for primary D^0 mesons in different D^0 transverse momentum intervals (the last bin extends to infinite momentum). The purple star–like markers represent the result of the fit with a simple Gaussian function to the central peak of the distribution obtained without any cut applied. In the other cases the function in Eq. 7.2 has been used to fit the distributions, recovered with different cut selections (described in the text).

impact parameters strongly enhances the fraction of secondary D^0 mesons since displaced tracks are selected. In Fig. 7.4 (left panel) the distributions of the product of the pion and kaon track impact parameters recovered for primary and secondary D^0 are compared. A

Table 7.1: Minimum bias collection ($\sim 5.4 \cdot 10^7$ events): signal (S), background (B), relative background error, significance ($\mathcal{S}$) recovered from the invariant mass analysis applying the “modified cuts” defined in the text. The signal and background estimated from the fit are compared to the Monte Carlo values. The significance extrapolation to the reference number of events expected for ≈ 1 year data taking is shown.

p_t[GeV/c] bin	S [MC S]	B [MC B]	δB/B (%)	$\mathcal{S}$ (MC)	$\mathcal{S}(10^9$ev.)
$1 < p_t < 2$	$207 \pm 63\,[64]$	$2729 \pm 50\,[2803]$	2.6	1.2	6.1
$2 < p_t < 3$	$53 \pm 16\,[84]$	$182 \pm 7\,[132]$	27	5.5	28.2
$3 < p_t < 5$	$225 \pm 32\,[208]$	$536 \pm 18\,[509]$	5.3	7.5	38.4
$p_t > 5$	$157 \pm 26\,[173]$	$196 \pm 20\,[150]$	30	9.1	46.6

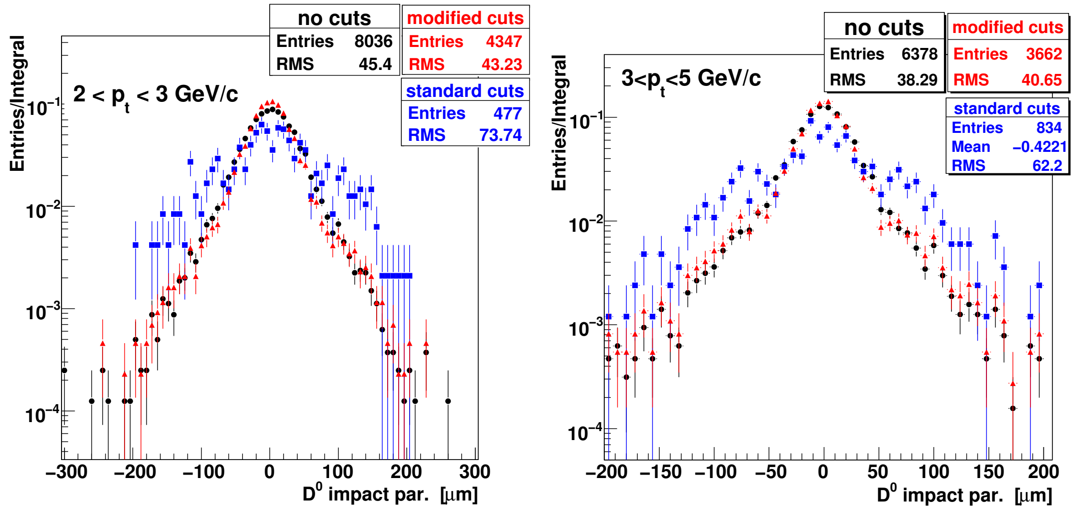

Figure 7.7: Comparison of primary D^0 impact parameter distributions (normalized to the same integral) obtained without cut selection (black circles), with the standard set of cuts (blue square markers) and with the “modified” cuts (red triangles). See text for cuts definition.

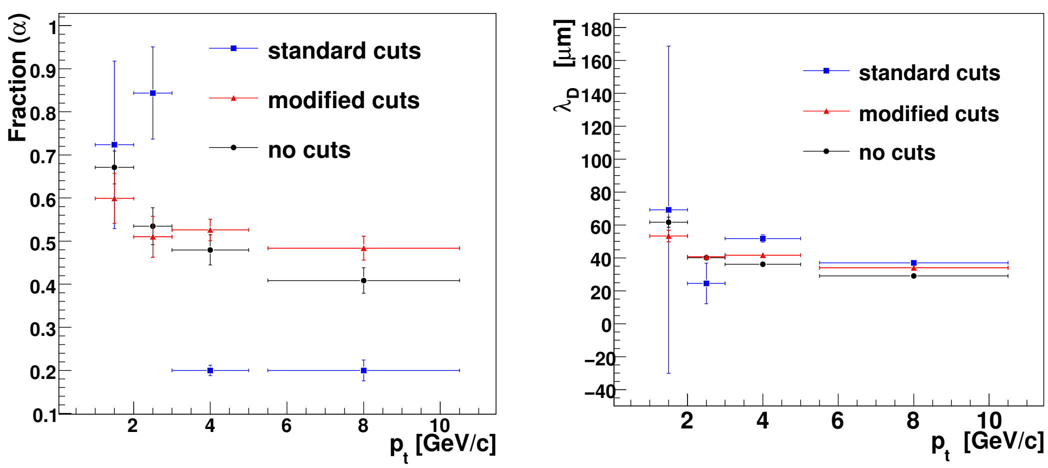

Figure 7.8: Gaussian term fraction α (left panel) and exponential tail parameter λ_D (right panel) obtained from the fit of primary D^0 meson impact parameter distributions in different D^0 transverse momentum intervals (the last bin extends to infinite momentum) and for different selections on the candidates (see text) using the fit function in Eq. 7.2.

too strong selection on the product of the pion and kaon track impact parameters influences the shape of the primary D^0 impact parameter distribution, reducing its Gaussian part (see Section 7.1.2). This constitutes a major difficult for the method discussed here. Therefore two distinct sets of cuts are considered in this section. For the first set (“standard cuts”), the values reported in Table 6.2 are chosen. The second set (“modified cuts”) differs from the previous one for a softer selection on the product of the kaon and pion track impact parameters and on the single track impact parameter:

- $|d_0^{K,\pi}| < 1000 \quad \mu m$
- $d_0^K \times d_0^\pi < 0 \quad .$

In Fig. 7.4 (right panel) the ratio between secondary and primary D^0 produced per event is shown without cuts and for the two sets of cuts described. The by–product of a softer selection is the increase of the amount of background and, thus, of the statistical error on the charm production measurement. The significance recovered with this new set of cuts from the analysis of $\sim 5.4 \cdot 10^7$ minimum bias events is shown in Table 7.1. A large worsening with respect to the "standard cuts" case (Table 6.3) is present only in the first $p_{\rm t}$ bin considered, while in the others the results are similar.

7.1.2 The detector resolution impact parameter function for primary D^0 mesons

The D^0 impact parameter is calculated as the distance between the primary vertex and the direction of the D^0 momentum vector. In Fig. 7.5 the impact parameter distributions obtained for primary D^0 without cut selection are shown for different transverse momentum intervals. The function in Eq. 7.2 has been used to fit the histograms. For primary D^0, the central peak of the distribution is properly described by a Gaussian function because it is basically determined by the spatial resolution proper of the kaon and pion track reconstruction. The purple star–like markers in Fig. 7.6 represent the sigma of Gaussian fits to the D^0 distribution peaks obtained when no cuts are applied. The kaon and pion average momenta are higher for higher momentum D^0 and their tracks are reconstructed with better precision (e.g. see impact parameter resolution in Fig. 4.3). Accordingly also the D^0 impact parameter is better estimated, explaining the observed trend in Fig. 7.6. A suitable fitting function, used also by CDF, covering the entire distribution consists of a Gaussian term plus exponential tails:

$$F_{\rm det}(d_0) = \frac{\alpha}{\sqrt{2\pi}\sigma_D} e^{-\frac{d_0^2}{2\sigma_D^2}} + \frac{1-\alpha}{2\lambda_D} e^{\frac{-|d_0|}{\lambda_D}} \quad . \tag{7.2}$$

α represents the fraction of the distribution described by the Gaussian peak. The sigma obtained by fitting the distributions in Fig. 7.5 with the above function are represented by the filled black circles in Fig. 7.6. The distributions are "pre–fitted" in an iterative procedure, fitting separately the peaks and the tails until the optimal parameters are found. These are used as starting parameters to re–fit the distributions with fitting parameters constrained to stay within 10% from the starting ones. As shown in Fig. 7.6, the values of the sigma are quite close to those recovered with the simple Gaussian fits. The cut selection modifies the impact parameter distribution. In Fig. 7.7 the distributions obtained without any selection, with "standard cuts" selection and with the "modified cuts" (defined in the previous section) are compared. As already mentioned, a too stringent selection on the product of the kaon and pion impact parameters strongly affects the shape of the distribution of the reconstructed D^0 impact parameter. This problem has not been completely understood yet. In Fig. 7.8 the fraction of the Gaussian contribution α and the exponential tail parameter λ_D recovered in the three cases are shown. The values obtained for the "no cuts" and "modified cuts" cases are much more similar than those in the "standard cuts" case. In particular, the much lower α (~ 0.2) at high $p_{\rm t}$ implies that $F_{\rm det}$ can be hardly interpreted as a detector "resolution" function in the "standard cuts" case. However, the quality of the fit is very bad, highlighting that the function in Eq. 7.2 cannot be used to describe the impact parameter distribution shape properly with this set of cuts. Two solutions have been attempted: the first consists in adopting the "modified cuts", with the by-product of increasing the amount of background and, thus, the statistical error on the charm production measurement. For the second solution, which is still under study, no functional shape is assumed for describing the impact parameter distribution and histograms are directly used in place of $F_{\rm det}$ and F_B, without any fit.

7.1.3 The true impact parameter distribution function for secondary D^0

B mesons decay according to the exponential decay law with a proper decay length $c\tau \approx 460 - 490$ μm and cover a mean distance in the laboratory frame $\sim \beta\gamma c\tau$, that, at high energies, can consist of few millimetres (~ 1 mm at 10 GeV/c). The relatively long lifetime strongly influences the impact parameter of the decay products. In Fig. 7.9 the true impact parameter distributions of secondary D^0 mesons are shown for different D^0 transverse momentum intervals. Their shapes can be described by a double exponential function,

$$F_B(d_0) = \frac{\varepsilon}{2\lambda_1} e^{-\frac{|d_0|}{\lambda_1}} + \frac{1-\varepsilon}{2\lambda_2} e^{-\frac{|d_0|}{\lambda_2}}\,, \tag{7.3}$$

where ε is the fraction ascribed to the first exponential. As it is clear from the distributions shown and from the fitting parameters recovered, one of the two exponential functions describes the very central part of the distribution, while the other the most of the distribution. The parameters recovered depend on the $p_{\rm t}$. The cut selection (applied only in the four lower panels in the figure) is performed on the reconstructed candidates (not at the Monte Carlo level).

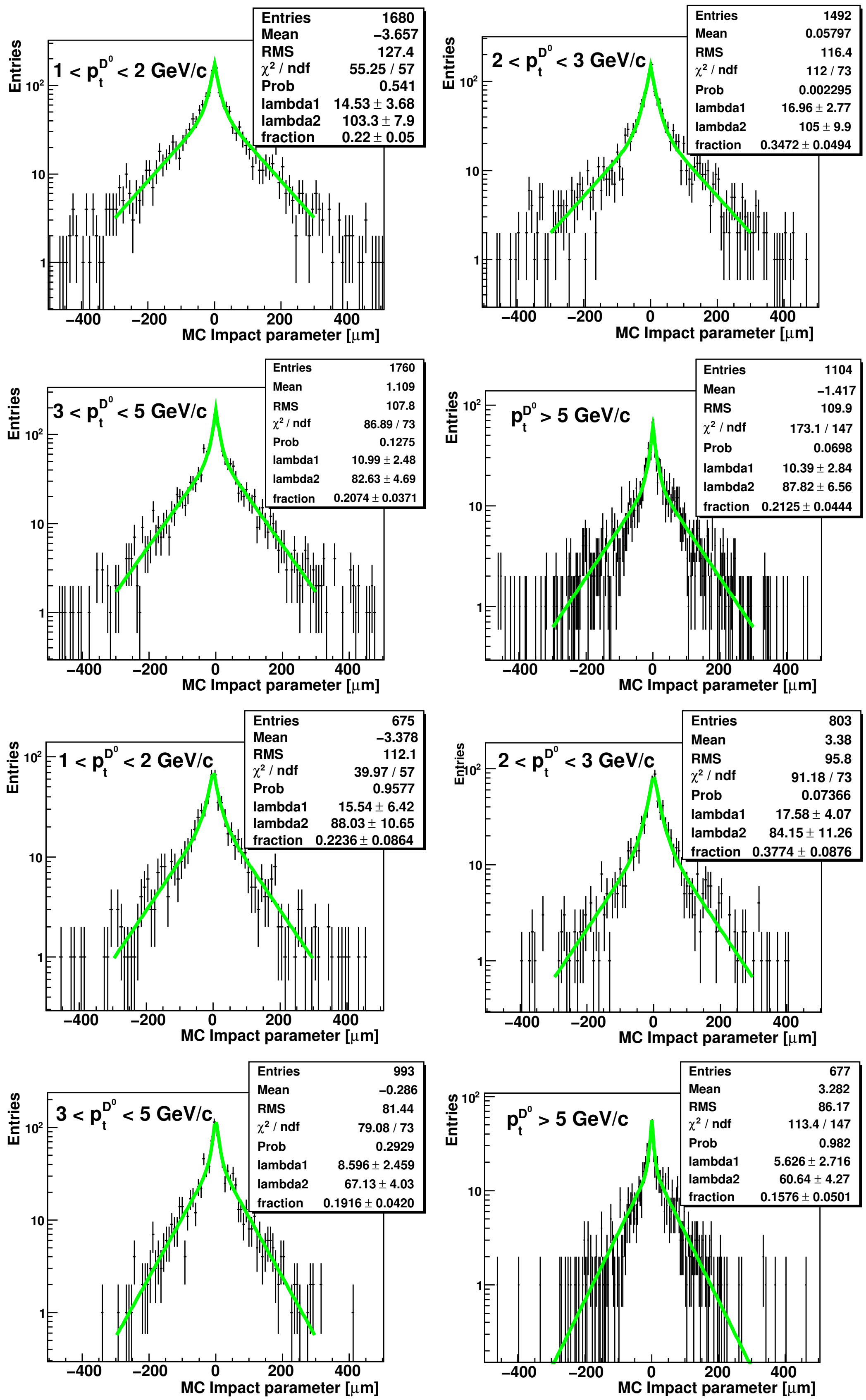

Figure 7.9: Monte Carlo impact parameter distribution for D^0 coming from B mesons in different $p_{\rm t}$ intervals without cut selection (four upper panels) and after cut selection (four lower panels) with the “modified cuts” set. The histograms are fitted (continuous lines) to the function defined in Eq. 7.3.

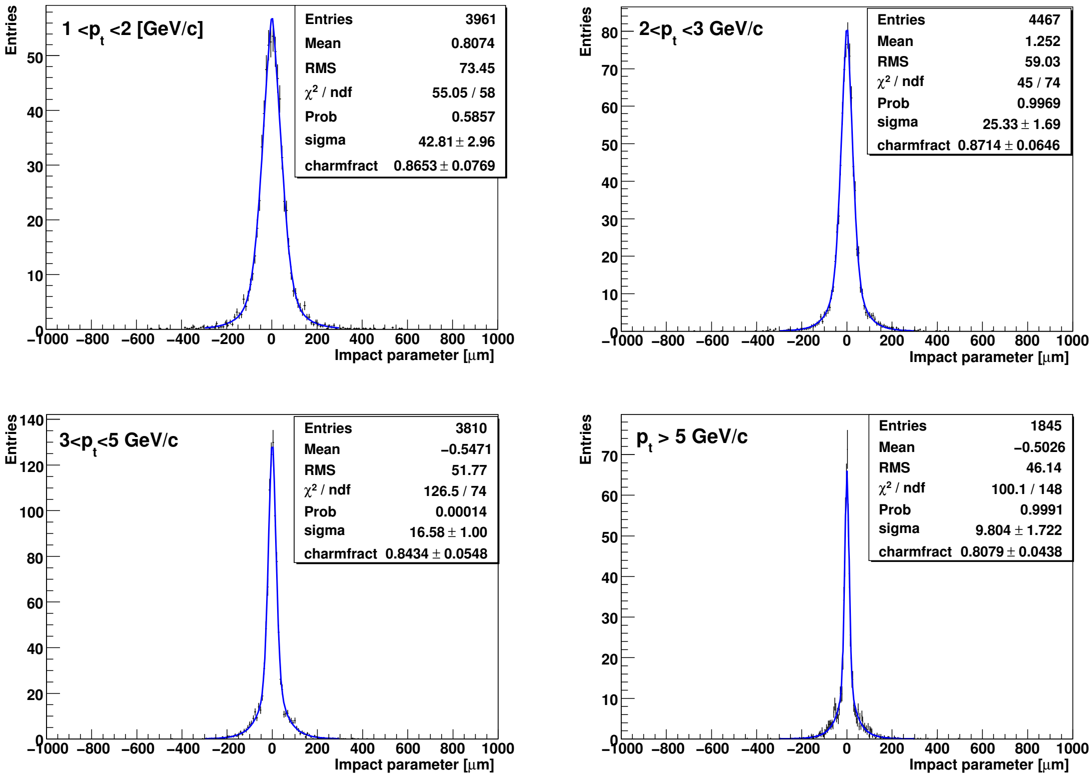

Figure 7.10: Fits to the impact parameter distributions obtained with a cocktail of 85% primary D^0 and 15% of secondary D^0 after the cut selection with the "modified cuts" set (see text). The fitting function used is defined in Eq. 7.1.

7.1.4 Tests without background contribution

Ad–hoc histograms are created merging, with proper weights, histograms from the "beauty–enriched" sample and histograms from the "charm–enriched" sample without background candidates in. The distributions obtained are fitted using the function defined in Eq. 7.1. The convolution is performed numerically even if the integral can be solved analytically. f_D and σ_D are taken as the fit parameters.

In the CDF analysis, the $F_{\rm det}$ shape is determined via the analysis of the $K^0_S \to \pi^+\pi^-$ decay channel applying to the candidate K^0_S the same selection criteria adopted for the D^0 case. The selected K^0_S are mostly primary (the fraction of secondaries is estimated to be smaller than 5%). A fit to the K^0_S impact parameter distribution, using the $F_{\rm det}$ function, fixes the Gaussian fraction α and the ratio σ_D/λ_D in the subsequent D^0 analysis. With this approach, the use of Monte Carlo simulations in the determination of $F_{\rm det}$ is avoided. A similar study has not been attempted yet for ALICE: the α parameter and the σ_D/λ_D ratio are recovered from Monte Carlo simulations fixing the F_D shape. The σ_D parameter in the final fit is constrained to stay within 10% to the input parameter: this condition was set while attempting to use this method also with the "standard cuts". With the "modified cuts" as well as without cuts this condition is always met even without constraints. In Fig. 7.10 the

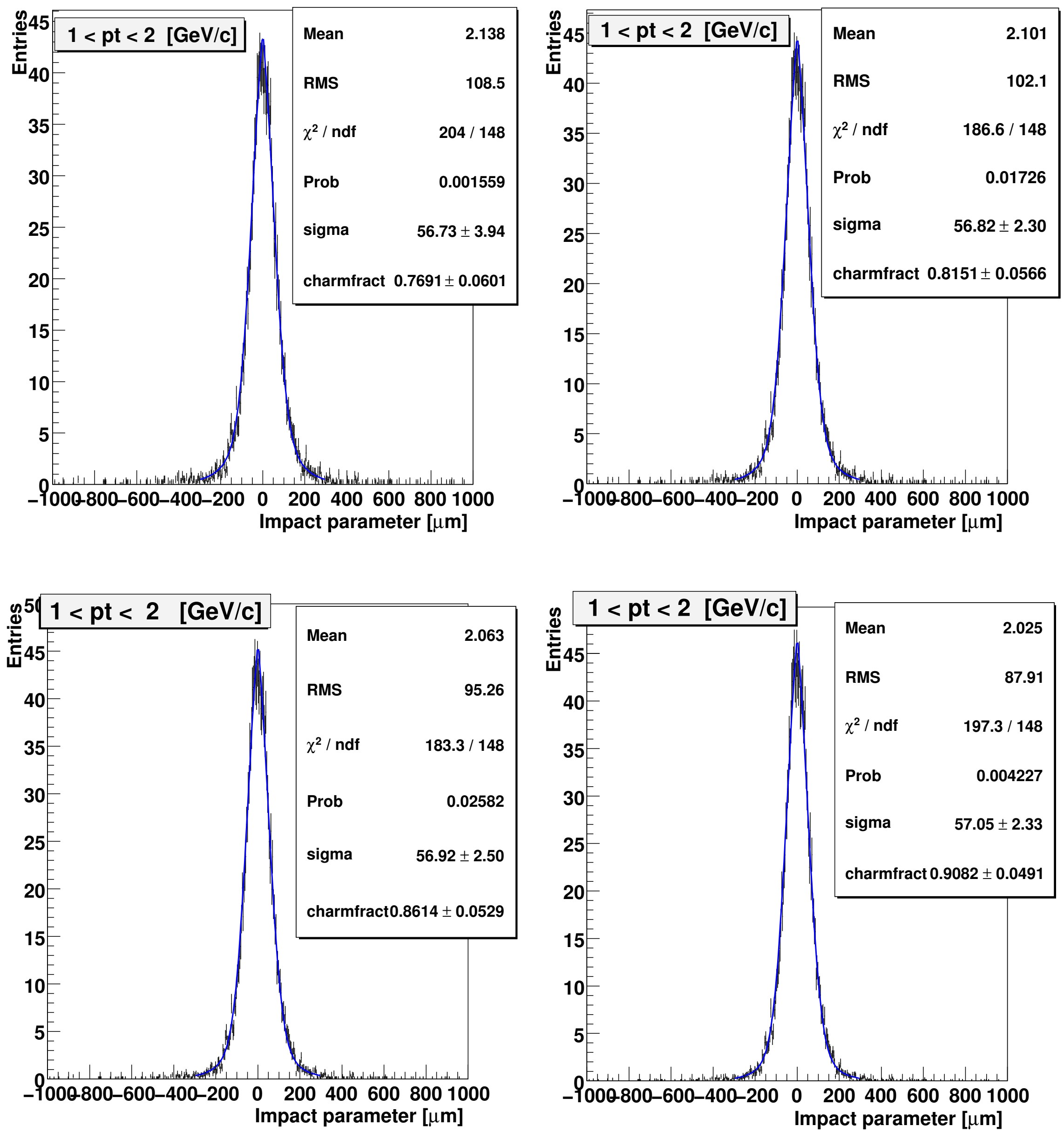

Figure 7.11: Fits to the impact parameter distributions obtained with different cocktails of primary and secondary D^0 in the interval $1 < p_{\rm t}^{D^0} < 2$ GeV/c without any cut selection. The fraction of primary D^0 are (in clockwise order starting from the upper left panel): 0.75, 0.8, 0.85, 0.9.

function defined in Eq. 7.1 is used to fit the distributions obtained with a fraction of prompt D^0 mesons $f_D = 0.85$. The histograms refer to the "modified cuts" case. The recovered fraction is compatible with the input fraction within errors in all the $p_{\rm t}$ intervals considered. In Fig. 7.11 for a fixed $p_{\rm t}$ interval ($1 < p_{\rm t}^{D^0} < 2$ GeV/c) the distributions obtained with different fractions of prompt D^0 mesons are shown for the "No Cuts" case. The results obtained are summarized in Table 7.2. The fractions recovered from the fit are always compatible with the input fractions within errors. It must be pointed out that systematic trends may arise because the input distributions are not independent. Therefore, the systematic underestimation of the recovered fractions in the higher $p_{\rm t}$ bin in the "modified cuts" case, absent in the "no cuts" case, could be related to statistical fluctuations affecting the specific impact parameter distribution observed for the primary D^0 candidates in this $p_{\rm t}$ interval.

7.1.5 Background contribution

Eq. 7.1 does not account for the contribution of the background candidates. Adding a background term, Eq. 7.1 can be rewritten as:

$$F_{d_0} = \frac{S}{T}\left(f_D F_{\rm det}(d_0) + (1-f_D)\int F_B(x)F_{\rm det}(d_0-x){\rm d}x\right) + \frac{B}{T}F_{\rm back}(d_0)\,. \tag{7.4}$$

The signal (S) and background (B) contributions can be estimated from the invariant mass analysis. The background distribution ($F_{\rm back}$) can be approximated with the impact parameter distribution observed for candidates in the sidebands of the invariant mass peak, defined by the mass interval $6\sigma(M) < |M - M_{D^0}| < 12\sigma(M)$. The sideband region has been chosen far enough from the signal invariant mass peak to exclude eventual contributions from the reflected signal (Section 6.2.5). The background distribution, normalized to the proper background contribution (B) is directly subtracted from the total distribution. To avoid any biases, background subtraction must proceed via the following steps:

Table 7.2: Recover primary D^0 fraction f_D and σ_D for different input fractions in the case that no background contribution is present. σ_D are in μm.

$p_{\rm t}$ bin [GeV/c]	input f_D	No cuts f_D reco	No cuts σ_D input	No cuts σ_D reco	Modified cuts f_D reco	Modified cuts σ_D input	Modified cuts σ_D reco
$1 \div 2$	0.50	0.57 ± 0.08	57 ± 1	59 ± 4	0.52 ± 0.11	43 ± 1	42 ± 6
	0.75	0.78 ± 0.06	57 ± 1	58 ± 3	0.77 ± 0.09	43 ± 1	43 ± 3
	0.85	0.87 ± 0.05	57 ± 1	58 ± 2	0.86 ± 0.08	43 ± 1	43 ± 3
	0.90	0.91 ± 0.05	57 ± 1	58 ± 2	0.91 ± 0.07	43 ± 1	43 ± 3
$2 \div 3$	0.50	0.58 ± 0.05	34 ± 0.8	36 ± 2	0.57 ± 0.08	24.8 ± 0.8	26 ± 4
	0.75	0.79 ± 0.04	34 ± 0.8	35 ± 2	0.78 ± 0.07	24.8 ± 0.8	25 ± 2
	0.85	0.88 ± 0.04	34 ± 0.8	35 ± 1	0.87 ± 0.06	24.8 ± 0.8	25 ± 2
	0.90	0.92 ± 0.03	34 ± 0.8	35 ± 1	0.92 ± 0.06	24.8 ± 0.8	25 ± 2
$3 \div 5$	0.50	0.52 ± 0.04	19.8 ± 0.6	19 ± 1	0.53 ± 0.06	17.3 ± 0.1	16 ± 2
	0.75	0.76 ± 0.04	19.8 ± 0.6	20 ± 1	0.75 ± 0.06	17.3 ± 0.1	16 ± 1
	0.85	0.86 ± 0.03	19.8 ± 0.6	19.8 ± 0.9	0.84 ± 0.05	17.3 ± 0.1	17 ± 1
	0.90	0.91 ± 0.03	19.8 ± 0.6	19.8 ± 0.8	0.89 ± 0.05	17.3 ± 0.1	17 ± 1
> 5	0.50	0.53 ± 0.04	11.3 ± 0.1	10 ± 2	0.51 ± 0.04	10.9 ± 0.1	10 ± 1
	0.75	0.76 ± 0.04	11.3 ± 0.1	10.8 ± 0.7	0.72 ± 0.04	10.9 ± 0.1	10 ± 1
	0.85	0.86 ± 0.03	11.3 ± 0.1	11.0 ± 0.6	0.81 ± 0.04	10.9 ± 0.1	10 ± 2
	0.90	0.91 ± 0.03	11.3 ± 0.1	11.1 ± 0.6	0.86 ± 0.05	10.9 ± 0.1	10 ± 1

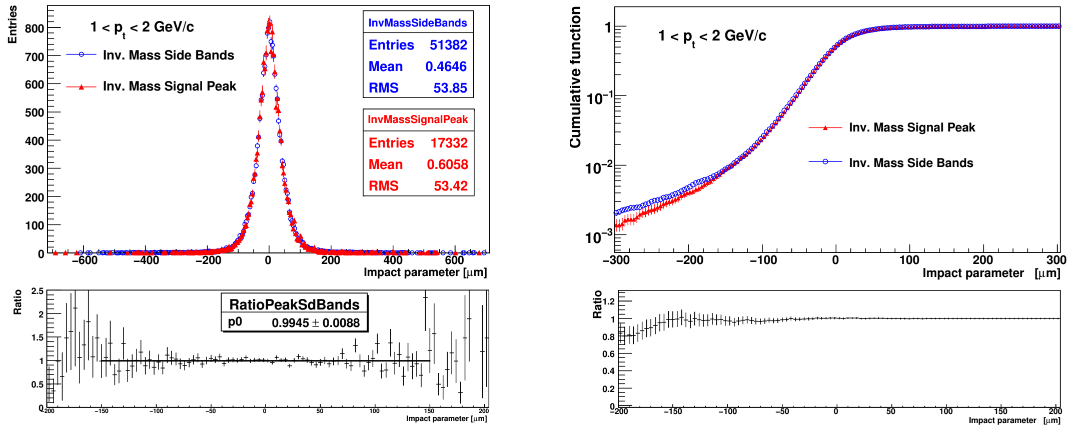

Figure 7.12: Comparison between the impact parameter distribution of background D^0 in the invariant mass signal region and in the the invariant mass side band region defined in the text. The set of "modified cuts" has been used for the candidate selection. On the left, large panel: comparison between the two distributions normalized to the same integral. The bin–by–bin division is shown in the small panel. The continuous line represents the average (p0 parameter). On the right, large panel: cumulative distributions obtained from the distributions in the left panel. The bin–by–bin division is shown in the small panel. The continuous line represents the average (p0 parameter).

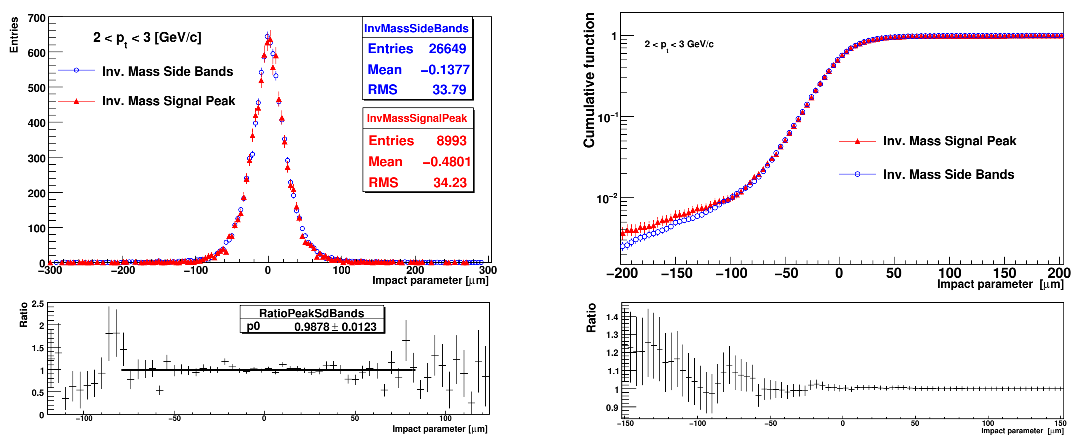

Figure 7.13: Same as in Fig. 7.12 but for a different D^0 transverse momentum interval.

On the data :

1. Extract the background amount B from the invariant mass analysis.
2. Extract the background impact parameter shape, F_{back}, from the impact parameter distribution of the candidates in the invariant mass side band region.

On the simulation :

3. Check that the background impact parameter distribution is not correlated to

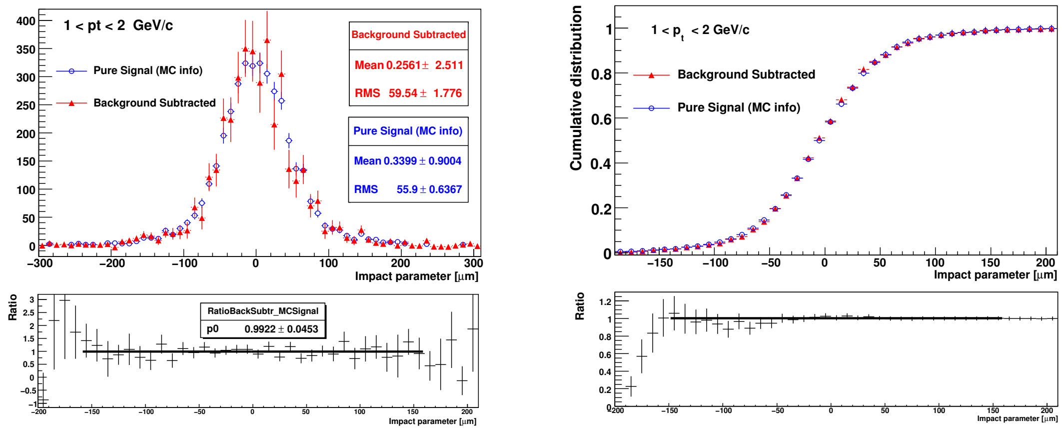

Figure 7.14: Comparison between the impact parameter distribution for signal D^0 and the impact parameter distribution obtained by subtracting to the impact parameter distribution of all the selected candidates the impact parameter distribution of the candidates in the invariant mass side bands, with the true amount of background (B) used as weight. The set of "modified cuts" has been used for the candidate selection. On the left, in the upper panel, the two distributions are shown, in the lower panel they are divided bin–by–bin. The continuous line represents the average ratio (p0 parameter). On the right, large panel: cumulative distributions obtained from the distributions on the left panel. The bin–by–bin division is shown in the small panel. The continuous line represents the average (p0 parameter).

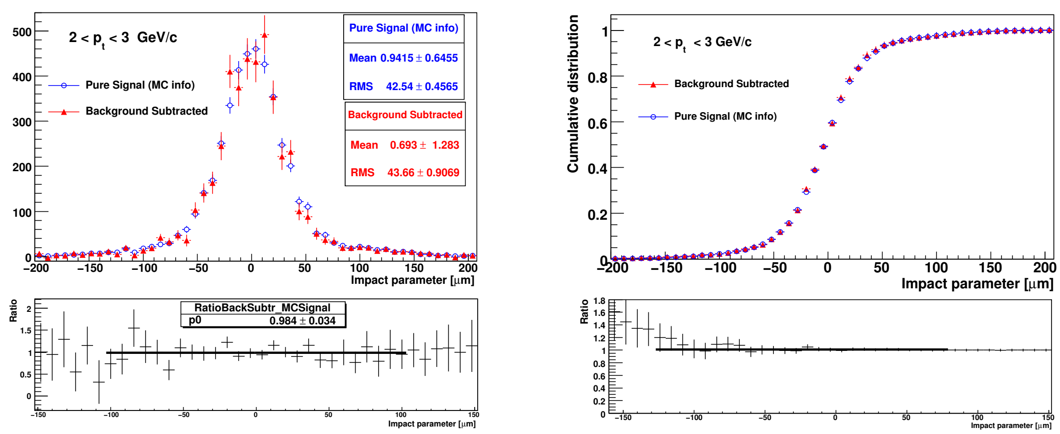

Figure 7.15: Same as in Fig. 7.14 but for a different D^0 transverse momentum interval.

the invariant mass, that is, check that the impact parameter distribution has the same shape for background candidates in the invariant mass sidebands and in the invariant mass signal region.

4. Check that the background impact parameter distribution observed on the data, F_{back}, is compatible with the one recovered on simulated events.

On the data :

5. If the last two conditions are fulfilled, $BF_{\mathrm{back}}(d_0)$ can be safely subtracted from the total candidate impact parameter distribution without introducing biases.

In Fig. 7.12 and 7.13 the comparison between the impact parameter distribution of background D^0 in the invariant mass signal region and in the the invariant mass side band region is shown. The set of "modified cuts" has been used in the candidate selection. For both p_{t} intervals shown, the two distributions, normalized to the same integral, are compatible bin-by-bin within errors (larger panels on the left). The bin–by–bin ratio (smaller panels on the left) is always close to unity, at least in the regions where a minimum statistics is present for both distributions. The average (p0 parameter in the figure) is very close to 1. To highlight possible differences in the shape, the cumulative distributions are considered, shown in the right larger panels in the same figures[2]. The cumulative distribution is less sensitive to statistical fluctuations than the distribution from which it is constructed. As it is clear from the figures, in both p_{t} intervals the cumulative distributions in the invariant mass side bands and in the signal regions are compatible. The bin–by–bin ratio confirms this as well.

In Fig. 7.14 and 7.15 (upper panels) the impact parameter distribution for signal D^0 is compared to the impact parameter distribution obtained by subtracting, from the distribution of all the selected candidates, the impact parameter distribution of the candidates in the invariant mass side bands. Background subtraction is performed using the true amount of background instead of the information from the invariant mass fit. The agreement is quite good as it can be also seen from the bin–by–bin ratio in the lower panels. The "modified cuts" were applied in the analysis.

Tests similar to those in Section 7.1.4 can be repeated using the background subtracted impact parameter distribution instead of the signal distribution. Examples of the fits are shown in Fig. 7.16. The results obtained are summarized in Table 7.3 for the "no cuts" and "modified cuts" cases. Of course, due to the larger absolute fluctuations in the impact parameter distribution of the background candidates, larger deviations, arising from background subtraction, are visible in the "no cuts" case. The input fraction is always recovered within errors. Also in this case it must be pointed out that the distributions are not independent, thus systematic trends are possible. This could explain the systematic underestimation of the recovered fractions in the higher p_{t} bin in the "modified cuts" case, absent in the "no cuts" case.

Even if in Table 7.1 the relative error on the background reaches 30% in the two p_{t} interval with the smaller amount of background, it is reasonable to assume that, with a significant statistics the relative error on the background should be contained within 5%. As shown in Table 7.4, a variation of the amount of subtracted background within ±5% causes a variation within ±0.02 in the recovered primary D^0 fractions.

7.1.6 Prospects for the feed–down from B meson correction

The analyses performed so far offer a preliminary overview on the possibility to measure the fraction of primary produced D^0 without relying on Monte Carlo simulations of beauty production. It has been shown that the input fraction is always recovered within errors. With the "modified cuts" the relative error on f_D is $5-10\%$, thus competitive with the systematic

[2]The cumulative distribution of a function $f(x)$ is defined as $F(x) = \int_{-\infty}^{x} f(z)\mathrm{d}z$

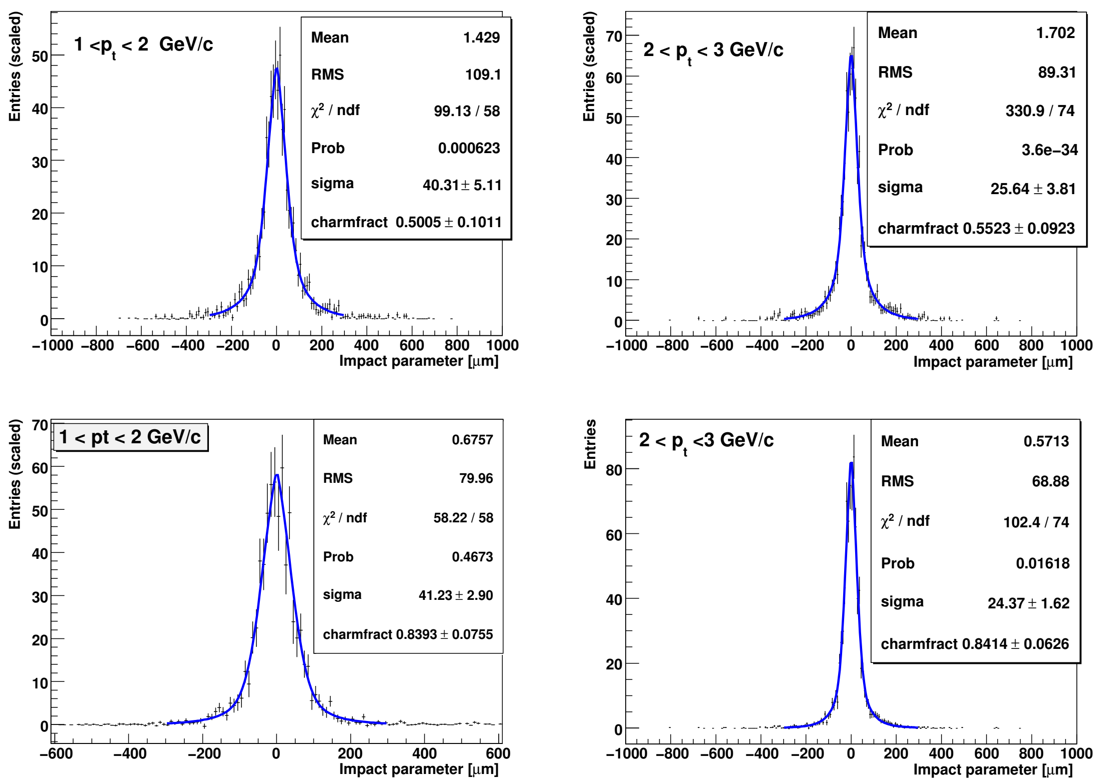

Figure 7.16: Fits to the distributions obtained with different cocktails of the impact parameter distribution of primary D^0 after background subtraction and the impact parameter distribution of secondary D^0. The distributions are weighted in order to have a fraction of primary D^0 f_D=0.5 in the two upper panels and 0.85 in the two lower panels. The "modified cuts" have been used for the candidate selection. The fitting function used is defined in Eq. 7.1.

error affecting the f_D calculation from MC simulations. Even if the results are promising the method requires a rather high statistics. It should work safely with the statistics expected after one year data taking ($\sim 10^9$ events). The use of a different set of cut values causes a relevant loss of significance at low p_t, thus a larger statistical error. At higher p_t (> 2 GeV/c) there are no large differences. The results shown in this chapter must be considered as a preliminary test to check the feasibility of the method. The same tests should be repeated on a large minimum bias sample and for different subsamples in order to check that the differences between the recovered and the input primary charm fractions are of statistical origin. Only this kind of test could verify whether the fit error on f_D is realistic or overestimates/underestimates the error. This is of fundamental importance in view of the analysis on the data. The impact parameter distribution of the background candidate might have a different shape in the minimum bias sample with respect to the charm enriched sample: this has also to be checked. The possibility to subtract the background from the study of like–sign pairs has also been considered with positive results (not shown here). Further studies aimed at optimising the cut values and at estimating the minimal statistics needed to use this method are in progress. As already mentioned, the possibility to use template histograms in place of F_{det} and F_B, without any fit and without assuming a functional shape for these terms, is under study. This option could improve the use of the method with tighter cuts, provided that F_{det} remains a "detector" resolution term, i.e. equal for primary and secondary D^0 mesons.

Table 7.3: Recovered primary D^0 fraction f_D and σ_D for different input fractions. Background subtraction exploiting the invariant mass side bands has been applied (see text). σ_D back sub is the σ of the background subtracted distribution fitted with Eq. 7.2. All σ_D are in μm. For each p_t bin the input σ_D is the same indicated in Table 7.2.

p_t bin	input	No cuts			Modified cuts		
[GeV/c]	f_D	f_D reco	σ_D back sub.	σ_D reco	f_D reco	σ_D back sub.	σ_D reco
$1 \div 2$	0.50	0.54 ± 0.08	57 ± 1	59 ± 4	0.50 ± 0.10	41 ± 1	40 ± 5
	0.75	0.72 ± 0.06	57 ± 1	58 ± 3	0.74 ± 0.08	41 ± 1	41 ± 3
	0.85	0.79 ± 0.05	57 ± 1	57 ± 2	0.84 ± 0.08	41 ± 1	41 ± 3
	0.90	0.83 ± 0.05	57 ± 1	57 ± 2	0.89 ± 0.07	41 ± 1	41 ± 3
$2 \div 3$	0.50	0.60 ± 0.06	38.4 ± 0.6	36 ± 2	0.55 ± 0.09	24.4 ± 0.7	26 ± 4
	0.75	0.82 ± 0.04	38.4 ± 0.6	36 ± 2	0.75 ± 0.07	24.4 ± 0.7	25 ± 2
	0.85	0.93 ± 0.04	38.4 ± 0.6	36 ± 1	0.84 ± 0.06	24.4 ± 0.7	24 ± 2
	0.90	0.99 ± 0.14	38.4 ± 0.6	37 ± 1	0.89 ± 0.06	24.4 ± 0.7	24 ± 2
$3 \div 5$	0.50	0.52 ± 0.04	20.7 ± 0.4	19 ± 1	0.53 ± 0.06	17.0 ± 0.1	16 ± 2
	0.75	0.74 ± 0.03	20.7 ± 0.4	20 ± 1	0.75 ± 0.05	17.0 ± 0.1	16 ± 2
	0.85	0.83 ± 0.03	20.7 ± 0.4	19.3 ± 0.8	0.84 ± 0.05	17.0 ± 0.1	16 ± 1
	0.90	0.87 ± 0.03	20.7 ± 0.4	19.3 ± 0.8	0.89 ± 0.05	17.0 ± 0.1	16 ± 1
> 5	0.50	0.53 ± 0.05	11.8 ± 0.2	11 ± 2	0.50 ± 0.04	10.4 ± 0.1	10 ± 1
	0.75	0.77 ± 0.04	11.8 ± 0.2	11.6 ± 0.7	0.71 ± 0.04	10.4 ± 0.1	10 ± 2
	0.85	0.87 ± 0.04	11.8 ± 0.2	11.8 ± 0.6	0.80 ± 0.05	10.4 ± 0.1	10 ± 1
	0.90	0.91 ± 0.03	11.8 ± 0.2	11.8 ± 0.6	0.85 ± 0.05	10.4 ± 0.1	10 ± 1

Table 7.4: Recovered f_D and σ_D varying the amount of background subtracted. σ_D is in μm. The input f_D is 0.85. The results refer to the "modified cuts" case. For each p_t bin the input σ_D is the same indicated in Table 7.2.

p_t bin [GeV/c]	Back. var.(%)	f_D reco	σ_D reco
$1 \div 2$	-5	0.86 ± 0.06	40 ± 2
	-2	0.85 ± 0.07	41 ± 2
	2	0.83 ± 0.08	42 ± 3
	5	0.82 ± 0.10	44 ± 3
$2 \div 3$	-5	0.85 ± 0.06	24 ± 1
	-2	0.85 ± 0.06	24 ± 2
	2	0.84 ± 0.07	25 ± 2
	5	0.83 ± 0.07	25 ± 2

Conclusions

The target of this thesis was the preparation of the measurement of the cross section for the production of D^0 mesons in proton-proton collisions at the ALICE experiment via the exclusive reconstruction of the decay channel $D^0 \rightarrow K^-\pi^+$. The measurement of charm and beauty hadron production in Pb–Pb collisions is one of the main items of the ALICE physics program, allowing the investigation of heavy–quark propagation and hadronization in the hot and dense strongly-interacting medium formed in these collisions. The measurement performed with Pb–Pb collisions must be related to the analogous measurement in proton-proton collisions, where the formation of the QGP is not expected, to extract information on the medium properties.

The strategy adopted to extract the D^0 yield is based on the invariant mass analysis of selected pairs of opposite charge reconstructed tracks. Without any selection, the signal–to–combinatorial background ratio is very low ($\sim 10^{-4}$). Most of the combinatorial background consists of pairs of tracks from particles produced at the primary vertex of interaction. The selection criterion exploits the typical signature of the $D^0 \rightarrow K^-\pi^+$ decay channel, the presence of two opposite charge tracks displaced from the primary vertex of interaction, with a typical impact parameter of the order of 100 μm. For each pair a decay vertex (secondary vertex) is computed. The resolving power to distinguish between secondary and primary vertices is provided by the high spatial resolution on tracks position at the primary vertex deriving from the Inner Tracking System micrometric precision.

The understanding of the response and of the properties the ITS is thus a key element for the measurement of charm production. In particular, misalignment can degrade the detector spatial resolution. Each ITS subdector is composed of many modules (more than 2000 in total) that can be displaced from the design position due to the finite precision of the assembly. The ITS alignment challenge consists in the determination of the real position of each modules: this implies the calculation of more than 13000 parameters (six rototranslation parameters per each module). In this thesis, the ITS alignment problem was studied in details. The results obtained with cosmic data collected during summer 2008 (about 10^5 tracks) for the SSD survey validation and for the ITS alignment with track-based algorithms have been shown [6, 7]. Three different methods have been used to validate the survey measurements performed during SSD assembly and mounting phase. From the first, based on the analysis of double points in SSD module overlaps, it was concluded that the residual misalignment on the position of the modules on the ladder is compatible with the survey precision ($\lesssim 5$ μm) for the local x coordinate. From the analysis of track-to-point residuals and track-to-track matching a spatial effective resolution $\sigma^{\text{eff}}_{\text{loc}\,x} \approx 25$ μm has been estimated. The comparison with the ideal resolution, $\sigma_{\text{loc}\,x} = 18.5$, gives an uncertainty on the ladder position after the survey below 20 μm. The absence of relevant misalignments at module level allows to neglect the alignment of the SSD modules with respect to the ladders, with a consequently huge reduction of the degrees of freedom. Besides this, due to the good alignment status after the survey, the SSD was used as a reference for the track–based alignment of the other ITS sub-detectors.

One of the two alignment algorithms, based on tracks-to-measured-points residuals minimization, has been studied and improved in this work of thesis. It performs a (local) minimization for each single module and accounts for correlations between modules by iterating the procedure until convergence is reached. This "module–by–module iterative" approach has been extensively tested on simulation data, proving its applicability and then used for the SPD alignment with 2008 cosmic data. The alignment quality achieved is comparable to that obtained with the Millepede algorithm, the main ITS alignment method, which performs a global fit to all residuals, extracting all the alignment parameters simultaneously. A 14 μm effective space point resolution is estimated for the SPD in the most precise direction, to be compared with about 11 μm extracted from the Monte Carlo simulation without misalignments. This difference of $\approx 25\%$ (from 11 to 14 μm) is already quite close to the 20%, which is the final target of the alignment. In addition, the measured incidence angle dependence of the spread of the double points residuals is well reproduced by Monte Carlo simulations that include random residual misalignments with a gaussian sigma of about 7 μm. For the time being, the SSD could be aligned only at the level of large sets of ladders with the Millepede algorithm.

After the detector commissioning phase with cosmic data and, in particular, from the study of the residual misalignment affecting the ITS, realistic detector working conditions were established as expected few months after the start up of the LHC operations. Therefore the analysis procedures for the reconstruction of the $D^0 \to K^-\pi^+$ decay channel could be tested in proton-proton collision simulations taking into account a realistic detector scenario. The secondary vertex reconstruction, the cut variables and the raw signal extraction from the invariant mass fit have been described. The statistical error on the raw signal obtained from the analysis of $\sim 3.7 \cdot 10^7$ simulated events is of the order $10 - 15\%$: from this value a statistical error below 5% can be extrapolated for about one year data taking.

The main systematic errors derive from the efficiency correction and from the B mesons feed–down. To recover the number of produced D^0, the raw signal is divided by an efficiency factor accounting for the fraction of D^0 not reconstructed due to the limited detector acceptance or rejected by the cut selection. The efficiency correction is calculated, using Monte Carlo generated events, as the ratio between the reconstructed and the generated D^0. Systematic errors arise if the momentum spectrum of the generated mesons and the detector properties and response are not correctly reproduced in the simulation. Misalignment can be one of the main causes of this discrepancy. Tools to monitor the alignment quality module–by–module reducing this possibility are under development. Further studies to quantify the residual misalignment contribution to systematic errors are needed. Previous studies [3] estimated that the overall systematic error due to the efficiency correction is of the order of 10%.

The systematic error on the feed–down from B mesons is due to the theoretical uncertainty on the b quark production at LHC energies. A possible way to extract the fraction of secondary D^0 coming from the decay of a B meson directly from data without relying on Monte Carlo simulations of B hadron production has been presented. The fraction of primary D^0 is recovered via a fit to the impact parameter distribution of the reconstructed candidate D^0. The primary D^0 meson impact parameter is basically determined by the spatial precision on the kaon and pion track position at the primary vertex. This is described by a Gaussian-like detector resolution term in the fitting function. The shape of the impact parameter distribution of secondary D^0 is described by the convolution of the same detector resolution function with a double exponential term accounting for the B decay lenght ($c\tau \sim 460-490$ μm). Preliminary tests have shown that the fraction of primary D^0 mesons is generally recovered within 5%. This approach is thus competitive with the theoretical correction. However the method requires a rather high statistics. Moreover, a different set of cut values must be adopted for the method to work properly. This results in a slightly lower significance, thus a slightly larger statistical error. Further studies aimed to optimize the cut values and to estimate the minimal statistics needed to use this method are in progress.

Appendix A

Soft and hard particle production

As described in [20], according to QCD and asymptotic freedom, the production of high-$p_{\rm t}$ partons can be calculated perturbatively and is proportional to the number of binary nucleon-nucleon collisions that, for a nucleus-nucleus collision $A{+}B$ at impact parameter b, is given by

$$N_{\rm coll}(b) = \sigma_0 \int dx\, dy\, T_A(x{+}b/2, y) \cdot T_B(x{-}b/2, y). \tag{A.1}$$

In the formula, σ_0 is the total inelastic nucleon-nucleon cross section, the integral is over the transverse plane, and $T_A(x,y) = \int \rho_A(x,y,z)\, dz$ is the nuclear thickness function of a nucleus of mass A with density profile ρ_A. The impact parameter b can be estimated from the total charge multiplicity, by equating equal fractions of the total multiplicity divided by the maximum multiplicity measured in the most central collisions with the corresponding fractions of the total cross section, calculated geometrically as a function of b [98]. For a fixed impact parameter the number of produced hadrons fluctuates, hence, the determination of b from $dN_{\rm ch}/dy$ has an uncertainty of a fraction of 1 fm, which induces a corresponding uncertainty in the relation between $N_{\rm coll}$ and $dN_{\rm ch}/dy$ [98].

The argument that hard particle production should scale $\sim N_{\rm coll}$ exploits the fact that hard particles are produced on short time scales $\tau \sim 1/p_{\rm t}$, and that hard particle production on successive nucleons in the nucleus therefore happens incoherently. Converesly, soft hadron production involves the coherent scattering of a projectile nucleon with several target nucleons, due to the Landau-Pomeranchuk-Migdal (LPM) effect of a finite formation (or "decoherence") time (see for instance [100] for an explanation of the LPM effect). The net result of the LPM effect is a reduction of soft particle production by destructive interference, resulting in its phenomenologically observed approximate scaling with the number $N_{\rm part}$ of participating (or "wounded") nucleons: each struck nucleon contributes only once to soft particle production, and, suffering more than one collision in sequence, does not increase the soft particle yield. The number $N_{\rm part}$ of wounded nucleons can be calculated geometrically, by a formula similar to Eq. (A.1) but involving the sum of the nuclear thickness functions instead of their product (see e.g. Ref. [99]).

Cronin–Effect

In the 5% most central Au–Au collisions at $\sqrt{s_{\rm NN}} = 200$GeV at RHIC, the average number of participating nucleons is $\langle N_{\rm part}\rangle \approx 344$ (i.e. 172 times higher than in a p+p collision) whereas the number of binary nucleon–nucleon collisions is $\langle N_{\rm coll}\rangle \approx 1074$ (i.e.1074 times higher than in a p+p collision) [98]. The difference between "participant scaling" (expected for soft particles) and "binary collision scaling" (expected for hard processes) is in this case a factor of $1074/172 = 6.2$. In the absence of energy loss, $R_{AA} = 1$ is expected for particles whose production scales with $N_{\rm coll}$ and $R_{AA} \simeq 0.16$ is expected for particles whose production scales with $N_{\rm part}$. Thus, as a function of increasing $p_{\rm t}$, R_{AA} is expected to rise from a value near 1/6 at low $p_{\rm t}$ to about 1 at high $p_{\rm t}$. However, it has been known for over 25 years from minimum bias proton–nucleus collisions at Fermilab [42] that R_{AA} reaches values even larger than 1 at $p_{\rm t} \gtrsim 2{\rm GeV}/c$ due to the "Cronin effect": at high transverse momenta the $p_{\rm t}$-spectrum of hadrons produced in pA collisions is not only shifted *up* in normalization by a factor $N_{\rm coll} \simeq A$ as appropriate for a hard scattering process, but on top of this, also *horizontally* towards higher $p_{\rm t}$ (which at fixed $p_{\rm t}$, manifests itself as an additional gain due to the falling shape of the $p_{\rm t}$-spectrum). The latter feature arises from the fact that the partons inside the projectile nucleon, before making the hard collision which ends up producing the measured high-$p_{\rm t}$ hadron, already suffer multiple elastic collisions with other target nucleons which they encounter first, thereby acquiring transverse momentum $k_{p_{\rm t}}$ which grows in a random walk with the square root of the number of elastic collisions. The extra "initial $k_\perp$" is then reflected statistically as an extra $k_{p_{\rm t}}$ for the hard parton produced in the hard inelastic scattering process from which the final high–$p_{\rm t}$ hadron is observed. The Cronin enhancement is expected to disappear as $p_{\rm t} \to \infty$ and to become weaker as the collision energy increases. Due to the Cronin enhancement at intermediate $p_{\rm t}$ [101], the *nuclear modification factor*, $R_{\rm AA}$, defined in Eq. 1.8, should approach the value 1 at large $p_{\rm t}$, not from *below* due to soft scaling at low $p_{\rm t}$, but rather from *above*.

Bibliography

[1] K. Aamodt *et al.* [ALICE Collaboration], Journal of Instrumentation **3** (2008) S08002.

[2] F. Carminati *et al.* [ALICE Collaboration], J. Phys. G: Nucl. Part. Phys. **30** (2004) 1517.

[3] B. Alessandro *et al.* [ALICE Collaboration], J. Phys. G: Nucl. Part. Phys. **32** (2006) 1295.

[4] M. Mangano, P. Nason and G. Ridolfi, Nucl. Phys. B **373** (1992) 295.

[5] V. Blobel and C. Kleinwort, contribution to the Conference on Advanced Statistical Techniques in Particle Physics, Durham, March, 18–22, 2002.

[6] A. Dainese, A. Rossi, M.V. Leeuwen, ALICE Internal Note, ALICE-INT-2009-045 (2009).

[7] C. Bombonati *et al.*, ALICE Internal Note, ALICE-INT-2009-035 (2009).

[8] D. Acosta *et al.* [CDF Collaboration], Phys. Rev. Lett. **91** (2003) 241804.

[9] F. Karsch *et al.*, Phys. Rev. B**478** (2000) 447.

[10] K.G. Wilson, Phys. Rev. D **10** (1974) 2445.

[11] P. Braun–Munzinger and J. Stachel, NATURE **448** (2007) 302-309.

[12] M.E. Peskin and D.V. Schroeder, *An Introduction to Quantum Field Theory*, Addison Wesley (1995).

[13] F. Halzen and A.D. Martin,*Quarks & Leptons*, John Wiley & Sons (1984).

[14] C. Alcock, *The Astrophysics and Cosmology of Quark-Gluon Plasma*, in *Quark-Gluon Plasma*, Springer-Verlag (1990).

[15] P. Coles and F. Lucchini, *COSMOLOGY, The Origin and Evolution of Cosmic Structure*, John Wiley & Sons (2003).

[16] F. Karsch and E. Laermann, Phys. Rev. D **50** (1994) 6954.

[17] B.I. Abelev *et al.* [STAR Collaboration], Phys. Rev. C **79** (2009) 034909.

[18] J.D.Bjorken, Phys. Rev. D **27**, Number 1 (1983).

[19] Margetis,S. *et al.* [NA49 Collaboration], Phys. Rev. Lett. **75** (1995) 3814.

[20] U. Heinz,*Concepts of heavy–ion physiscs*, arXiv:hep-ph/0407360 v1 (2004).

[21] J. Adams *et al.* [STAR Collaboration], Phys. Rev. Lett. **92** (2004) 052302.

[22] J. Adler *et al.* [STAR Collaboration], Phys. Rev. Lett. **87** (2001) 182301.

[23] J. Adams *et al.* [STAR Collaboration], Nucl. Phys. A **757** (2005) 102-183.

[24] R. Snellings for the STAR and ALICE Collaborations, Eur. Phys. J. C **49** (2007) 87-90.

[25] F. Beccattini and G. Pettini, Phys. Rev. C **67** 015205 (2003).

[26] A. Andronic *et al.*, Nucl. Phys. A **772** (2006) 167-199.

[27] K. Fanebust *et al.* [NA57 Collaboration], J. Phys. G: Nucl. Part. Phys. **28** (2002) 1607.

[28] T. Matsui and H. Satz, Phys. Lett. B **178** (1986).

[29] F. Karsch, D. Kharzeev and H. Satz, Phys. Lett. B **637** (2005).

[30] A. Adare *et al.* [PHENIX Collaboration] Phys. Rev. Lett. **101** (2008) 122301.

[31] C. Young and E. Shuryak, Phys. Rev. C **79** (2009) 034907.

[32] R.L. Thews and M.L. Mangano, Phys. Rev. C **73** (2006) 014904.

[33] M.B. Johnson *et al.*, Phys. Rev. Lett. **86** (2001) 4483.

[34] V. Guzey *et al.*, Phys. Lett. B **603** (2004) 173.

[35] R. Baier *et al.*, Ann. Rev. Nucl. Part. Sci. **50** (2000) 37.

[36] S. Gavin and R. Vogt, Nucl. Phys. A **610** (1996) 442c.

[37] S. S. Adler *et al.* [PHENIX Collaboration], Phys. Rev. Lett. **96** (2006) 202301.

[38] J. Adams *et al.* [STAR Collaboration], Phys. Rev. Lett. **91** (2003) 072304.

[39] J. Adams *et al.* [STAR Collaboration], Phys. Rev. Lett. **91** (2003) 172302.

[40] S. S. Adler *et al.* [PHENIX Collaboration], Phys. Rev. Lett. **91** (2003) 072301.

[41] S. S. Adler *et al.* [PHENIX Collaboration], Phys. Rev. Lett. **94** (2005) 232301.

[42] D. Antreasyan, J.W. Cronin, H.J. Frisch, M.J. Shochet, L. Kluberg, P.A. Piroue and R.L. Sumner, Phys. Rev. D **19** (1979) 764.

[43] C. Adler *et al.* [STAR Collaboration], Phys. Rev. Lett. **90** (2003) 032301.

[44] J. Adams *et al.* [STAR Collaboration], Phys. Rev. Lett. **93** (2004) 252301.

[45] S. Mioduszewski *et al.* [PHENIX Collaboration], Nucl. Phys. A **715** (2003) 199c-208c.

[46] S. Esumi for the PHENIX Collaboration, J. Phys. G: Nucl. Part. Phys. **36** (2009) 064060.

[47] S. Salur for the STAR Collaboration, Eur. Phys. J. C **61** (2009) 761-767.

[48] J. Putschke for the STAR Collaboration, Eur. Phys. J. C **61** (2009) 629-635.

[49] S. Salur for the STAR Collaboration, Eur. Phys. J. C **62** (2009) 119-165.

[50] P.M. Jacobs and M. van Leeuwen, Nucl. Phys. A **774** (2006) 237-246.

[51] K.J. Eskola, K. Kajantie, P.V. Ruuskanene and K. Tuominen, Nucl. Phys. B **570** (2000) 379.

[52] K. Kajantie, Nucl. Phys. A **715** (2003) 432c.

[53] V.N. Gribov, L.N. Lipatov, Sov. J. Nucl. Phys. **15** (1972) 438 and 675;
G. Altarelli, G. Parisi, Nucl. Phys. B **126** (1977) 298;
Yu.L. Dokshitzer, Sov. Phys. JETP **46** (1977) 641.

[54] Proceedings of the workshop "HERA and the LHC A workshop on the implications of HERA for LHC physics", DESY-PROC-2005-001 (2005), DESY-PROC-2009-002 (2008).

[55] K.J. Eskola *et al.*, International Journal of Modern Physics E **12** (2003) 177-195.

[56] ALICE collaboration, Eur. Phys. J. C **65** (2010) 111.

[57] A.Dainese, *Charm production and in-medium QCD energy loss in nucleus-nucleus collisions with ALICE. A performance study*, PHD thesis (2003).

[58] C. Amsler *et al.* [Particle Data Group], Phys. Lett. B **667** (2008) 1-1340.

[59] G. Altarelli, M. Diemoz, G. Martinelli and P. Nason, Nucl. Phys. B **308** (1988) 724.

[60] A. Adare *et al.* [PHENIX Collaboration], Phys. Rev. Lett. **97** (2006) 252002.

[61] A. Adare *et al.* [PHENIX Collaboration], Phys. Rev. Lett. **98** (2007) 172301.

[62] B.I. Abelev *et al.* [STAR Collaboration], http://www.citebase.org/abstract?id=oai:arXiv.org:0805.0364 (2008).

[63] J. Adams *et al.* [STAR Collaboration] Phys. Rev. Lett. **94** (2005) 062301.

[64] M. Cacciari *et al.*, Phys. Rev. Lett. **95** (2005) 122001.

[65] N. Carrer and A. Dainese, ALICE Internal Note, ALICE-INT-2003-019 (2003).

[66] A.D. Martin, R.G. Roberts, W.J. Stirling and R.S. Thorne, Eur. Phys. J. C **4** (1998) 463.

[67] H.L. Lai *et al.* [CTEQ Collaboration], Eur. Phys. J. C **12** (2000) 375.

[68] M. Gyulassy and X.N. Wang, Nucl. Phys. B **420** (1994) 583, arXiv:nucl-th/9306003.

[69] R. Baier, Y.L. Dokshitzer, A.H. Mueller, S. Peigne and D. Schiff, Nucl. Phys. B **483** (1997) 291, arXiv:hep-ph/9607355.

[70] R. Baier, Y.L. Dokshitzer, A.H. Mueller, S. Peigne and D. Schiff, Nucl. Phys. B **484** (1997) 265, arXiv:hep-ph/9608322.

[71] B.G. Zakharov, JETP Lett. **63** (1996) 952, arXiv:hep-ph/9607440.

[72] U.A. Wiedemann, Nucl. Phys. B **588** (2000) 303, arXiv:hep-ph/0005129.

[73] C.A. Salgado and U.A. Wiedemann, Phys. Rev. D **68** (2003) 014008, arXiv:hep-ph/0302184.

[74] M. Gyulassy, P. Levai and I. Vitev, Nucl. Phys. B **571** (2000) 197, arXiv:hep-ph/9907461.

[75] M. Gyulassy, P. Levai and I. Vitev, Phys. Rev. Lett. **85** (2000) 5535, arXiv:nucl-th/0005032.

[76] M. Gyulassy, P. Levai and I. Vitev, Nucl. Phys. B **594** (2001) 371, arXiv:nucl-th/0006010.

[77] A. Dainese, C. Loizides and G. Paic, Eur. Phys. J. C **38** (2005) 461, arXiv:hep-ph/0406201.

[78] K.J. Eskola, H. Honkanen, C.A. Salgado and U.A. Wiedemann, Nucl. Phys. A **747** (2005) 511, arXiv:hep-ph/0406319.

[79] A. Accardi, M. Gyulassy, Phys. Lett. B **586** (2003) 244, arXiv:nucl-th/0308029.

[80] M.G. Mustafa, D. Pal, D.K. Srivastava and M. Thoma, Phys. Lett. B **428** (1998) 234, arXiv:nucl-th/9711059.

[81] Z.w. Lin and R. Vogt, Nucl. Phys. B **544** (1999) 339.

[82] Y.L. Dokshitzer and D.E. Kharzeev, Phys. Lett. B **519** (2001) 199.

[83] Y.L. Dokshitzer, V.A. Khoze and S.I. Troian, J. Phys. G: Nucl. Part. Phys. **17** (1991) 1602.

[84] N. Armesto, C.A. Salgado and U.A. Wiedemann, Phys. Rev. D **69** (2004) 114003, arXiv:hep-ph/0312106.

[85] N. Armesto, A. Dainese, C.A. Salgado and U.A. Wiedemann, Phys. Rev. D **71** (2005) 054027, arXiv:hep-ph/0501225.

[86] A. Dainese, J. Phys. G: Nucl. Part. Phys. **31** (2005) S589, arXiv:hep-ph/0501292.

[87] S.S. Adler *et al.* [PHENIX Collaboration], Phys. Rev. Lett. **91** (2003) 072303.

[88] M. Biasini *et al.*, Proceedings of the workshop “HERA and the LHC 2nd workshop on the implications of HERA for LHC physic” DESY-PROC-2009-002 (2008).

[89] R. Vogt, Eur. Phys. J. Special Topics **155** (2008) 213–222.

[90] S.S. Adler *et al.* [PHENIX Collaboration], Phys. Rev. Lett. **96** (2006) 032301.

[91] B.I. Abelev *et al.* [STAR Collaboration], Phys. Rev. Lett. **98** (2007) 192301.

[92] W.A. Zajc, J. Phys. G: Nucl. Part. Phys. **36** 064043 (2009).

[93] C. Ivan, PHD thesis, Utrecht University, 2009.

[94] E. Bruna, PHD thesis, Università degli Studi di Torino, 2007.

[95] S. Senyukov, PHD thesis, Università degli Studi di Torino, 2009.

[96] R. Romita, PHD thesis (in Italian), Università degli Studi di Bari, 2009.

[97] TOTEM, *Total cross section, elastic scattering and diffractive dissociation at the LHC: Technical Proposal*, CERN-LHCC-99-007; LHCPP-P-5 (1999).

[98] D. Kharzeev and M. Nardi, Phys. Lett. B **507** (2001) 121.

[99] P.F. Kolb, P. Huovinen, U. Heinz, K. Eskola and K. Tuominen, Nucl. Phys. A **696** (2001) 175.

[100] M. Gyulassy and M. Plümer, Phys. Lett. B **243** (1990) 432; M. Gyulassy and X.N. Wang, Nucl. Phys. B **420** (1994) 583; X.N. Wang, M. Gyulassy and M. Plümer, Phys. Rev. D **51** (1995) 3436.

[101] X.N. Wang, Phys. Rev. C **61** (2000) 064910.

[102] ALICE Time Of Flight, Technical Design Report, CERN/LHCC 2000-12.

[103] ALICE Off-line framework, AliRoot, http://aliceinfo.cern.ch/Offline

[104] R. Grosso, in *Proceedings of the first LHC Detector Alignment Workshop*, September 4 - 6 2006, CERN.

[105] A. Rashevsky et al., Nucl. Inst. Meth. A **572** (2007) 125.

[106] G. Batigne et al., Journal of Instrumentation **3** (2008) P06004.

[107] ROOT, http://root.cern.ch.

[108] T.Sjöstrand, P.Edén,C.Friberg,L.Lönnblad,G.Miu,S.Mrenna and E.Norrbin, Computer Phys. Commun. **135** (2001);
T.Sjöstrand, Compuetr Phys. Commun. **82** 74;
The code can be found at http://www.thep.lu.se/ torbjorn/Pythia.html

[109] Wang X-N and M. Gyulassy, Phys. Rev. D **44** 3501 (1991);
M. Gyulassy and Wang X-N Comput. Phys. Commun. **83** 307-31 (1994);
The code can be found at http://www-nsdth.lbl.gov/ xnwang/hijing/

[110] R. Brun, F. Bruyant, M. Maire, A.C. McPherson and P. Zanarini *GEANT3 User Guide* CERN Data Handling Division DD/EE/84-1 (1985) http://wwwinfo.cern.ch/asdoc/geantold/GEANTMAIN.html

[111] S. Agostinelli *et al*, *Geant4 A Simulation Toolkit* CERN-IT-20020003 (2003), KEK Preprint 2002-85, SLACPUB- 9350; Nucl. Inst. Meth. A **506** 250 http://wwwinfo.cern.ch/asd/geant4/geant4.html

[112] Fass'o A *et al* Proc. Computing in High Energy and Nuclear Physics (La Jolla, CA) (2003) http://www.slac.stanford.edu/econf/C0303241/proc/papers/MOMT004.PDF

[113] E. Bruna et al., ALICE Internal Note 2009-018 (2009).

[114] B. Batyunya, Yu. Belikov, K. Šafařík, ALICE Internal Note, ALICE-INT-97-24 (1997).

[115] P. Saiz *et al*, Nucl. Inst. Meth. A **502** (2003) 437-440 .

[116] http://alien.cern.ch.

[117] V. Karimaki *et al.*, CMS Note 1997/051 (1997).

[118] M. Chemarin *et al.* [L3 Collaboration], Nucl. Phys. Proc. Suppl. **85** (2000) 361.

[119] C. Bombonati *Commissioning of the Silicon Pixel Detector of ALICE and perspectives for beauty production at LHC*, PHD thesis.

[120] F. Prino, *Results from the commissioning of the ALICE Inner Tracking System with cosmics*, arXiv/0907.2848 (2009).

[121] A. Rivetti *et al.*, Nucl. Inst. Meth. A **541** (2005) 267.

[122] F. Agnese *et al.*, Nucl. Inst. Meth. A , **562** (2006) 110-119.

[123] S. Blusk, *et al.*, in *Proceedings of the first LHC detector alignment workshop*, CERN, September 4–6, 2006, CERN-2007-004.

[124] F.-P. Schilling, *Proceedings of the first LHC detector alignment workshop*, CERN, September 4–6, 2006, CERN-2007-004.

[125] V. Karimaki *et al.*, CMS Note 2006/008 (2006).

[126] P. Brückman de Renstrom, *Proceedings of the first LHC detector alignment workshop*, CERN, September 4–6, 2006, CERN-2007-004.

[127] V. Blobel, in *Proceedings of the first LHC detector alignment workshop*, CERN, September 4–6, 2006, CERN-2007-004.

[128] R.A. Frazer, W.J. Duncan and A.R. Collar, *Elementary Matrices and Some Applications to Dynamics and Differential Equations*, Cambridge University Press, Cambridge (1938).

[129] G.E. Bruno *et al.*, ALICE Internal Note 2005-011 (2005).

[130] G.E. Bruno *et al.*, ALICE Internal Note 2005-022 (2005).

[131] S. Petrera and G. Romano, Nucl. Inst. Meth. **174** (1980) 61.

[132] R. Bala, A. Dainese and A. Rossi, ALICE Internal Note, ALICE-INT-97-24 (2009).

[133] A. Rossi, Diploma thesis (in Italian), http://alice.pd.infn.it/docs/TesiRossi.pdf

Acknowledgements

I would like to thank all the people that helped me in the development of this thesis and supported me in this three-years PHD experience.
First of all I would really like to thank Andrea Dainese, for his constant help and all his advices. Without his expertise the best parts of this thesis could never be written.
Thanks to my supervisor, Enrico Fragiacomo, for all the suggestions and his constant support. Giacomo Vito Margagliotti always supported me by encouraging me to attend schools, conferences and to spend time at CERN; he and Enrico always fulfilled my needs with blind trust. I want to thank Paolo Camerini for his humanity and for all the precious hints on the writing of this thesis. I am looking at the words I am writing on a wonderful monitor that Rosario Turrisi provided me. Thanks for this and for all the opportunities you offered me.

Many people contributed to this thesis. I really enjoyed working with Sandra Moretto and Marcello Lunardon, who also gave me important advices for the writing of the alignment chapters. Chiara Bianchin helped me substantially, I really owe a a lot of work to her (the promised beer is coming!). I am grateful to all the people in the ITS Alignment group, in particular to Marco van Leeuwen, Adam Jacholkowski, Cvetan Cheshkov, for the many fruitful discussions. Thanks to Francesco Prino for the information on the ITS commissioning. I am also grateful to Federico Antinori and to all the people I worked with in the D2H group for the useful suggestions about charm analysis. Thanks to Renu Bala to share the efforts on the GRID.

Then I would like to thank Rinaldo Rui for accepting being my supervisor and all people in the Trieste ALICE group. Thanks to Giacomo Contin (and Alessia too) for their hospitality (I am waiting for you in Padova), Massimo Venaruzzo (...torneremo campioni!) and Raffaele Grosso. Thanks to Marco Bregant who saved me from a night under the rain!
I spent most of these three years in Padova, and I really enjoyed to share my office with Andrea, Julien Faivre and his sweet French expressions and now with Raghunath Sahoo. I would like to thank all other ALICE people there, in particular Davide Caffarri, Yuan Xian Bao (and Hao Xin too for the wonderful Chinese dinners), Maurizio Morando, Daniela Fabris, Francesca Soramel, Giuseppe Viesti and Silvia Pesente. Thanks to Carlo Bombonati for the time spent together complaining on root (but on Monkey Island secrets too) and because now we know how to frighten a herd of enraged bulls with a sewing needle.

I am extremely grateful to my parents for their love and constant, unreserved support. Thanks to my brother Paolo, his wife Elisa and the best news of 2009 ...the little Davide! Thanks to my uncle Ennio (in bocca al lupo!), who is still waiting for me to discover a new form of energy and to all my relatives.

Then, all my friends in Mantova, Mauro, Alice, Tino, Tania, Lusaz, Vanya, Izio, Angela, Mazzo, Manu e Fabri and in Padova, Miki, Enrico, Just, Tullio Saverio, Verroi, Phobos, Seba, Lucia, Marcos, Andrea Degiu, Davide, Simone, Kate, Nicola and Nicoletta: too many reasons to thank all of you here, I will do it in front of a bottle of good wine!

My special thank and all my love goes to Elisa, who colours my hours with her presence. Thanks for your incomparable help, this thesis is dedicated also to you, and to our future!